Title
Engineering Tools to Study and Control Signaling in Neural Stem Cells

Author
Spelke, Dawn Pall

Publication Date
2015

Peer reviewed|Thesis/dissertation

Engineering Tools to Study and Control Signaling in Neural Stem Cells

By

Dawn Pall Spelke

A dissertation submitted in partial satisfaction of the

requirements for the degree of

Joint Doctor of Philosophy
with the University of California, San Francisco

in

Bioengineering

in the

Graduate Division

of the

University of California, Berkeley

Committee in charge:

Professor David V. Schaffer, Chair
Professor Zev J. Gartner
Professor Henk Roelink

Fall 2015

Abstract

Engineering Tools to Study and Control Signaling in Neural Stem Cells

by

Dawn Pall Spelke

Doctor of Philosophy in Bioengineering

University of California, Berkeley

Professor David V. Schaffer, Chair

Adult neurogenesis, the process by which new neurons develop in the adult mammalian central nervous system, was thought to be nonexistent by accepted scientific dogma until the discovery of adult neural stem cells (NSCs) in the 1990s. NSCs have been found in two regions of the adult brain: the subventricular zone of the lateral ventricles and the subgranular zone of the hippocampal dentate gyrus, and have the capacity to differentiate into neurons, astrocytes, and oligodendrocytes. Importantly, hippocampal NSCs play key roles in learning and memory, and have been implicated in a number of pathologies, including Alzheimer's disease. NSCs reside in complex niches that provide the physical, chemical, and biological signals regulating stem cell maintenance and differentiation. A thorough understanding of NSC biology and niche signals can provide both insight into the mechanisms of adult neurogenesis, and inform stem cell based therapeutics to treat neurological injury and disease. Since the discovery of NSCs, a body of work has emerged characterizing the wide array of signals and intracellular pathways that mediate NSC behavior. Some of these findings, however, point to complex signaling mechanisms, the further study of which requires techniques outside the standard biological "toolbox". The goal of this dissertation, therefore, was to engineer novel tools to enable the study and control of complex signaling systems in NSCs, and their application towards novel biological discoveries.

The work presented here investigates two aspects of NSC biology: heterogeneity and cell-cell signaling. Stem cells are inherently heterogeneous; NSCs give rise to diverse progeny, including neurons and astrocytes, and *in vitro,* NSCs can differentially respond to the same set of cues. To probe this heterogeneity, a single cell Western blotting (scWestern) platform was developed. scWesterns enabled the interrogation of the proteome of thousands of single cells in about four hours, and multiplexing allowed for up to eleven targets to be detected from a single cell. We utilized the scWestern to probe heterogeneity in NSC signaling upon mitogen stimulation and differentiation. These studies provided unprecedented insight into differential single NSC responses to homogenous presentation of proliferation and differentiation factors.

Cell-cell signaling in the NSC niche is comprised of paracrine and juxtacrine signals presented by supportive niche cells. Ephrin-B2 on hippocampal astrocytes was recently discovered to induce NSC neuronal differentiation through the receptor EphB4. Ephs and ephrins are both cell-

surface bound and require oligomerization for downstream signal activation, so further investigation of ephrin-B2-mediated neurogenesis can benefit from novel tool development. This system was the focus of three studies, comprising the remainder of the dissertation. First, to better recapitulate the physical interactions between membrane-bound receptors and ligands, a supported lipid bilayer system was developed to present laterally mobile, monomeric ephrin-B2 to NSCs. We observed EphB4/ephrin-B2 co-clustering, and for the first time showed membrane-bound monomeric ephrin-B2 activation of EphB4 signaling and NSC differentiation in a synthetic system. By employing spatial mutation strategies to control ephrin-B2 diffusion and receptor-ligand complex size, we demonstrated that EphB4 signaling and NSC differentiation are sensitive to spatial properties of apposing cell membranes. This finding reveals novel regulatory mechanisms of both EphB4 signaling and NSC niche dynamics.

Established Eph:ephrin signaling targets do not overlap with known neurogenic factors, so we next investigated ephrin-B2-induced downstream signaling in NSCs. Utilizing multivalent ephrin-B2 conjugates to enhance stimulation and mass spectrometry to identify signaling effectors, a number of novel kinases were identified, including activated Cdc42 kinase 1 (Ack1), Fyn proto-oncogene (Fyn), and Src proto-oncogene (Src). CRISPR/Cas9 genome engineering was then employed to knock down these proteins, which prevented ephrin-B2-induced NSC neurogenesis, demonstrating a role for these kinases in signaling downstream of EphB4 stimulation. Ack1 is a novel effector of Eph:ephrin signaling, and Ack1 and Fyn are novel regulators of NSC differentiation; therefore, this work reveals a number of previously unknown biological mechanisms.

Finally, to examine dynamics of EphB4 signaling in NSCs, optogenetic methods for ephrin-independent Eph clustering and activation in response to blue light were created. We first developed generalized tools to apply a recently published method of optically targeting, clustering, and stimulating transmembrane receptors towards any signaling system of interest. We then harnessed these tools to study EphB4 signaling in NSCs by testing a number of EphB4-targeting optogenetic constructs. While none of the tested vectors were able to cluster and activate EphB4, a number of interesting observations were made that point to future areas for optimization. Moreover, we were able to perform a proof-of-concept study of the application of the generalized optogenetic tools developed.

In summary, this dissertation presents work on both the development of novel tools for probing stem cell complexities, and the implementation of these tools towards the discovery of a number of novel biological mechanisms.

Table of Contents

List of Figures

List of Tables

Acknowledgements

The years I have spent in graduate school have been stimulating, insightful, and sometimes difficult. I learned more about the scientific process and myself than I ever could have imagined when I started. The many individuals who guided, supported, and encouraged me throughout this journey made my PhD both attainable and rewarding, and for this I thank you wholeheartedly.

First, to my graduate advisor Dave Schaffer, my PhD would not have been possible without your mentorship and advice over the past six and a half years. Your passion for science was infectious and I found every meeting with you enlightening and encouraging. You gave me the freedom to pursue my interests and the guidance to succeed. I can only hope one day to be as strong of a scientist and as effective of a mentor as you have demonstrated time and again.

To my committee members, Zev Gartner and Henk Roelink, I greatly appreciate the feedback and support you have provided over the years on both my qualifying exam and dissertation.

The Schaffer Lab was an amazing place to carry out my PhD work and I cannot thank the many members over the years enough for the help, camaraderie, and encouragement. To Noem, you kept the lab running and your support both professionally and personally meant so much to me. To Randolph Ashton, Albert Keung, and Anthony Conway, thank you for helping me to get started. I would also like to thank Ashley Fritz, Sisi Chen, Tandis Vazin, Lukasz Bugaj, Thomas Gaj, and many others for the support and fun times both in and out of lab. I especially want to point out two individuals. Prajit Limsirichai, you have been a great colleague and friend; our late night conversations have kept me sane and I cannot express how grateful I have been for your encouragement over the years. And finally, to Jorge Satiago-Ortiz, I could not have asked for a better labmate, neighbor, coffee date, lunch buddy, party goer, bridesman, and above all, lifelong friend. You have been there with me nearly every step of the way, through all of the ups and downs, with a smile on your face and encouraging words. I hope you know how much you mean to me.

Research is a collaborative endeavor and I have been fortunate enough to work closely with a number of great colleagues. To Alex Hughes, Meimei Dong, and Lukasz Bugaj, thank you for sharing your time and expertise with me. I learned so much from all of you and I am extremely proud of the work we accomplished together.

I was also very lucky to mentor three amazing individuals. To Emily Connelly, my undergraduate researcher, thank you so much for all of your time and help; much of this work would not have been possible without your assistance. And, thank you for bearing with me as I learned how to effectively mentor; your patience was very much appreciated. To Delphine Blondel and Christina Fuentes, thank you for your input and hard work. I know you will both continue to have great success as you continue your scientific careers.

My bioengineering cohort provided so much support as we all made it through our PhDs. To my brunch crew Sophie Wong, Yekaterina Miroshnikova, Wiktor Stopka, Arunan Skandarajah, Sergey Boyarskiy, Philip Guan, and Sean McFarland, thank you for the much needed breaks. To

Monica, you have been a truly great friend and shoulder to lean on, as well as a steadfast nails companion. Thank you for always being there. And finally, to Augusto Tentori, Sophie Wong, and Michael Lee, my fellow BE ’09 MITers, we’ve been classmates for a decade – and now we all made it! I especially want to thank Mike; you have been a wonderful roommate and friend. I couldn’t have asked for a better companion to maneuver through undergraduate and graduate school with; through all of the psets, exams, and stress, including moving across the country together, you’ve always been there for me and it has meant so much.

To my amazing family, you have shown me unwavering support during graduate school and I cannot thank you enough. Your understanding during our brief conversations while I walked around Berkeley has meant the world to me. Mom and dad, I could not have asked for better role models. Dad, your advice on navigating academia has been invaluable, and our (too infrequent) phone calls about everything from politics to the state of the fall foliage has kept me grounded. Mom, you are my rock, and your love and encouragement in every aspect of my life has been incredible. To Pam, my twin, your love and support has meant so much to me, and I cannot wait to spend more time with you now that I’m done. To my grandma, you are an inspiration, and your eagerness to see me finish has helped with this final push – you can have your glass of wine now!

Finally, to Don, your love and encouragement during the end of my PhD has been invaluable. You’ve added laughter and adventure to this stressful time in my life, and I cannot wait to see what the future holds.

Chapter 1: Introduction

1.1 Stem Cells

Stem cells are defined by their ability to both self-renew to remain in an undifferentiated state and differentiate into more specified lineages. Since their discovery in the bone marrow of mice in the 1960s[1], stem cells have been an area of intense study and have been found in virtually every multicellular organism. In mammals, two classes of stem cells exist. Pluripotent stem cells, including embryonic stem cells (ESCs), are capable of differentiating into every cell type of the adult body. Adult stem cells are more defined multipotent cells that reside in specific tissues and are capable of differentiating into a restricted set of cell lineages. Examples of adult stem cells include hematopoietic stem cells (HSCs) found in bone marrow and which give rise to blood and immune cells[2], and neural stem cells (NSCs) found in specific neurogenic regions of the adult brain and which give rise to central nervous system (CNS) cells including neurons[3]. Recently, an engineered subclass of pluripotent stem cells termed induced pluripotent stem cells (iPSCs) has emerged. iPSCs are derived from somatic cells, which have been reprogrammed into a pluripotent state though the overexpression of a defined set of genes[4].

Stem cell research holds great promise for basic biological discovery and therapeutic application. In biology, stem cell research furthers our understanding of normal and pathological development, as well as adult function[5]. iPSC technology additionally enables the modeling of genetic diseases by studying iPSCs generated from patients[6], such as the complex neurological disorder Amyotrophic Lateral Sclerosis (ALS)[7]. Therapeutically, stem cells can be utilized in regenerative medicine to replace diseased or damaged cells. Using an *ex vivo* approach, exogenous stem cells are manipulated outside the body and then implanted, where they can migrate, differentiate, and integrate into host tissue. A number of clinical trials have been carried out in this area; these include the injection of mesenchymal stem cells (MSCs) to treat ischemic cardiomyopathy[8], and the transplantation of ESC-derived oligodendrocyte progenitor cells to treat spinal cord injury[9]. An alternative approach is an *in vivo* strategy whereby endogenous stem cells are stimulated by bioactive molecules, proteins, or gene therapy for therapeutic benefit. For example, injection of insulin-like growth factor 1 (IGF-1) has been shown to enhance NSC proliferation in rats[10], and injection of a CXCR4 antagonist in healthy humans led to mobilization of HSCs from bone marrow into blood[11]. The potential of stem cells therapies is truly incredible, but continuing progress will depend upon our ability to dissect the complexities of stem cell biology.

1.2 The Stem Cell Niche

The stem cell niche is the *in vivo* microenvironment in which stem cells reside (Fig. 1.1). The niche provides the physical, chemical, and biological signals that regulate stem cell maintenance and differentiation. Of note, stem cell signaling and differentiation are inherently heterogeneous processes, as single cells can give rise to diverse progeny during development and stem cell populations *in vitro* can differentially respond to the same set of cues. A method to study this heterogeneity will be the focus of some of the work presented here. Components of the niche include soluble factors, neighboring niche cells, the extracellular matrix, and biomechanical forces. Niche components are highly combinatorial and dynamic, resulting in complex

intracellular signaling and cellular responses. A number of excellent reviews on stem cell niche biology have been published[12,13], so for the purpose of providing an introduction to the work that follows, soluble factors and cell-cell interactions will be the focus here.

Soluble ligands in the stem cell niche include growth factors, hormones, and cytokines that bind to stem cell surface receptors to induce downstream signaling and regulate cell behavior. They may be received by the stem cell from cells in a remote location in the body (endocrine), neighboring niche cells (paracrine), or the stem cell itself (autocrine). The elicited cell response is concentration dependent and often influenced by a complex interplay between many signaling factors. For example, the relative concentration of multiple cytokines has been shown to influence HSC expansion[14]. The temporal presentation of soluble ligands can also influence stem cell responses, a phenomenon particularly apparent during development. For instance, neural patterning is dependent on both the concentration and timing of the morphogen sonic hedgehog (Shh)[15]. Additionally, the spatial presentation of soluble ligands may be altered by immobilization to the ECM or cell surface, which functions to increase local concentration as well as alter stability. For example, heparan sulfate proteoglycans can bind to and concentrate signaling molecules containing heparin binding domains[16]. In ESCs, heparin has been shown to facilitate fibroblast growth factor (FGF) and bone morphogenic protein (BMP) dependent mesoderm lineage commitment[17]. Spatial organization of soluble niche factors can also be controlled by lipid modification. For instance, Shh and Wingless (Wnt) proteins utilize lipid tails to anchor and localize to cellular lipid membranes[18]. Lipid modifications may also influence the soluble form of signaling molecules, such as Shh, which can form multimers that are freely diffusible and able to engage in long-range signaling[19].

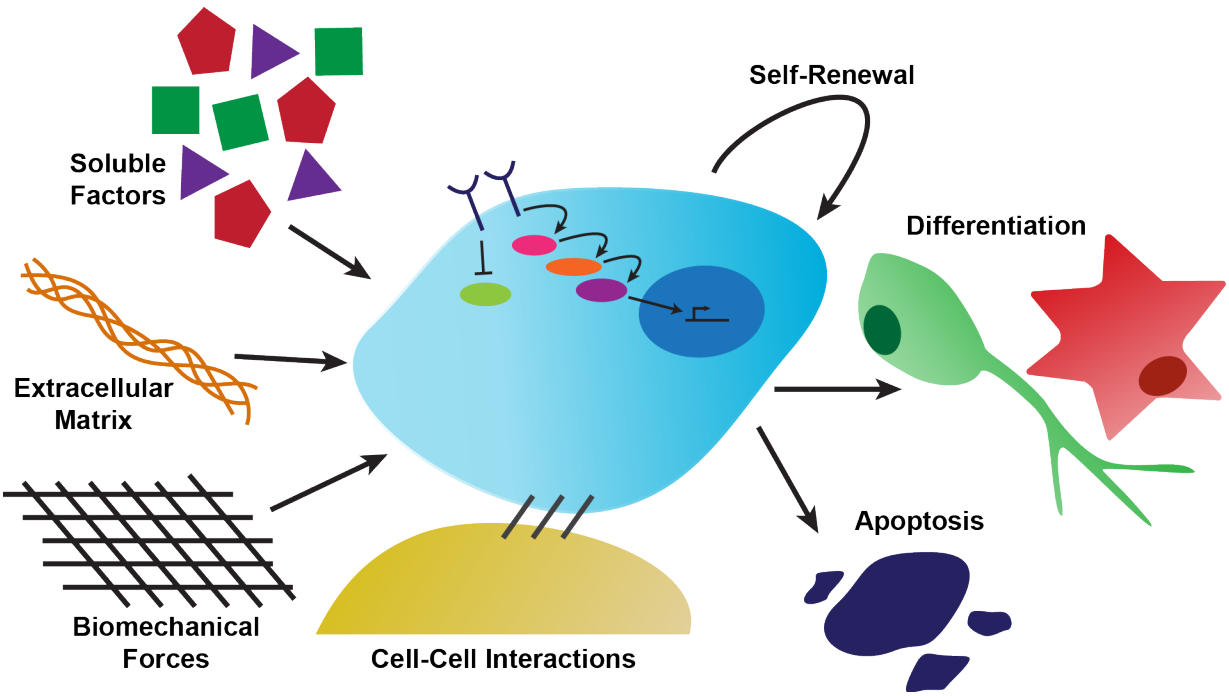

Figure 1.1. **The stem cell niche.** Niche signals include soluble factors, extracellular matrix proteins, biomechanical forces, and cell-cell interactions. These stimuli are transduced in the stem cell through signaling cascades, leading to changes in gene expression. In response, stem cells can self-renew, differentiate, or undergo apoptosis.

Cell-cell interactions in the stem cell niche are comprised of both paracrine soluble ligands as discussed above and juxtacrine molecules that depend on direct contact between stem and niche cells. One function of juxtacrine niche factors is to anchor stem cells to the niche, such as through the adhesive cadherin molecules. For example, osteoblast attachment to HSCs is mediated by N-cadherin[20]. Juxtacrine ligands may also function as signaling molecules to regulate self-renewal or differentiation of neighboring stem cells. In the hippocampal NSC niche, membrane-bound ephrin-B2 on astrocytes can induce neuronal differentiation of adjacent NSCs[21]. As juxtacrine ligands are associated with cell membranes, spatial organization of these cues is more complex than soluble factors. On a cellular level, the orientation of a niche cell relative to a stem cell can induce polarity in stem cell signaling, resulting in asymmetric cell division[22]. Subcellular spatial organization of ligands can also influence juxtacrine interactions. Most simply, these factors are confined within the membrane so orientation is fixed and transport is limited to diffusion in two dimensions (compared to three dimensions for soluble factors). Cell surface molecules can also be localized within lipid membranes by a number of mechanisms, such as segregation into lipid rafts or interactions with cytoskeletal proteins[23]. For instance, ephrinB ligands have been shown to interact with adapter proteins and localize to rafts in response to stimulation[24]. Finally, some membrane-bound ligands require oligomerization to induce downstream signaling in target cells. For example, dimeric ephrins can bind and phosphorylate Eph receptors, but signal transduction and cell regulation requires multimeric ephrins[25] – Ephs and ephrins will be discussed in greater detail below. Because of these complexities in ligand presentation, recapitulating both the biochemistry and the structure of signaling events in the niche for biological discovery or therapeutic application requires novel engineering-based approaches.

1.3 Stem Cell Niche Engineering

Stem cell niche engineering is a broad field, ranging from biomaterials that mimic niche stiffness to bioreactors that dynamically supply soluble factors to micropatterned surfaces presenting combinations of signaling molecules. Here, the focus will be on tethered cell-cell signaling-dependent soluble and juxtacrine ligands in engineered niches.

Soluble ligands can be incorporated into artificial niches via addition to media, capture by bioactive polymers[26], release from degradable hydrogels[27], or immobilization to materials. Covalent tethering of soluble ligands influences both the stability of the ligand and its presentation to stem cells, which can enhance or alter biological response[28]. Increased stability of immobilized ligands is due to prevention of receptor-mediated endocytosis, whereby a cell internalizes a receptor-ligand complex resulting in degradation of the ligand. This increase in ligand availability can lead to enhanced and sustained signal activation. For example, surface-tethered epidermal growth factor (EGF) increased MSC survival compared to saturating concentrations of soluble EGF and enhanced osteogenic differentiation[29,30]. Similarly, immobilized Leukemia inhibitory factor (LIF) supported ESC cultures for more than two weeks without additional LIF supplementation[31]. Beyond stability, immobilized ligands present differing local concentrations and orientations compared to soluble factors, which can influence cellular signaling. For example, soluble Shh enhanced MSC growth rate, while surface-immobilized Shh did not; however, in conjugation with BMPs, tethered Shh enhanced osteogenic differentiation over soluble Shh[32]. Therefore, how a signaling factor is incorporated into an

artificial niche greatly influences its function, and ligand immobilization is a key design component.

Tethering of soluble ligands can be integrated into biomaterials of any configuration, including 2D surfaces for stem cell culture[29,31] and 3D hydrogels for stem cell transplantation[33,34]. The innumerable chemical conjugation techniques employed to immobilize ligands is beyond the scope of this chpater, but a couple of design considerations are worth noting. First, the density of tethered ligand must be sufficiently high to allow receptor engagement and signal activation. Receptors can diffuse within the stem cell membrane, but as the ligands are spatially constrained, an adequate supply of ligand must be present in direct contact with the cell. Additionally, many receptors exhibit multivalent properties in that they act in concert with other receptors[35]. To promote these multivalent interactions, the nanoscale organization of immobilized ligands can be controlled, such as through presentation as dimers or higher order multimers rather than monomers[36]. Along these lines, isolated multivalent ligands have been developed that can cluster receptors to promote multivalent signaling. For example, a multivalent Shh produced by conjugating Shh monomers to a flexible hyaluronic acid (HyA) polymer exhibited enhanced bioactivity at high valencies compared to soluble Shh[37]. In combination with additional cytokines, this multivalent Shh was shown to greatly enhance neuronal differentiation of ESCs[38]. The enhanced potency of multivalent ligands is due to increased avidity, which can be thermodynamically modeled[37,39]. A second design consideration is the microscale organization of immobilized ligands. By micropatterning factors on the order of cell size, stem cell localization and cell shape within an engineered niche can be controlled[40]. Additionally, if a gradient of signaling factors is patterned, stem cells may chemotax (migrate) or extend cellular processes along the gradient[41]. For example, MSC migration in response to patterned gradients of EGF has recently been studied[42]. Micropatterning methods range from microcontact printing to photolithography to microfluidic patterning[40,41], and novel techniques continue to emerge.

Cell-cell contact dependent interactions can be introduced into artificial niches both by directly regulating cell-cell contacts and by incorporation of juxtacrine ligands into synthetic niche materials. Cell-cell contact can be manipulated either by controlling for stem cell density in the case of homotypic interactions or through co-culture systems for heterotypic interactions between stem and supportive niche cells[43]. Alternatively, juxtacrine ligands can be integrated into artificial niches to mimic these cell-cell interactions in a cell-independent manner. This approach is the focus here as it offers a number of advantages over cell-based systems, such as the ability to precisely study the role of a single factor without confounding additional cellular inputs, and the capacity to develop fully defined artificial niches for therapeutic applications.

Juxtacrine ligand incorporation follows similar principles to immobilized soluble ligands as previously discussed. As juxtacrine ligands are biologically present within cellular membranes, integrating these factors into artificial niches often requires recapitulating this more complex spatial presentation. Notch is one of the most well studied cell-cell signaling pathways in stem cell biology and involves the interaction between the Notch receptor on one cell and the ligands Delta and Jagged on a neighboring cell[44]. Studies have shown that the extracellular domains of Delta and Jagged when immobilized to a surface, but not in the soluble form, are capable of binding to Notch and activating downstream signaling[45,46]. Orientation of the immobilized ligand may also influence activity. For example, Jagged immobilized in an orientation-regulated

manner promoted HSC proliferation, while randomly oriented Jagged did not[47]. Additionally, as with soluble factor immobilization, juxtacrine ligand density is an important design consideration. For example, hematopoietic precursors differentiated into early B and T cell precursors when exposed to low densities of Delta, but higher Delta densities enhanced T cell differentiation[48]. Cell-cell contact dependent adhesion molecules can also integrated into synthetic niches. For example, E-cadherin and N-cadherin coated substrates have successfully been utilized to culture ESCs[49,50]. Juxtacrine ligands can be incorporated into more complex niche systems as well, such as through integration into 3D scaffolds[51], immobilization on microbeads[52,53], and addition to micropatterned materials[54]. Multivalency is a key property of some juxtacrine interactions, thus incorporation of these signals into artificial niches may require multivalent ligands. For example, using an approach similar to the multivalent Shh previously described, multivalent ephrinB molecules were developed and utilized to enhance differentiation of ESCs and NSCs[55]. Finally, synthetic membrane systems[56] may be employed to improve biomimetic juxtacrine ligand presentation. Supported lipid bilayers (SLBs), for instance, mimic properties of a cellular membrane including diffusion. Functionalizing SLBs with juxtacrine ligands can, therefore, recapitulate cell-cell interactions in a more physiologically relevant manner compared to statically immobilized ligands. This approach has been applied to study ephrin signaling in cancer cells[57] and N-cadherin adhesion in periosteum derived multipotent cells[58]. Future work in this area could improve both our understanding of cell-cell signaling in stem cell niches, as well as improve our ability to recapitulate these signals for therapeutic applications.

1.4 Adult Neural Stem Cells

NSCs were discovered in two regions of the adult brain in the 1990s: the subventricular zone (SVZ) of the lateral ventricles[59] and the subgranular zone of the hippocampal dentate gyrus[60]. The work in the following chapters focuses on adult hippocampal NSCs (herein simply NSCs), the study of which has numerous applications. Most simply, understanding the maintenance and differentiation mechanisms of NSCs reveals how adult neurogenesis occurs. NSCs can remain in a quiescent state, proliferate, or differentiate into neurons, astrocytes, and oligodendrocytes[61], so dissecting the responsible signaling pathways informs both basic biology and potential therapeutic targets. Functionally, NSCs play key roles in learning and memory[62] and NSC proliferation declines with age[63]; therefore, interventions to enhance NSC activity could potentially combat aging-related mental decline. Disruption of NSC function is also associated with a number of pathologies. For example, the hippocampus is severely afflicted by Alzheimer's disease, and amyloid β-peptide, a hallmark of Alzheimer's, inhibits NSC proliferation and neuronal differentiation[64]. Additionally, seizures have been shown to induce aberrant NSC neurogenesis[65]. The ability to target endogenous NSCs, therefore, could be of great use in regenerative medicine efforts.

The effectors, signaling pathways, and genetic regulatory mechanisms governing NSC activity are numerous and an area of intense study. A number of excellent reviews have been written on this subject[66,67], so only a few factors relevant to this work will be discussed here. NSC self-renewal is a complex process involving the maintenance of a multipotent radial glial stem cell population and the proliferation of a transient amplifying progenitor cell population[66]. Soluble signaling molecules in the NSC niche that promote proliferation include FGF-2[61], Shh[68], vascular

endothelial growth factor (VEGF)[69], and Wnt7a[70]. *In vitro* cultures of adult rat hippocampal NSCs (the cell type used in these studies) rely on FGF-2 for proliferation. Differentiation of NSCs is a similarly complex process, with the focus here on neuronal differentiation. Soluble factors in the NSC niche promoting neurogenesis include retinoic acid[71] and Wnt3[72,73]. Supportive cells in the niche also instruct NSC fate as co-cultures of NSCs with hippocampal astrocytes have been shown to promote neuronal differentiation by both soluble and cell-cell contact dependent cues[21,74]. Wnt3a, acting through the canonical Wnt/β-catenin pathway, has been implicated as the soluble factor[72,73]. We have recently shown that ephrin-B2 is the cell contact dependent cue acting through EphB4 receptors on NSCs[21,55]. Developing tools to enable further study of Eph:ephrin signaling in NSCs was the goal of much of the work presented here.

1.5 Ephs and Ephrins

Ephs and ephrins are cell surface-bound signaling molecules. Ephrin ligands – which include GPI-linked A-types or transmembrane B-types – bind to Eph receptors, the largest family of receptor tyrosine kinases. Upon binding, bidirectional signaling occurs in both the Eph and ephrin presenting cells, which results in a wide range of responses[75-77]. During development, Eph:ephrin signaling mediates processes including morphogenesis, cell positioning, and boundary formation in many tissues. Examples include skeletal patterning[78] and angiogenesis[79]. In the developing CNS, Eph and ephrins direct neuronal migration[80], retinal axon guidance[81], and post-synaptic dendrite formation in hippocampal neurons[82]. In the adult brain, Eph:ephrin signaling continues to guide neural activity, by mechanisms such as axonal retraction[83] and dendritic spine morphogenesis[84]. In stem cell niches, Ephs and ephrins have integral roles in mediating cell-cell signaling. In intestinal crypts, Eph:ephrin signaling controls the migration and positioning of differentiated stem cell progeny[85]. NSC dynamics in both the SVZ and SGZ are mediated by Ephs and ephrins as well. Eph:ephrin signaling has been shown to inhibit NSC proliferation in the SVZ[86,87], regulate plasticity of niche cells in the SVZ[88], control NSC proliferation and migration in the SGZ[89,90], and induce NSC neuronal differentiation in the SGZ[21], as discussed above. Finally, Ephs and ephrins have been implicated in a number of developmental disorders and cancers[75], including skeletal malformations[91], Alzheimer's[92], breast cancer[93], and glioblastoma[94]. A thorough understanding of Eph:ephrin signaling, therefore, can reveal novel mechanisms of cell-cell signaling and may inform potential therapeutic targets.

Notably, Eph:ephrin signaling exhibits unique spatial dependence. Interactions require cell-cell contact, as both the ligand and receptor are membrane bound, so physical organization is particularly important[76,95,96]. High affinity Eph:ephrin dimers initially form, followed by low-affinity circular tetramers, then finally oligomerized clusters[76,97] (Fig. 1.2). Because of this multivalent requirement, soluble ephrin monomers cannot induce Eph phosphorylation[98], and while dimerized ephrins can, higher order oligomers are required for downstream signaling[25]. The traditional method of inducing Eph:ephrin signaling, in the absence of a co-culture system, is to cluster a soluble Fc-fused Eph/ephrin extracellular domain using a complementary antibody[25]. The result of this synthetic clustering is a globular, oligomeric signaling molecule that can induce signaling, but in an indistinct manner than poorly recapitulates biological presentation and likely prevents maximal activation due to steric hindrance. To enhance precision of clustering and enhance signaling, we recently developed a multivalent ephrin by conjugating the extracellular domain to a linear hyaluronic acid (HyA) polymer at defined

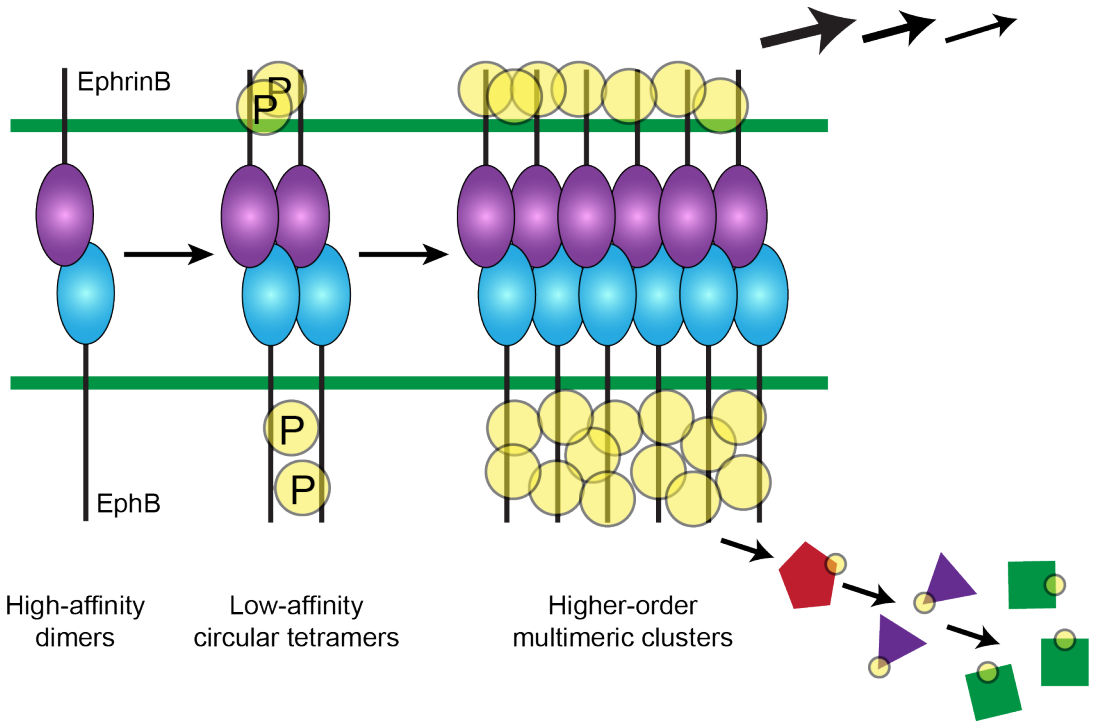

Figure 1.2. **Eph:ephrin clustering.** Transmembrane Eph on one cell binds to ephrin on an apposing cell membrane. Upon binding high affinity dimers form, which then combine into low-affinity circular tetramers capable of trans-phosphorylation. These complexes then coalesce into higher-order multimeric clusters, which can induce phosphorylation cascades resulting in downstream signal activation in both the Eph and ephrin-presenting cells.

valencies[55,99]. This HyA-ephrin-B2 was shown to induce NSC neuronal differentiation at a higher level than antibody-clustered ephrin-B2[55], so it is a promising tool for further study of this novel neurogenic mechanism. Additional engineering approaches to better mimic physiologic ephrin presentation and cluster Eph in a ligand-independent manner will be the focus of some of the work presented here.

1.6 Scope of the Dissertation

This dissertation was motivated by two goals. First, there is a need to develop novel tools enabling both the study and control of complex biological processes in stem cells. Second, NSCs are the source of adult neurogenesis and they hold great therapeutic promise, and a more thorough understanding of NSC neurogenic signaling will increase our understanding of this important cell type and could reveal novel mechanisms and/or targets for intervention. In **Chapter 2**, a single cell Western blotting platform is developed and then leveraged to probe NSC heterogeneity in signaling and differentiation. In **Chapter 3**, a supported lipid bilayer system is developed to study cell-cell signaling in the NSC niche and then applied to Eph:ephrin signaling, revealing a novel spatiomechanic sensitivity. In **Chapter 4**, novel downstream signaling pathways involved in Eph:ephrin-mediated NSC neurogenesis are investigated utilizing multivalent ephrin conjugates, proteomics, and gene editing. In **Chapter 5**, an optogenetic method for ephrin-independent Eph activation in NSCs through light-induced clustering is developed and tested. Overall, this work presents both the development of tools for stem cell interrogation and their implementation towards novel biological discovery.

1.7 References

1. Becker, A. J., McCulloch, E. A. & Till, J. E. Cytological demonstration of the clonal nature of spleen colonies derived from transplanted mouse marrow cells. *Nature* **197,** 452–454 (1963).
2. Morrison, S. J. & Scadden, D. T. The bone marrow niche for haematopoietic stem cells. *Nature* **505,** 327–334 (2014).
3. Fuentealba, L. C., Obernier, K. & Alvarez-Buylla, A. Adult neural stem cells bridge their niche. *Cell Stem Cell* **10,** 698–708 (2012).
4. Takahashi, K. & Yamanaka, S. Induction of pluripotent stem cells from mouse embryonic and adult fibroblast cultures by defined factors. *Cell* **126,** 663–676 (2006).
5. Laird, D. J., Andrian, von, U. H. & Wagers, A. J. Stem cell trafficking in tissue development, growth, and disease. *Cell* **132,** 612–630 (2008).
6. Bellin, M., Marchetto, M. C., Gage, F. H. & Mummery, C. L. Induced pluripotent stem cells: the new patient? *Nat Rev Mol Cell Biol* **13,** 713–726 (2012).
7. Burkhardt, M. F. *et al.* A cellular model for sporadic ALS using patient-derived induced pluripotent stem cells. *Mol Cell Neurosci* **56,** 355–364 (2013).
8. Hare, J. M. *et al.* Comparison of allogeneic vs autologous bone marrow–derived mesenchymal stem cells delivered by transendocardial injection in patients with ischemic cardiomyopathy: the POSEIDON randomized trial. *JAMA* **308,** 2369–2379 (2012).
9. Alper, J. Geron gets green light for human trial of ES cell-derived product. *Nature biotechnology* **27,** 213–214 (2009).
10. Trejo, J. L., Carro, E. & Torres-Aleman, I. Circulating insulin-like growth factor I mediates exercise-induced increases in the number of new neurons in the adult hippocampus. *J Neurosci* **21,** 1628–1634 (2001).
11. Liles, W. C. *et al.* Mobilization of hematopoietic progenitor cells in healthy volunteers by AMD3100, a CXCR4 antagonist. *Blood* **102,** 2728–2730 (2003).
12. Jones, D. L. & Wagers, A. J. No place like home: anatomy and function of the stem cell niche. *Nat Rev Mol Cell Biol* **9,** 11–21 (2008).
13. Morrison, S. J. & Spradling, A. C. Stem cells and niches: mechanisms that promote stem cell maintenance throughout life. *Cell* **132,** 598–611 (2008).
14. Zandstra, P. W., Conneally, E., Petzer, A. L., Piret, J. M. & Eaves, C. J. Cytokine manipulation of primitive human hematopoietic cell self-renewal. *Proc Natl Acad Sci USA* **94,** 4698–4703 (1997).
15. Dessaud, E. *et al.* Interpretation of the sonic hedgehog morphogen gradient by a temporal adaptation mechanism. *Nature* **450,** 717–720 (2007).
16. Burgess, W. H. & Maciag, T. The heparin-binding (fibroblast) growth factor family of proteins. *Annu. Rev. Biochem.* **58,** 575–606 (1989).
17. Kraushaar, D. C. *et al.* Heparan sulfate facilitates FGF and BMP signaling to drive mesoderm differentiation of mouse embryonic stem cells. *J Biol Chem* **287,** 22691–22700 (2012).
18. Mann, R. K. & Beachy, P. A. Novel lipid modifications of secreted protein signals. *Annu. Rev. Biochem.* **73,** 891–923 (2004).
19. Zeng, X. *et al.* A freely diffusible form of Sonic hedgehog mediates long-range signalling. *Nature* **411,** 716–720 (2001).

20. Zhang, J. *et al.* Identification of the haematopoietic stem cell niche and control of the niche size. *Nature* **425,** 836–841 (2003).
21. Ashton, R. S. *et al.* Astrocytes regulate adult hippocampal neurogenesis through ephrin-B signaling. *Nat Neurosci* **15,** 1399–1406 (2012).
22. Knoblich, J. A. Mechanisms of asymmetric stem cell division. *Cell* **132,** 583–597 (2008).
23. Manz, B. & Groves, J. Spatial organization and signal transduction at intercellular junctions. *Nat Rev Mol Cell Biol* (2010).
24. Brückner, K. *et al.* EphrinB ligands recruit GRIP family PDZ adaptor proteins into raft membrane microdomains. *Neuron* **22,** 511–524 (1999).
25. Stein, E. *et al.* Eph receptors discriminate specific ligand oligomers to determine alternative signaling complexes, attachment, and assembly responses. *Genes Dev* **12,** 667–678 (1998).
26. Hudalla, G. A., Kouris, N. A., Koepsel, J. T., Ogle, B. M. & Murphy, W. L. Harnessing endogenous growth factor activity modulates stem cell behavior. *Integrative Biology* **3,** 832–842 (2011).
27. Xu, X., Jha, A. K., Duncan, R. L. & Jia, X. Heparin-decorated, hyaluronic acid-based hydrogel particles for the controlled release of bone morphogenetic protein 2. *Acta Biomater* **7,** 3050–3059 (2011).
28. Ito, Y. Covalently immobilized biosignal molecule materials for tissue engineering. *Soft matter* **4,** 46–56 (2008).
29. Fan, V. H. *et al.* Tethered epidermal growth factor provides a survival advantage to mesenchymal stem cells. *STEM CELLS* **25,** 1241–1251 (2007).
30. Platt, M. O., Roman, A. J., Wells, A., Lauffenburger, D. A. & Griffith, L. G. Sustained epidermal growth factor receptor levels and activation by tethered ligand binding enhances osteogenic differentiation of multi-potent marrow stromal cells. *J Cell Physiol* **221,** 306–317 (2009).
31. Alberti, K. *et al.* Functional immobilization of signaling proteins enables control of stem cell fate. *Nat Methods* **5,** 645–650 (2008).
32. Ho, J. E., Chung, E. H., Wall, S., Schaffer, D. V. & Healy, K. E. Immobilized sonic hedgehog N-terminal signaling domain enhances differentiation of bone marrow-derived mesenchymal stem cells. *J Biomed Mater Res A* **83,** 1200–1208 (2007).
33. Leipzig, N. D., Wylie, R. G., Kim, H. & Shoichet, M. S. Differentiation of neural stem cells in three-dimensional growth factor-immobilized chitosan hydrogel scaffolds. *Biomaterials* **32,** 57–64 (2011).
34. Yin, F. *et al.* Cartilage Regeneration of Adipose-Derived Stem Cells in the TGF-β1-Immobilized PLGA-Gelatin Scaffold. *Stem Cell Rev* (2014). doi:10.1007/s12015-014-9561-9
35. Kiessling, L. L., Gestwicki, J. E. & Strong, L. E. Synthetic multivalent ligands as probes of signal transduction. *Angew Chem Int Ed Engl* **45,** 2348–2368 (2006).
36. Petrie, T. A. *et al.* Multivalent integrin-specific ligands enhance tissue healing and biomaterial integration. *Sci Transl Med* **2,** 45ra60 (2010).
37. Wall, S. T. *et al.* Multivalency of Sonic hedgehog conjugated to linear polymer chains modulates protein potency. *Bioconjug Chem* **19,** 806–812 (2008).
38. Vazin, T. *et al.* The effect of multivalent Sonic hedgehog on differentiation of human embryonic stem cells into dopaminergic and GABAergic neurons. *Biomaterials* (2014).
39. Kane, R. S. Thermodynamics of multivalent interactions: influence of the linker. *Langmuir* **26,** 8636–8640 (2010).

40. Yap, F. L. & Zhang, Y. Protein and cell micropatterning and its integration with micro/nanoparticles assembly. *Biosens Bioelectron* **22,** 775–788 (2007).
41. Sant, S., Hancock, M. J., Donnelly, J. P., Iyer, D. & Khademhosseini, A. BIOMIMETIC GRADIENT HYDROGELS FOR TISSUE ENGINEERING. *Can J Chem Eng* **88,** 899–911 (2010).
42. Miller, E. D. *et al.* Spatially directed guidance of stem cell population migration by immobilized patterns of growth factors. *Biomaterials* **32,** 2775–2785 (2011).
43. Battiston, K. G., Cheung, J. W. C., Jain, D. & Santerre, J. P. Biomaterials in co-culture systems: towards optimizing tissue integration and cell signaling within scaffolds. *Biomaterials* **35,** 4465–4476 (2014).
44. Koch, U., Lehal, R. & Radtke, F. Stem cells living with a Notch. *Development* **140,** 689–704 (2013).
45. Beckstead, B. L., Santosa, D. M. & Giachelli, C. M. Mimicking cell-cell interactions at the biomaterial-cell interface for control of stem cell differentiation. *J Biomed Mater Res A* **79,** 94–103 (2006).
46. Varnum-Finney, B. *et al.* Immobilization of Notch ligand, Delta-1, is required for induction of notch signaling. *J Cell Sci* **113 Pt 23,** 4313–4318 (2000).
47. Toda, H., Yamamoto, M., Kohara, H. & Tabata, Y. Orientation-regulated immobilization of Jagged1 on glass substrates for ex vivo proliferation of a bone marrow cell population containing hematopoietic stem cells. *Biomaterials* **32,** 6920–6928 (2011).
48. Dallas, M. H. Density of the Notch ligand Delta1 determines generation of B and T cell precursors from hematopoietic stem cells. *Journal of Experimental Medicine* **201,** 1361–1366 (2005).
49. Haque, A., Yue, X.-S., Motazedian, A., Tagawa, Y.-I. & Akaike, T. Characterization and neural differentiation of mouse embryonic and induced pluripotent stem cells on cadherin-based substrata. *Biomaterials* **33,** 5094–5106 (2012).
50. Nagaoka, M. *et al.* E-cadherin-coated plates maintain pluripotent ES cells without colony formation. *PLoS ONE* **1,** e15 (2006).
51. Lee, J. & Kotov, N. A. Notch ligand presenting acellular 3D microenvironments for ex vivo human hematopoietic stem-cell culture made by layer-by-layer assembly. *Small (Weinheim an der Bergstrasse, Germany)* **5,** 1008–1013 (2009).
52. Taqvi, S., Dixit, L. & Roy, K. Biomaterial-based notch signaling for the differentiation of hematopoietic stem cells into T cells. *J Biomed Mater Res A* **79,** 689–697 (2006).
53. Tung, J. C., Paige, S. L., Ratner, B. D., Murry, C. E. & Giachelli, C. M. Engineered Biomaterials Control Differentiation and Proliferation of Human-Embryonic-Stem-Cell-Derived Cardiomyocytes via Timed Notch Activation. *Stem Cell Reports* **2,** 271–281 (2014).
54. Wang, Y., Xu, Z., Kam, L. C. & Shi, P. Site-specific differentiation of neural stem cell regulated by micropatterned multicomponent interfaces. *Adv Healthc Mater* **3,** 214–220 (2014).
55. Conway, A. *et al.* Multivalent ligands control stem cell behaviour in vitro and in vivo. *Nature Nanotech* **8,** 831–838 (2013).
56. Loose, M. & Schwille, P. Biomimetic membrane systems to study cellular organization. *J Struct Biol* **168,** 143–151 (2009).
57. Salaita, K. *et al.* Restriction of receptor movement alters cellular response: physical force sensing by EphA2. *Science* **327,** 1380–1385 (2010).

58. Evans, S. F. *et al.* Solid-supported lipid bilayers to drive stem cell fate and tissue architecture using periosteum derived progenitor cells. *Biomaterials* **34,** 1878–1887 (2013).
59. Lois, C. & Alvarez-Buylla, A. Long-distance neuronal migration in the adult mammalian brain. *Science* **264,** 1145–1148 (1994).
60. Eriksson, P. S. *et al.* Neurogenesis in the adult human hippocampus. *Nat Med* **4,** 1313–1317 (1998).
61. Palmer, T. D., Ray, J. & Gage, F. H. FGF-2-responsive neuronal progenitors reside in proliferative and quiescent regions of the adult rodent brain. *Mol Cell Neurosci* **6,** 474–486 (1995).
62. Zhang, C.-L., Zou, Y., He, W., Gage, F. H. & Evans, R. M. A role for adult TLX-positive neural stem cells in learning and behaviour. *Nature* **451,** 1004–1007 (2008).
63. Kuhn, H. G., Dickinson-Anson, H. & Gage, F. H. Neurogenesis in the dentate gyrus of the adult rat: age-related decrease of neuronal progenitor proliferation. *J Neurosci* **16,** 2027–2033 (1996).
64. Haughey, N. J. *et al.* Disruption of neurogenesis by amyloid beta-peptide, and perturbed neural progenitor cell homeostasis, in models of Alzheimer's disease. *J Neurochem* **83,** 1509–1524 (2002).
65. Jessberger, S. *et al.* Seizure-associated, aberrant neurogenesis in adult rats characterized with retrovirus-mediated cell labeling. *J Neurosci* **27,** 9400–9407 (2007).
66. Faigle, R. & Song, H. Signaling mechanisms regulating adult neural stem cells and neurogenesis. *Biochim Biophys Acta* **1830,** 2435–2448 (2013).
67. Gage, F. H. & Temple, S. Neural stem cells: generating and regenerating the brain. *Neuron* **80,** 588–601 (2013).
68. Lai, K., Kaspar, B. K., Gage, F. H. & Schaffer, D. V. Sonic hedgehog regulates adult neural progenitor proliferation in vitro and in vivo. *Nat Neurosci* **6,** 21–27 (2003).
69. Jin, K. *et al.* Vascular endothelial growth factor (VEGF) stimulates neurogenesis in vitro and in vivo. *Proc Natl Acad Sci USA* **99,** 11946–11950 (2002).
70. Qu, Q. *et al.* Orphan nuclear receptor TLX activates Wnt/|[beta]|-catenin signalling to stimulate neural stem cell proliferation and self-renewal. *Nat Cell Biol* **12,** 31–40 (2010).
71. Takahashi, J. & Palmer, T. Retinoic acid and neurotrophins collaborate to regulate neurogenesis in adult-derived neural stem cell cultures. *J Neurobiol* (1999).
72. Kuwabara, T. *et al.* Wnt-mediated activation of NeuroD1 and retro-elements during adult neurogenesis. *Nat Neurosci* **12,** 1097–1105 (2009).
73. Lie, D.-C. *et al.* Wnt signalling regulates adult hippocampal neurogenesis. *Nature* **437,** 1370–1375 (2005).
74. Song, H., Stevens, C. F. & Gage, F. H. Astroglia induce neurogenesis from adult neural stem cells. *Nature* **417,** 39–44 (2002).
75. Barquilla, A. & Pasquale, E. B. Eph receptors and ephrins: therapeutic opportunities. *Annu Rev Pharmacol Toxicol* **55,** 465–487 (2015).
76. Himanen, J.-P., Saha, N. & Nikolov, D. B. Cell-cell signaling via Eph receptors and ephrins. *Curr Opin Cell Biol* **19,** 534–542 (2007).
77. Klein, R. Eph/ephrin signalling during development. *Development* **139,** 4105–4109 (2012).
78. Compagni, A., Logan, M., Klein, R. & Adams, R. H. Control of skeletal patterning by ephrinB1-EphB interactions. *Dev Cell* **5,** 217–230 (2003).

79. Wang, H. U., Chen, Z. F. & Anderson, D. J. Molecular distinction and angiogenic interaction between embryonic arteries and veins revealed by ephrin-B2 and its receptor Eph-B4. *Cell* **93,** 741–753 (1998).
80. Sentürk, A., Pfennig, S., Weiss, A., Burk, K. & Acker-Palmer, A. Ephrin Bs are essential components of the Reelin pathway to regulate neuronal migration. *Nature* **472,** 356–360 (2011).
81. Yates, P. A., Roskies, A. L., McLaughlin, T. & O'Leary, D. D. Topographic-specific axon branching controlled by ephrin-As is the critical event in retinotectal map development. *J Neurosci* **21,** 8548–8563 (2001).
82. Xu, N.-J., Sun, S., Gibson, J. R. & Henkemeyer, M. A dual shaping mechanism for postsynaptic ephrin-B3 as a receptor that sculpts dendrites and synapses. *Nat Neurosci* **14,** 1421–1429 (2011).
83. Takeuchi, S., Katoh, H. & Negishi, M. Eph/ephrin reverse signalling induces axonal retraction through RhoA/ROCK pathway. *J. Biochem.* mvv042 (2015).
84. Penzes, P. *et al.* Rapid induction of dendritic spine morphogenesis by trans-synaptic ephrinB-EphB receptor activation of the Rho-GEF kalirin. *Neuron* **37,** 263–274 (2003).
85. Batlle, E. *et al.* Beta-catenin and TCF mediate cell positioning in the intestinal epithelium by controlling the expression of EphB/ephrinB. *Cell* **111,** 251–263 (2002).
86. Holmberg, J. *et al.* Ephrin-A2 reverse signaling negatively regulates neural progenitor proliferation and neurogenesis. *Genes Dev* **19,** 462–471 (2005).
87. Ricard, J., Salinas, J., Garcia, L. & Liebl, D. J. EphrinB3 regulates cell proliferation and survival in adult neurogenesis. *Mol Cell Neurosci* **31,** 713–722 (2006).
88. Nomura, T., Göritz, C., Catchpole, T., Henkemeyer, M. & Frisén, J. EphB signaling controls lineage plasticity of adult neural stem cell niche cells. *Cell Stem Cell* **7,** 730–743 (2010).
89. Chumley, M. J., Catchpole, T., Silvany, R. E., Kernie, S. G. & Henkemeyer, M. EphB receptors regulate stem/progenitor cell proliferation, migration, and polarity during hippocampal neurogenesis. *J Neurosci* **27,** 13481–13490 (2007).
90. Hara, Y., Nomura, T., Yoshizaki, K., Frisén, J. & Osumi, N. Impaired hippocampal neurogenesis and vascular formation in ephrin-A5-deficient mice. *Stem Cells* **28,** 974–983 (2010).
91. Davy, A., Bush, J. O. & Soriano, P. Inhibition of gap junction communication at ectopic Eph/ephrin boundaries underlies craniofrontonasal syndrome. *PLoS Biol* **4,** e315 (2006).
92. Cissé, M. *et al.* Reversing EphB2 depletion rescues cognitive functions in Alzheimer model. *Nature* **469,** 47–52 (2011).
93. Macrae, M. *et al.* A conditional feedback loop regulates Ras activity through EphA2. *Cancer Cell* **8,** 111–118 (2005).
94. Binda, E. *et al.* The EphA2 receptor drives self-renewal and tumorigenicity in stem-like tumor-propagating cells from human glioblastomas. *Cancer Cell* **22,** 765–780 (2012).
95. Bethani, I., Skånland, S. S., Dikic, I. & Acker-Palmer, A. Spatial organization of transmembrane receptor signalling. *EMBO J* **29,** 2677–2688 (2010).
96. Pasquale, E. B. Eph-ephrin bidirectional signaling in physiology and disease. *Cell* **133,** 38–52 (2008).
97. Himanen, J., Rajashankar, K. & Lackmann, M. Crystal structure of an Eph receptor-ephrin complex. *Nature* (2001).

98. Davis, S. *et al.* Ligands for EPH-related receptor tyrosine kinases that require membrane attachment or clustering for activity. *Science* **266,** 816–819 (1994).
99. Conway, A., Spelke, D. P. & Schaffer, D. V. Conjugation of proteins to polymer chains to create multivalent molecules. *Methods Mol Biol* **1202,** 95–102 (2014).

Chapter 2: Single-Cell Western Blotting

This chapter is adapted from a manuscript published as

Hughes, A.J.*, Spelke, D.P.*, Xu, Z., Kang, C., Schaffer, D.V. & Herr, A.E. Single-cell western blotting. *Nat Methods* **11,** 749-755 (2014).

**Authorship equally shared*

2.1 Introduction

Heterogeneity is inherent in cellular processes including stem cell differentiation[1,2], development[3], cancer[4,5], pharmaceutical efficacy[6], and immune response[7]. Owing in large part to technological advances, genomic and transcriptomic studies of cell-to-cell heterogeneity are flourishing[5,8]. However, recent single-cell and population-wide studies comparing transcriptomes to proteomes in microorganismal and mammalian cells found only mild correlations between mRNA and protein expression[9-11]. Therefore, to fully understand diverse and often rare behaviors in complex cell populations, researchers need analytical tools that are optimized for protein analysis of many cells, offer single-cell resolution, provide quantitative and highly specific detection of target proteins, and do not employ labels that may perturb protein and cell function[12].

Single-cell proteome-wide studies are currently limited to readouts from synthetic fluorescent protein fusion libraries[9,11], which, though illuminating, are challenging to generate and can potentially perturb protein function. Single-cell protein immunoassays (for example, flow cytometry[7] and immunocytochemistry (ICC)[13]) have proved immensely important for assessing cell-to-cell heterogeneity, yet existing methods depend on analyte discrimination with antibody probes that often have limited specificity. This dependence on antibody probe quality limits assay performance, as cross-reactivity can create misleading background signals that are difficult to correct for[14-16], even with careful controls[17,18]. This vulnerability broadly impacts antibody-based assays (such as ELISAs and protein microarrays[14]). The widely used western blot is less affected by antibody cross-reactivity because proteins are first separated by molecular mass (via electrophoresis) before the antibody probing step, thereby enabling clear discrimination between on-target and off-target signals, even in complex backgrounds such as cell lysates[19,20]. However, the cell population averaging required by existing blotting methods masks the rich single-cell behaviors found in complex populations[19,21]. Although microwestern arrays afford remarkable target multiplexing and throughput, lysate pooled from ~10^3 cells is required for each electrophoresis assay (~250 ng of protein)[19]. Capillary and microfluidic designs reduce mass demands, but their form factors are not readily scalable to the thousands of concurrent electrophoresis assays required to measure variation within a population of single-cells[21].

We address the need for high-specificity protein assays capable of measuring cell-to-cell heterogeneity within complex populations of cells by introducing a single-cell western blot (scWestern) method. Specifically, a scalable open-microwell array architecture permits simultaneous assays of ~2,000 individual cells in <4 h. We applied the scWestern to study variability in stem cell signaling and differentiation responses to homogeneous *in vitro* stimuli.

2.2 Results

Development and characterization of scWesterns

scWestern analysis employs a microscope slide coated with a thin photoactive polyacrylamide (PA) gel[21] micropatterned with an array of 6,720 microwells (Fig. 2.1a). The microwells (20 μm in diameter) are patterned during polymerization of a 30 μm-thick PA gel against a silicon wafer studded with SU-8 microposts (Fig. 2.1a). To allow for concurrent western analysis of thousands of single cells, the scWestern integrates all key western blotting steps (Fig. 2.1b,d) in a dense array format.

Three fundamental design principles underpin the scWestern. First, we address the scWestern globally in terms of fluidic, optical, and electrical interfacing. Global interfacing yields highly parallel analyses by eliminating independent hardware access to each of the thousands of microwells. Initially, a cell suspension is seeded into microwells via passive gravity-driven cell settling, resulting in capture of 0–4 cells per microwell in 5–10 min. For neural stem cell (NSC) densities of 1,000–1,800 cells per mm^2 slide area (2×10^6–3.5×10^6 cells in total), we observed single cells in 40–50% of microwells (Fig. A.1). Notably, FACS can be integrated with scWesterns to analyze subpopulations of ~200 cells with single-cell resolution (Fig. A.2), enabling analyses of rare or precious cells. Next, we perform buffer exchange to a denaturing radioimmunoprecipitation assay (RIPA) buffer that lyses cells in the microwells in 2.6 ± 1.5 sec (± s.d., n = 6 cells), solubilizing intracellular proteins while providing a suitable conductivity for subsequent electrophoresis. Protein diffusion from cells occurred within ~10 sec of lysis (Fig. 2.1e). Simulations suggest that diffusion of cell contents from microwells is responsible for the moderate protein losses of 40.2% ± 3.6% observed during lysis buffer introduction (± s.d., n = 3 microwells from 3 separate slides; Fig. A.3 and Note A.1). Future innovation in microwell enclosure methods or the use of higher-viscosity lysis buffers may reduce these losses.

As a second design principle, we achieve a high-density scWestern array by optimizing for short-separation-distance PA gel electrophoresis (PAGE). To initiate electrophoresis after cell lysis, we apply an electric field across the submerged scWestern slide, electrophoresing proteins through the microwell walls and into the thin PA gel sheet. To characterize this process, we assayed a ladder of purified fluorescently labeled proteins (27–132 kDa, Fig. 2.1c) that partition into microwells (Fig. A.4 and Note A.2). Under our denaturing, non-reducing PAGE conditions, we (i) observed stacking of purified proteins during electromigration into the bulk PA gel, (ii) verified a log-linear relationship between protein molecular mass and migration distance in scWestern separations, as anticipated for SDS-PAGE[21,22] (R^2 = 0.97; Fig. A.5), and (iii) resolved covalent protein dimers (Fig. A.6). Moderate PAGE performance was achieved, with molecular mass differences of 51% ± 1.6% (± s.d., n = 3 separations) resolvable in ~500 μm separation lengths and 30 sec separation times. In general, we observed agreement between scWestern separations and conventional western blotting (Note A.3). For comparison, a microwestern array setup (integrated with robotic bulk cell lysate printing) offers similar resolving power but requires 18-fold longer separation distances (9 mm)[19].

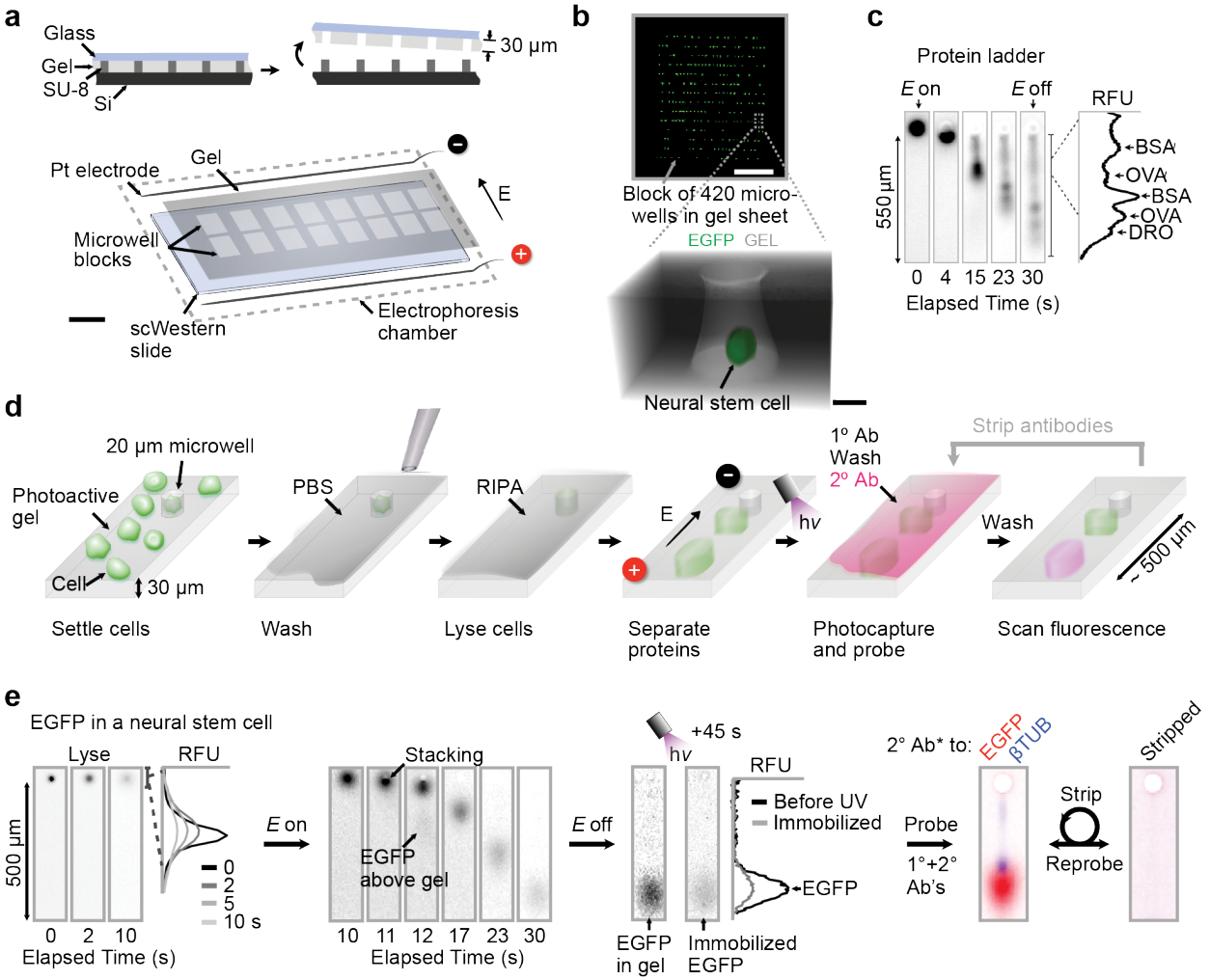

Figure 2.1. **Single-cell western blotting.** (**a**) The scWestern array consists of thousands of microwells (20 µm in diameter, 30 µm deep) patterned in a 30-µm-thick photoactive polyacrylamide gel seated on a glass microscope slide. The array is comprised of 16 blocks of 14 × 30 microwells (6,720 in total) cast against an SU-8 photoresist master fabricated by soft lithography. *E*, electric field. Scale bar, 10 mm. (**b**) Top, wide-field micrograph of a microwell block containing 15-µm fluorescent microspheres. Scale bar, 2 mm. Bottom, confocal micrograph of a live EGFP-expressing NSC settled in a rhodamine-tagged gel (GEL). Scale bar, 10 µm. (**c**) PAGE resolves five fluorescently labeled proteins in a 550-µm separation distance (DRO, Dronpa, 27 kDa; OVA, ovalbumin, 45 kDa; BSA, bovine serum albumin, 66 kDa; OVA′, OVA dimer, 90 kDa; BSA′, BSA dimer, 132 kDa). (**d**) Open-gel scWestern analysis is a 4-h, six-stage assay comprising cell settling, chemical lysis with a denaturing RIPA buffer, PAGE, UV-initiated protein immobilization onto the gel (hν, photon energy), diffusion-driven antibody probing (i.e., primary and fluorescently labeled secondary antibody probes: 1° Ab and 2° Ab*) and fluorescence imaging. (**e**) scWestern analysis of EGFP and βTUB from a single NSC. RFU, relative fluorescence units. Distinct fluorescent dyes on each 2° Ab* enable multiplexed target analysis (EGFP, Alexa Fluor 488–labeled 2° Ab*; βTUB, Alexa Fluor 555–labeled 2° Ab*). Chemical stripping and reprobing allows multiplexed scWestern analysis.

The third scWestern design principle harnesses small characteristic lengths for reaction (protein immobilization) and transport (antibody probing). Following PAGE, protein immobilization relies on a benzophenone methacrylamide co-monomer crosslinked into the PA gel. We measure protein photocapture in the gel at 27.5% ± 2.9% of EGFP from EGFP-expressing NSCs after brief (45 s) gel exposure to UV light (± s.d., n = 6 single cells from experiments on 4 separate days, Fig. 2.1e). Photoimmobilization benefits from small diffusion lengths between proteins and

benzophenone moieties within the PA gel[21]. Probing of the separated, immobilized proteins is performed by sequential diffusion of primary and secondary antibodies into the thin PA gel layer, taking advantage of the short 30 μm characteristic transport length (Fig. A.7 and Note A.2). scWestern antibody consumption is comparable to that of conventional western blotting and ICC, with potential for additional optimization (Note A.2).

Analysis of multiple protein targets is crucial to understanding cell functions such as signal transduction[1]. Our scWesterns are organized into 16 assay "blocks" of 420 microwells each, a layout that allows application of different antibody solutions to different blocks. After probing, imaging with a fluorescence microarray scanner yields scWesterns of up to 48 targets per array (3-plex target quantitation for 16 microwell blocks). To further advance multiplexed analyte detection, we adopted serial stripping of antibodies using a strongly denaturing buffer. Using 11 antibody probe sets during nine stripping and re-probing rounds; nine unique targets were successfully detected in the same cell by scWestern blotting and validated by conventional western blotting (Fig. A.8). Stripping successfully removed antibody probes from scWestern slides, leading to greater-than-tenfold reductions in the signal-to-noise ratios (SNRs) compared to initial SNRs (Figs. 2.1e and A.9). Furthermore, reprobing after the first stripping round led to full recovery of initial probe signals, and signal recoveries of 50% were typical even after nine stripping and reprobing rounds (Figs. A.8b and A.9). Robust signal recovery is likely enabled by stable, covalent protein immobilization, in contrast to the relatively poor recovery observed in conventional platforms that utilize noncovalent blotting[23]. As a result, scWestern slides can be stored for long-term archiving and reanalysis of single-cell separations.

Quantitative performance and calibration of scWesterns

We sought to assay cellular signaling and differentiation in stem cells, which often exhibit diverse behaviors in response to homogeneous stimuli[1,2], using scWesterns. Initially we applied the scWestern to NSCs transduced with a retroviral vector encoding EGFP, using 12 blocks of a single slide (Fig. 2.2a). 4,128 separations of a possible 5,040 (82%) passed semi-automated gating on dust particles and gel defects. Additionally, of those, 1,608 separations (39%) came from single cells, on the basis of bright-field microwell occupancy determination (cells per microwell); and the microwell occupancy running average ranged between 0 and 2.1 cells per microwell with a mean of 1.1 cells per microwell (Fig. 2.2b). Automated occupancy scoring was used for all other data sets to identify single-cell-per-microwell separations, and in all cases, large numbers of microwells housed single cells.

Two protein targets, EGFP and β-tubulin (βTUB), were probed on the same scWestern slide, and the resulting probed band intensities were correlated with microwell occupancy (Figs. 2.2a,b and A.10). We observed a monotonic but nonlinear relationship between total fluorescence of the βTUB band and microwell occupancy (Fig. 2.2b), likely due to cell size-related bias for microwells with more than one cell (Note A.4). The βTUB fluorescence distribution for single-cell separations was well described by a gamma distribution derived from a stochastic kinetic model of transcription and translation in a homogeneous population of dividing cells[24]. Our scWestern analysis of βTUB thus agrees with gamma-distributed single-cell protein expression profiles reported for fluorescent protein fusion libraries in *Escherichia coli*[11,25] and mammalian cells[26].

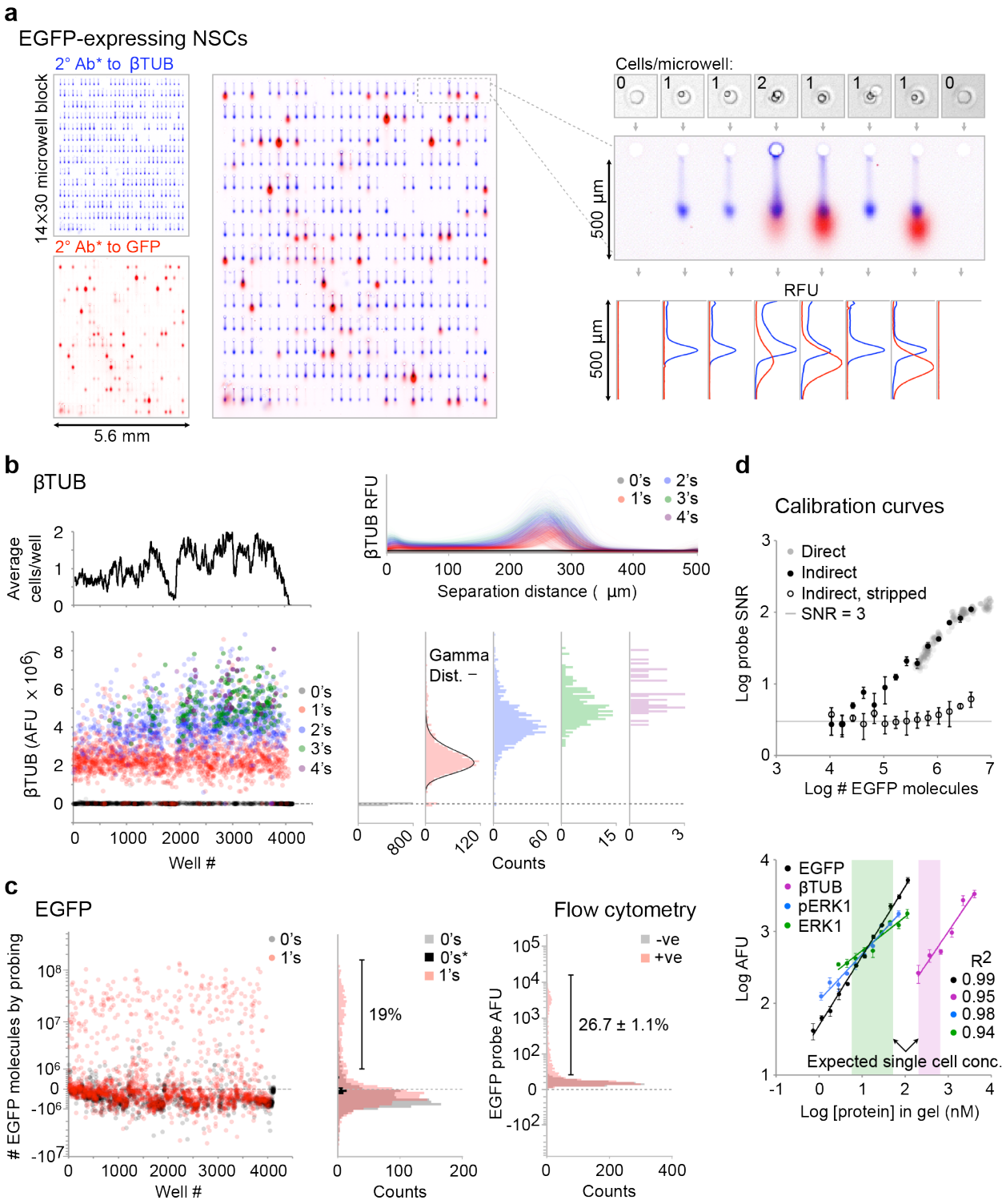

Figure 2.2. **scWestern blotting of NSCs.** (**a**) 420 concurrent scWesterns of EGFP-expressing NSCs for βTUB (Alexa Fluor 647–labeled secondary antibody (2° Ab*)) and EGFP (Alexa Fluor 555–labeled 2° Ab*). Bright-field imaging determines the number of cells-per-microwell. RFU, relative fluorescence units. (**b**) Top right, scWestern fluorescence for 4,128 separations by cells-per-microwell. Left, area under the curve for βTUB with (above) running average of cells per microwell (window size, 30 microwells). Microwells are indexed from left to right of the array. AFU, arbitrary fluorescence units. Bottom right, fit of fluorescence distribution for single cells to a gamma distribution (dist.) stemming from Poissonian mRNA production and exponentially distributed protein burst sizes.

(**c**) EGFP fluorescence for one- and zero-cells-per-microwell blots compared to flow cytometry of fixed NSCs (+ve, EGFP transfected; −ve, untransfected). Note arcsinh-transformed scales. Technical noise was estimated from scWesterns with zero cells-per-microwell in a sparsely cell-seeded region (0*, separations 4,100–4,128; Note A.5). The fraction of EGFP+ cells is mean ± s.d. for $n = 3$. (**d**) SNR estimates for determining the limit of detection at 27,000 molecules using purified EGFP through direct and indirect methods (mean ± s.d., $n = 3$ regions of interest per dot blot). Bottom, linear indirect calibration curves for purified standards (mean ± s.d., $n = 3$ regions of interest per dot blot) span physiologically relevant βTUB and ERK concentrations (concentration in a probed band estimated from in-cell concentrations, see shaded regions; colors correspond to calibration curves[10,27]).

When benchmarked against flow cytometry, we observed 19% and 26.7% ± 1.1% of the NSCs to be EGFP+ (i.e., probed band signals above technical noise) by scWestern analysis and flow cytometry, respectively (± s.d., $n = 3$ technical replicates; Fig. 2.2c). The dynamic ranges were comparable (Note A.5).

To determine the linearity and sensitivity of scWestern fluorescence readouts, we undertook "direct" calibration of EGFP and "indirect" calibration of both EGFP and βTUB, as well as phosphorylated and total levels of the signaling protein ERK (Fig 2.2d). Direct calibration correlates the number of purified EGFP molecules in a coverglass-enclosed microwell separation to probe fluorescence after immunoprobing, whereas the indirect method uses a partition-coefficient measurement to infer the number of molecules in a dot-blotted scWestern band (Figs. A.11-13 and Note A.6). The calibration results agree for EGFP (Fig. 2.2d) and, together with the indirect calibration data, suggest a linear dynamic range of 1.3–2.2 orders of magnitude, from a limit of detection of 45 zeptomoles (27,000 molecules, comparable to fluorescence cytometry detection limits of 10^3–10^7 molecules[28]). This detection limit matches an ideal noise threshold of 25,000 molecules set by the fluorescence microarray scanner to within 10%, is 45-fold more sensitive than microwestern arrays[19] and is 3.2-fold more sensitive than microfluidic western blotting[21] (Note A.5). For context, a median protein copy number of 50,000 has been reported for murine fibroblasts[10]; indicating that >50% of the mammalian proteome may be accessible via scWesterns (given the availability of suitable antibodies).

Heterogeneity in signaling after FGF-2 stimulation of NSCs

A defining property of stem cells is self-renewal, or maintenance of an immature state[29]. Fibroblast growth factor-2 (FGF-2) is a mitogen and self-renewal signal for adult hippocampal NSCs[29,30], acting via the FGFR-1 receptor to activate the Ras-MAPK, p38 MAP, and PI3K-Akt pathways[30]. Signals are transmitted in MAPK cascades by sequential phosphorylation of downstream kinases including MEK and ERK. We applied scWesterns to study MAPK signaling dynamics within single NSCs that were starved of FGF-2, suspended, settled into scWestern microwells and stimulated with FGF-2 over a 60 min time course (Fig. 2.3). We first probed for phosphorylated ERK1/2 (pERK) and MEK1/2 (pMEK), after which we reprobed for total ERK1/2 and MEK1/2 (Figs. 2.3a and A.14). In parallel, βTUB and EGFP probing allowed estimation of molecular mass, and all targets were within 10% of their nominal masses.

scWestern analysis for pERK reported two proteins reactive to the anti-pERK antibody: the expected 38.8 ± 1.0 kDa protein, along with a heavier one of 103 ± 3 kDa (± s.d., $n = 3$ separations). We hypothesize that the 103 kDa protein arose from off-target antibody probing because its pERK and ERK antibody fluorescence signals did not correspond (Fig. 2.3a). This off-target band may be ERK5 (~80–100 kDa), as ERK5 has high sequence homology with

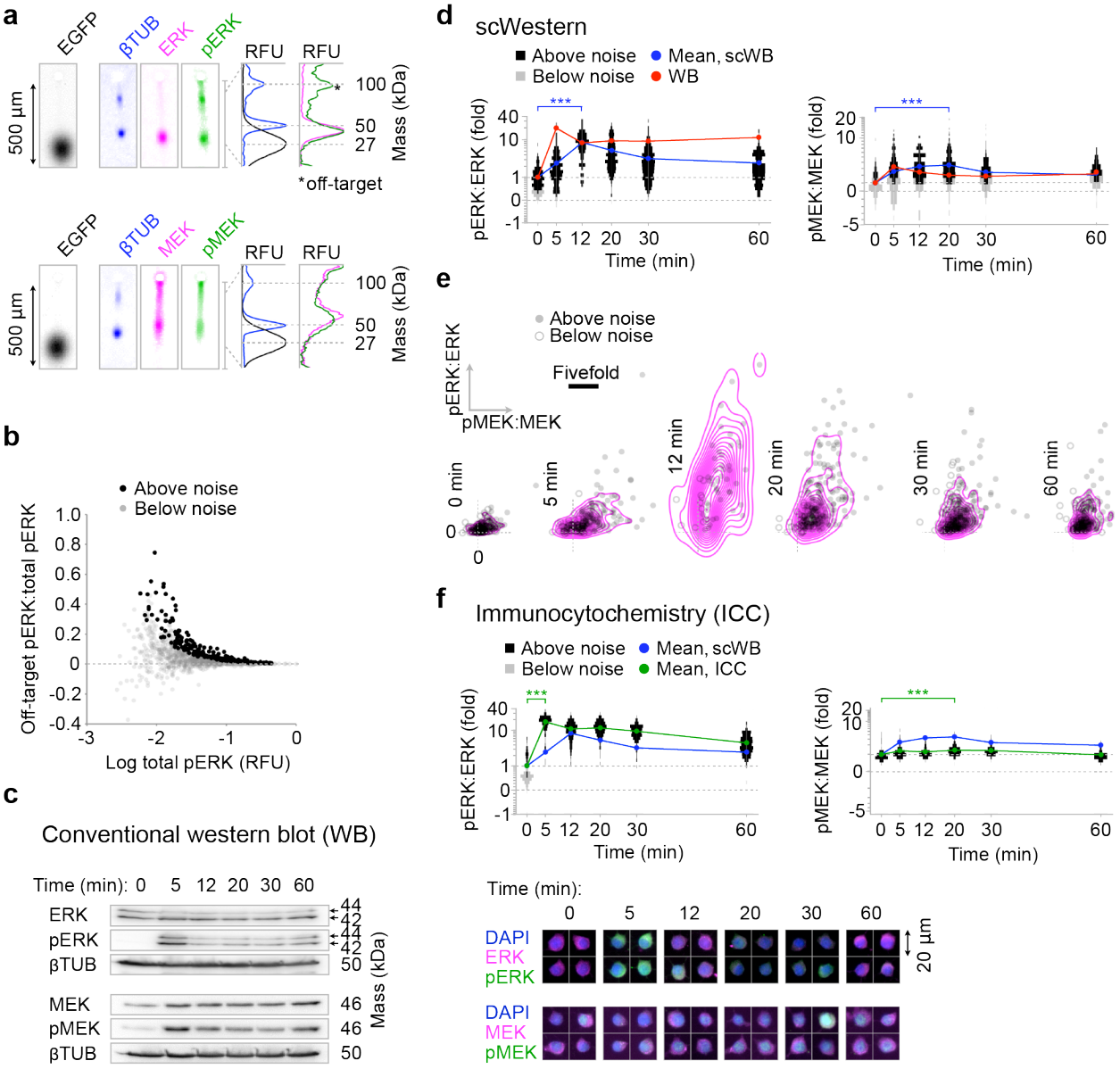

Figure 2.3. scWesterns capture FGF-2 signaling dynamics. (**a**) Fluorescence micrographs of scWesterns for ERK, pERK, MEK and pMEK in NSCs, with βTUB and EGFP ladders. RFU, relative fluorescence units. For each target pair, the EGFP image is from a distinct separation in the same microwell array row. The 103-kDa off-target peak (via pERK antibody) does not coincide with the ERK band. Secondary antibodies were Alexa Fluor 555 labeled (except EGFP: Alexa Fluor 488), in order: pERK, ERK and EGFP coprobe, βTUB, pMEK and MEK, with stripping between probings. (**b**) Ratio of off-target pERK to total fluorescence for 1,117 scWesterns at time points from **d** and **e**. (**c**) Conventional western blots (20 ng/ml FGF-2), cropped to show regions of interest (full-length blots in Fig. A.16). (**d**) Fold change of pERK and pMEK relative to total ERK and MEK, respectively, with signals below technical noise indicated. Note arcsinh-transformed scales. Overlay from conventional western blot (WB) densitometry. ***$P < 0.001$, Mann-Whitney. n = 186, 186, 57, 236, 278 and 208 scWesterns for time points of 0, 5, 12, 20, 30 and 60 min, respectively. (**e**) Fold change from **d** with spatial density contours. (**f**) ICC coprobing for pERK-ERK and pMEK-MEK pairs; Alexa Fluor 555–labeled secondary phospho-antibodies and Alexa Fluor 647–labeled secondary total antibodies. ***$P < 0.001$, Mann-Whitney. pERK:ERK n = 160, 115, 186, 158, 172 and 197 cells, and pMEK:MEK n = 184, 216, 220, 223, 223 and 270 cells, for time points 0, 5, 12, 20, 30 and 60 min, respectively.

ERK1/2 and because pERK1/2 antibodies have been previously shown to cross-react with pERK5[31]. The off-target band for pERK exhibited considerable cell-to-cell variability, did not correlate with on-target pERK signal, and would have contributed up to 52% (with an average of 13%) of the overall pERK signal in unstimulated cells if not electrophoretically resolved from specific signal (Figs. 2.3b and A.15). Off-target probe binding can substantially influence existing single-cell immunofluorescence assays (such as ICC and flow cytometry) unless complex target-specific knock-down experiments are performed[16,17]. In contrast, scWestern analysis is intrinsically well suited to identifying and discarding off-target probing signals.

Both scWesterns and conventional western blotting revealed dynamic, transient ERK and MEK phosphorylation responses (Figs. 2.3c-e and A.16), while the scWestern enabled analysis of statistical differences (Note A.7). Maximal pMEK:MEK phosphorylation levels agreed quantitatively, with ~3.5-fold increases compared to levels at time point 0 (for single-cell data, fold-change is relative to a mean fold-change of 1 at time point 0). A larger maximum fold change in the pERK:ERK ratio was observed, consistent with signal amplification in the MAPK phosphorylation cascade[32].

We next compared scWesterns to a conventional single-cell technique: high-throughput ICC (Figs. 2.3f and A.17-20). pERK:ERK responses by ICC were similar to those measured by scWestern and conventional western assays, whereas pMEK:MEK responses by ICC were strongly attenuated with a maximum mean fold change of <2 (Note A.7). We attribute the lower apparent response to nonspecific signal from spurious nuclear localization of the pMEK antibody (a common artifact in ICC[16]), which obscures the subtle phosphorylation dynamics measurable by scWestern analysis.

Unlike conventional western blots, scWesterns quantified highly variable NSC responses to external stimuli. MEK was activated within 5 min in response to FGF-2, followed closely by ERK, as expected (Fig. 2.3e). However, a considerable spread in the MEK signal was observed, which was strongly amplified into a broad distribution in ERK activation at 12 min, followed by a transient decay in phosphorylation of both enzymes. This propagation of variation from MEK to ERK upon pathway activation is reflected in interquartile ranges of 3.7 and 7.3 fold-change units at 12 min for pMEK:MEK and pERK:ERK, respectively. The pERK:ERK distributions were skewed toward higher phosphorylation levels for the 0 and 60 min time points owing to the presence of rare activated cells (Figs. 2.3e and A.21). This rare activated state may arise from constitutive signaling or transient FGF-independent excursions from baseline phosphorylation states[33].

Heterogeneity in NSC differentiation

In addition to self-renewal, a second hallmark of NSCs is multipotent differentiation from an immature state (markers SOX2+ and nestin, NEST+) into multiple lineages, such as astrocytes (glial fibrillary acidic protein, GFAP+) and neurons (βIII-tubulin, βIIITUB+)[13]. As with many stem cells, exposure of NSCs to uniform culture conditions can drive stochastic differentiation[13,33]. We applied the scWestern to study immature NSCs and their differentiation over a 6 d period under mixed differentiation conditions that yielded both astrocytes and neurons (Fig. 2.4). Every 24 h, differentiating NSCs were settled into microwells (Fig. 2.4a-c) and analyzed. ICC in scWestern microwells did not suggest cell type or shape bias upon transfer of

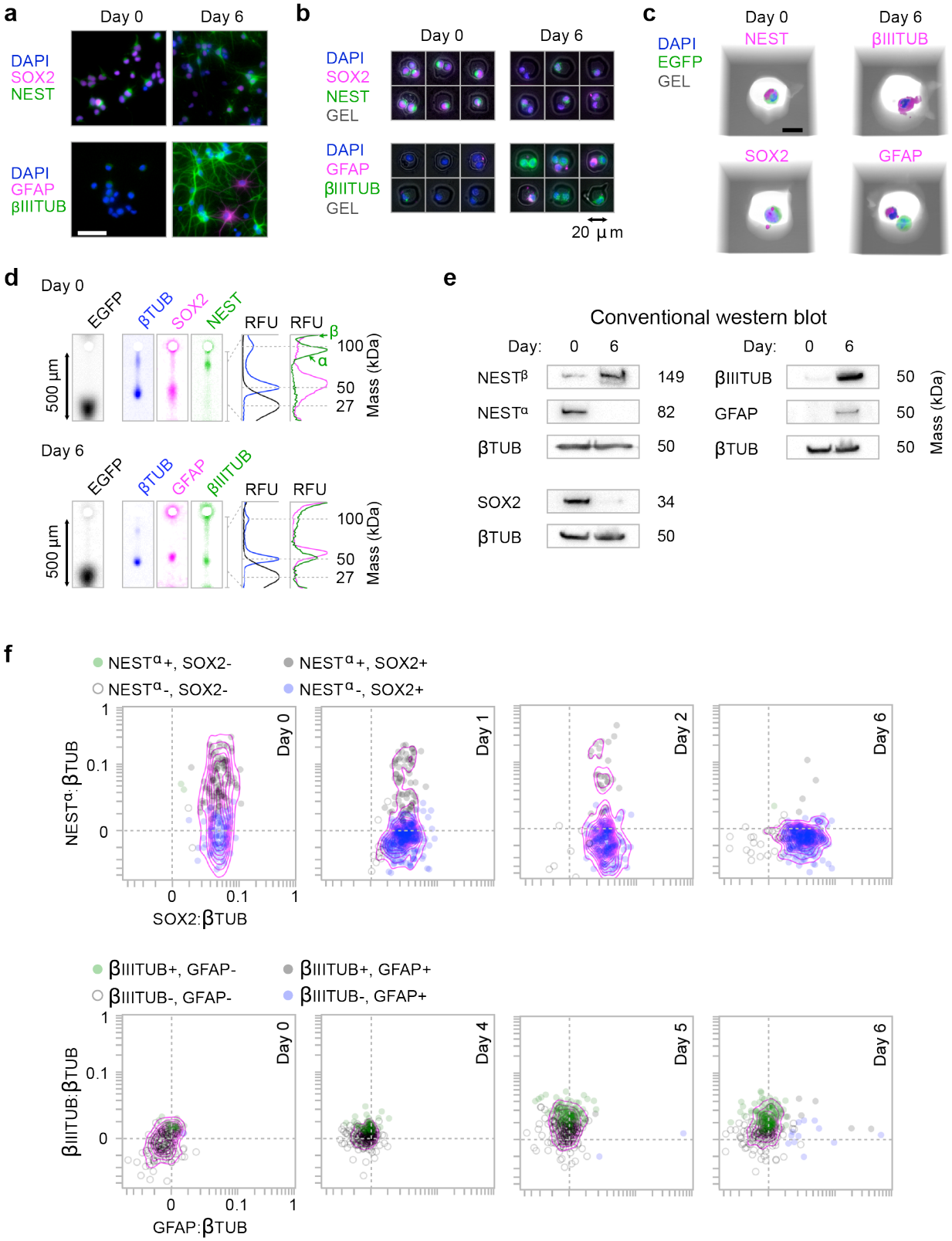

Figure 2.4. scWesterns track NSC lineage commitment during differentiation. (**a**) ICC micrographs of mixed NSC differentiation cultures at days 0 and 6 for stem cell (nestin, NEST; SOX2) and differentiation markers (βIII-tubulin, βIIITUB; glial fibrillary acidic protein, GFAP). Scale bar, 50 μm. (**b**) Micrographs of NSCs in scWestern microwells, fixed and stained as in **a**. (**c**) Confocal images of fixed and stained stem cells (NEST+,SOX2+), neurons

(βIIITUB+) and astrocytes (GFAP+) in a rhodamine-tagged gel (GEL). Scale bar, 10 μm. (**d**) Inverted fluorescence micrographs of scWesterns. SOX2 (Alexa Fluor 555–labeled secondary antibody) and NEST (α and β isoforms; Alexa Fluor 488) were coprobed in separate blocks from GFAP (Alexa Fluor 555) and βIIITUB (Alexa Fluor 488); both block sets were stripped and coprobed for βTUB (Alexa Fluor 555) and EGFP (Alexa Fluor 488). Image sets from each day are the same separation, except EGFP images, which are from the same microwell array row as the corresponding image set. RFU, relative fluorescence units. (**e**) Cropped conventional western blots at differentiation days 0 and 6 (full-length blots in Fig. A.25). (**f**) scWestern fluorescence normalized by βTUB (arbitrary units). Note arcsinh-transformed scales. Spatial density is indicated by contours. scWestern blot NSC marker sample sizes: n = 189, 353, 175 and 274 at 0, 1, 2 and 6 days, respectively. Differentiation marker sample sizes: n = 178, 253, 303 and 280 at 0, 4, 5 and 6 days, respectively. Data are from one of two biological replicates performed.

differentiated cells to microwells (Table A.1). The scWesterns successfully reported single bands for SOX2 (43.3 ± 1.9 kDa), βIIITUB (47.2 ± 0.7 kDa), and GFAP (54.0 ± 1.0 kDa, ± s.d., n = 3 separations; Figs. 2.4d and A.22). Each target protein was within 30% of its expected mass (Note A.8).

NEST is an intermediate filament protein hypothesized to regulate structural dynamics and cytoplasmic trafficking within neural stem and progenitor cells undergoing rapid rounds of division[34]. Intermediate filament proteins often undergo regulation by alternative mRNA splicing, producing diverse isoforms that impact cell responses to stress and modulate intracellular signaling[35]. In agreement with literature reports[36,37], NEST exhibited low and high molecular mass bands by scWestern analysis that we denote NEST$^{\alpha}$ (95.7 ± 3.5 kDa, ± s.d., n = 3 separations) and NEST$^{\beta}$ (retained near the microwell edge), respectively (Figs. 2.4d and A.22). NEST$^{\beta}$ fully penetrated the scWestern gel for longer separation distances, indicating that this species is not an insoluble form of NEST (Fig. A.23).

We further scrutinized NEST$^{\alpha}$ and NEST$^{\beta}$ by conventional western and scWestern analysis with a second antibody (rat-401) against an epitope known to be excised by alternative splicing in a third, 46 kDa, isoform, Nes-S[38]. As for Nes-S, NEST$^{\alpha}$ was not detected by the rat-401 antibody (Fig. A.24), suggesting that NEST$^{\alpha}$ may be an alternatively spliced (or otherwise truncated) form of NEST$^{\beta}$ distinct from Nes-S. Intriguingly, NEST$^{\beta}$ was present at all time points over the 6 d experiment, whereas NEST$^{\alpha}$ was variably expressed between cells and sharply downregulated during differentiation. Indeed, contributions of NEST$^{\beta}$ unrelated to proliferative capacity may account for the apparent promiscuity in NEST expression observed in various mature neural cells by ICC[39] (including in our data, Fig. 2.4a). NEST also exhibited two bands in conventional western blotting (114 and 270 kDa, respectively; Figs. 2.4e and A.25), though the extensive cell-to-cell variation in NEST$^{\alpha}$ expression was not detectable with a conventional western.

Consistent with progressive conversion of NSCs to differentiated lineages, conventional western blotting confirmed greater-than-tenfold reductions in NEST$^{\alpha}$ (but not NEST$^{\beta}$) and SOX2, with accompanying greater-than-tenfold increases in βIIITUB and GFAP over the 6 d period (Fig. 2.4e). Likewise, both culture-plate and in-microwell ICC showed a corresponding reduction in total NEST+ NSCs, from ~90% to 40% of all cells. Similar overall trends were observed for scWestern data, normalized to constitutively expressed βTUB (Figs. 2.4f and A.26). On day 6, scWesterns put the fractions of committed βIIITUB+ neurons and GFAP+ astrocytes at 53% and 7.1%, respectively, matching ICC to within 15% (Table A.1).

Notably, scWesterns revealed high cell-to-cell marker expression variability, including profound increases in GFAP expression in the relatively rare astrocyte population over the course of differentiation, spanning a range of 46-fold on day 6. Single-cell expression levels of NEST$^{\alpha}$ at day 0 spanned a range of 22-fold relative to its technical noise threshold, and the proportion of cells expressing NEST$^{\alpha}$ dropped from 53% to 2% between days 0 and 6.

Additionally, scWestern blots successfully resolved off-target antibody signal of approximately equal magnitude to specific signal for MASH1 (ASCL1, a 34 kDa transcription factor involved in neuronal fate commitment) in late-passage, undifferentiated NSCs, as corroborated by conventional western blotting (Fig. A.27). These data confirm the ability of scWestern assays to accurately capture population expression dynamics by combining the single-cell capabilities of ICC with the molecular mass specificity of conventional western blotting.

2.3 Discussion

scWesterns are a single-cell protein analysis technique capable of quantitative, multiplexed, and at-the-bench operation, offering an avenue to advance our understanding of cell-to-cell variation in protein-mediated cell functions. Given the often mediocre performance of antibodies as probes[16,40], advances in assay specificity are necessary to discriminate between legitimate and spurious protein signals. Western blotting offers high protein specificity, as the technique reports both target molecular mass (via protein electrophoresis) and probe binding (via subsequent antibody probing), not simply probe binding[18]. scWesterns bring this specificity to the analysis of single cells, pointing toward a rich, graded heterogeneity in stem cell signaling trajectories. Furthermore, by reporting molecular mass as well as antibody binding, the scWestern could, we showed, identify two putative nestin isoforms and suggest that one (NEST$^{\alpha}$) better reflects the exit of NSCs from the immature state. In contrast, antibody-binding assays (ICC or flow cytometry) struggle to distinguish such isoforms. Clonal lineage tracing — aided by scWestern analyses — may enable further mechanistic insights into the functions of NEST isoforms[26].

More broadly, we envision a role for scWesterns in applications that integrate upstream functional or morphological screens, quantify cell-to-cell response to pharmaceutical agents (including rare circulating tumor cells[4]), and advance affinity-reagent performance by easing library screens.

2.4 Materials and Methods

Cell culture

Neural stem cells (NSCs) were isolated from the hippocampi of adult female Fisher 344 rats[29] and cultured on tissue culture-treated polystyrene plates coated with 10 μg/mL polyornithine (Sigma-Aldrich) and 5 μg/mL laminin (Life Technologies). NSCs were found to be *Mycoplasma* free within 12 months both before and following use in experiments. NSCs were cultured in 1:1 DMEM-F12 (Life Technologies) supplemented with N-2 (Life Technologies) and 20 ng/mL recombinant human FGF-2 (PeproTech) and were subcultured at 80% confluency using Accutase (Life Technologies) for cell detachment.

EGFP-expressing NSC cell lines were created through stable retroviral infection. The retroviral vector pCLPIT-GFP[41] was packaged[42] and purified virus was titered on NPCs. High-expressing EGFP NSCs were infected at a multiplicity of infection of 3 (MOI = 3) and analyzed in Fig. 2.2, while low-expressing EGFP NSCs were infected at MOI = 0.5 and used in all other studies. Stable cell lines were obtained through selection in medium containing 0.3 μg/mL puromycin for 72 h (Sigma-Aldrich).

EGFP-expressing NSCs for scWestern EGFP expression studies were cultured as described for uninfected NSCs. For scWestern signaling studies, EGFP-expressing NSCs were FGF-2 starved for 16 h. Cells were detached with Accutase, and suspensions analyzed by scWesterns (see "*scWestern*" below). EGFP-expressing NSCs for scWestern differentiation studies were cultured in DMEM-F12-N2 supplemented with 0.5 ng/mL FGF-2, 1 μM retinoic acid (RA, Enzo Life Sciences), and 1% fetal bovine serum (FBS, ThermoFisher Scientific) for 0–6 d. Cells were detached with trypsin-EDTA (Corning Cellgro) and analyzed (N.B., cells were not differentiated within microwells; see "*scWestern*").

Proteins and reagents

15 μm fluorescent polystyrene microspheres were from Life Technologies. Alexa Fluor 488-labeled purified ovalbumin and bovine serum albumin were also from Life Technologies. Purified standards for scWestern calibration were: β-tubulin from bovine brain (Cytoskeleton); recombinant EGFP, His-tagged (BioVision); and recombinant human pERK1 (Abcam). Aliquots of these purified standards were labeled with Alexa Fluor 568 using a protein labeling kit according to vendor instructions (Life Technologies) for the determination of partition coefficients in indirect calibration experiments (see "*scWestern calibration"*).

Purified His-tagged Dronpa was expressed in Rosetta competent cells transformed using a pET His6 tobacco etch virus (TEV) ligase independent cloning (LIC) vector, 2BT (EMD Millipore), grown in 2YT medium at 37°C to an OD600 of 0.5, induced with 0.5 mM IPTG and grown for an additional 2.5 h at 37°C before harvesting. Cells were pelleted by centrifugation for 15 min at 4°C, and the pellets were resuspended in Nickel buffer A supplemented with protease inhibitors (25 mM HEPES pH 7.5, 400 mM NaCl, 10% glycerol, 20 mM imidazole, 1 μg/mL leupeptin and pepstatin, 0.5 mM PMSF). Cells were lysed using an Avestin C3 homogenizer at a pressure of 15,000 psi. Cell debris was pelleted at 15,000 rpm for 30 min. The clarified lysate was loaded onto a 5 mL HisTrap FF Crude column (GE Healthcare), and unbound material was washed out with Nickel buffer A. Bound protein was eluted with a 10CV gradient up to 400 mM imidazole in Nickel buffer A. Absorption of the eluting material was monitored at 503 nm as well as at 280 nm to aid in pooling the target protein. Fractions containing Dronpa were pooled and desalted into IEX buffer A (50 mM sodium phosphate pH 6.5). Desalted protein was loaded onto a 5 mL SP HP ion exchange column (GE Healthcare) and unbound material was washed out with IEX buffer A. Bound material was eluted with a 20CV gradient up to 1 M NaCl in IEX buffer A. Fractions containing Dronpa were pooled and assayed for aggregation by analytical size-exclusion chromatography on a Superdex 200 5/150 column (GE Healthcare) equilibrated in 25 mM HEPES, 400 mM NaCl, 10% glycerol, 1 mM DTT. Samples were finally desalted into storage buffer (50 mM sodium phosphate pH 6.5, 150 mM NaCl, 10% glycerol, 1 mM DTT).

N-[3-[(4-benzoylphenyl)formamido]propyl] methacrylamide (BPMAC) was synthesized in-house via the reaction of the succinimidyl ester of 4-benzoylbenzoic acid with *N*-(3-aminopropyl)methacrylamide hydrochloride in the presence of catalytic triethylamine according to standard protocols[21,43].

Fabrication of microwell scWestern substrates

SU-8 microposts were fabricated on mechanical-grade silicon wafers by standard soft lithography methods. SU-8 2025 photoresist (MicroChem) was spun to a thickness of (typically) 30 μm according to manufacturer guidelines and exposed to 365 nm UV light at ~40 mW/cm^2 for 12 sec under a mylar mask printed with 20 μm circular features at 20,000 dpi (CAD/Art Services). The features were arranged in a square configuration with a pitch of 500 μm in the direction of separations and 190 μm in the transverse direction (a pitch of 700 μm yielded separation lengths sufficient for NEST$^\beta$ to fully enter the scWestern gel). 2 × 8 blocks of 14 × 30 features (6,720 total) were spaced 9 mm apart to match the dimensions of a 2 × 8-well microarray hybridization cassette (AHC1X16, ArrayIt). 1 mm-thick rails spanning the length of the micropost array at a spacing of 24 mm were also patterned to support glass substrates at the height of the microposts. Uniformity of features was verified by optical profilometry after exposure and development using SU-8 developer solution (MicroChem). The measured feature heights and diameters within a micropost block were 30.30 ± 0.15 μm (± s.d., n = 4 microposts) and 20.52 ± 0.68 μm (± s.d., n = 4 microposts) for respective nominal dimensions of 30 μm and 20 μm. Between-block CV's in the height and diameter measurements for blocks spaced across the full length of the array were 1.1% and 5.2%, respectively (n = 3 microposts). Wafers were silanized by vapor-deposition of 2 mL of the hydrophobic silane dichlorodimethylsilane (DCDMS, Sigma-Aldrich) for 1 h *in vacuo,* washed thoroughly with deionized (DI) water, and dried under a nitrogen stream immediately prior to use. Silanized wafers were robust to reuse after rinsing with DI water in excess of 20 times with moderate delamination of micropost structures.

Plain glass microscope slides (VWR) were silanized to establish a self-assembled surface monolayer of methacrylate functional groups according to standard protocols[44]. Silanized slides were placed facedown onto micropost wafers and manually aligned to the SU-8 rail and micropost features. Gel precursor solutions were 8%T (w/v total acrylamides), 2.7%C (w/w of the crosslinker N,N'-methylenebisacrylamide) from a 30%T, 2.7%C stock (Sigma-Aldrich); 3 mM BPMAC from a 100 mM stock in DMSO, 0.1% SDS (BioRad), 0.1% Triton X-100 (Fisher), 0.0006% riboflavin 5' phosphate (Sigma-Aldrich), 0.015% ammonium persulfate (APS, Sigma-Aldrich), and 0.05% tetramethylethylenediamine (TEMED, Sigma-Aldrich) in 75 mM Tris buffer titrated with HCl to a pH of 8.8. For confocal imaging of cells in rhodamine-tagged scWestern gels, the precursor included the fluorescent monomer methacryloxyethyl thiocarbamoyl rhodamine B (Polysciences) at 3 μM from a 100 μM stock in DMSO. The precursor mixture was sonicated and degassed (Aquasonic 50D, VWR) for 1 min *in vacuo* immediately prior to the addition of detergents (SDS, Triton) and polymerization initiators (riboflavin, APS, TEMED). The precursor was then injected into the gap between the glass slide and silicon wafer using a standard 200 μL pipet. After allowing ~30 sec for precursor to wick through the gap, the slide was exposed to blue light for 7.5 min at 470 1× (advanced light meter, Sper Scientific) from a collimated 470 nm LED (Thor Labs) mounted at a 45° angle above the slide. Polymerization was allowed to continue for an additional 11 min. Gel-fabricated glass

slides were wetted at their edges using 2 mL of phosphate-buffered saline (PBS), pH 7.4 (Corning) and carefully levered from wafers using a razor blade. Fabricated slides could be stored at 4°C in PBS for up to 2 weeks before use without loss of protein separation or photocapture properties.

scWestern

Fabricated slides were removed from PBS and excess liquid drained to a corner by gravity and absorbed using a kimwipe (Kimberly-Clark). 1–2 mL of cell suspension was applied evenly across the surface of the slide and allowed to settle on a flat surface within a 100 × 100 mm petri dish. Settling times varied from 5 to 30 min, with microwell occupancy monitored by bright-field microscopy until single-cell occupancies of roughly 40–50% were achieved. Intermittent, gentle movement of the petri dish every 2–5 min for 10 sec was sufficient to ensure cell access to microwells through cell rolling on the gel surface. After settling, slides were lifted to a 10–20° angle from one of the short edges to remove excess cell media, and cells on the surface of the slide were removed by gentle pipetting of 4 or 5 1 mL aliquots of PBS to the raised edge of the slide surface, with excess buffer removed from the lower edge by vacuum. Slides were placed flat and prepared for cell counting by applying 1 mL of PBS onto the slide. A second plain glass slide was applied to the PBS layer from one short edge to the other to prevent entrapment of bubbles and lowered to form a "sandwich" of slides. Microwells within the sandwich were imaged by bright-field microscopy at 4× magnification (Olympus UPlanFLN; numerical aperture (NA), 0.13) using 50 ms exposure times at 1 × 1-pixel binning and a preset position list to guide a mechanical stage (Olympus IX71 inverted fluorescence microscope equipped with iXon+ EMCCD camera, Andor; motorized stage, ASI; and shuttered mercury lamp light source, X-cite, Lumen Dynamics; controlled by MetaMorph software, Molecular Devices). All 6,720 features could be imaged in ~4 min.

After cell counting, the top glass slide was removed from the sandwich by sliding gently across the gel layer. The scWestern slide with settled cells was then immediately transferred to a custom 60 mm × 100 mm horizontal electrophoresis chamber fabricated from 3 mm-thick Perspex plastic. Platinum wire electrodes (0.5 mm diameter, Sigma-Aldrich) were placed along the long edge of the chamber and interfaced with alligator clips to a standard electrophoresis power supply (Model 250/2.5, BioRad). Slides were temporarily adhered to the bottom face of the chamber using petroleum jelly. 10 mL of a denaturing RIPA lysis/electrophoresis buffer consisting of 0.5% SDS, 0.1% v/v Triton X-100, 0.25% sodium deoxycholate (Sigma-Aldrich) in 12.5 mM Tris, 96 mM glycine pH 8.3 (0.5× from a 10× stock, BioRad) was poured over the slide to lyse cells. This buffer was supplemented with 1 mM sodium fluoride and sodium orthovanadate for phosphoprotein analyses (Sigma-Aldrich). The RIPA buffer provides denaturing but non-reducing conditions, since reduction typically requires heating in the presence of a reducing agent for timescales longer than protein diffusion from microwells[21]. Lysis proceeded for 10 sec with electric field off, followed by application of 200V (E = 40 V/cm) for ~30sec. Separations from single EGFP-expressing NSCs were monitored in real time at 10× magnification (UPlanFLN; 0.3 NA objective) using a filter set optimized for EGFP (XF100-3, Omega Optical), 4 × 4 camera binning, 250 ms exposure time. Following separations, slides were immediately exposed for 45 sec from above using a UV mercury arc lamp (Lightningcure LC5, Hamamatsu) directed through a Lumatec series 380 liquid light guide with inline UV filter (300 to 380 nm bandpass, Omega Optical) suspended approximately 10 cm

above the slide with UV power at the slide surface of ~40 mW/cm^2 (320–400 nm UV meter, Hamamatsu).

Following separation and photocapture of cell contents, slides were washed using 10 mL of the denaturing RIPA buffer, followed by 10 mL of TBST (100 mM Tris titrated to pH 7.5 with HCl, 150 mM NaCl, 0.1% Tween 20, EMD Millipore), each for 10 min. Slides could be stored before successful immunoprobing for at least 1 week at 4°C in TBST.

In FGF-2 stimulation experiments, cells were stimulated between cell-per-microwell counting and lysis/electrophoresis steps by applying 1 mL of 20 ng/mL FGF-2-spiked culture medium to the slide surface for the desired stimulation time.

Purified protein scWesterns

Purified proteins were assayed using a similar protocol to that for single cells. Gel slides were incubated with purified proteins in denaturing RIPA buffer for 30 min, submerged in fresh denaturing RIPA for 5 s, and "sandwiched" with a second glass slide to trap proteins within the gel layer. The glass slide sandwich was subjected to electrophoresis, UV-mediated protein capture, washing, and probing as in single-cell assays; the top glass layer was removed after the capture step.

scWestern probing, imaging, and stripping

Slides were probed with primary and fluorescently labeled secondary antibodies by diffusive delivery in 2 × 8-well microarray hybridization cassettes (ArrayIt).

Primary antibodies with folddilutions employed for single-cell, purified protein, and calibration assays (unless otherwise noted) were rabbit anti-ovalbumin (1:20, ab1221, Abcam), goat anti-GFP (1:20, ab6673, Abcam), rabbit anti-β-tubulin (1:20, ab6046, Abcam), rabbit anti-pERK1/2 (1:40, Thr202/Tyr204, 4370, Cell Signaling), rabbit anti-ERK1/2 (1:20, 4695, Cell Signaling), mouse anti-ERK1/2 ("ERK #2," 1:20, 4696, Cell Signaling), rabbit anti-pMEK1/2 (1:40, Ser217/Ser221, 9154, Cell Signaling), rabbit anti-MEK1/2 (1:20, 9126, Cell Signaling), goat anti-SOX2 (1:20, sc-17320, Santa Cruz Biotechnology), mouse anti-nestin ("NEST," 1:20, 611658, BD Biosciences), mouse anti-nestin ("NEST #2," 1:20, MAB353, clone: rat-401, EMD Millipore), goat anti-EphB4 (1:20, AF446, R&D Systems), mouse anti-MASH1 (1:20, 556604, BD Biosciences), mouse anti-SRC (1:20, 05-184, EMD Millipore), goat anti-GFAP (1:20, ab53554, Abcam), mouse anti-βIII-tubulin (1:20, T8578, Sigma-Aldrich). Secondary antibodies were Alexa Fluor 488–, 555–, or 647–labeled donkey anti-mouse, rabbit or goat IgG from Life Technologies (A31571, A31573, A21447, A31570, A31572, A21432, A21202, A21206, A11055), except for the probing of ovalbumin in Fig. A.7, which used Alexa Fluor 568-labeled goat anti-rabbit IgG (A-11011, Life Technologies). All were used at the same dilution factor as that of the corresponding primary antibody.

Each block of separations was incubated at room temperature with 40 μL of primary antibody solution diluted in TBST supplemented with 2% bovine serum albumin (BSA, Sigma-Aldrich) for 1 h under gentle orbital shaking. Slides were removed from hybridization cassettes and washed three times in 10 mL TBST for 15 min per wash (45 min total), also under gentle orbital shaking. Slides were then similarly probed and washed with fluorescently labeled secondary

antibodies in TBST supplemented with 2% BSA. Slides were washed a final time in 10 mL DI water for 5 min and dried under a nitrogen stream. Imaging was conducted using a GenePix 4300A microarray scanner with PMT gains of 400–550 and laser powers of 30–100%, optimized for maximum dynamic range without saturation of target band fluorescence values. Filter sets were employed for three-channel detection using Alexa Fluor 488, 555, and 647-labeled secondary antibodies using 488, 532, and 635 nm lasers, respectively. 12.5 mm diameter emission filters for the 488 and 532 nm spectral channels were from Omega Optical (XF3405 and XF3403, respectively); the 635 nm channel employed a built-in far-red emission filter.

Spectral bleed-through was below noise thresholds of on-target fluorescence line profiles, except for co-probing of ERK or β-tubulin (Alexa Fluor 555-labeled secondary antibody) with EGFP (Alexa Fluor 488-labeled secondary antibody) in Figs. 2.3 and 2.4 respectively. Ratio metrics in Fig. 2.3d,e for which ERK bands were affected by EGFP bleed-through above technical noise were discarded from analysis. Ratio metrics in Fig. 2.4f derived from β-tubulin bands similarly affected by EGFP bleed-through were also discarded. No fluorescence micrographs or derived data sets were fluorescence-compensated for spectral bleed-through.

Stripping of slides was performed via 3 h incubations in a stripping buffer heated to 50°C consisting of 2.5% SDS and 1% β-mercaptoethanol (Sigma-Aldrich) in 62.5 mM Tris titrated to pH 6.8 with HCl. Following stripping, slides were washed three times in 10 mL aliquots of TBST for 5 min per wash and stored in TBST at 4°C until reprobing. For longer-term archiving, stripped, air-dried slides could be successfully reprobed after extended (>1 month) storage at 4°C.

scWestern data analysis

Cell-per-microwell scoring was conducted manually or via custom software designed in-house that employed scripts to mate thresholding and particle analysis on the basis of cell size and circularity in ImageJ (http://rsbweb.nih.gov/ij/) to downstream gating to identify microwells containing single cells in R (http://www.r-project.org).

To quantify the performance of automated cell-per-microwell scoring, we calculated precision = tp/(tp+fp) and sensitivity = tp/(tp + fn), where tp is the number of microwells scored as containing single cells that actually contained single cells, fp is the number of microwells scored as containing single cells that did not contain single cells, and fn is the number of microwells scored as not containing single cells that actually contained single cells[45]. Precision = 1 means that all microwells scored as containing single cells actually contained single cells. Sensitivity = 1 means that all microwells actually containing single cells were scored as containing single-cells. Precision and sensitivity metrics were 0.90 ± 0.09 and 0.68 ± 0.17 respectively (± s.d., n = 56 blocks of 420 microwells on 8 separate slides), reflecting stringent selection of single-cell microwells at the expense of the total number of microwells included in downstream analysis.

Fluorescence images from the GenePix scanner were registered using landmark correspondences in Fiji (http://fiji.sc/Fiji). A custom script extracted line profiles from grids of regions of interest (ROIs) from each fluorescence image. Line profiles were background subtracted using linear interpolation between points set to the approximate boundaries of peaks of interest. Data quality control was performed by manually reviewing separation ROIs flagged due to outlying line

profiles. Separations that were clearly affected by the presence of, for example, autofluorescent particulates were discarded from data sets, as were zero-cells-per-microwell separations incorrectly scored as single-cell separations that did not contain β-tubulin loading control signals above technical noise.

Total areas under peaks (AUCs) of interest (or metrics derived from them, such as AUC ratios and calibrated AUCs) were transformed, where applicable, using the function AUC_t = arcsinh(AUC/F), where AUC_t is the arcsinh-transformed value and F is a cofactor prescribing the transition from linear to log-like behavior. The value of F was optimized by setting it according to $F = \mu_{ones,below} + 3\sigma_{ones,below}$, where $\mu_{ones,below}$ and $\sigma_{ones,below}$ are the mean and s.d. of the set of single-cell-per-microwell separations with fluorescence AUCs (or metrics) below a technical noise threshold. The technical noise threshold T was set at $T = \mu_{zeros} + 3\sigma_{zeros,}$ where μ_{zeros} and σ_{zeros} are the mean and s.d. of the AUCs or metric values from zero-cells-per-microwell separations in a given experiment. Where applicable, separations with AUCs in the numerator of ratio metrics falling below T were flagged to display as such when plotted. Separations with AUCs below T in the denominator were discarded from data sets.

For analysis of βTUB distribution in Fig. 2.2b, histogram data were fit to the gamma distribution $f(x) = (x^{a-1}e^{-x/b})/(\Gamma(a)b^a)$ using an implementation of the least-squares Marquardt-Levenberg algorithm in gnuplot (http://www.gnuplot.info); x = total probed band fluorescence, $a = \mu_p^2/\sigma_p^2 = 14.8$, $b = \sigma_p^2/\mu_p = 1.6 \times 10^5$ AFU, μ_p = mean band fluorescence, σ_p^2 = variance in band fluorescence and Γ is the gamma function.

Statistical analysis

Nonparametric comparison of scWestern data (single comparisons only) was performed using the Mann-Whitney *U*-test in conjunction with Shapiro-Wilk and Levine tests for normality and equality of variance, respectively, in SPSS v.21 software (IBM).

scWestern calibration

A conceptual overview and schematics of "direct" and "indirect" calibration assays are provided in Fig. A.11 and Note A.6. For direct calibration of EGFP, an eight-aliquot dilution series (40 µl per aliquot) of EGFP in denaturing RIPA buffer supplemented with 4 µM BSA (approximating total protein levels in single-cell separations) was added to distinct microwells of scWestern slides in the ArrayIt hybridization cassette (Fig. A.12**)**. Slides were sandwiched and assayed as for purified protein assays (see "*Purified protein scWesterns"*) with one additional step. A subset of microwells in each block were imaged for EGFP fluorescence (10× magnification, 200 ms exposure time, 1 × 1-pixel binning) immediately before the electrophoresis step using a preset position list to guide the mechanical stage on the IX71 fluorescence microscope. Partition coefficients across the concentration range were determined from these images according to $K = ([EGFP]_{gel} - [EGFP]_{gel,bg})/([EGFP]_{microwell} - [EGFP]_{microwell,bg})$, where $[EGFP]_{gel}$ and $[EGFP]_{microwell}$ are in-gel and in-microwell concentrations of EGFP at equilibrium determined by fluorescence calibration in a separate microfluidic channel of 30 µm depth (Fig. A.4). Custom straight-channel microfluidic chips were fabricated in soda lime glass using standard wet-etching processes (PerkinElmer). $[EGFP]_{gel,bg}$ and $[EGFP]_{microwell,bg}$ correct for the background fluorescence of the scWestern slide prior to incubation with the EGFP solutions. The number of

molecules of EGFP in each microwell voxel was also estimated from these data, assuming cylindrical microwells of nominal dimensions: 20 μm diameter, 30 μm depth (9.4 pL volume).

Indirect calibration was performed by capturing to the scWestern gel and probing a dilution series of a given purified protein in denaturing RIPA supplemented with 4 μM BSA in the absence of an electrophoresis step (Figs. A.11-12**)**. Spot UV exposures were applied to the underside of the slide within each microwell block via the 10× objective for 45 sec each on the Olympus IX71 fluorescence microscope through a custom UV-longpass filter set (excitation 300–380 nm, emission >410 nm; XF1001, XF3097; Omega Optical) with a UV power at the slide surface of ~40 mW/cm^2 (320 to 400 nm; UV meter; Hamamatsu). The in-gel concentrations of purified proteins captured in this manner were determined from separate partition coefficient measurements using Alexa Fluor 568-labeled aliquots of each protein (Fig. A.4). Indirect calibration of EGFP reports molecule number using the inferred in-gel concentrations for a voxel size equivalent to that of a typical probed EGFP band from an scWestern experiment (45 μm × 45 μm in area, 30 μm in depth). Probe AFU and SNR values in indirect calibration data were corrected for fluorescence background caused by nonspecific probing of UV-exposed gel spots in the absence of calibration standard.

Integration of scWestern analysis with FACS

Live EGFP NSCs were sorted using an Influx v7 Sorter (BD Biosciences). BD FACS Sortware 1.0.0.650 was used to establish a 4 x 16 grid over the surface of a dried scWestern slide for deposition of sorted cells. 10 μm polystyrene fluorescent microspheres (Flow-Check Fluorospheres, Beckman Coulter) were test sorted for fine positioning adjustment. Cells were gated for EGFP expression, and sorting was calibrated so that each droplet exiting the nozzle contained a single EGFP-positive cell or no cells. The sorting purity was ~96%. After FACS, gel slides were rehydrated by immersion in PBS and analyzed by scWestern. For propidium iodide (PI) cell staining, PI (1 mg/mL, Life Technologies) was added to cell suspensions at 1:100 dilution. Dead cells were imaged after drying of FACS droplets on scWestern slides by fluorescence microscopy.

Determination of bulk buffer velocity during in-microwell lysis

Bulk maximum flow speeds during lysis (ignoring vector information) were estimated by wide-field fluorescence microscopy (4× objective, EGFP filter set) during pouring of a 15 μm fluorescent microsphere-spiked RIPA buffer over a scWestern slide (10^5 microspheres/mL) at an exposure time of 10 ms (Fig. A.3). Velocities were extracted from fluorescence streaks caused by movement of microspheres in the horizontal plane over the exposure period, with the objective focused ~1 mm above the center of the scWestern slide plane to observe bulk fluid behavior.

COMSOL fluid modeling

Fluid flow in *sc*Westerm microwells was modeled in COMSOL Multiphysics 4.2a (Fig. A.3 and Note A.1). Bulk flow above microwells was simulated as steady-state laminar flow of water in a square channel of cross-section 100 μm × 100 μm. The top and side walls of the channel were set to a slip boundary condition. The bottom wall of the channel and the microwell walls were set to no-slip. Inlet velocity was set to 0.0087 m/s to achieve a maximum bulk flow velocity of 0.013

m/s. Outlet pressure was set to 0. Microwell recirculation flow was visualized by the particle tracing module in COMSOL.

Flow cytometry

For flow cytometry for EGFP expression; EGFP-expressing NSCs and uninfected NSCs were detached with Accutase, fixed by suspension in 4% paraformaldehyde (Sigma-Aldrich) for 15 min, and then blocked and permeabilized with flow staining buffer (5% donkey serum with 1 mg/mL saponin (Sigma-Aldrich) in PBS) for 15 min. Cells were incubated with goat anti-GFP (1:100; see "*scWestern probing, imaging, and stripping*" for product details) in flow staining buffer for 1 h; followed by incubation with Alexa Fluor 555-labeled donkey anti-goat IgG (1:100) in flow staining buffer for 1 h. Cells were washed twice for 5 min each with staining buffer between application of primary and secondary antibodies, and finally for 5 min with staining buffer and twice for 5 min each with PBS immediately prior to performing flow analysis. Flow cytometry was performed using an EMD Millipore EasyCyte 6HT-2L.

Conventional western blotting

For the signaling study in Fig. 2.3c, EGFP-expressing NSCs were seeded at 2.5×10^5 cells per well in a six-well culture plate. Cells were FGF-2 starved for 16 h, incubated with 20 ng/mL FGF-2 for the desired stimulation time, and lysed in RIPA buffer (50 mM Tris, 150 mM NaCl, 1% NP-40, 0.5% sodium deoxycholate, 0.1% SDS, pH 8) containing protease and phosphatase inhibitor cocktails (ThermoFisher Scientific) and 10 mg/mL PMSF (Sigma-Aldrich). For the differentiation assay in Fig. 2.4e, EGFP-expressing NSCs were seeded at 5×10^5 cells per dish in 6 cm dishes. Day 0 differentiated cells were lysed the following day; day 6 differentiated cells were cultured in differentiation medium (DMEM-F12-N2, 0.5 ng/mL FGF-2, 1 μM RA, 1% FBS) for 6 d and then lysed. Cell lysates of equal total protein concentrations determined by a bicinchoninic acid assay (ThermoFisher Scientific) were mixed with 5x Laemmli buffer (final 50 mM Tris, 2% SDS, 0.1% Bromophenol Blue, 10% glycerol), 2-mercaptoethanol was added to 10% v/v, and samples were boiled at 95°C for 5 min. Samples were electrophoretically separated on SDS-PAGE gels of between 6 and 10%T and transferred onto nitrocellulose membranes using standard methods. Blots were blocked for 1 h in TBST and 3% BSA for phoshoprotein antibodies or 5% nonfat powdered milk (EMD Millipore) for all other antibodies. Blots were probed overnight with primary antibodies in the same blocking buffer: rabbit anti-pERK1/2 (1:2,000; see "*scWestern probing, imaging, and stripping*" for product details), rabbit anti-ERK1/2 (1:1,000), mouse anti-ERK1/2 ("ERK #2", 1:1,000), mouse anti-MASH1 (1:1,000), mouse anti-SRC (1:1,000), goat anti-EphB4 (1:1,000), goat anti-GFP (1:1,000), rabbit anti-pMEK1/2 (1:1,000), rabbit anti-MEK1/2 (1:1,000), goat anti-SOX2 (1:500), mouse anti-nestin (1:1,000), mouse anti-nestin ("NEST #2", clone: rat-401, 1:2,000), goat anti-GFAP (1:1,000), mouse anti-βIII-tubulin (1:2,000), rabbit anti-β-tubulin (1:500); followed by 1 h incubation with appropriate horseradish peroxidase-conjugated secondary antibodies: mouse anti-goat HRP (1:5,000, 31400), goat anti-mouse HRP (1:10,000, 32430), goat anti-rabbit HRP (1:10,000, 32460), all from ThermoFisher Scientific. Protein bands were detected using SuperSignal West Dura Chemiluminescent Substrate (ThermoFisher Scientific), and blots were digitally imaged on a ChemiDoc XRS+ Imaging System (BioRad). Blots were stripped in a solution of 3% acetic acid, 0.5M NaCl, pH 2.5, for 10 min, neutralized with 0.5 M NaOH for 1 min, and then reprobed as needed. Blot densitometry was performed in ImageJ by measuring background-subtracted ROI intensities.

For purified protein samples (Fig. A.6), 1 μg of Alexa Fluor 488-labeled OVA and/or 1 μg Alexa Fluor 488-labeled BSA were incubated in denaturing or standard RIPA buffer for 30 min at room temperature, protected from light. Samples were then mixed with 5× Laemmli buffer. For reducing conditions, 2-mercaptoethanol was added to samples to 10% v/v. For boiling conditions, samples were boiled at 95°C for 5 min; non-boiled samples were incubated at room temperature for 5 min. All samples were electrophoretically separated on a 10% SDS-PAGE gel. Fluorescent protein bands were directly imaged in-gel via the ChemiDoc instrument.

Immunocytochemistry

For the signaling study in Fig. 2.3f, EGFP-expressing NSCs were seeded at 5×10^3 cells per well in a 96-well plate. Cells were FGF-2 starved and stimulated as described for conventional western blotting. For the differentiation assay in standard cell culture conditions (Fig. 2.4a), EGFP-expressing NSCs were seeded at 4×10^4 cells per well in a 24-well plate and differentiated. For scWestern microwells, EGFP-expressing NSCs were differentiated in culture plates, suspended on the appropriate day, settled into scWestern slides, and processed within ArrayIt hybridization cassettes. Cell cultures and settled cells were fixed with 4% paraformaldehyde for 15 min, and then blocked and permeabilized with staining buffer (5% donkey serum with 0.3% Triton-X100 in PBS) for 30 min. Cultures and cells were incubated 24–48 h with combinations of primary antibodies in staining buffer: rabbit anti-pERK1/2 (1:200; see "*scWestern probing, imaging, and stripping*" for product details), mouse anti-ERK1/2 (1:50, 4696, Cell Signaling), rabbit anti-pMEK1/2 (1:200), mouse anti-MEK1/2 (1:25, 4694, Cell Signaling), goat anti-SOX2 (1:100), mouse anti-nestin (1:200), goat anti-GFAP (1:500), mouse anti-βIII-tubulin (1:500); followed by 2 h incubations with appropriate Cy3-, Alexa Fluor 555-, and 647- labeled donkey anti-mouse, rabbit, or goat IgG secondary antibodies (1:250, Life Technologies; 15-165-150, 715-605-150, 711-605-152, 705-605-147, Jackson ImmunoResearch), with 4,6-diamidino-2-phenylindole (DAPI) as a nuclear counterstain (5 μg/mL, Life Technologies). Cell cultures were imaged using a Nikon Eclipse T*i* inverted fluorescence microscope (Nikon Instruments) or an ImageXpress Micro XL Widefield High Content Screening System (Molecular Devices). In-microwell cells were imaged using the Olympus IX71 microscope (see "*scWestern*").

Confocal images were obtained on a BX51W1 microscope (Olympus) with swept-field confocal optics (Prairie Technologies) and analyzed with Icy bioinformatics software (http://icy.bioimageanalysis.org). For confocal imaging of differentiated cells in scWestern microwells in Fig. 2.4c, rabbit anti-GFAP (1:500, Abcam) was used; all other antibody reagents were identical to those listed.

Immunocytochemistry data analysis

For the signaling study in Fif. 2.3f**,** cells were identified via custom ImageJ scripts using thresholding and particle analysis to locate DAPI-stained nuclei. Single cells for analysis were isolated and selected by gating for distance to nearest neighbor cells and uniformity of background signal in R. Fluorescence was quantified by summing pixel intensities of a background-subtracted 75 × 75-pixel ROI around each single cell. Approximately 50% of pixels in each ROI consisted of background signal, which was Gaussian in distribution. The intensity value with highest pixel count was taken to be the mean background intensity and used for background subtraction for individual ROIs. A noise threshold was set to $T = 3\sigma_{bg}$, where σ_{bg} is

the maximum s.d. of background signal intensity in the fluorescence micrographs at each experimental condition. Measurements with fluorescence below *T* in the numerator were identified as such in plotted data. Measurements with fluorescence below *T* in the denominator were discarded from data sets.

Fluorescence micrographs from ICC experiments in culture plates and scWestern microwells for the differentiation experiment in Fig. 2.4a,b were manually scored for marker expression according to arbitrarily determined fluorescence thresholds in ImageJ. Different, blinded researchers conducted ICC counting and scWestern marker expression analyses.

2.5 Acknowledgements

We acknowledge E. Connelly for assistance with cell culture and conventional western blots, K. Heydari at the UC Berkeley Cancer Research Laboratory Flow Cytometry Facility for assistance with interfacing with FACS; R. Lin, L. Bugaj, E. Woods, and C. Nilson for critical discussion; and the QB3 Biomolecular Nanotechnology Center (BNC) at UC Berkeley for partial infrastructure support. A.J.H. is a 2013 Siebel Scholar. D.P.S. is a 2014 Siebel Scholar and was supported by a California Institute for Regenerative Medicine training grant. A.E.H. is an Alfred P. Sloan Research Fellow in chemistry. This work was supported by a U.S. National Institutes of Health (NIH) New Innovator Award (DP2OD007294 to A.E.H.), a Medical Research Program Grant from the W.M. Keck Foundation (to A.E.H.), a UC Berkeley Bakar Fellowship (to A.E.H); and a U.S. NIH research project grant (R01ES020903 to D.V.S).

2.6 References

1. Altschuler, S. J. & Wu, L. F. Cellular heterogeneity: do differences make a difference? *Cell* **141,** 559–563 (2010).
2. Chang, H. H., Hemberg, M., Barahona, M., Ingber, D. E. & Huang, S. Transcriptome-wide noise controls lineage choice in mammalian progenitor cells. *Nature* **453,** 544–547 (2008).
3. Raj, A., Rifkin, S. A., Andersen, E. & van Oudenaarden, A. Variability in gene expression underlies incomplete penetrance. *Nature* **463,** 913–918 (2010).
4. Balic, M., Williams, A., Lin, H., Datar, R. & Cote, R. J. Circulating tumor cells: from bench to bedside. *Annu. Rev. Med.* **64,** 31–44 (2013).
5. Dalerba, P. *et al.* Single-cell dissection of transcriptional heterogeneity in human colon tumors. *Nat Biotechnol* **29,** 1120–1127 (2011).
6. Lazzara, M. J. *et al.* Impaired SHP2-mediated extracellular signal-regulated kinase activation contributes to gefitinib sensitivity of lung cancer cells with epidermal growth factor receptor-activating mutations. *Cancer Res* **70,** 3843–3850 (2010).
7. Bendall, S. C. *et al.* Single-cell mass cytometry of differential immune and drug responses across a human hematopoietic continuum. *Science* **332,** 687–696 (2011).
8. Zong, C., Lu, S., Chapman, A. R. & Xie, X. S. Genome-wide detection of single-nucleotide and copy-number variations of a single human cell. *Science* **338,** 1622–1626 (2012).
9. Newman, J. R. S. *et al.* Single-cell proteomic analysis of S. cerevisiae reveals the architecture of biological noise. *Nature* **441,** 840–846 (2006).
10. Schwanhäusser, B. *et al.* Global quantification of mammalian gene expression control. *Nature* **473,** 337–342 (2011).

11. Taniguchi, Y. *et al.* Quantifying E. coli proteome and transcriptome with single-molecule sensitivity in single cells. *Science* **329,** 533–538 (2010).
12. Wei, W. *et al.* Microchip platforms for multiplex single-cell functional proteomics with applications to immunology and cancer research. *Genome Med* **5,** 75 (2013).
13. Ashton, R. S. *et al.* Astrocytes regulate adult hippocampal neurogenesis through ephrin-B signaling. *Nat Neurosci* **15,** 1399–1406 (2012).
14. Sevecka, M. & MacBeath, G. State-based discovery: a multidimensional screen for small-molecule modulators of EGF signaling. *Nat Methods* **3,** 825–831 (2006).
15. Spurrier, B., Ramalingam, S. & Nishizuka, S. Reverse-phase protein lysate microarrays for cell signaling analysis. *Nat Protoc* **3,** 1796–1808 (2008).
16. Stadler, C. *et al.* Immunofluorescence and fluorescent-protein tagging show high correlation for protein localization in mammalian cells. *Nat Methods* **10,** 315–323 (2013).
17. Maecker, H. T. & Trotter, J. Flow cytometry controls, instrument setup, and the determination of positivity. *Cytometry A* **69,** 1037–1042 (2006).
18. Schulz, K. R., Danna, E. A., Krutzik, P. O. & Nolan, G. P. Single-cell phospho-protein analysis by flow cytometry. *Curr Protoc Immunol* **Chapter 8,** Unit 8.17–8.17.20 (2007).
19. Ciaccio, M. F., Wagner, J. P., Chuu, C.-P., Lauffenburger, D. A. & Jones, R. B. Systems analysis of EGF receptor signaling dynamics with microwestern arrays. *Nat Methods* **7,** 148–155 (2010).
20. Towbin, H., Staehelin, T. & Gordon, J. Electrophoretic transfer of proteins from polyacrylamide gels to nitrocellulose sheets: procedure and some applications. *Proc Natl Acad Sci USA* **76,** 4350–4354 (1979).
21. Hughes, A. J. & Herr, A. E. Microfluidic Western blotting. *Proc Natl Acad Sci USA* **109,** 21450–21455 (2012).
22. Shapiro, A. L., Viñuela, E. & Maizel, J. V. Molecular weight estimation of polypeptide chains by electrophoresis in SDS-polyacrylamide gels. *Biochem Biophys Res Commun* **28,** 815–820 (1967).
23. Gallagher, S., Winston, S. E., Fuller, S. A. & Hurrell, J. G. R. Immunoblotting and immunodetection. *Curr Protoc Immunol* **Chapter 8,** Unit 8.10–8.10.28 (2008).
24. Friedman, N., Cai, L. & Xie, X. S. Linking stochastic dynamics to population distribution: an analytical framework of gene expression. *Physical review letters* **97,** 168302 (2006).
25. Cai, L., Friedman, N. & Xie, X. S. Stochastic protein expression in individual cells at the single molecule level. *Nature* **440,** 358–362 (2006).
26. Cohen, A. A. *et al.* Protein dynamics in individual human cells: experiment and theory. *PLoS ONE* **4,** e4901 (2009).
27. Fujioka, A. *et al.* Dynamics of the Ras/ERK MAPK cascade as monitored by fluorescent probes. *J Biol Chem* **281,** 8917–8926 (2006).
28. Bendall, S. C., Nolan, G. P., Roederer, M. & Chattopadhyay, P. K. A deep profiler's guide to cytometry. *Trends Immunol* **33,** 323–332 (2012).
29. Gage, F. H. *et al.* Survival and differentiation of adult neuronal progenitor cells transplanted to the adult brain. *Proc Natl Acad Sci USA* **92,** 11879–11883 (1995).
30. Peltier, J., O'Neill, A. & Schaffer, D. V. PI3K/Akt and CREB regulate adult neural hippocampal progenitor proliferation and differentiation. *Dev Neurobiol* **67,** 1348–1361 (2007).
31. Jensen, K. J. *et al.* An ERK-p38 subnetwork coordinates host cell apoptosis and necrosis during coxsackievirus B3 infection. *Cell Host Microbe* **13,** 67–76 (2013).

32. Huang, C. Y. & Ferrell, J. E. Ultrasensitivity in the mitogen-activated protein kinase cascade. *Proc Natl Acad Sci USA* **93,** 10078–10083 (1996).
33. Eldar, A. & Elowitz, M. B. Functional roles for noise in genetic circuits. *Nature* **467,** 167–173 (2010).
34. Chou, Y.-H., Khuon, S., Herrmann, H. & Goldman, R. D. Nestin promotes the phosphorylation-dependent disassembly of vimentin intermediate filaments during mitosis. *Mol Biol Cell* **14,** 1468–1478 (2003).
35. Hyder, C. L., Isoniemi, K. O., Torvaldson, E. S. & Eriksson, J. E. Insights into intermediate filament regulation from development to ageing. *J Cell Sci* **124,** 1363–1372 (2011).
36. Sahlgren, C. M. *et al.* Mitotic reorganization of the intermediate filament protein nestin involves phosphorylation by cdc2 kinase. *J Biol Chem* **276,** 16456–16463 (2001).
37. Yang, H. Y., Lieska, N., Goldman, A. E. & Goldman, R. D. Colchicine-sensitive and colchicine-insensitive intermediate filament systems distinguished by a new intermediate filament-associated protein, IFAP-70/280 kD. *Cell Motil. Cytoskeleton* **22,** 185–199 (1992).
38. Su, P.-H. *et al.* Identification and cytoprotective function of a novel nestin isoform, Nes-S, in dorsal root ganglia neurons. *J Biol Chem* **288,** 8391–8404 (2013).
39. Hendrickson, M. L., Rao, A. J., Demerdash, O. N. A. & Kalil, R. E. Expression of nestin by neural cells in the adult rat and human brain. *PLoS ONE* **6,** e18535 (2011).
40. Marx, V. Finding the right antibody for the job. *Nat Methods* **10,** 703–707 (2013).
41. Yu, J. H. & Schaffer, D. V. Selection of novel vesicular stomatitis virus glycoprotein variants from a peptide insertion library for enhanced purification of retroviral and lentiviral vectors. *J. Virol.* **80,** 3285–3292 (2006).
42. Peltier, J. & Schaffer, D. V. Viral packaging and transduction of adult hippocampal neural progenitors. *Methods Mol Biol* **621,** 103–116 (2010).
43. Hughes, A. J., Lin, R. K. C., Peehl, D. M. & Herr, A. E. Microfluidic integration for automated targeted proteomic assays. *Proc Natl Acad Sci USA* **109,** 5972–5977 (2012).
44. Hughes, A. J. & Herr, A. E. Quantitative enzyme activity determination with zeptomole sensitivity by microfluidic gradient-gel zymography. *Anal. Chem* **82,** 3803–3811 (2010).
45. Selinummi, J. *et al.* Bright field microscopy as an alternative to whole cell fluorescence in automated analysis of macrophage images. *PLoS ONE* **4,** e7497 (2009).

Chapter 3: Spatial Regulation of Eph:Ephrin Signaling in Neural Stem Cells

This chapter is the product of a collaboration with Meimei Dong, PhD in the laboratory of Jay Groves, Ph.D.

3.1 Introduction

Eph receptors (EphA1-8,10 and EphB1-4,6) constitute the largest family of receptor tyrosine kinases. Their ephrin ligands are glycophosphatidylinositol-linked A-type (ephrinA1-10) or transmembrane B-type (ephrinB1-3) proteins. Since Eph and ephrins are both membrane-bound, signaling is cell-cell contact dependent[1,2]. The resulting juxtacrine cues play an integral role in normal developmental processes such as tissue patterning[3] and axonal pathfinding[4], as well as in abnormal pathological conditions such as developmental disorders and cancer[5,6].

Eph receptors are a unique class of receptor tyrosine kinases for which activity requires not only Eph dimerization and trans-phosphorylation, but also multivalent oligomerization as well as higher order cluster formation to initiate downstream signaling[7,8]. Furthermore, Eph receptors can exhibit homotypic (same Eph type) and heterotypic (different Eph type) cis-interactions in addition to intercellular trans-interactions with various Ephs and ephrins to form complex signaling clusters[2,9]. Given the dynamic and biophysical nature of Eph:ephrin interaction, it has been suggested that cluster size, spatial organization, and mechanical regulation may modulate signal strength and regulate functional outcomes[10,11]. Mechanical sensitivity and spatial organization of cell surface receptors are increasingly recognized as a relevant cellular stimuli[12]. For instance, studies have recently shown the singular role of EphA2 receptors in physical force sensing. When mechanical forces restrict EphA2 receptor movement in breast cancer, the initial formation and geometric assembly of EphA2/ephrin-A1 clusters are reorganized. This spatial modification results in a change in proximal membrane signaling events, such as the distribution of the downstream signaling effector ADAM10[13] and ephrin-A1 trans-endocytosis[14].

A particularly important system in which Eph:ephrin signaling has been widely studied is neural development, where downstream signal transduction controls neural stem cell (NSC) proliferation, migration, and survival both during early development and in adulthood[15-17]. Eph:ephrin signaling was recently demonstrated to regulate adult hippocampal neurogenesis; ephrin-B2 expressed by astrocytes in the NSC niche induces the neuronal differentiation of NSCs via EphB4 signaling[18,19]. Structural experiments have confirmed that ephrin-B2 binds EphB4 receptors to form heterodimers[20], and a recent study has shown increased downstream activity in NSCs with increasingly multivalent ephrin-B2 ligands[19]. Thus, biophysical mechanisms of receptor activation likely play a vital role in this therapeutically relevant system. Motivated by the work on the spatiomechnical sensitivity of the EphA2 receptor and the regulatory role of the EphB4 receptor in NSC signaling, we hypothesized that NSC differentiation may be sensitive to spatial manipulation of EphB4/ephrin-B2 clustering and physical organization.

Previous studies have induced EphB4 signaling by pre-clustering ephrin-B2 in solution to artificially generate multimeric receptor-ligand complexes[18,19]. However, these methods do not

recapitulate the physical interactions between membrane-bound receptors and ligands. We therefore turned to supported lipid bilayers, a well-suited system for studying cell-cell contact dependent signaling[21]. Here, we develop a hybrid system to reconstitute the juxtacrine signaling geometry between NSCs and astrocytes by depositing NSCs expressing EphB4 receptors onto supported lipid bilayers displaying laterally mobile, monomeric ephrin-B2 ligands. This system provides a physiologically relevant microenvironment for investigating EphB4:ephrin-B2 signaling. It also allows us to precisely control the chemical composition of the ligands and membranes, as well as the physical geometry of receptor-ligand complexes using the technique of spatial mutation. Spatial mutation is the orchestrated physical disruption of the spatial patterning of proteins on a lipid bilayer, which is achieved by nanofabricating chromium (Cr) structures on glass substrates. These features function as diffusion barriers inhibiting receptor-ligand diffusion, thereby controlling the cluster size and number of receptor-ligand complexes that can form[22].

To enable studies on the slow time scale needed to observe differentiation, a novel functionalization strategy was required, as previously utilized methods were only stable for about 1 h[14]. Here, we developed a DNA-SNAP-tag based technique to crosslink ephrin-B2 ligands on supported lipid bilayers, enabling ephrin-B2 ligands to remain stably attached for an extended period of time (12-24 h). Using this reconstituted juxtacrine signaling platform, we observed EphB4/ephrin-B2 co-clustering, and demonstrated for the first time membrane-bound monomeric ephrin-B2 activation of EphB4 signaling and downstream neuronal differentiation in a synthetic system. Furthermore, employing spatial mutation, we showed that EphB4 signaling and NSC differentiation are sensitive to spatial properties of apposing cell membranes. These findings provide insight into novel regulatory mechanisms of both EphB4 signaling and NSC niche dynamics.

3.2 Results

Development of a novel DNA-SNAP-tag functionalization strategy

To investigate the effect of membrane-bound ephrin-B2-induced signaling on NSC differentiation, we developed a DNA-SNAP-tag biochemical conjugation method to tether ephrin-B2 ligands to a SLB for extended presentation. DNA oligonucleotides are a popular tool for conjugation because hybridization of complementary DNA strands is highly specific and sensitive[23]. SNAP-tag, a 20 kDa mutant of the DNA repair protein O^6-alkylguanine-DNA alkyltransferase, has been widely used to functionalize proteins as it can perform a site-specific irreversible covalent reaction with a benzylguanine (BG) substrate[24,25]. In step one, a fusion protein of the extracellular domain of ephrin-B2 and SNAP-tag was recombinantly produced, and then conjugated to a 20 base pair single stranded (ss) DNA (Seq1) oligonucleotide. This ssDNA was decorated with a BG molecule on the 5' end for SNAP-tag chemistry, and a Cy5 tag on the 3' end for fluorescent imaging (Fig. 3.1a). In step two, a thiol-modified complementary ssDNA (Seq2) oligonucleotide was functionalized to a maleimide-presenting membrane, allowing for subsequent hybridization with ephrin-B2-SNAPtag-Seq1 (Fig. 3.1a). The fluidity of the bilayer and the mobility of ephrin-B2 were confirmed by fluorescence recovery after photobleaching (FRAP) experiments (Fig. 3.1b,c). To further characterize the membrane density of ephrin-B2 ligands, we applied fluorescence correlation spectroscopy (FCS) analysis and observed an ephrin-B2 ligand density of 120/μm^2 with a diffusion coefficient of 4.0 μm^2/s. This

result is standard for lipid diffusion on supported membranes[26,27]. A typical time autocorrelation function of fluorescence intensity fluctuations from membrane-bound ephrin-B2 is shown in Fig. 3.1d. Of note, in the FCS experiments, we tested the ligand surface densities of two solution concentrations of ephrin-B2 and obtained similar values for both the membrane ephrin-B2 density and the diffusion coefficient. We concluded, therefore, that we had reached the saturation point for ligand binding to the SLB.

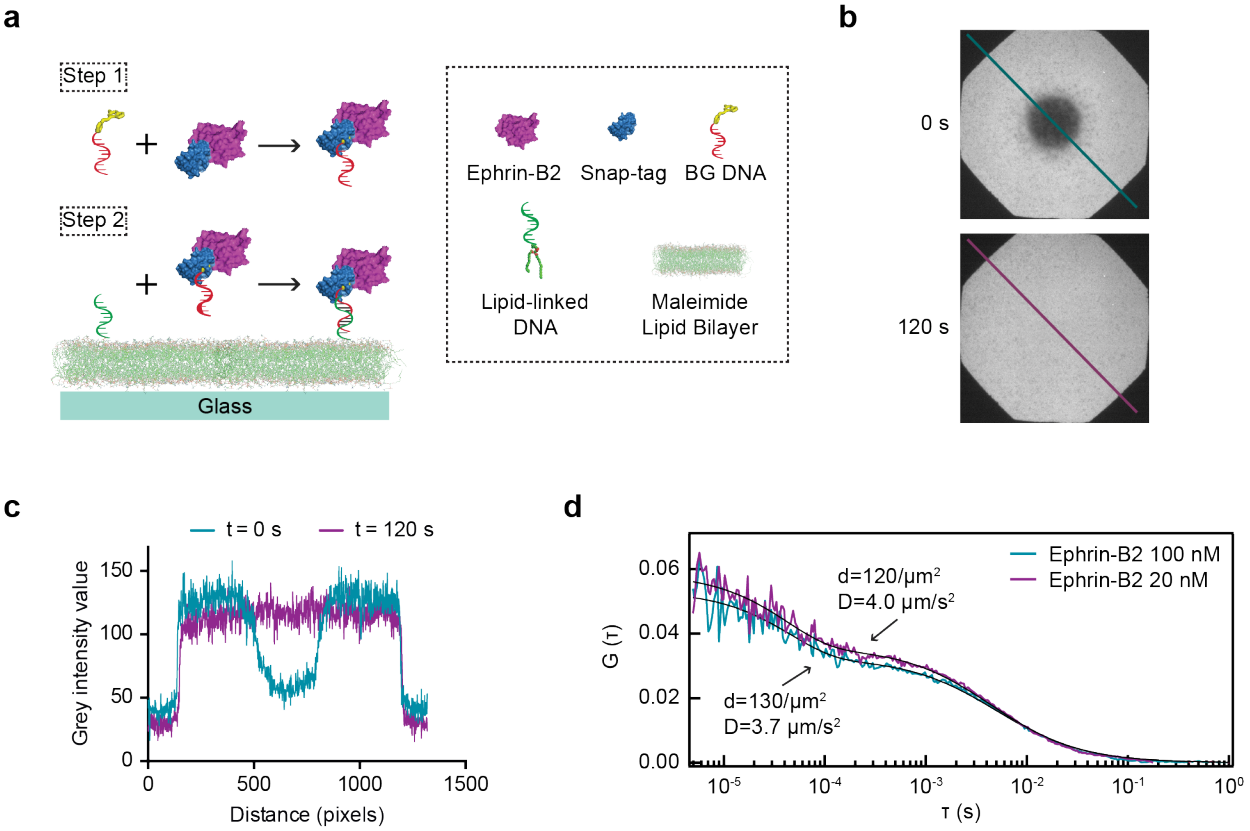

Figure 3.1. Development of DNA-ephrin-B2-SNAP-tag functionalized SLB. (**a**) Schematic of a two-step conjugation tethering ephrin-B2 ligands onto SLB. In step one, ephrin-B2-SNAP-tag is conjugated to Cy5-BG-modified ssDNA. In step two, thiol-modified ssDNA is bound to a maleimide-decorated DOPE lipid bilayer, and then hybridized with ephrin-B2-DNA complex. (**b**) Fluorescence recovery after photobleaching (FRAP) characterization of ephrin-B2-displaying SLB. A region of the bilayer was bleached for 1 min with 647 nm epifluorescent light. Images were captured every 30 sec after photobleaching, with representative images at 0 sec and 120 sec. (**c**) Fluorescent intensity analysis of a line scan in (**b**) verified the lateral mobility of the ephrin-B2 linked to the membrane. (**d**) Characterization of ephrin-B2 SLB surface properties. Fluorescence correlation spectroscopy (FCS) was used to determine the physical properties of the membrane-bound ephrin-B2 and the resulting autocorrelation $G_0(\tau)$ was fit to a two-dimensional Gaussian diffusion model. Incubating with 20 nM ephrin-B2 resulted in a diffusion coefficient of 4.0 μm/s^2 and a ligand density of 120/μm^2. Incubating with 100 nM ephrin-B2 resulted in a diffusion coefficient of 3.7 μm/s^2 and a ligand density of 130/μm^2.

NSCs cluster membrane-bound monomeric ephrin-B2

To reconstitute the juxtacrine geometry of Eph:ephrin signaling, we seeded NSCs on ephrin-B2 functionalized SLBs (Fig. 3.2a). Utilizing total internal reflection fluorescence (TIRF) microscopy, we recorded live NSC interactions with the bilayer. Time-lapse imaging demonstrated the spatial distribution and cluster formation of ephrin-B2 at the NSC-SLB interface. Upon NSC landing, membrane-bound ephrin-B2 diffused rapidly and immediately

formed micro-clusters under the cell; these clusters continued to transport inwardly and eventually stabilized into a large centralized cluster within 45 min. Reflection interference contrast microscopy (RICM) images were taken to map the footprint of cells on the underlying SLB, which showed regions of NSC adhesion to the bilayer co-localized with ephrin-B2 clusters (Fig. 3.2b). As cells failed to adhere to ligand-free bilayers (data not shown), the only significant binding between NSCs and the SLBs occurred via ephrin-B2 ligands.

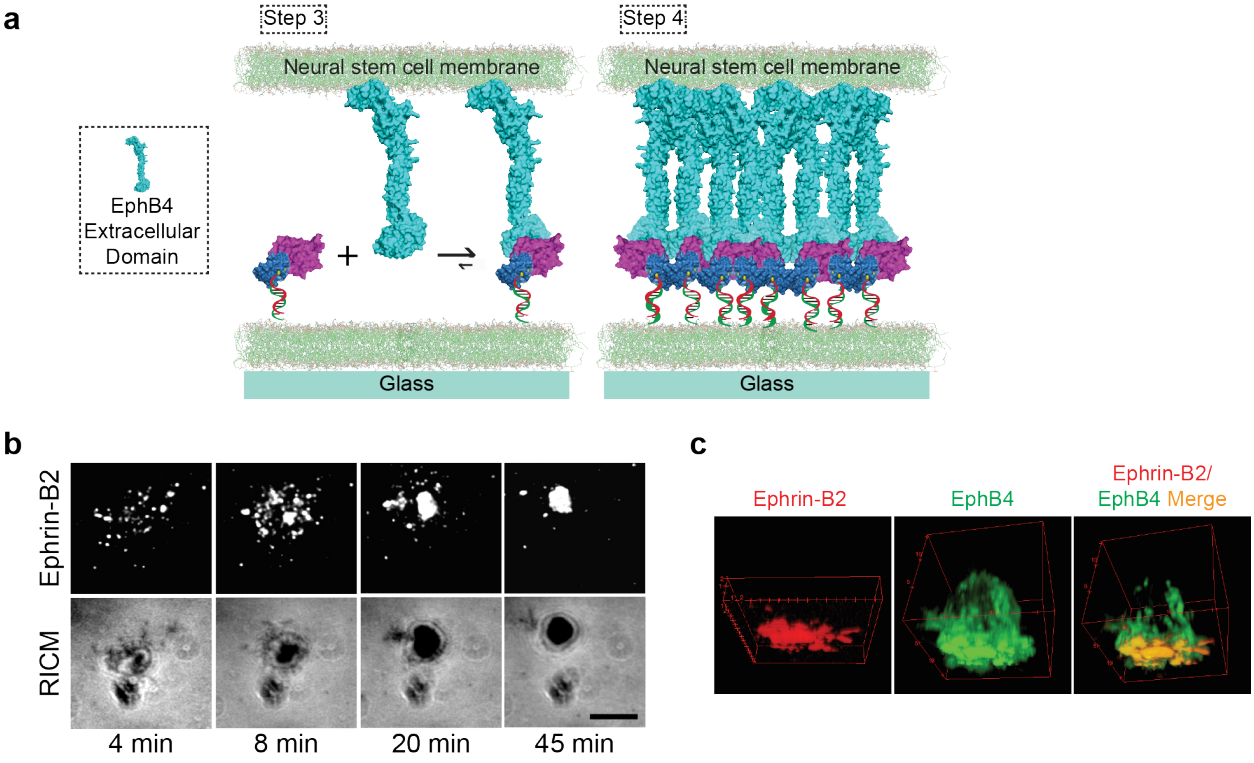

Figure 3.2. Reconstitution of EphB4:ephrin-B2 signaling junction at SLB-cell interface. (**a**) Schematic of a NSC interacting with an ephrin-B2 SLB. (**b**) Time-lapse TIRFM images of a representative NSC landing and clustering ephrin-B2. NSCs were seeded then imaged over 45 min. By 4 min, diffuse ephrin-B2 clusters formed and the area of adhesion was small, over time ephrin-B2 continued to diffuse and the contact area grew, and finally by 45 min, a large micron-scale ephrin-B2 cluster formed. Cy5-labeled ephrin-B2 visualized by TIRFM (top); cell adhesion imaged by RICM (bottom). Scale bar, 10 μm. (**c**) Confocal image of an EphB4-mCherry expressing NSC on an ephrin-B2 SLB 45 min after seeding. EphB4/ ephrin-B2 co-localization at the NSC-SLB interface is apparent.

EphB4 is the key transducer of ephrin-B2 induced neurogenesis in NSCs[18]. To investigate whether the formation of ephrin-B2 micro-clusters on SLBs involved binding of EphB4 receptors, a NSC line stably expressing an EphB4-mCherry fusion was developed and then seeded on ephrin-B2 SLBs. By confocal microscopy, we observed EphB4 localization to the cell-bilayer interface and a strong co-localization of EphB4 and ephrin-B2 (Fig. 3.2c). This co-localization was also demonstrated by TIRF microscopy (Fig. B.1). Blocking EphB4 receptors on NSCs by incubation with an EphB4 antibody prior to seeding decreased the number of cells bound to SLBs, but did not eliminate adhesion completely, suggesting that other Ephs may be involved in binding to ephrin-B2. Ephrin-B2 interacts with a number of Ephs in addition to EphB4, including EphB2[28]. Blocking EphB2 receptors alone also resulted in decreased NSC

binding, but to a lesser degree than EphB4 blocking, while blocking both EphB4 and EphB2 resulted in adhesion levels similar to EphB4 blocking (Fig. B.2). These observations indicate that multiple Ephs, though predominantly EphB4, are responsible for NSC adhesion to the SLBs.

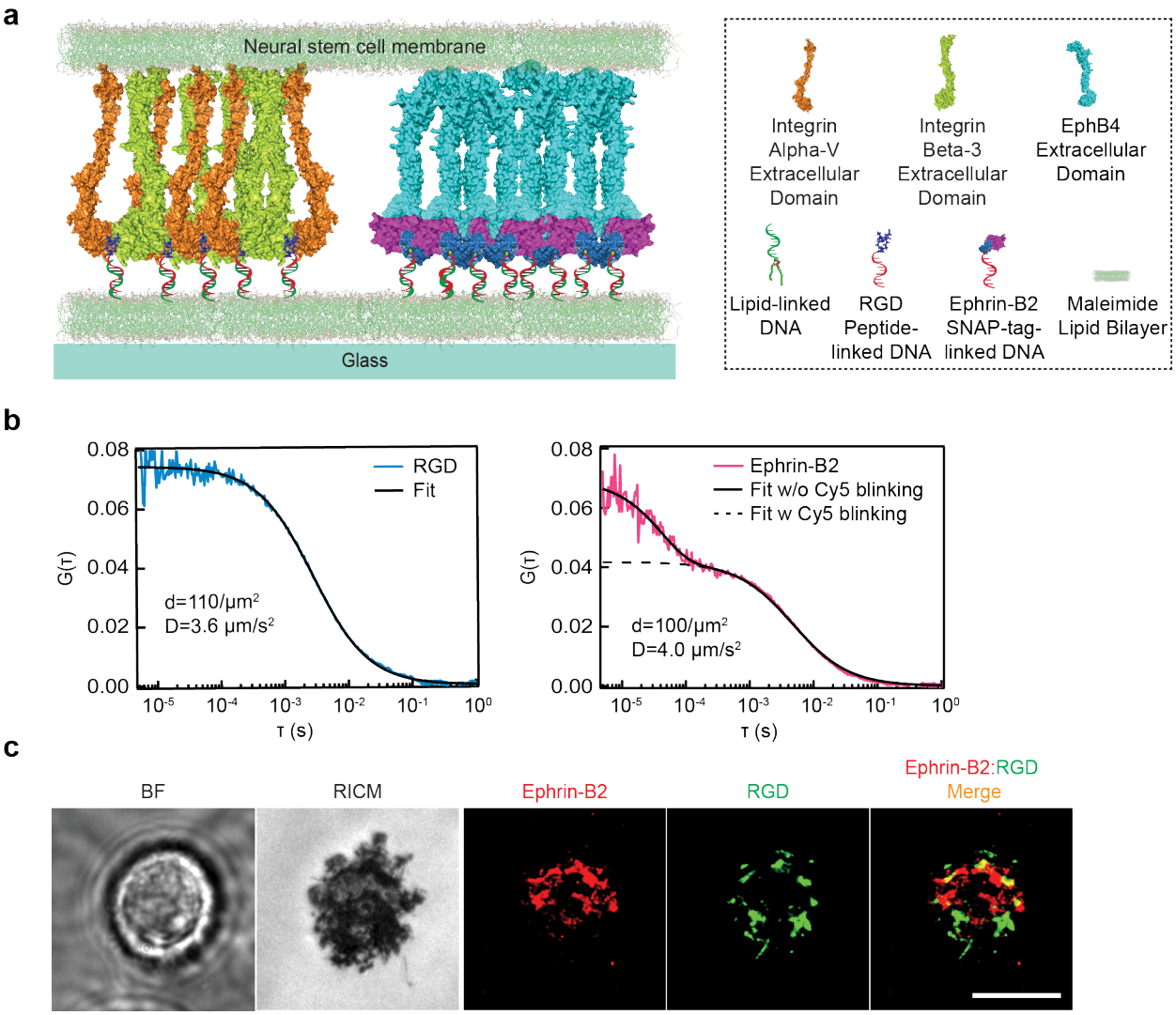

Figure 3.3. RGD:ephrin-B2 binary SLB reveals EphB4 passive transport. (**a**) Schematic of RGD:ephrin-B2 binary SLB interacting with cell surface receptors on an apposing membrane. RGD peptides bind to integrin receptors on NSCs, while ephrin-B2 ligands bind to EphB4 receptors on NSCs. (**b**) FCS data show RGD molecules and ephrin-B2 molecules diffuse laterally on binary SLB. RGD molecules were displayed at a molecular density of 110/μm^2 and a diffusion coefficient of 3.6 μm^2/s. Ephrin-B2 ligands were displayed at a ligand density of 100/μm^2 and a diffusion coefficient of 4.0 μm^2/s. (**c**) Brightfield, RICM, and epifluorescent images of a NSC binding to RGD:ephrin-B2 SLB. Scale bar, 10 μm.

EphB4 clustering is dependent on passive transport

The observation that ephrin-B2 transported radially inward under adhered NSCs led us to investigate whether EphB4:ephrin-B2 clustering is dependent on active receptor transport or primarily due to passive transport in the membrane. To address this question, we provided an additional mechanism for NSC adhesion to the bilayer, specifically a cyclic RGD (Arg-Gly-Asp) peptide, and examined the effect of this non-ephrin dependent adhesion on ephrin-B2 transport.

The RGD peptide was fluorescently-tagged and conjugated to a ssDNA (Seq1) that hybridized with membrane-bound ssDNA (Seq2) (Fig. 3.3a). This RGD-DNA complex served as a binding partner for integrin receptors on NSCs[29] and was presented as a binary mixture with ephrin-B2 on the SLB. We titrated RGD and ephrin-B2 densities on the bilayer to obtain an optimal balance between adhesion and ephrin-B2 cluster formation. FCS measurements demonstrated that a binary bilayer of RGD:ephrin-B2 at a molar concentration of 1:20 resulted in similar surface densities and diffusion coefficients for both ligands (Fig. 3.3b). After 45 min of NSC incubation on RGD:ephrin-B2 SLBs, cells spread uniformly and formed large contact areas at the cell-bilayer interface as shown by RICM. Fluorescent imaging revealed the binding patterns of RGD and ephrin-B2. In the presence of RGD, the centralized ephrin-B2 clusters seen in previous experiments did not develop. Instead, ephrin-B2 formed scattered micro-clusters that generally co-localized with the strongest contact areas at the membrane interface. RGD-integrin focal adhesions largely formed a ring-like morphology surrounding the ephrin-B2 clusters, with few areas of co-localization (Fig. 3.3c). These observations suggest that EphB4 clusters primarily through a passive transport process as providing an additional means of adhesion and increasing the contact area through RGD co-presentation impaired the formation of a centralized cluster. If active receptor transport was involved, EphB4 inward transport would have been unaffected by this addition. Therefore, upon EphB4 binding to ephrin-B2, cluster formation is likely solely a result of indirect intermembrane anchoring between the receptors and ligands, which results in coalescing of complexes at the contact area. Notably, this finding contrasts the active transport of EphA2 in cancer cells seen in previous studies[13].

NSCs undergo neuronal differentiation on ephrin-B2 SLBs

To examine the biological activity of our reconstituted EphB4:ephrin-B2 signaling system, we studied the differentiation of NCSs cultured on the ephrin-B2 SLBs. In addition to the SNAP-tag functionalization strategy developed to stably tether ephrin-B2, multi-day cellular studies required the implementation of adhesion capabilities post-bilayer degradation. Adhesive moieties were introduced by supplementing the culture media with laminin 18 h post-seeding. Laminin enabled the NSCs to bind to the glass and extend processes similarly to standard NSC tissue culture on polyornithine/ laminin coated surfaces.

Neuronal differentiation was assessed 5 days post-seeding on both ephrin-B2 SLBs and standard surfaces with soluble stimulation. Remarkably, NSCs on ephrin-B2 SLBs underwent neuronal differentiation at levels similar to NSCs exposed to continuous mixed differentiation media (retinoic acid + fetal bovine serum (RA/FBS)) or antibody clustered soluble ephrin-B2 (Fc-ephrin-B2), as measured by the percent of cells expressing the neuronal marker βIII-tubulin (Fig. 3.4a). Morphologically, the ephrin-B2 SLB-induced neurons had 2-5 branching βIII-tubulin$^+$ processes, which closely resembled Fc-ephrin-B2-induced neurons (Fig. 3.4b). Importantly, the length of ephrin-B2 exposure required for NSC neuronal differentiation was unknown. A single exposure to Fc-ephrin-B2 had no effect on differentiation. In stark contrast, NSCs on SLBs were only exposed to the ephrin-B2 present on the bilayer at seeding (for <24 h), but this signal was strong enough to induce neuronal differentiation (Fig. 3.4). Finally, to study the role of EphB4, NSCs were incubated with an anti-EphB4 antibody prior to seeding on SLBs. EphB4-blocked NSCs exhibited a 19% reduction in the fraction of βIII-tubulin$^+$ NSCs (Fig. 3.4a), and induced neurons developed fewer processes (Fig. 3.4b), confirming the role of EphB4 in transducing the

ephrin-B2 signal. These findings demonstrate the functional role of membrane-bound monomeric ephrin-B2 ligands in inducing neuronal differentiation.

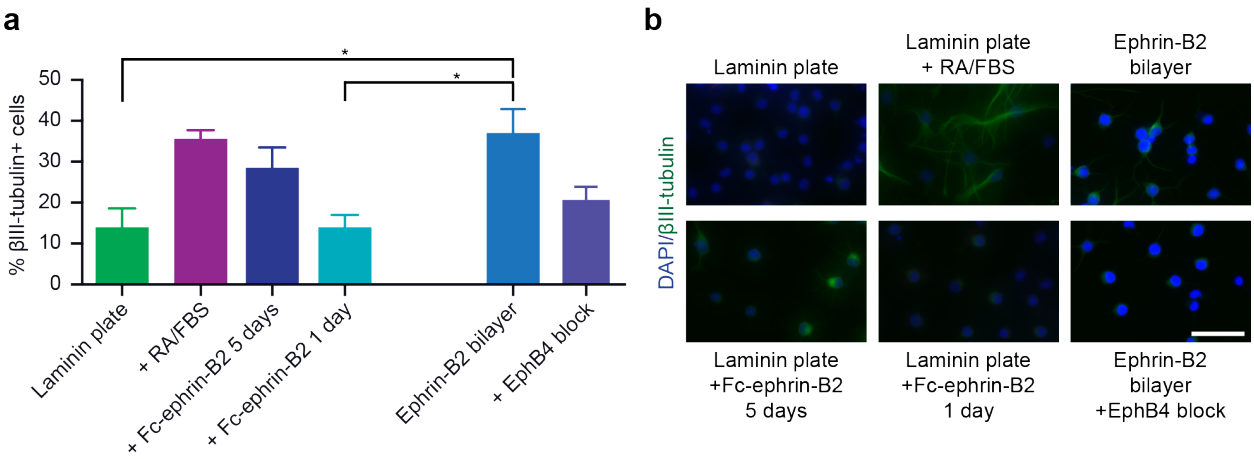

Figure 3.4. NSCs undergo neuronal differentiation on monomeric membrane-bound ephrin-B2 mediated by EphB4. (**a**) Quantification of neuronal differentiation 5 days post-seeding by immunostaining, as measured by the percent of NSCs expressing the neuronal marker βIII-tubulin. NSCs were cultured on ephrin-B2 SLBs with or without pre-blocking with an anti-EphB4 antibody, or on standard tissue culture substrates under naïve, mixed differentiation, or soluble antibody-clustered Fc-ephrin-B2 (for 1 or 5 days) conditions. Error bars represent standard error of the mean. *P < 0.05, ANOVA with Tukey-Kramer multiple comparison, n = 3 experimental replicates. (**b**) Representative fluorescent images from (**a**) showing neuronal processes (βIII-tubulin+, green) and total nuclei (DAPI, blue). Scale bar, 50 μm.

Spatial mutation impairs cluster formation but not immediate downstream signaling

Spatial mutation, the physical disruption of functionalized protein mobility on SLBs, has been successfully applied to investigate spatial organization in immunological synapses[30-33] and more recently in EphA receptor signaling[13,14,34]. On solid glass substrates with nanofabricated chromium (Cr) metal lines, lipid diffusion is hindered, as the Cr lines physically partition SLBs formed on these surfaces into separated lipid corrals (Fig. 3.5a). FRAP experiments confirmed that ephrin-B2 diffusion was constrained within corrals, as fluorescent imaging and intensity line scan data demonstrated that corral-patterned bilayers cannot recover fluorescence after photobleaching (Fig. 3.5b,c).

To study the effect of spatially mutated ephrin-B2 SLBs on EphB4 clustering and NSC behavior, a number of patterned substrates were fabricated. These included square grid patterns with 5 μm × 5 μm, 4 μm × 4 μm, 3 μm × 3 μm, and 2 μm × 2 μm corralled areas, and a control pattern consisting of arrayed posts with 2 μm spacing. NSCs seeded on patterned ephrin-B2 bilayers experienced spatial perturbations exclusively through Eph:ephrin receptor-ligand interactions. On all substrates, NSCs landed and adhered, with the area of adhesion similar regardless of patterning. Ephrin-B2 mobility, however, was physically restricted by grid lines. 45 min after NSC seeding, EphB4:ephrin-B2 cluster formations were re-distributed and confined by 4 μm and 2 μm grid patterns. On control 2 μm array substrates, ephrin-B2 could laterally diffuse around patterned posts, so a large central ephrin-B2 cluster still formed (Fig. 3.5d).

To examine the effect of spatial mutation on early downstream signaling, NSCs were seeded on bilayers for 1 h and then assayed by western blot. Pan phosphorylated-tyrosine and known

EphB4/ ephrin-B2 signaling targets, including phosphorylated-ERK[35] and active β-catenin[18], were examined. Ephrin-B2-induced signaling was observed on non-patterned (off grid), control 2 μm arrayed, and 2 μm, 3 μm, and 5 μm gridded ephrin-B2 SLBs, but not on ephrin-B2 free (plain) SLBs (Fig. 3.5e). Therefore, despite altered ephrin-B2 spatial re-organization, immediate downstream signaling in NSCs was not impaired on substrates imposing spatial mutation.

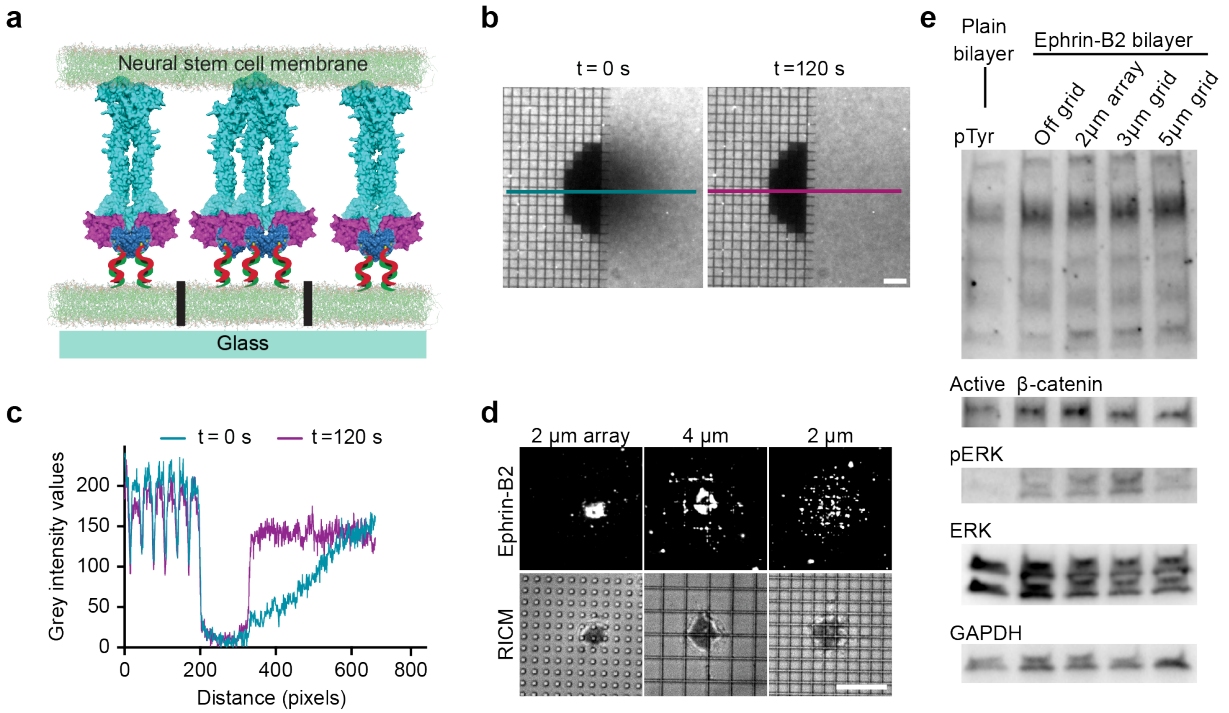

Figure 3.5. Spatial mutation impairs ephrin-B2 clustering but does not affect immediate downstream signaling. (**a**) Schematic of spatial mutation strategy. A NSC expressing EphB4 interacts with a SLB displaying ephrin-B2. Cr diffusion barriers physically perturb EphB4 receptor movement and cluster formation. (**b**) FRAP characterization of a SLB formed on a nanofabricated 4 μm gridded substrate. A region of the bilayer at the pattern edge was photobleached with 647 nm epifluorescent light as shown at 0 sec. After 120 sec, a recovery image was taken. Scale bar, 10 μm. (**c**) Line-scan intensity measurements of (**b**) were taken across the bleached area. Only the non-gridded areas were able to fully recover after photobleaching. (**d**) Ephrin-B2 clustering is disrupted on 4 μm and 2 μm gridded substrates as diffusion is confined to corralled regions. Control 2 μm arrayed substrates permit diffusion around posts so a central cluster still forms. Cy5-labeled ephrin-B2, TIRFM (top); cell adhesion, RICM (bottom). Scale bar, 10 μm. (**e**) Western blots of NSCs after 1 h incubation on plain SLBs, non-patterned (off grid) ephrin-B2 SLBs, and patterned ephrin-B2 SLBs. Pan-phosphotyrosine, active β-catenin, and phosphorylated ERK levels increased on all ephrin-B2 SLBs. ERK and GAPDH were used as loading controls.

Spatial mutation inhibits NSC neuronal differentiation on ephrin-B2 SLBs

The effect of spatial mutation on NSC differentiation was then examined. Although short term signaling was not impaired, it was still conceivable that the complex and protracted process of differentiation may be sensitive to EphB4 spatial regulation by mechanisms that don't impact direct downstream signaling target activation. 5 days post-seeding, NSC differentiation was analyzed. NSCs underwent neuronal differentiation at similar levels on non-patterned (off grid), control arrayed, and 5 μm gridded SLBs. However, NSCs exhibited impaired neurogenesis when cultured on 3 μm gridded bilayers. The percent of βIII-tubulin$^+$ cells significantly decreased, and processes did not develop (Fig. 3.6). Therefore, while immediate downstream signaling was not

affected by spatial mutation, ephrin-B2-induced NSC neuronal differentiation was sensitive to the spatial properties of ligand presentation in the apposing membrane on the scale of microns.

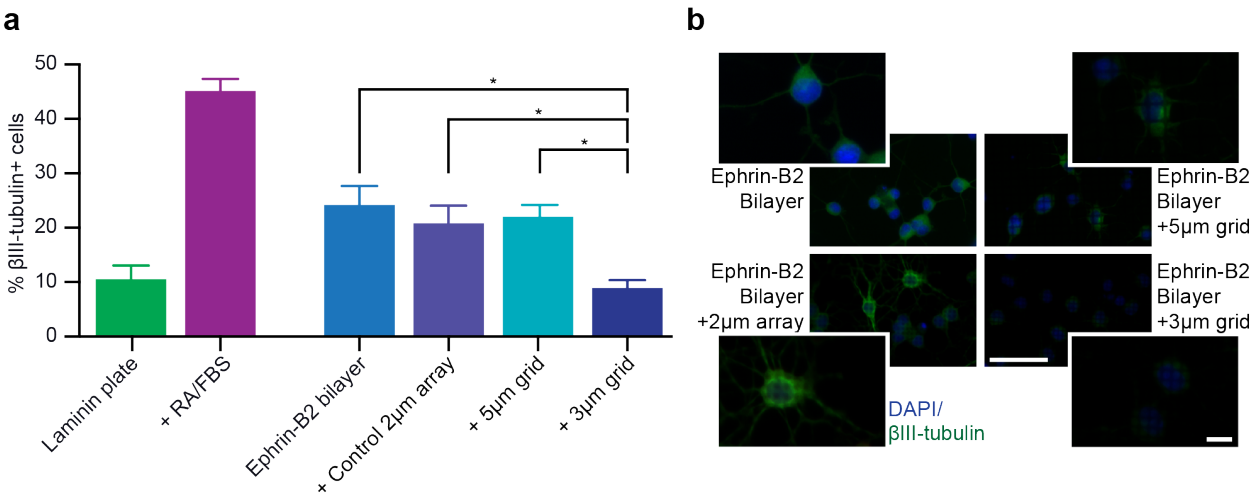

Figure 3.6. Spatial mutation of EphB4 receptors inhibits NSC neuronal differentiation on ephrin-B2 SLBs. (**a**) Quantification of neuronal differentiation by βIII-tubulin expression. NSCs were cultured on non-patterned (off-grid) ephrin-B2 SLBs, patterned ephrin-B2 SLBs, or on standard tissue culture substrates under naïve or mixed differentiation conditions. Error bars represent standard error of the mean. *P < 0.05, ANOVA with Tukey-Kramer multiple comparison, n = 4 experimental replicates. (**b**) Representative fluorescent images from (**a**) showing fields of NSCs (center) and magnified cells (outer insets) on patterned SLBs. Scale bar, full field: 50 μm, inset: 10 μm.

3.3 Discussion

The spatial properties of receptor-ligand interactions can influence receptor activation and signal propagation, but studying this phenomenon requires the development of systems capable of recapitulating complex biophysical traits. In this study, we reconstituted the juxtacrine geometry of Eph:ephrin signaling transduced by ephrin-B2 presenting astrocytes in contact with EphB4 expressing NSCs. By displaying laterally mobile monomeric ephrin-B2 on SLBs, we mimicked the membrane presentation of ephrin-B2. Furthermore, we were able to probe the role of spatial presentation in NSC signaling and differentiation using the technique of spatial mutation. The key technical advance enabling these days-long studies was the development of a DNA-SNAP-tag conjugation method providing stable ligand presentation for the duration of bilayer stability. In our hands, bilayers remained defect-free for 12-24 h, and ephrin-B2 presentation was presumed to persist for the same period. A number of methods have been developed to prolong bilayer stability, such as enhanced lipid deposition protocols[36] and tethering of lipids to glass substrates[37], so the combination of these techniques with the SNAP-tag strategy in future work could greatly enhance the timeline of presentation.

To analyze biological activity and test the feasibility of our system as a tool for probing spatial properties of ephrin-B2-induced NSC neurogenesis, we seeded NSCs on ephrin-B2 functionalized SLBs and examined Eph:ephrin localization and differentiation. Ephrin-B2 rapidly clustered under NSCs and co-localized with EphB4 on the NSC membrane. As differentiation is a multiday process, the ability of an ephrin-B2 SLB that is stable for 12-24 h to induce neurogenesis was unknown. Surprisingly, 5 days post-seeding, NSCs underwent neuronal differentiation at levels similar to NSCs stimulated with antibody-clustered soluble ephrin-B2.

Of note, a 1-day pulse of soluble ephrin-B2 was insufficient to induce differentiation. Although ephrin-B2 concentration cannot be directly compared, it appears that membrane presentation provides increased signal strength compared to solution presentation. Therefore, we concluded that membrane-bound monomeric ephrin-B2 ligands successfully induced Eph:ephrin interactions in NSCs and recapitulated astrocyte-induced neurogenesis in the NSC niche[18].

Ephs and ephrins are known to exhibit a high level of cross-talk among family members, so ephrin-B2 on SLBs may interact with other Eph types on NSCs. Indeed, antibody blocking experiments suggested that both EphB4 and EphB2 were responsible for NSC binding, but as concurrent blocking did not completely ablate adhesion, other Ephs may be interacting as well. In addition to EphB4 and EphB2, ephrin-B2 has been shown to bind EphB1[38], EphB3[39], EphB6[40], and EphA4[41], so future work will aim to examine the potential role of these receptors. Regarding NSC biological activity, however, EphB4 was confirmed to be largely responsible for transducing ephrin-B2 signaling as blocking EphB4 abrogated neuronal differentiation.

Our results have revealed that Eph signaling in NSCs is sensitive to the spatial properties of apposing membranes on the scale of microns. Restricting the movement of ephrin-B2 ligands directly prevented EphB4 receptors from forming centralized clusters. Physical manipulation of EphB4:ephrin-B2 microclusters altered cellular response in NSCs. And, as a result, neuronal differentiation was impacted. On 3 μm grids, but not 5 μm grids or control arrayed patterns, neurogenesis was significantly reduced. A number of observations regarding this finding are worth noting. First, the patterned substrates all presented roughly the same density of ephrin-B2. Cr grids served only as diffusion barriers to restrict the movement of lipid molecules and ephrin-B2 ligands. The grids did not affect the concentration of ephrin-B2. Therefore, NSCs seeded on each SLB were exposed to the same surface concentration of ligands. Second, Eph:ephrin clustering is a passive transport process in that binding and clustering occurs solely at sites of contact. RGD co-presentation altered central cluster formation, which would not be the case if receptors were being actively transported radially inwards, as we previously saw with EphA2[13]. So, differences in NSC differentiation in response to spatial mutation were probably not due to the disruption of active transport machinery. Finally, the length scale of the spatial mutations was on the order of microns, so nanoscale molecular interactions were most likely not disrupted. In all corrals, visible micro-clusters formed, and analysis revealed that phosphorylation cascades were unaffected. As the Eph:ephrin clusters likely contained hundreds of molecules, this activation of downstream signaling is not surprising. However, the question then arises: What is the mechanism of the observed spatial sensitivity of ephrin-B2 induced NSC neuronal differentiation?

We propose two potential mechanisms. First, while the observed clusters on all patterned substrates were large enough to induce downstream activation of examined targets, there remains the possibility that decreased cluster size is in fact responsible for lowered neurogenesis through an unknown pathway. We have shown that increased oligomerization on the nanoscale induces higher levels of neurogenesis[19], but the role of microscale clustering is undetermined. The signaling cascade(s) responsible for transduction of ephrin-B2 stimulation into neurogenic signals has not yet been elucidated, so cluster size may directly affect an unidentified immediate target or indirectly influence the amplification and accumulation of signals, which must reach a threshold level to induce neurogenesis. A second potential mechanism is that the spatial

disruption of Eph receptor movement inhibits neurogenesis through mechanical regulation of receptor function. A number of studies have previously demonstrated the mechanosensitivity of transmembrane receptors due to physical properties of ligand presentation, such as lateral mobility[42,43] and tugging forces at cell-cell junctions[44]. Future work will aim to tease out the mechanical forces in our system and further probe this potentially novel non-canonical receptor force sensing.

This study presents further evidence that all Eph receptors, maybe all receptors, exhibit spatial sensitivity to ligand presentation. We have now shown regulation with EphAs[13] and EphBs, and in cancer cells that overexpress Eph[13] as well as stem cells with low levels of endogenous expression. A wide array of physical attributes of receptor-ligand interactions can influence signaling. Therefore, more work needs to be done in this area to truly understand the complex and far-reaching role that spatial regulation plays in cell-cell signaling.

3.4 Materials and Methods

Protein expression and purification

The extracellular domain of mouse ephrin-B2 (a gift from Anthony Conway, Schaffer Lab, UC Berkeley) was extended by strand overlap PCR to include the natural ephrin-B2 N-terminal secretory signal sequence, and then cloned into a pFastBac vector (a gift from Kate Alfieri, Groves Lab, UC Berkeley) containing the SNAP-tag and His10 sequences. The vector was then introduced into DH10Bac™ *E. coli* cells to form a recombinant expression bacmid using the Bac-to-Bac® baculovirus expression system (Life Technologies). The bacmid was then used to transfect SF9 insect cells (obtained from Ann Fischer, UC Berkeley). Ephrin-B2-SNAPtag-His10 fusion protein was secreted from transfected SF9 cells, precipitated via centrifugation, purified using a gravity flow column containing Ni^{2+}-NTA resin (Qiagen), and eluted by an imidazole gradient. To confirm expression and purity, protein was separated by sodium dodecyl sulfate polyacrylamide gel electrophoresis (SDS-PAGE) and stained, and a single band at the expected molecular weight of 47.759 kDa was detected.

Preparation of benzylguanine (BG) modified DNA

The DNA sequence used was Seq1: 5'-CCCTAGAGTGAGTCGTATGA-3'[45]. Seq1 with an amino modifier C6 on the 5' end and a Cy5™-Sp modifier on the 3' end was purchased from Integrated DNA Technologies. NH2-Seq1-Cy5 was dissolved in TE buffer at 5 mg/mL, precipitated in ethanol, then rehydrated in distilled water, and stored at -20°C. BG-NHS-GLA (New England Biolabs) was dissolved in anhydrous *N, N'*-dimethylformamide (DMSO) (Solulink) at 50 mM and reacted with 25 molar equivalents of NH2-Seq1-Cy5 at room temperature for 2 h, then kept overnight at 4°C. The following day, the reaction was analyzed by matrix-assisted laser desorption/ionization (MALDI) mass spectrometry. A peak of modified mass intensity charge confirmed the completion of the reaction. The reaction was then desalted with a NAP-5 column (GE Healthcare) equilibrated in 50 mM phosphate buffer with 150 mM NaCl, pH 7.4. BG-Seq1-Cy5 was ethanol precipitated, reconstituted in distilled water, and stored at -20°C.

Synthesis of BG-DNA and ephrin-B2-SNAPtag-His10

BG-Seq1-Cy5 was reacted with 2 molar equivalents of ephrin-B2-SNAPtag-His10 protein at 37°C for 60 min, and then kept overnight at 4°C. The following day, the reaction was filtered through a 0.22 μm microcentrifuge spin filter at 5000g for 5 min, then purified with a Superdex 200 size exclusion chromatography column using the AKTAexplorer system (GE Healthcare). Ephrin-B2-SNAPtag-BG-Seq1-Cy5 was analyzed by SDS-PAGE to confirm the molecular weight of the conjugate.

Preparation of thiol-modified DNA

The DNA sequence used was Seq2: 5'-TCATACGACTCACTCTAGGG-3'[45]. Seq2 with a thiol modifier C6 on the 5' end was purchased from Integrated DNA Technologies. SH-Seq2 was dissolved in TE buffer at 5 mg/mL, precipitated in ethanol, then rehydrated in distilled water, and stored at -20°C. For SLB experiments, SH2-Seq2 was reduced in tris (2-carboxyethyl) phosphine (TCEP) buffer (0.5 mM TCEP, 10 mM 4-(2-hydroxyethyl)-1-piperazineethanesulfonic acid buffer (HEPES), pH 8) for 90 min at 37°C. SH2-Seq2 was then filtered through two Bio-spin 6 columns (BioRad) equilibrated in 50 mM phosphate buffer with 150 mM NaCl, pH 7.4 and used for experiments.

Preparation of RGD-Alexa488-DNA

Cyclic RGD peptide (cyclo (Arg-Gly-Asp-D-Phe-Lys)) was obtained from Peptides International and dissolved in 100 mM HEPES buffer at 10 mM. To make RGD-maleimide, 4 molar equivalents of PEGylated SMCC crosslinker (Life Technologies) was reacted with cyclic RGD in 100 mM HEPES buffer. The reaction was incubated at room temperature for one h or longer until until completed, as confirmed by MALDI mass spectrometry. RGD-maleimide was then purified by reverse phase C18 column HPLC and fractions were analyzed by MALDI mass spectrometry.

The DNA sequence Seq1 with a thiol modifier C6 on the 5' end and an amino modifier C6 on the 3' end was purchased from Integrated DNA Technologies. SH-Seq1-NH2 was dissolved in TE buffer at 5 mg/mL and precipitated in ethanol. To make SH-Seq1-Alexa488, 10 molar equivalents of Alexa Fluor 488 Carboxylic Acid, 2,3,5,6-Tetrafluorophenyl Ester), 5-isomer (Life Technologies) was reacted with SH-Seq1-NH2 in 50 mM bicarbonate, 50 mM phosphate buffer with 150 mM NaCl, pH 7.4. The reaction was incubated at room temperature for 2 h, and reaction completion was confirmed by MALDI mass spectrometry. SH-Seq1-Alexa488 was then desalted with a NAP5 column, ethanol precipitated, rehydrated in distilled water, and stored at -20°C as previously described.

To conjugate SH-Seq1-Alexa488 with RGD-maleimide, DNA was reduced with TCEP and desalted with Bio-spin 6 columns (Biorad) as previously described, then reacted with 2 molar equivalents of RGD-maleimide for 2 h at room temperature, followed by MALDI mass spectrometry to confirm reaction completion. The reaction was purified by reverse phase C18 column HPLC and fractions were analyzed by MALDI mass spectrometry. RGD-Seq1-Alexa488 was ethanol precipitated, reconstituted in distilled water, and stored at -20°C.

Preparation and functionalization of supported lipid bilayers (SLBs)

Circular or square microscope coverslips with No. 1.5 thickness (Fisher Scientific) were soaked in 1:1 (vol/vol) 2-propanol and distilled water overnight, then sonicated for 30 min the following day. Coverslips were rinsed thoroughly with distilled water and then etched in piranha solution (1:3 vol/vol) hydrogen peroxide and sulfuric acid) for 20 min. Coverslips were rinsed thoroughly and then dried under a nitrogen stream. Lipids were purchased from Avanti Lipids. Standard methods were employed to produce lipid vesicles[46]. DOPC (1,2-dioleoyl-*sn*-glycero-3-phosphocholine) and MCC-DOPE (1,2-dioleoyl-sn-glycero-3-phosphoethanolamine-*N*-[4-(*p*-maleimidomethyl) cyclohexane-carboxamide]) were mixed (95% DOPC, 5% MCC-DOPE) in a chloroform solution, evaporated with a rotary evaporator, then further dehydrated under a nitrogen stream for 30-60 min. Lipid vesicles were rehydrated in distilled water to a final concentration of 0.5 mg/mL, then sonicated for 1 min to generate small unilamellar vesicles (SUVs). SUVs were diluted with phosphate buffered saline (PBS) (1:1 vol/vol) and then deposited and incubated on a piranha etched dry coverslip for 30 min to allow the formation of a SLB. Finally, the SLB was rinsed in an excess of PBS buffer. 2 mg/mL casein in PBS was added to SLBs for 10 min to block nonspecific binding, then washed with PBS. Reduced SH-Seq2 DNA (prepared above) was added to SLBs and incubated for 90 min, then washed with PBS. To form ephrin-B2 SLBs, ephrin-B2-SNAPtag-BG-Seq1-Cy5 was added to SLBs to a final solution concentration of 100 nM and incubated for 1 h, then washed with PBS. To form RGD/ ephrin-B2 SLBs, 100 nM ephrin-B2 and 5 nM RGD-Seq1-488 were added after SH-Seq2-DNA reaction with SLB. For NSC studies, SLBs were buffer exchanged with cell culture medium prior to seeding.

Nanofabrication

Chromium (Cr) patterns were fabricated using two methods: photolithography and e-beam lithography. For photolithography patterning, glass coverslips were cleaned by sonication in acetone for 5 min, then rinsed with distilled water and dried under a nitrogen stream. A 7 nm-thick Cr layer was deposited using e-beam evaporation (Solution, CHA Industries) at 5×10^{-6} torr with the deposition rate maintained at ~0.01 nm/sec. The Cr substrates were again cleaned by sonication in acetone for 5 min and rinsing with distilled water. The substrates were then dried under a nitrogen stream and heated at 130°C for 10 min to remove residual moisture. S1805 positive photoresist (PR) (MicroChem Corporation) was spun on the cleaned and dried substrate at 4000 rpm for 35 sec, and the PR film-coated substrate was then soft baked at 115°C for 60 sec. PR was exposed to UV through a Quartz Cr mask with a UV dose of 27 mJ/cm^2, then developed in MIF-321 developer (MicroChem Corporation). To generate Cr patterns, the underlying Cr layer was etched through a patterned photoresist mask using CR-7 Cr etchant (Cyantek Corporation). Finally, residual PR was removed using Microposit Remover 1165 (MicroChem Corporation).

For e-beam lithography patterning, glass coverslips were cleaned by sonication in distilled water for 5 min to remove gross particulate matter, then etched in piranha solution for 5 min. Etched coverslips were rinsed with distilled water, immersed in isopropanol, and dried under a nitrogen stream. Residual moisture was removed by heating at 140°C for 10 min. Coverslips were spin-coated for 45 sec at 1000 rpm with electron-beam resist 1:3 ZEP-520A/anisole (Zeon) and Aquasave conductive polymer (Mitsubishi Rayon). Resist was then exposed via e-beam lithography (CABL-9510CC, Crestec) to fabricate 2 μm and 4 μm grid patterns with line widths

of 80 nm. Conductive polymer was removed by rinsing with deionized water, and resist was developed for 1 min in isoamyl acetate. Cr with a thickness of 7 nm was then deposited by e-beam evaporation (EB3 e-beam evaporator, Edwards). Finally, the resist mask was lifted from coverslip surfaces by sonication in ice-cold methylene chloride for 10 min.

Cell culture

Neural stem cells (NSCs) isolated from the hippocampi of adult female Fisher 344 rats were cultured on 5 μg/mL polyornithine (Sigma-Aldrich) and 10μg/mL laminin (Life Technologies) coated tissue-culture plates. NSCs were grown in 1:1 DMEM/F12 (Life Technologies) with N-2 supplement (Life Technologies) and 20 ng/mL recombinant human FGF-2 (PeproTech). Upon reaching 80% confluency, NSCs were subcultured using Accutase (Life Technologies) and re-seeded at 20% confluency.

The EphB4-mCherry NSC line was created through stable retroviral infection. Total RNA was extracted from NSCs using TRIzol reagent (Life Technologies) and then full-length cDNA transcripts were synthesized from 5 μg RNA using the ThermoScript RT-PCR System with Oligo$(dT)_{20}$ primers (Life Technologies). The rat EphB4 gene was amplified from the cDNA using the primer pair: forward, 5'-CCATGGAGCTCAGAGCGC-3'; reverse, 5'-GGTCAGAACTGCTGGGTTGG-3', and then inserted into a subcloning vector using a TOPO TA Cloning Kit (Life Technologies). EphB4 was then amplified with the linker GSGS and inserted into the pmCherry-N1 Vector (Clontech) between Nhe1 and Age1 sites, to produce pEphB4-mCherry. Finally, EphB4-mCherry was amplified and inserted into the MMLV retroviral vector CLPIT[47] between Sfi1 and Pme1, resulting in CLPIT-EphB4-mCherry, which was then packaged, purified, and titered on NSCs as previously described[48]. NSCs were infected with the virus at a multiplicity of infection of 1, and a stable cell line was produced by selection in 0.6 μg/mL puromycin (Sigma-Aldrich) for 96 h.

For the blocking assay, NSCs were detached, spun down, and resuspended in PBS. Cells were counted and equal numbers were used for each condition. NSCs were incubated with no blocking, 2× (8 μg/mL) EphB4 antibody (AF446, R&D Systems), 2× EphB2 antibody (AF467, R&D Systems), or 1× (4 μg/mL) EphB4 and 1x EphB2 antibodies at 4°C, rotating for 1 h. NSCs were seeded on SLBs and allowed to adhere for 30 min. Unattached cells were then washed off and adhered cells were imaged.

Differentiation studies and immunostaining

NSCs were seeded on SLBs or polyornithine/ laminin coated eight-well glass chamber slides (Fisher Scientific) at 2×10^4 cells per well in DMEM/F12+N2 supplemented with 0.5 ng/mL FGF-2. Mixed differentiation medium additionally contained 1μM RA (Enzo Life Sciences) and 2% FBS (Life Technologies). Antibody clustered ephrin-B2 was generated by incubating recombinant mouse ephrin-B2/Fc (R&D Systems) with a goat anti-human IgG Fc antibody (Jackson ImmunoResearch) at a 1:9 ratio (wt/wt) for 90 min at 4°C. To block EphB4 receptors, NSCs were incubated with 4 μg/mL EphB4 antibody for 30 min at 37°C before seeding on SLBs. SLB cultures were supplemented with 10 μg/mL laminin 18 h after seeding to enable attachment to coverslips. Media changes were performed for all conditions every 2 days.

Cell cultures were fixed with 4% paraformaldehyde (Sigma-Aldrich) for 15 min, then blocked and permeabilized with 5% donkey serum (Sigma-Aldrich) and 0.3% Triton X-100 (Fisher-Scientific) for 1 h. Cultures were incubated with primary antibody mouse anti-βIII-tubulin (1:500, T8578, Sigma-Aldrich) for 48 h, then with secondary antibody Alexa Fluor 488-conjugated donkey anti-mouse IgG (1:1250, 715-545-151, Jackson ImmunoResearch) for 2 h, and finally with 4,6-diamidino-2-phenylindole (DAPI, 5 μg/ml, Life Technologies) as a nuclear counterstain for 20 min.

Western blotting

Prior to signaling studies, NSCs were cultured in DMEM/F12+N2 supplemented with 0.5ng/mL FGF-2 for 16 h. NSCs were seeded at 4×10^5 cells per SLB in FGF-free medium and incubated for 1 h. For each condition, culture media and PBS washes from replicates were pooled and spun down. The cell pellet was then re-suspended in NP-40 lysis buffer (1% NP-40 (Sigma), 150 mM sodium chloride, 50 mM Tris, pH 8.) containing protease and phosphatase inhibitor cocktails (Life Technologies). In parallel, lysis buffer was added to the substrates, and adhered cells were scraped off and combined with the resuspended pellets. Cells were lysed on ice for 30 min, spun down, and then lysates were concentrated using 3 kDa NMWL centrifugal filters (EMD Millipore) to reduce volume ~50%. Protein concentration was determined with a BCA Protein Assay Kit (Life Technologies). Samples of equal protein content were electrophoretically separated on 10% SDS-PAGE gels, and then transferred onto nitrocellulose membranes (BioRad) using standard methods. Blots were probed overnight with the primary antibodies: rabbit anti-active (non-phospho) β-catenin (Ser33/37/Thr41) (1:1000, 8814), rabbit anti-ERK1/2 (1:1000, 4695), rabbit anti-phospho-ERK1/2 (Thr202/Tyr204) (1:2000, 4370), mouse anti-phosphotyrosine (P-Tyr-100) (1:1000, 9411) (all Cell Signaling), and rabbit anti-GAPDH (1:2500, ab9485, Abcam). Blots were then incubated for 1 h with appropriate horseradish peroxidase-conjugated secondary antibodies: goat anti-mouse HRP (1:10,000, 32430, Life Technologies) and goat anti-rabbit HRP (1:10,000, 32460, Life Technologies). Protein bands were detected using SuperSignal West Dura Chemiluminescent Substrate (Life Technologies), and then digitally imaged on a ChemiDoc XRS+ Imaging System (BioRad). When blots were stripped and re-probed (up to 2 times), phosphorylated epitopes were probed first.

Optical microscopy

TIRF, FRAP, RICM, epifluorescent and brightfield images were taken on a Nikon Eclipse Ti-E/B motorized inverted microscope (Technical Instruments) using Nikon 100× Apo TIRF 1.49 NA oil immersion and 20×/0.5, DIC M/N2, WD 2.1 objectives. The microscope was equipped with a motorized Epi/TIRF illuminator, a motorized Intensilight mercury lamp, a Nikon Perfect Focus system (Technical Instruments), a motorized stage (MS-2000, Applied Scientific Instrumentation), and an Orca-R2 interline charge-coupled device camera (Hamamatsu). Dichroics were 2 mm thick and mounted in metal cubes to preserve optical flatness: ZT488rdc, ZT561rdc, and ZT640rdc. Three different long-pass emission filters were used: ET500lp, ET575lp, and ET660lp. Bandpass emission filters were installed below the dichroic turret in a motorized filter wheel (Lambda 10-3, Sutter): ET525/50m, ET600/50m, and ET700/75m. RICM was performed using a 50/50 beam splitter with a D546/10 filter. A 100mW 561 nm optically pumped solid-state laser (Sapphire, Coherent), and a 100mW 640 nm diode laser (Cube, Coherent) were used for TIRF experiments. All filters and dichroics listed above were purchased

from Chroma. Live-cell imaging was performed using a stage-top incubator and objective heater (Chamlide TC-A, Quorum Technology).

For confocal microscopy, a 200mW 488 nm Ar-ion laser (177G, Spectra Physics) was used in addition to lasers above. All lasers were operated using an acousto-optic tunable filter and aligned into a dual-fiber launch built by Solamere. One single-mode polarization maintaining fiber (Oz Optics) was connected to the TIRF illuminator, while another was connected to the spinning disk confocal unit. A spinning disk confocal head (Yokogawa CSU-X1-M1N-E, Solamere) was custom fit to the microscope and camera. The dichroic in the spinning disk head was a T405/488/568/647 multiline (Semrock). Emission filters were installed in a custom-mounted filter wheel (FW-1000, Applied Scientific Instrumentation): ET525/50M, ET605/52M, and ET700/75M (Chroma). Confocal images were captured using a 1024 × 1024 pixel electron-multiplying charge-coupled device camera (iXon3 888, Andor), typically at gain setting 200 and with 1 × 1 binning. Axial slice step size was 0.5 mm and extended 20 mm above the coverslip.

Micromanager (University of California, San Francisco) and ImageJ (National Institutes of Health) were used to collect, analyze, and process images.

Fluorescence correlation spectroscopy (FCS)

Dual-color FCS was performed on a home-built spectrometer with a modified inverted microscope (TE2000, Nikon). Excitation wavelengths were selected by bandpass filters (Chroma) from a pulsed white light laser source (SuperK Extreme EXW-12, NKT Photonics), combined into a single mode optical fiber, then sent through a multi-color dichroic cube (Di01-R405/488/561/635-25×36, Semrock) before entering the microscope. Notch filters (Chroma) were used to remove excess excitation intensity. Fluorescence signal was collected by a Nikon 100× Apo TIRF 1.49 NA oil immersion objective and recorded by avalanche photodiode detectors (Hamamatsu). The signal was directly converted into autocorrelation signal by a hardware correlator (Correlator.com). 488 nm and 640 nm wavelengths were used to simultaneously excite Alexa Fluor 488 and Cy5. Average power ranged between 0.5 and 5.0 μW, depending on the fluorophore quantum yield and the surface density, which is equivalent to the irradiance range of 0.4 ~ 4.0 kW/cm^2 calculated with the calibrated spot sizes. The resulting autocorrelation $G_0(\tau)$ was fit to the two-dimensional Gaussian diffusion model[49],

$$\mathrm{G_0}(\tau) = \frac{1}{N}\left(\frac{1}{1+\tau/\tau_D}\right)$$

where τ is time delay, N is the number of particles in the focus spot, and τ_D is the diffusion correlation time. To calibrate the spot size of the confocal focus, a bilayer with a known surface density of fluorescent lipids of each color, BODIPY-FL-DHPE (for 488 nm) and ATTO665-DPPE (for 640 nm) (Avanti) was measured, which consistently yielded the radius of 0.20 ± 0.01 μm and 0.27 ± 0.01 μm for 488 nm and 640 nm wavelengths, respectively. The diffusion coefficient D was calculated by using the relation,

$$D = w^2/4\tau_D$$

where w is the radius of the focus spot size.

Cy5 exhibits fast blinking kinetics due to a long-lived triplet state that contributes to the photo-physics. In FCS, blinking appears on the microsecond to millisecond timescales. Therefore, for

Cy5, the autocorrelation model required an extra term in order to account for the additional intensity fluctuation from blinking. The model becomes,

$$\mathrm{G}(\tau) = \left(\frac{1 - F + Fe^{-\frac{\tau}{\tau_e}}}{1 - F} \right) \mathrm{G}_0(\tau)$$

where F is the fraction of molecules in the dark state at equilibrium, and τ_e is the lifetime of the dark triplet state.

.

Statistical analysis

Statistical analysis was performed in MATLAB (MathWorks). Statistical significance of the results was determined by analysis of variance (ANOVA) paired with a multiple comparison test (Tukey-Kramer method). All error bars represent ± standard error of the mean.

3.5 Acknowledgements

We acknowledge E. Connelly for experimental assistance with cell culture, immunostaining, and western blots; and S. Lord for critical discussion regarding experimental design and assistance with microscopy.

3.6 References

1. Himanen, J.-P., Saha, N. & Nikolov, D. B. Cell-cell signaling via Eph receptors and ephrins. *Curr Opin Cell Biol* **19,** 534–542 (2007).
2. Lisabeth, E. M., Falivelli, G. & Pasquale, E. B. Eph receptor signaling and ephrins. *Cold Spring Harb Perspect Biol* **5,** (2013).
3. Cayuso, J., Xu, Q. & Wilkinson, D. G. Mechanisms of boundary formation by Eph receptor and ephrin signaling. *Dev Biol* **401,** 122–131 (2015).
4. Klein, R. & Kania, A. Ephrin signalling in the developing nervous system. *Current opinion in neurobiology* **27,** 16–24 (2014).
5. Barquilla, A. & Pasquale, E. B. Eph receptors and ephrins: therapeutic opportunities. *Annu Rev Pharmacol Toxicol* **55,** 465–487 (2015).
6. Pasquale, E. B. Eph receptors and ephrins in cancer: bidirectional signalling and beyond. *Nat Rev Cancer* **10,** 165–180 (2010).
7. Davis, S. *et al.* Ligands for EPH-related receptor tyrosine kinases that require membrane attachment or clustering for activity. *Science* **266,** 816–819 (1994).
8. Stein, E. *et al.* Eph receptors discriminate specific ligand oligomers to determine alternative signaling complexes, attachment, and assembly responses. *Genes Dev* **12,** 667–678 (1998).
9. Janes, P. W. *et al.* Eph receptor function is modulated by heterooligomerization of A and B type Eph receptors. *J Cell Biol* **195,** 1033–1045 (2011).
10. Janes, P. W., Nievergall, E. & Lackmann, M. Concepts and consequences of Eph receptor clustering. *Seminars in cell & developmental biology* **23,** 43–50 (2012).
11. Schaupp, A. *et al.* The composition of EphB2 clusters determines the strength in the cellular repulsion response. *J Cell Biol* **204,** 409–422 (2014).
12. Bethani, I., Skånland, S. S., Dikic, I. & Acker-Palmer, A. Spatial organization of transmembrane receptor signalling. *EMBO J* **29,** 2677–2688 (2010).

13. Salaita, K. *et al.* Restriction of Receptor Movement Alters Cellular Response: Physical Force Sensing by EphA2. *Science* **327,** 1380–1385 (2010).
14. Greene, A. C. *et al.* Spatial organization of EphA2 at the cell-cell interface modulates trans-endocytosis of ephrinA1. *Biophys J* **106,** 2196–2205 (2014).
15. Chumley, M. J., Catchpole, T., Silvany, R. E., Kernie, S. G. & Henkemeyer, M. EphB receptors regulate stem/progenitor cell proliferation, migration, and polarity during hippocampal neurogenesis. *J Neurosci* **27,** 13481–13490 (2007).
16. Holmberg, J. *et al.* Ephrin-A2 reverse signaling negatively regulates neural progenitor proliferation and neurogenesis. *Genes Dev* **19,** 462–471 (2005).
17. Nomura, T., Göritz, C., Catchpole, T., Henkemeyer, M. & Frisén, J. EphB signaling controls lineage plasticity of adult neural stem cell niche cells. *Cell Stem Cell* **7,** 730–743 (2010).
18. Ashton, R. S. *et al.* Astrocytes regulate adult hippocampal neurogenesis through ephrin-B signaling. *Nat Neurosci* **15,** 1399–1406 (2012).
19. Conway, A. *et al.* Multivalent ligands control stem cell behaviour in vitro and in vivo. *Nature Nanotech* **8,** 831–838 (2013).
20. Chrencik, J. E. *et al.* Structural and biophysical characterization of the EphB4*ephrinB2 protein-protein interaction and receptor specificity. *J Biol Chem* **281,** 28185–28192 (2006).
21. Yu, C.-H. & Groves, J. T. Engineering supported membranes for cell biology. *Med Biol Eng Comput* **48,** 955–963 (2010).
22. Nair, P., Salaita, K. & Petit, R. Using patterned supported lipid membranes to investigate the role of receptor organization in intercellular signaling. *Nat Protoc* (2011).
23. Chandra, R. A., Douglas, E. S., Mathies, R. A., Bertozzi, C. R. & Francis, M. B. Programmable Cell Adhesion Encoded by DNA Hybridization. *Angewandte Chemie* **118,** 910–915 (2006).
24. Engin, S. *et al.* Benzylguanine Thiol Self-Assembled Monolayers for the Immobilization of SNAP-tag Proteins on Microcontact-Printed Surface Structures. *Langmuir* **26,** 6097–6101 (2010).
25. Keppler, A. *et al.* A general method for the covalent labeling of fusion proteins with small molecules in vivo. *Nat Biotechnol* **21,** 86–89 (2003).
26. Knight, J. D., Lerner, M. G., Marcano-Velázquez, J. G., Pastor, R. W. & Falke, J. J. Single molecule diffusion of membrane-bound proteins: window into lipid contacts and bilayer dynamics. *Biophys J* **99,** 2879–2887 (2010).
27. Moran, U., Phillips, R. & Milo, R. SnapShot: key numbers in biology. *Cell* **141,** 1262–1262.e1 (2010).
28. Himanen, J., Rajashankar, K. & Lackmann, M. Crystal structure of an Eph receptor-ephrin complex. *Nature* (2001).
29. Ruoslahti, E. RGD and other recognition sequences for integrins. *Annu Rev Cell Dev Biol* **12,** 697–715 (1996).
30. Dustin, M. L. & Groves, J. T. Receptor signaling clusters in the immune synapse. *Annu. Rev. Biophys. ...* **41,** 543–556 (2012).
31. Hartman, N. C., Nye, J. A. & Groves, J. T. Cluster size regulates protein sorting in the immunological synapse. *Proc Natl Acad Sci USA* **106,** 12729–12734 (2009).
32. Manz, B. N., Jackson, B. L., Petit, R. S., Dustin, M. L. & Groves, J. T-cell triggering thresholds are modulated by the number of antigen within individual T-cell receptor clusters. *Proc Natl Acad Sci USA* **108,** 9089–9094 (2011).

33. Mossman, K., Campi, G. & Groves, J. Altered TCR signaling from geometrically repatterned immunological synapses. *Science* (2005).
34. Xu, Q., Lin, W.-C., Petit, R. S. & Groves, J. T. EphA2 receptor activation by monomeric Ephrin-A1 on supported membranes. *Biophys J* **101,** 2731–2739 (2011).
35. Xiao, Z. *et al.* EphB4 promotes or suppresses Ras/MEK/ERK pathway in a context-dependent manner: Implications for EphB4 as a cancer target. *Cancer Biol. Ther.* **13,** 630–637 (2012).
36. Möller, I. & Seeger, S. Solid supported lipid bilayers from artificial and natural lipid mixtures – long-term stable, homogeneous and reproducible. *Journal of Materials Chemistry B* **3,** 6046–6056 (2015).
37. Jackman, J., Knoll, W. & Cho, N.-J. Biotechnology Applications of Tethered Lipid Bilayer Membranes. *Materials 2012, Vol. 5, Pages 2637-2657* **5,** 2637–2657 (2012).
38. Williams, S. E. *et al.* Ephrin-B2 and EphB1 mediate retinal axon divergence at the optic chiasm. *Neuron* **39,** 919–935 (2003).
39. Cortina, C. *et al.* EphB-ephrin-B interactions suppress colorectal cancer progression by compartmentalizing tumor cells. *Nat Genet* **39,** 1376–1383 (2007).
40. Allonby, O. *et al.* Ligand stimulation induces clathrin- and Rab5-dependent downregulation of the kinase-dead EphB6 receptor preceded by the disruption of EphB6-Hsp90 interaction. *Cell Signal* **26,** 2645–2657 (2014).
41. Qin, H. *et al.* Structural characterization of the EphA4-Ephrin-B2 complex reveals new features enabling Eph-ephrin binding promiscuity. *J Biol Chem* **285,** 644–654 (2010).
42. Narui, Y. & Salaita, K. Membrane tethered delta activates notch and reveals a role for spatio-mechanical regulation of the signaling pathway. *Biophys J* **105,** 2655–2665 (2013).
43. Tsai, J. & Kam, L. C. Lateral Mobility of E-cadherin Enhances Rac1 Response in Epithelial Cells. *Cell Mol Bioeng* **3,** 84–90 (2010).
44. Liu, Z. *et al.* Mechanical tugging force regulates the size of cell-cell junctions. *Proc Natl Acad Sci USA* **107,** 9944–9949 (2010).
45. Hsiao, S. C. *et al.* Direct Cell Surface Modification with DNA for the Capture of Primary Cells and the Investigation of Myotube Formation on Defined Patterns. *Langmuir* **25,** 6985–6991 (2009).
46. Lin, W.-C., Yu, C.-H., Triffo, S. & Groves, J. T. Supported membrane formation, characterization, functionalization, and patterning for application in biological science and technology. *Curr Protoc Chem Biol* **2,** 235–269 (2010).
47. Yu, J. H. & Schaffer, D. V. Selection of novel vesicular stomatitis virus glycoprotein variants from a peptide insertion library for enhanced purification of retroviral and lentiviral vectors. *J. Virol.* **80,** 3285–3292 (2006).
48. Peltier, J. & Schaffer, D. V. Viral packaging and transduction of adult hippocampal neural progenitors. *Methods Mol Biol* **621,** 103–116 (2010).
49. Bacia, K., Haustein, E. & Schwille, P. Fluorescence correlation spectroscopy: principles and applications. *Cold Spring Harb Protoc* **2014,** 709–725 (2014).

Chapter 4: Investigation of Signaling in Ephrin-B2-Induced Adult Neural Stem Cell Neurogenesis

4.1 Introduction

Neurogenesis occurs in two regions of the adult brain – the subventricular zone (SVZ) of the lateral ventricles[1] and the subgranular zone (SGZ) of the hippocampal dentate gyrus[2]. In these areas, multipotent neural stem cells (NSCs) are capable of maintaining quiescence, proliferating to remain in an undifferentiated state, or differentiating into lineage restricted central nervous system (CNS) cells, including neurons, astrocytes, and oligodendrocytes[3]. Hippocampal NSCs play key roles in learning and memory[4], decline with age[5], and have been associated with a number of pathologies, including Alzheimer's[6] and seizures[7]. Therefore, understanding the mechanisms of NSC maintenance and differentiation can inform future efforts in regenerative medicine, either through directing *ex vivo* stem cell manipulation prior to transplantation or guiding *in vivo* stimulation of endogenous NSC populations.

The NSC niche, the microenvironment in which the stem cell resides, provides cues regulating NSC activity. In the SGZ, a number of factors have been shown to control NSC proliferation, including fibroblast growth factor-2[8], insulin like growth factor-2[9], sonic hedgehog[10], and Wnt7a[11]. NSC differentiation is likewise mediated by a diverse array of signals. Retinoic acid[12], transforming growth factor β[13], and GABAergic inputs[14] promote NSC neuronal differentiation. Hippocampal astrocytes in immediate proximity to NSCs induce neurogenesis as well[15], through secretory factors including Wnt3a[16,17] and, as we recently discovered, the cell-cell contact dependent signal ephrin-B2[18,19]. In our previous work, we demonstrated both *in vitro* and *in vivo* that juxtacrine signaling between ephrin-B2-expressing astrocytes and NSCs induces neuronal differentiation via the EphB4 receptor. Additionally, we showed that this signaling mediated neurogenesis through Wnt-independent increases in levels of active β-catenin and the proneuronal transcription factors *NeuroD1* and *Mash1*[18,19]. The immediate downstream signaling pathways involved in ephrin-B2:EphB4 signaling in NSCs, however, remain unknown.

Ephrins, classified as glycophosphatidylinositol-linked A-type or transmembrane B-type, are membrane-bound ligands that bind to Eph receptors, the largest family of receptor tyrosine kinases. Bidirectional signaling in both the ephrin and Eph-presenting cells occurs upon juxtacrine interaction, resulting in a diverse array of cellular responses[20]. In the CNS, Eph:ephrin signaling is involved in development, including retinal axon guidance[21] and neuronal maturation[22], as well as adult function, such as axonal retraction[23] and dendritic spine morphogenesis[24]. Additionally, adult NSC proliferation, differentiation, and migration in both the SVZ and SGZ have been shown to be mediated by Ephs and ephrins[18,25-27], with the sole report of neurogenesis discussed above.

The downstream pathways mediating Eph:ephrin signaling are numerous and varied, with new targets continuously being discovered[20,28]. This diversity is due to both the large number of ephrins (A1-6, B1-3) and Ephs (A1-10, B1-6), as well as the many cell types in which they function. Regarding NSC neuronal differentiation, the relevant pathways transducing ephrin-B2 stimulation are not readily apparent. No studies have demonstrated a direct link between Eph:ephrin signaling and β-catenin activation (though β-catenin mediated Eph transcription has

been reported[29]), and established Eph:ephrin targets do not overlap with known neurogenic signals. Therefore, dissecting the mechanisms of ephrin-B2-induced NSC neuronal differentiation could reveal novel Eph:ephrin signaling pathways, novel neurogenic pathways, and potentially point to novel targets for therapeutic intervention.

In this study, we investigated downstream signaling in ephrin-B2 mediated NSC neurogenesis. To enhance response, we developed and characterized an EphB4 overexpressing NSC line and demonstrated robust signal activation. We then utilized mass spectrometry to identify novel downstream targets of ephrin-B2 stimulation. Finally, we chose promising hits and developed knockdown NSC lines through CRISPR/Cas9-mediated gene editing. Knocking down the kinases Ack1, Fyn, and Src prevented ephrin-B2-induced NSC neuronal differentiation. These findings reveal novel pathways in both Eph:ephrin signaling and adult neurogenesis.

4.2 Results

Ephrin-B2 induces NSC neuronal differentiation but downstream signaling is not detectable

Prior to interrogating downstream signaling, we first confirmed our previously published findings of ephrin-B2-induced neurogenesis[18,19]. As Eph:ephrin signaling requires oligomerized cluster formation for downstream activity[30], solubilized ephrin ectodomains must be synthetically clustered to enable transduction of Eph mediated signaling. Adult hippocampal NSCs were stimulated *in vitro* with two forms of oligomerized ephrin-B2 for 5d. First, we used the traditional method of antibody-clustered Fc-fused ephrin molecules (Fc-ephrin-B2)[18]. Second, we employed multivalent ephrin-B2 created by conjugating ephrin to a linear hyaluronic acid (HyA) polymer at high valency[19]. Performing the conjugation reaction at 1:40 HyA:ephrin-B2 resulted in conjugates with a valency of 1:18 (HyA:ephrin-B2). Consistent with our previous work, both Fc-ephrin-B2 and HyA:ephrin-B2 strongly induced NSC neuronal differentiation (βIII-tubulin+ cells). Furthermore, HyA:ephrin-B2 more potently induced neurogenesis than Fc-ephrin-B2. Finally, in line with previous findings, both Fc-ephrin-B2 and HyA:ephrin-B2 induced mild astrocytic differentiation (glial fibrillary acidic protein, GFAP+ cells), though the increases was not significant. As a positive control for differentiation, NSCs were cultured in a mixed differentiation media containing retinoic acid and fetal bovine serum (RA/FBS), which induced both neuronal and astrocytic differentiation[31] (Fig. 4.1a,b).

Upon ephrin binding, Ephs trans-phosphorylate, which then induces signaling through phosphorylation cascades[20,28]. To examine general signal activation, we stimulated NSCs for 1h with Fc-ephrin-B2 or HyA:ephrin-B2, then probed for phosphorylated proteins by western blot using pan-phosphoserine (pSer), -phosphothreonine (pThr), and –phosphotyrosine (pTyr) antibodies. Surprisingly, compared to naïve cells, stimulation of NSCs with either form of ephrin-B2 did not result in changes in phosphorylation levels (Fig. 4.1c). Therefore, while NSCs underwent neuronal differentiation in response to ephrin-B2, downstream signaling was not detectable by conventional biochemical assays.

EphB4-overexpressing NSCs exhibit ephrin-B2-induced downstream signaling activation

To enable investigation of ephrin-B2-induced signaling in NSCs, downstream signaling levels needed to be enhanced. As ephrin-B2 stimulation in NSCs is transduced through the EphB4 receptor[18], we developed an EphB4-overexpressing NSC line. We hypothesized that ephrin-B2

was being provided to NSCs in excess of its cognate receptor, therefore increasing receptor levels would elevate downstream signaling, with the assumption that these targets were not being maximally activated by basal EphB4 stimulation. The rat EphB4 gene was PCR amplified from cDNA generated from NPCs and fused to an mCherry fluorescent protein to enable visualization. Of note, this is the first published mRNA sequence of rat EphB4 (Fig. 4.2a). EphB4-mCherry retroviral particles were then produced and NSCs were infected at a multiplicity of infection (MOI) of 1 to create an EphB4-mCherry NSC line (EphB4-mCh NSC). Imaging EphB4-mCh NSCs confirmed expression of a membrane-localized mCherry-fusion protein (Fig. 4.2b).

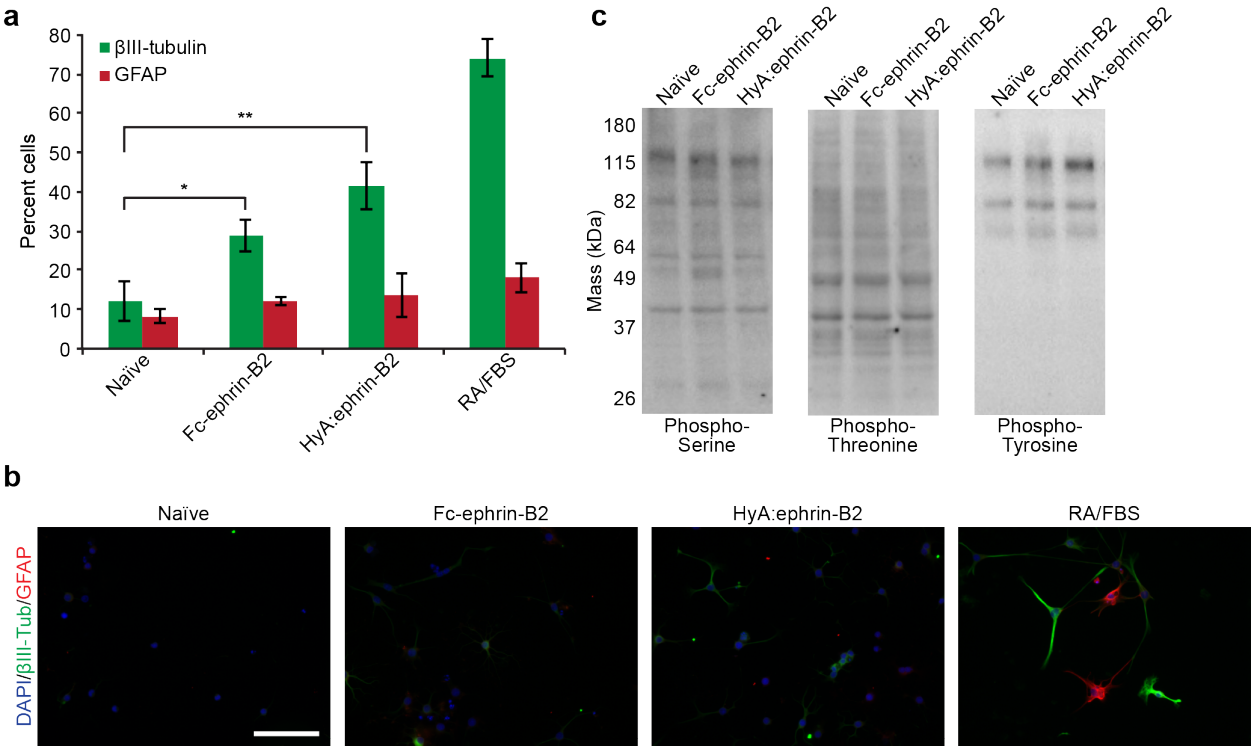

Figure 4.1. Ephrin-B2 induces neurogenesis but downstream signaling is undetectable. (**a**) Quantification of NSC differentiation after 5 days of stimulation with Fc-ephrin-B2, HyA:ephrin-B2, or RA/FBS. Cells were immunostained and the percent of cells differentiated into neurons (βIII-tubulin+/ DAPI) and astrocytes (GFAP+/ DAPI) was measured. *P < 0.5, **P < 0.05 by ANOVA and Tukey-Kramar multiple comparison, n = 3 experimental replicates, error bars are ± s.d. (**b**) Representative immunofluorescence images from (**a**) of NSCs stained for DAPI (blue), βIII-tubulin (green), and GFAP (red). Scale bar, 100 µm. (**c**) Western blots for phosphorylated proteins after 1 h of stimulation by Fc-ephrin-B2 or HyA:ephrin-B2.

We then characterized the EphB4-mCh NSC line by comparing EphB4 expression levels to untransduced NSCs. First, cells were immunostained for EphB4 and quantified, demonstrating ~3-fold increase in EphB4 expression (Fig 4.2c) Protein levels were further analyzed by western blot, which showed a strong band for the fusion protein at ~140 kDa (EphB4 ~110 kDa, mCherry ~30 kDa), but no detectable basal levels of EphB4 in either unstransduced or EphB4-mCh NSCs (Fig 4.2d). Extended exposure times did not aid in basal detection (data not shown). This discrepancy between immunofluorescence and western blot results was likely due to poor EphB4 antibody specificity, which we have seen in other studies. Next, mRNA levels were measured by quantitative reverse transcription polymer chain reaction (qRT-PCR). Using two different primer sets, EphB4 transcription in EphB4-mCh NSCs was found to be between ~50-100-fold greater

than untransduced NSCs (Fig 4.2e). This large increase in EphB4 expression validated western blot results, verifying overexpression of EphB4 in the EphB4-mCh NSCs. Notably, the barely detectable levels of basal EphB4 in untransduced NSCs may explain why downstream signaling

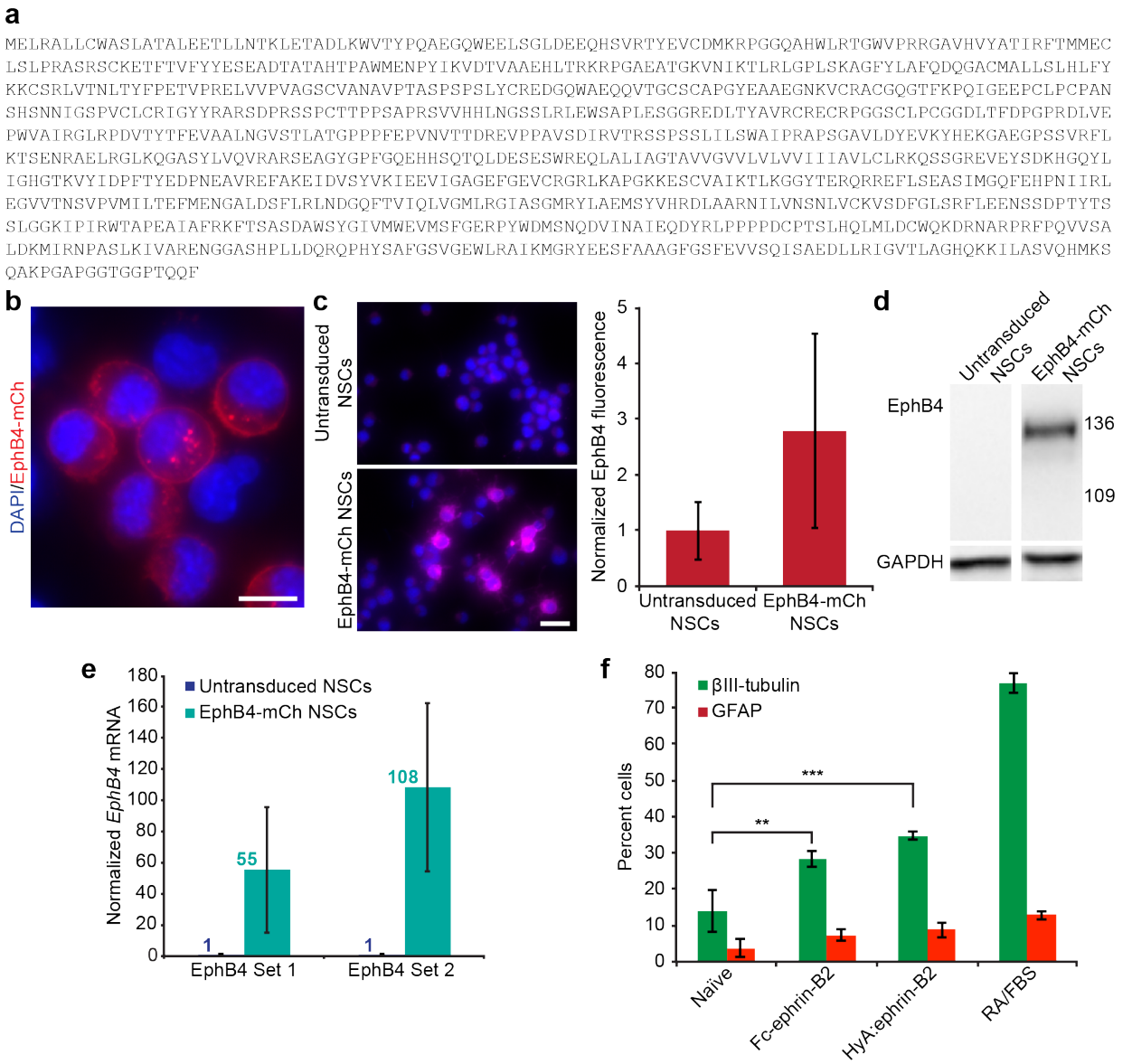

Figure 4.2. Development and characterization of an EphB4-mCh NSC line. (**a**) mRNA sequence of rat EphB4 amplified from NSC cDNA. (**b**) Representative immunofluorescence image of EphB4-mCh (red) NSCs counterstained with DAPI (blue). Scale bar, 10 µm. (**c**) Left: Representative immunofluorescence images of untransduced NSCs and EphB4-mCh NSCs stained for EphB4 (red) and DAPI (blue). Scale bar, 25 µm. Right: Quantification of EphB4 expression normalized to basal levels in untransduced NSCs. n = 6 experimental replicates, 5 cells per replicate. (**d**) Western blots for EphB4 and GAPDH. The 140 kDa band is the EphB4-mCherry fusion protein. (**e**) Quantification of EphB4 mRNA levels by qRT-PCR using two EphB4 primer sets. Expression in EphB4-mCh NSCs was normalized to EphB4 levels in untransduced NSCs. n = 3 experimental replicates, 3 technical replicates per experimental replicate. (**f**) Quantification of immunostaining of EphB4-mCh NSC differentiation after 5 days of stimulation with Fc-ephrin-B2, HyA:ephrin-B2, or RA/FBS for percent neurons (βIII-tubulin+/ DAPI) and astrocytes (GFAP+/ DAPI). **P < 0.005, ***P < 0.0005 by ANOVA and Tukey-Kramar multiple comparison, n = 3 experimental replicates. All error bars are ± s.d.

was not apparent in previous experiments. Finally, to confirm that EphB4 overexpression does not alter differentiation, EphB4-mCh NSCs were stimulated with Fc-Ephrin-B2, HyA:ephrin-B2, or RA/FBS and analyzed by immunostaining. Neuronal and astrocytic differentiation levels in all conditions were similar to those in untransduced NSCs (Fig. 4.2f).

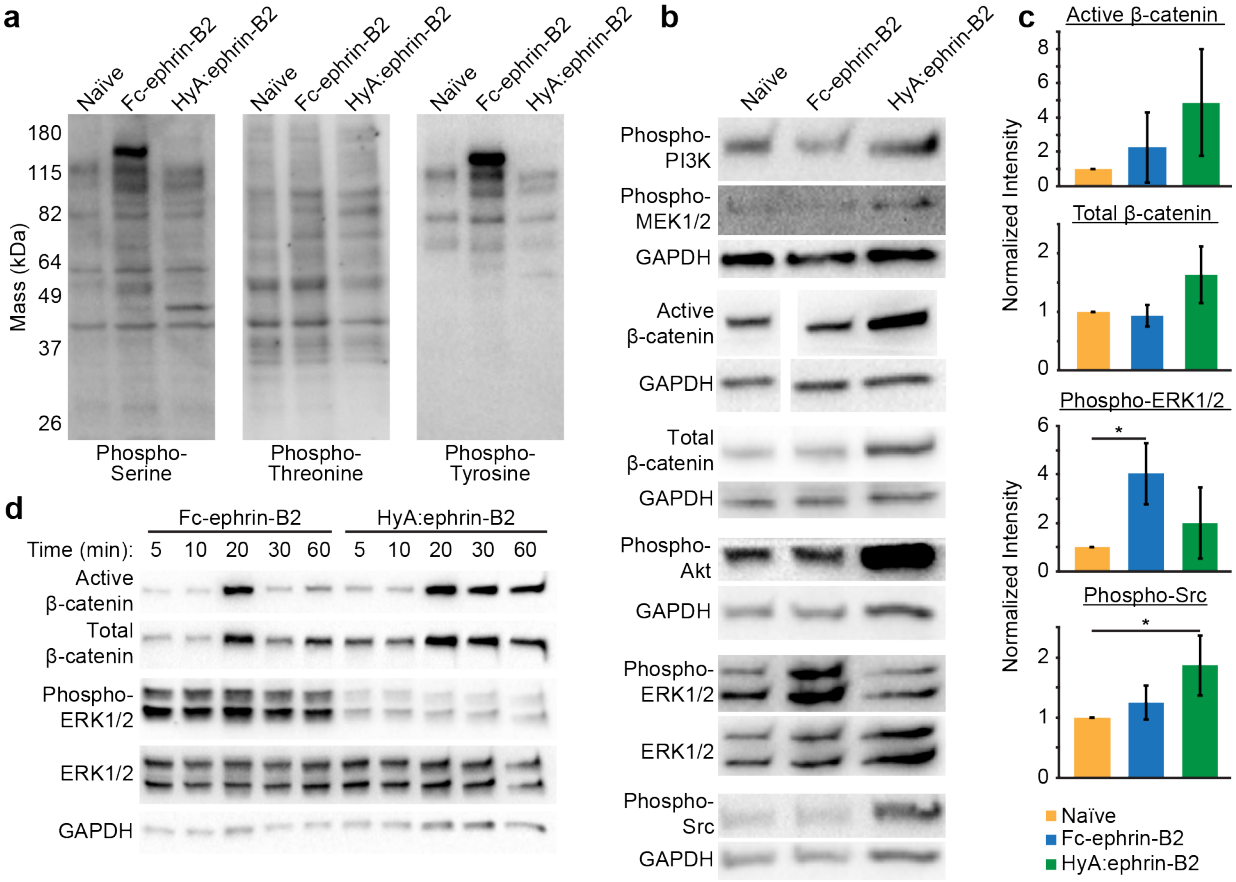

Figure 4.3. Ephrin-B2 induced downstream signaling in EphB4-mCh NSCs. (**a**) Western blots for phosphorylated proteins 1 h after Fc-ephrin-B2 or HyA:ephrin-B2 stimulation. (**b**) Representative western blots for downstream signaling targets after 1 h of stimulation by Fc-ephrin-B2 or HyA:ephrin-B2. (**c**) Quantification of selected western blots from (**b**) by densitometry analysis. Active β-catenin, total β-catenin, and phospho-Src levels were normalized to GAPDH. Phospho-ERK levels were normalized to total ERK. Ephrin-B2 stimulated levels were then normalized to naïve expression levels. *P < 0.05, by ANOVA and Tukey-Kramar multiple comparison, n = 3 blots, error bars are ± s.d.. (**d**) Western blots for signaling targets during a 1 h time course of stimulation with Fc-ephrin-B2 or HyA:ephrin-B2.

To investigate ephrin-B2 signaling in EphB4-mCh NSCs, we first probed for pan-pThr, -pSer, and –pTyr epitopes by western blot. In contrast to untransduced NSCs, a number of phosphorylated proteins were detectable in EphB4-mCh NSCs after 1 h of ephrin-B2 stimulation. Interestingly, while Fc-ephrin-B2 and HyA:ephrin-B2 both induced phosphorylation, the banding patterns on the pan-phospho-blots were noticeably different (Fig. 4.3a). This indicates that distinct downstream targets were being activated dependent on the method of ephrin-B2 oligomerization.

Next, specific proteins known to be downstream of ephrin-B2:EphB4 were probed; these included Akt, β-catenin, extracellular regulated MAP kinase (ERK), phosphoinositide 3-kinase

(PI3K), MAP kinase kinase (MEK), and Src proto-oncogene (Src)[18,32,33]. All of the targets examined were activated by ephrin-B2, assessed by increased phosphorylation of Akt, ERK, PI3K, and Src, and decreased phosphorylation and increased protein levels of β-catenin, active β-catenin and total β-catenin, respectively (Fig.4.3b,c). Again, as in the pan-phospho-blots, differential signaling was observed with Fc-ephrin-B2 and HyA:ephrin-B2 stimulation. For example, ERK was strongly phosphorylated in response to Fc-ephrin-B2, while Src was strongly phosphorylated in response to HyA:ephrin-B2. Of particular note were the increased levels of active β-catenin and total β-catenin after 1 h of stimulation. Our previous work similarly showed increased active β-catenin, but levels only became detectable after 4 h[18], leading us to hypothesize that β-catenin was a transcriptional target of ephrin-B2:EphB4 signaling. However, these findings of immediate activation point to β-catenin as a direct target of ephrin-B2:EphB4. To our knowledge, this is the first report of direct Eph:ephrin signal cross-talk with the canonical Wnt signaling pathway.

Finally, we investigated the time course of signaling. EphB4-mCh NSCs were stimulated with Fc-ephrin-B2 or HyA:Ephrin-B2 for 5, 10, 20, 30, or 60 min. Probing for active β-catenin, total β-catenin, and phsospho-ERK provided further insight into the observed discrepancies in downstream target activity dependent on the method of ephrin-B2 oligomerization. Phospho-ERK appeared within 5 min of Fc-ephrin-B2 stimulation and remained elevated for the duration of the time course. Active β-catenin and total β-catenin levels rose after 20 min of HyA:ephrin-B2 stimulation and persisted. Interestingly, active β-catenin and total β-catenin were also elevated in response to Fc-ephrin-B2, but levels peaked at 20 min and then fell by 60 min, replicating previous results (Fig 4.3d). Therefore, ephrin-B2 stimulation is transduced through multiple signaling cascades with complex temporal dynamics. And, Fc-ephrin-B2 and HyA:ephrin-B2 differentially stimulate these aspects of downstream signaling.

Mass spectrometry reveals novel signaling pathways

Established Eph:ephrin signaling pathways do not overlap with known neurogenic pathways. Additionally, they have not been shown to induce expression of the proneuronal transcription factors *NeuroD1 and Mash1*, which we have previously observed to be upregulated in NSCs in response to ephrin-B2 stimulation[18]. Thus, after confirming our ability to detect immediate signaling in EphB4-mCh NSCs, we chose to take an unbiased proteomics approach for further analysis. Mass spectrometry (MS), a technique from analytical chemistry, enables the identification of proteins in a complex mixture, such as cell lysate. By enriching for proteins bound to a target of interest or ones with a specific post-translational modification, signaling networks can be interrogated and novel targets identified[34]. Therefore, we carried out a MS study in our system with the aim of identifying potentially unknown downstream targets of ephrin-B2:EphB4 signaling that transduce ephrin-B2 stimulation into neurogenesis.

To investigate downstream signaling by MS, we took two approaches. First, as Eph:ephrin signaling initiates phosphorylation cascades, we examined the phosphoproteome of ephrin-B2 stimulated EphB4-mCh NSCs. HyA:ephrin-B2 was chosen for the MS studies as it had previously induced more diverse and intense signaling than Fc-ephrin-B2. EphB4-mCh NSCs were stimulated for 45 min with HyA:ephrin-B2 or left untreated (timing was based the on time course study), lysed, and then subjected to immunoprecipitation (IP). Phosphoproteins were captured with a pTyr antibody, bound to Protein A/G agarose, and then eluted with a low pH

glycine buffer. Samples were then trypsin digested, desalted, and sent for MS analysis. Peptides were identified by screening against a rat proteome database, and spectral counts of identified proteins were compared between stimulated and untreated groups (see *Materials and Methods*). As a confirmation of experimental design and analysis, EphB4 was more prevalent in ephrin-B2 stimulated samples, as was Src, a previously identified target. Three rounds of MS were performed, and proteins more abundant in ephrin-B2 treated cells in at least two data sets were determined to be upregulated, while proteins less abundant were determined to be downregulated (Tables C.1 and C.2).

Second, to gain more detailed insight into immediate signaling, we probed binding partners of EphB4 in ephrin-B2 stimulated cells. As the commercially available EphB4 antibodies we tested lacked specificity and sensitivity, we developed a FLAG-tagged EphB4-overexpressing NSC line (EphB4-FLAG NSCs) to enable efficient and specific pull-down. EphB4-FLAG NSCs were stimulated for 30min with HyA:ephrin-B2 or left untreated to capture early binding, and then lysed. EphB4-FLAG and interacting proteins were then captured using Anti-FLAG agarose and eluted by 3× FLAG peptide. Samples were prepared and analyzed by MS as described above. Again, three rounds of MS were performed, and upregulated and downregulated proteins were determined to be those more or less abundant, respectively, in ephrin-B2 stimulated cells in two out of three data sets (Tables C.3 and C.4).

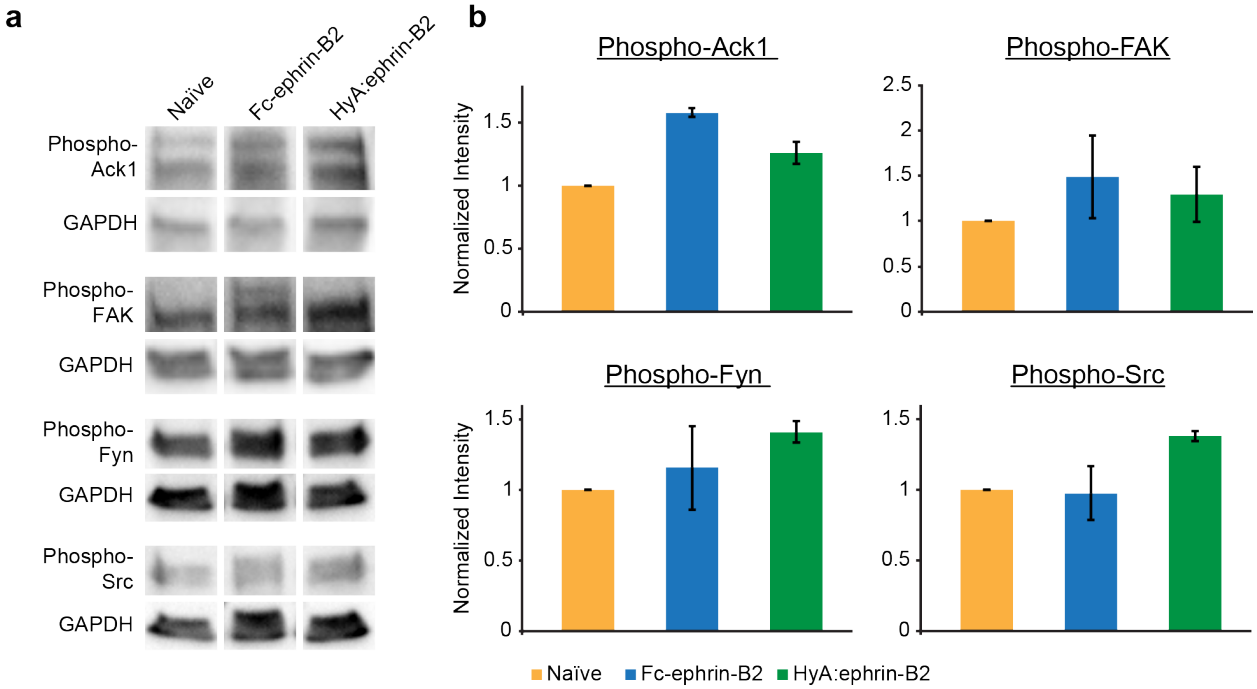

Figure 4.4. Validation of MS results. (**a**) Western blots for phosphorylated proteins chosen from MS analysis of pTyr IPs. EphB4-mCh NSCs were stimulated for 45 min with Fc-ephrin-B2 or Hy:ephrin-B2 then probed. (**b**) Quantification of western blots from (**a**) by densitometry analysis. Phospho-protein expression was normalized to GAPDH, then ephrin-B2 stimulated levels were then normalized to naïve expression levels. n = 2 blots, error bars are ± s.d..

MS analysis revealed many proteins upregulated by ephrin-B2 stimulation in pTyr IPs. Of these, we chose four for further analysis: activated Cdc42 kinase 1 (Ack1/ Tnk2), focal adhesion kinase (FAK/ Ptk2), Fyn proto-oncogene (Fyn), and Src (Table C.1). These targets were selected for a

couple of reasons: (i) they are kinases, thus representation in pTyr IPs was logical; and (ii) they have been shown to be activated by Eph:ephrin signaling, w.g. FAK, Fyn, and Src[32,35,36], or other receptor tyrosine kinases, e.g. Ack1[37]. Results from EphB4-FLAG pull-downs were less enticing, thus none of the upregulated or downregulated targets from these data sets were studied further.

To confirm upregulation of Ack1, FAK, Fyn, and Src activity, EphB4-mCh NSCs were stimulated with Fc-ephrin-B2 or HyA:ephrin-B2 for 45 min, and then probed by western blot. All four proteins exhibited increased phosphorylation levels in response to ephrin-B2 (Fig. 4.4). Therefore, the MS results were verified and the chosen targets were interrogated further.

Genetic knockdown of Ack1, Fyn, and Src inhibits ephrin-B2-induced neurogenesis

To investigate the role of Ack1, FAK, Fyn, and Src in ephrin-B2-induced NSC neuronal differentiation, we utilized the increasingly popular technique of Clustered Regularly Interspaced Short Palindromic Repeats (CRISPR)/Cas9 genome engineering to develop NSC lines with our targets of interest knocked down. This tool can be employed to cut virtually any genomic sequence in a cell or tissue by expressing both the Cas9 endonuclease and a guide RNA (gRNA) to direct the Cas9 to target DNA. Nuclease activity results in double-strand breaks, leading to subsequent mutations and knockdown of target protein. The most common CRISPR/Cas9 system, and the one we apply here, utilizes Cas9 derived from *S. pyogenes* (SpCas9) and gRNA targeting a 20 nucleotide sequence upstream of a Protospacer Adjacent Motif (PAM) recognized by SpCas9[38]. To knockdown Ack1, FAK, Fyn, and Src, five gRNAs were designed against each target, designated Ack1-1 – 5, FAK-1 – 5, etc. (Table 4.1). gRNAs directed towards Ack1, Fyn, and Src were all targeted to exon 1, while FAK gRNAs were directed to both exon 1 and 2 due to limited suitable sites in exon 1. Five gRNAs were designed to ensure successful targeting. Additionally, gRNAs were designed against both the sense and antisense DNA strands to increase variability and likelihood of success.

Table 4.1. gRNAs for CRISPR/Cas9 knockdown of signaling targets. Five guide RNAs (gRNAs) were designed and tested against rat Ack1, FAK, Fyn, and Src. Each gRNA targeted a 20 nucleotide sequence in exon 1 or 2 of the target genomic sequence, and was immediately upstream of a PAM (underlined) recognized by SpCas9.

Ack1		**FAK**	
Ack1-1	GGAGGGAACAGGCTGGCTGCTGG	FAK-1	GACTCACCTGGGTACTGGCACGG
Ack1-2	GCTGCTGGAGCTGCTGTCTGAGG	FAK-2	GGAACGGTCCCCTGGTGCAATGG
Ack1-3	CCGAGATGACCTCAACATTACCC	FAK-3	GCAGTAATGAGCCAACCACCTGG
Ack1-4	GTATGTCAAAAACGAAGACCTGG	FAK-4	CCAGTATTATCAGGCATGGAGAC
Ack1-5	GACCTGGAAAAGATTGGCATGGG	FAK-5	GGGAATCATTCAGAAGATAGTGG
Fyn		**Src**	
Fyn-1	GGCAGCCTGAACCAGAGCTCTGG	Src-1	CCAAGGACGCCAGCCAGAGGCGC
Fyn-2	CCGCTATGGCACAGACCCCACCC	Src-2	GCGCCGCAGCCTGGAGCCCGCGG
Fyn-3	CCCCTCAGCACTACCCCAGCTTC	Src-3	GCCTCCGCCGATGGCCACCGCGG
Fyn-4	CCATCCCGAACTACAACAACTTC	Src-4	CCCCGCGGCCGCCGAGCCCAAGC
Fyn-5	GGCCAGGGACTCACGGTCTTTGG	Src-5	GTCACCTCCCCACAAAGGGCGGG

All of the gRNAs (20 in total) were synthesized and cloned into a CRISPR/Cas9 lentiviral plasmid, which enabled expression of both SpCas9 and gRNA from one vector[39]. To examine genomic targeting, a Cel 1 nuclease assay was performed[40]. Briefly, in this assay, genomic DNA was isolated, the region of interest was amplified, and this product finally melted and re-annealed to form heteroduplexes between naïve and potentially cut amplicons. Samples were then treated with a nuclease that cuts only at mismatched DNA, so if target sites were cut and subsequently mutated by Cas9, banding patterns would seen in a gel of assayed products. As the production of lentiviruses is time-consuming and costly, we first tested the constructs in C6 glioma cells ,an easily transfectable rat cell line (Fig. 4.5a). Src-targeting gRNAs were the first group tested. C6 cells were transfected with Src-1 – 5 Cas9 vectors then assessed for cutting by the Cel 1 assay. Analysis showed cutting efficiencies in Src-3 and Src-4 transfected cells at levels of 8.1% and 18%, respectively (Fig. 4.5a*i*). These results were positive but cutting efficiencies were lower than expected, so in subsequent testing, C6 cells were co-transfected with a Cas9 vector and a fluorescent plasmid. Transfected cells were enriched for by fluorescence-activated cell sorting (FACS), then the Cel 1 assay was performed. By this method, Ack-1 – 5, FAK-1 – 5, and Fyn-1, -2,&-4 showed high levels of cutting in the range of 31% – 62% (Fig. 4.5a*ii-iv*). The low cutting efficiencies of the Src vectors, therefore, were likely due to poor transfection of C6 cells, an obstacle overcome by performing FACS prior to analysis. Overall, 15/20 vectors tested showed genomic cutting at their target sites.

The two most efficient vectors at genomic cutting of each target, as determined by testing in C6 cells, were chosen for further analysis in NSCs. These constructs encoded gRNAs Src-3&-4, Ack-1&-4, FAK-2&-5, and Fyn-1&-2. Lentiviruses were produced, and NSCs were infected at low multiplicities of infection (MOIs < 1) to minimize potential off-target effects. After transduction, infected NSCs were selected with puromycin, and then assessed for genomic cutting with the Cel 1 assay. All of the NSC lines showed cutting efficiencies greater than 50% (Fig. 4.5b*i-iv*), demonstrating robust activity. Of note, NSCs, not EphB4-overexpressing NSCs, were used for these and subsequent studies as ephrin-B2 does mediate neurogenesis in untransduced NSCs. Additionally, demonstrating activity of the chosen signaling targets in NSCs with basal levels of EphB4 expression would provide further validation for the use of the EphB4-mCh NSC line in the previously described signaling studies and MS analysis. Finally, one NSC line for each signaling target was chosen for biological studies. Src-3, FAK-2, and Fyn-1 NSC lines were selected as they displayed the highest levels of genomic cutting. The Ack1-1 NSC line was selected because, although the Ack1-4 NSCs showed slightly more efficient cutting, the Ack1-4 lentivirus did not package well and only enough NSCs survived puromycin selection to perform the Cel 1 assay. To confirm knockdown of target signaling proteins in the NSC lines, western blots were performed. Src-3, FAK-2, and Fyn-1 NSCs showed 70%, 45%, and 58% target knockdown, respectively (Fig. 4.5c*i,iii,iv*). Unfortunately, target knockdown in Ack1-1 NSCs was unquantifiable as the Ack1 antibody was highly unspecific (Fig. 4.5c*ii*). In summary, using CRISPR/Cas9 technology, a knockdown NSC line for each signaling target chosen from the MS analysis (Ack1, FAK, Fyn, and Src) was developed and characterized.

To determine if Ack1, FAK, Fyn, and Src mediate ephrin-B2-induced NSC neurogenesis, the NSC knockdown lines were assessed for differentiation. As a control, an empty lentivirus encoding spCas9 but no gRNA was produced and an “empty” NSC line was developed.

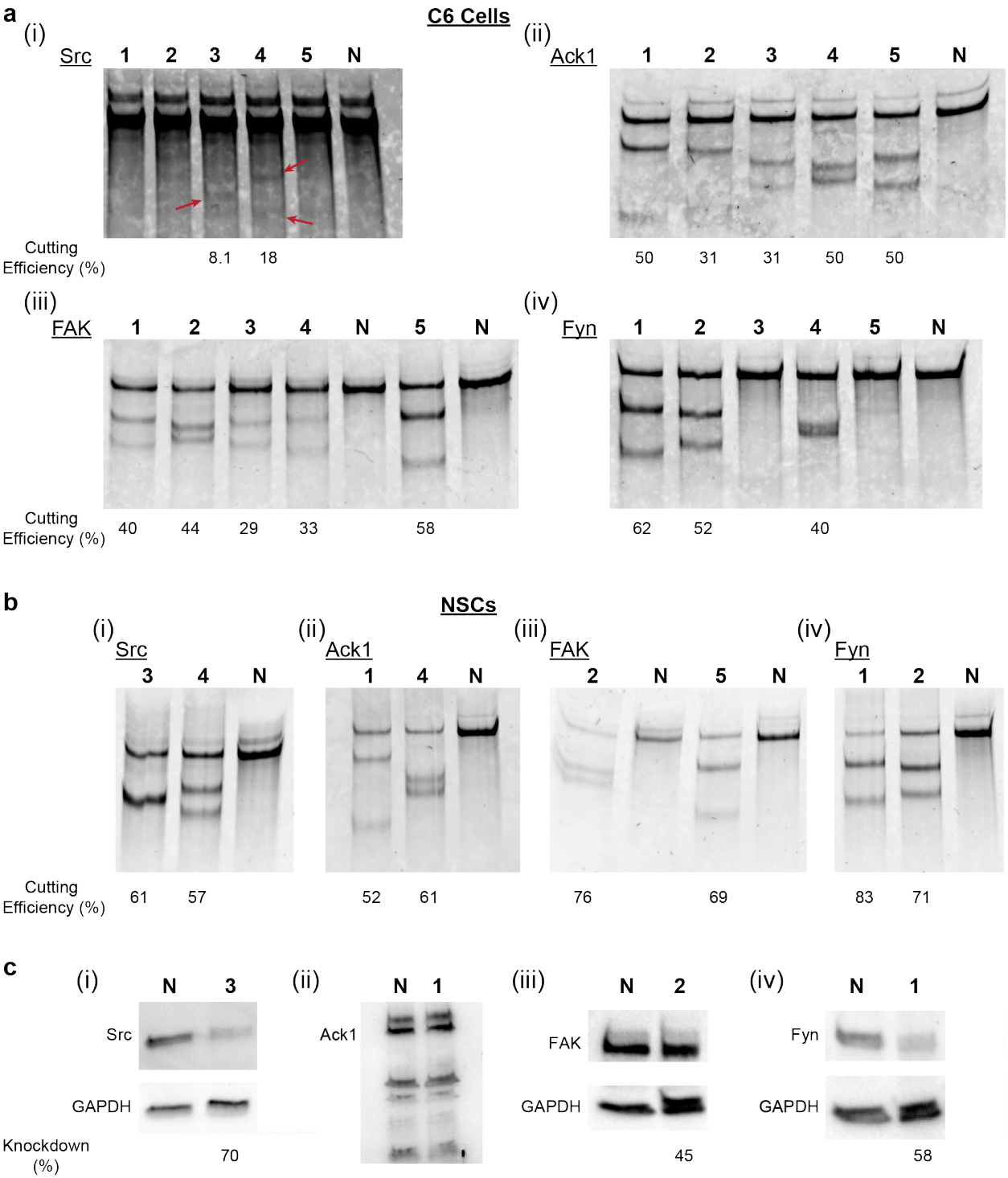

Figure 4.5. Characterization of Cas9 constructs and NSC knockdown lines. (**a**) Cel 1 assays for genomic cutting in C6 cells transfected with vectors encoding SpCas9 and gRNAs directed at signaling targets. (i) To test Src-targeted constructs, C6 cells were transfected and then assayed. (ii-iv) Subsequently, to test Ack1, FAK, and Fyn-targeted constructs, C6 cells were co-transfected with a fluorescent plasmid, enriched by FACS, then assayed. (**b**) (i-iv) Cel 1 assays of NSCs infected with lentiviruses expressing SpCas9 and the two most efficient gRNAs from (**a**) directed at each signaling target. NSCs were infected at MOI < 1, puromycin-selected, then analyzed. (**c**) Western blots for target protein levels in the final Cas9-mediated NSC knockdown lines. Cutting efficiency and knockdown were quantified by densitometry analysis. Cutting efficiency was measured as the percent of total product that was

cut. Knockdown was measured by first normalizing target expression levels to GAPDH, then comparing infected NSCs to untransduced NSCs.

Untransduced, empty, Ack1-1, FAK-2, Fyn-1, and Src-2 NSC were stimulated with HyA:ephrin-B2 for 5 days, and then analyzed by immunostaining for neuronal and astrocytic differentiation (Fig 4.6a,b). Empty NSCs exhibited levels of differentiation similar to untransduced NSCs, indicating that Cas9 expression by itself had no effect. FAK-2 NSC neurogenesis was similarly unaffected. Ack1-1, Fyn-1, and Src-3 NSCs, however, displayed significantly decreased ephrin-B2-induced neuronal differentiation compared to empty NSCs (Fig 4.6a). Additionally, trends of increased astrocytic differentiation in both naïve and ephrin-B2 stimulated FAK-2 and Fyn-1 NSCs were apparent, though not significant (Fig. 4.6b). To investigate if the signaling targets more broadly mediated NSC differentiation, all of the NSC lines were cultured in mixed differentiation media (RA/FBS) for 5 days and then analyzed (Fig 4.6c,d). Empty NSC, as well as Ack1-1, FAK-2, and Src-3 NSCs, exhibited levels of neuronal and astrocytic differentiation similar to untransduced NSCs. Fyn-1 NSCs, though, displayed significantly decreased neurogenesis compared to empty NSCs (Fig. 4.6c). Therefore, our results demonstrate a requirement for Ack1, Fyn, and Src signaling in ephrin-B2-induced NSC neurogenesis. Furthermore, Fyn additionally mediates RA-induced neuronal differentiation, suggesting a broad role for this kinase in NSC neurogenesis.

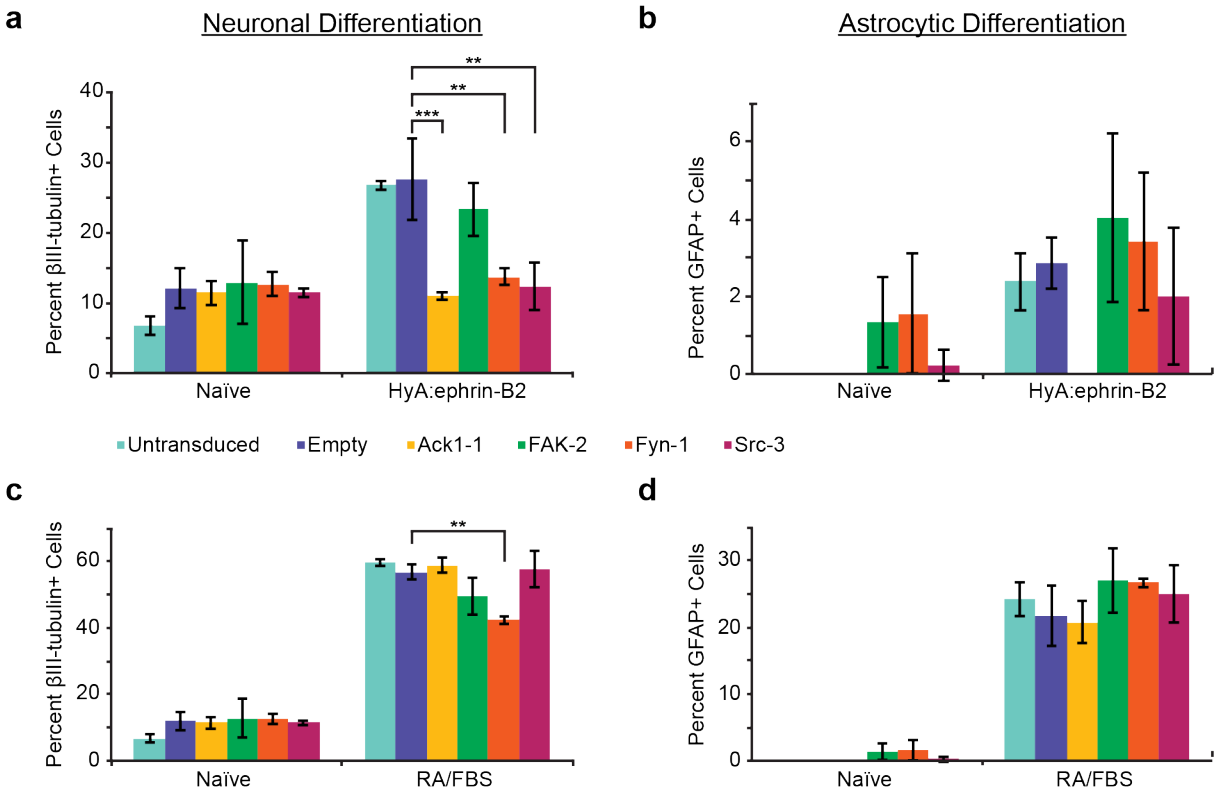

Figure 4.6. Differentiation of NSC knockdown lines. (**a-d**) Quantification of immunostaining for differentiation in untransduced, empty, and knockdown NSC lines after 5 days of stimulation with HyA:ephrin-B2 (**a,b**) or RA/FBS (**c,d**) for percent neurons (βIII-tubulin+/ DAPI) (**a,c**) and astrocytes (GFAP+/ DAPI) (**b,d**). *P < 0.5, **P < 0.005, ***P < 0.0005 by ANOVA and Tukey-Kramar multiple comparison, n = 3 experimental replicates. All error bars are ± s.d.

4.3 Discussion

Ephrin-B2 was recently found to be a neurogenic factor in the adult hippocampal NSC niche[18]. In this study, we investigated the signaling pathways mediating ephrin-B2 transduction in NSCs to gain further insight into this novel mechanism of neurogenesis. Through the development of an EphB4-overepxressing NSC line, MS analysis of the ephrin-B2 stimulated phosphoproteome, and CRISPR/Cas9 directed knockdown of putative signaling targets, we discovered three kinases required for ephrin-B2-induced neurogenesis: Ack1, Fyn, and Src.

NSCs expressing basal levels of EphB4 did not allow for the interrogation of downstream signaling by traditional biochemical analysis (i.e. western blots), so the development of an EphB4-overexpressing NSC line was needed. To enable creation of this line, EphB4 was amplified from NSC cDNA, resulting in the first published sequence of rat EphB4. Questions could be raised regarding the use of these NSCs in signaling studies, as the expression levels of EphB4 were much higher than untransduced NSCs, but targets identified by western blot and MS were validated in knockdown lines, so potential concerns were alleviated.

Studies in EphB4-mCh NSCs revealed discrepancies in downstream signaling between Fc-ephrin-B2 and HyA:ephrin-B2 stimulation, regarding both temporal dynamics and specific targets. This differential signaling warrants further investigation, as understanding this phenomenon could reveal novel spatial and mechanical regulatory mechanisms of Eph:ephrin signaling, as well as potentially inform the development of more potent engineered ligands. One hypothesis is that the two oligomerized forms of ephrin-B2 differentially impact EphB4 endocytosis. Endocytosis is a well studied mechanism of Eph:ephin signaling and regulation[41]. For example, ephrin-B2-induced cortical growth cone collapse was recently shown to be dependent on clathrin-mediated EphB2 endocytosis[42]. Additionally, studies on the epidermal growth factor receptor (EGFR) have demonstrated sustained EGF-induced signaling when EGFR internalization is prevented by stimulation with tethered EGF, as opposed to soluble EGF[43]. Similarly, HyA:ephrin-B2 is a stable, multivalent molecule, which induces large, multimeric EphB4 clusters[19]. Therefore, HyA:ephrin-B2 may prevent or delay endocytosis to a greater extent than Fc-ephrin-B2, resulting in the stronger and more sustained downstream signaling observed.

The MS analysis of pTyr IPs and EphB4-FLAG pull-downs in response to ephrin-B2 stimulation resulted in a rich data set. Here, we focused on four kinases upregulated in the pTyr IPs, however, many additional findings are worthy of further study. For example, a number of other kinases were upregulated, including breast cancer anti-estrogen resistance 1 (Bcar1) and embryonal Fyn-associated substrate (Efs). These proteins have known interactions with the studied kinases, including Fyn and Src[44], so future work could also explore their roles in ephrin-B2 signaling and induced neurogenesis. A second interesting discovery was the downregulation of other Eph family members in the EphB4-FLAG pull-downs. Previous studies have demonstrated Eph hetero-oligomerization in response to stimulation[45]. These findings, however, suggest that in a naïve state, EphB4 associates with other Eph family members, and upon ephrin-B2 binding, these interactions cease as EphB4 homo-oligomerizes. Of note though, Eph cross-family associations in the naïve cells may have been due to the high level of EphB4

overexpression, so additional studies are needed before conclusions can be drawn regarding Eph homo- and hetero-interactions in this system.

CRISPR/Cas9 technology was successfully utilized to develop Ack1, FAK, Fyn, and Src knockdown NSC lines. This is the first reported application of CRISPRs in NSCs. All of the lentiviruses encoding Cas9 and gRNA that packaged well resulted in high cutting efficiencies and substantial protein target knockdown, demonstrating the robustness of this tool and its usefulness for future NSC studies.

Knockdown of the kinases Ack1, Fyn, and Src significantly reduced ephrin-B2-induced NSC neurogenesis, demonstrating a requirement for these signaling molecules in transducing ephrin-B2 stimulation into neuronal differentiation. Src is a well-known Eph signaling target[32,46] and Fyn activity has been demonstrated in a few studies[46,47], however to the best of our knowledge, Ack1 has not been previously implicated in Eph:ephrin signaling. In NSCs and more broadly in the CNS, these kinases have also been studied to varying degrees. Src mediates a number of processes, including NSC differentiation in response to extracellular matrix stiffness[48] and embryonic NSC proliferation[49]. Fyn has not been implicated in NSC function, but does play a role in oligodendendrocyte precursor cell (OPC) differentiation[50] and axonal outgrowth[51]. Ack1, similarly, has no known function in NSCs, but regulates neurite outgrowth[52] and promotes tumorigenesis in many cancers, including gliomas[53]. Therefore, our finding of Ack1, Fyn, and Src activity in ephrin-B2-mediated NSC neurogensis reveals novel pathways in both Eph:ephrin and NSC signaling.

Future work into the signaling mechanisms of Ack1, Fyn, and Src in NSCs will further illuminate these novel pathways, and potentially uncover additional unknown neurogenic signals. A number of signaling nodes warrant further investigation. First, the signaling cascades transducing ephrin-B2 stimulation through the studied kinases could be dissected. Topics of investigation would include the mechanism of interaction with EphB4 (i.e. direct or indirect), and whether the kinases cross-talk with one another or propagate signals through unrelated pathways. Second, direct β-catenin activation downstream of ephrin-B2 has been noted, so interactions between the kinases and canonical Wnt signaling could be investigated. Third, Ack1, Fyn, and Src-mediated upregulation of the neuronal transcription factors *NeuroD1* and *Mash1* could be analyzed. Finally, the potential role of these kinases in ephrin-B2-indpendent NSC differentiation merits further exploration. Knockdown of Fyn impaired RA-induced neurogenesis, so Ack1, Fyn, and Src may signal downstream of other neurogenic stimuli, such as Wnt3a.

In summary, in this study we investigated the signaling pathways mediating ephrin-B2-induced NSC neurogenesis. We identified three kinases by MS analysis of an EphB4-overxpressing NSC line required for transducing ephrin-B2 stimulation: Ack1, Fyn, and Src. Ack1 is a novel component of Eph:ephrin signaling; and, Ack1 and Fyn are novel regulators of NSC function. These findings expand upon our limited understanding of NSC differentiation mechanisms and point to potential targets for future therapeutic intervention.

4.4 Materials and Methods

Cell culture

Neural stem cells (NSCs) were isolated from the hippocampi of adult female Fisher 344 rats[54] and cultured in 1:1 Dulbecco's Modified Eagle Medium: Nutrient Mixture F-12 (DMEM:F12, Life Technologies) supplemented with N-2 (Life Technologies) and 20 ng/mL recombinant human FGF-2 (PeproTech). NSCs were cultured on tissue culture-treated polystyrene plates coated with 10 μg/mL polyornithine (Sigma-Aldrich) and 5 μg/mL laminin (Life Technologies), and subcultured at 80% confluency using Accutase (Life Technologies) for cell detachment.

C6 rat glioma cells were cultured in DMEM (Corning) with 10% bovine calf serum (BCS, Life Technologies) and 1% penicillin/streptomycin (P/S) (Life Technologies). C6 cells were cultured on tissue culture-treated polystyrene plates and subcultured at 90% confluency using Trypsin - Ethylenediaminetetraacetic acid (EDTA) 1× (Corning).

EphB4-mCh NSC and EphB4-FLAG NSC line development

The EphB4-mCherry NSC line was created through stable retroviral infection. Total RNA was extracted from NSCs using TRIzol reagent (Life Technologies) and then full-length cDNA transcripts were synthesized from 5 μg RNA using the ThermoScript™ RT-PCR System for First-Strand cDNA Synthesis with Oligo$(dT)_{20}$ primers (Life Technologies) according to manufacturer's instructions. The rat EphB4 gene was amplified from the cDNA using the primer pair: forward, 5'-CCATGGAGCTCAGAGCGC-3'; reverse, 5'-GGTCAGAACTGCTGGGTTGG-3', and then inserted into a subcloning vector using a TOPO TA Cloning Kit (Life Technologies). EphB4 was then amplified with the linker GSGS and inserted into the pmCherry-N1 Vector (Clontech) between Nhe1 and Age1 sites, to produce pEphB4-mCherry. Finally, EphB4-mCherry was amplified and inserted into the MMLV retroviral vector CLPIT[55] between Sfi1 and Pme1, resulting in CLPIT-EphB4-mCherry, which was then packaged, purified, and titered on NSCs as previously described[56]. NSCs were infected with the virus at MOI = 1, and a stable cell line was produced by selection in 0.6 μg/mL puromycin (Sigma-Aldrich) for 96 h.

EphB4-FLAG was created by PCR amplifying EphB4 out of CLPIT-EphB4-mCherry with the addition of a 3' GSGS linker and a FLAG peptide (DYKDDDDK) using the primer pair: forward, 5'-GCTAGGGCCGCCTCGGCCGCCACC-3'; reverse: 5'-GCTAGGTTTAAACCTACTTGTCATCGTCGTCCTTGTAATCTGAGCCGCTTCCGAACTG CTGGG-3'. EphB4-FLAG was then re-inserted into CLPIT between Sfi1 and Pme1, resulting in CLPIT-EphB4-FLAG. Retroviral production and NSC line creation were carried out as above.

CRISPR/Cas9 vector construction and cell line development

Oligonucleotides encoding gRNAs and BsmB1 restriction sites of the form: forward, 5'-CACCG-(20nt_gRNA)-3'; reverse, 5'AAAC-(20nt_gRNA_reverse_complement)-C-3', were synthesized (Elim Biopharmaceuticals). Oligonucleotide pairs were dephosphorylated and annealed at 1 uM with T4 Polynucleotide Kinase (New England BioLabs) in T4 DNA Ligase Reaction Buffer (New England BioLabs) for 30 min at 4°C, then incubated for 5 min at 95°C to inactivate the enzyme. Annealed oligonucleotides were then diluted 1:25 and 1 uL was ligated into 10 ng of BsmB1-digested lentiCRISPR v2[57] (Plasmid #52961, Addgene). Lentiviruses were

packaged and purified as previously described[56]. NSCs were infected and stable cell lines were generated by selection in 0.6 μg/mL puromycin for 96 h. Infections were estimated to be at MOIs < 1 as less than 50% of NSCs survived selection.

Cel 1 assay

For initial validation studies, C6 glioma cells were seeded in 24-well culture plates at 2×10^5 cells per well in DMEM with 10% BCS and 1% P/S. The following day, cultures were switched to P/S free media and then transfected using Lipofectamine® 3000 Transfection Reagent (Life Technologies) with 800 ng Cas9 vector for Src-1 – 5 testing, or co-transfected with 800 ng Cas9 vector and 50 ng pAAV GFP[58] for Ack-1 – 5, FAK-1 – 5, and Fyn-1 – 5 testing. 3 days post-transfection genomic DNA was isolated using QuickExtract™ DNA Extraction Solution (Epicentre). For Src samples, DNA was extracted from the bulk transfected C6 cell population. For Ack1, FAK, and Fyn testing, FACS was performed at the Flow Cytometry Facility at UC Berkeley to isolate GFP+ transfected C6 cells, and DNA was then extracted from this population.

For characterization of cutting in NSC lines, genomic DNA was extracted using QuickExtract™ DNA Extraction Solution after puromycin selection was completed.

Target sites were amplified by nested PCR using the primers listed in Table 4.2. To measure cutting efficiency, Cel 1 assays were performed using a Surveyor® Mutation Detection Kit (Integrated DNA Technologies) according to manufacturer's instructions. Digested products were then run on a TBE-PAGE gel using standard methods, and digitally imaged on a ChemiDoc XRS+ Imaging System (BioRad). Densitometry analysis was performed in Image Lab software (BioRad).

Table 4.2. Primers for nested PCR of genomic targets.

gRNA	PCR Step	Forward Primer	Reverse Primer
Ack1-1 − 5	External	CTTACTGCATCTGTGTTGAGAGCG	CAATTAGCTCTGAGTGGTCACAGC
	Internal	GTGCTTTGAGTTCTGTAGGATGTGG	TTACAACCAAACCATTCCCTGGG
FAK-1 − 4	External	AGAGAGAGCACAGTGATTGTGTGG	TGCTGGGGAATCAAACACAAAGC
	Internal	GACTAGAGAACAGTGTTTGTGACAC	AGAAAGAAAAGGTTAACATTTCTGC
FAK - 5	External	TTAAGATTTCCCATAACGGCTGG	CAAAGACCATGAAAGGAGACAAGG
	Internal	CAGATACACAGGCAGGCAAAACC	CTACTGCTAATTTCCTCTACACAGG
Fyn-1 − 5	External	TCATCGAGGGAAGTTGTACCTGG	AGTTTGATCCCTGGAGAGATCCC
	Internal	CTTTGGCCCTATTTTAGTCGGCC	CTCCTGGAAGTTGTCCTCCAACC
Src-1 − 5	External	TATCTGTAGCTGTGTCCTAAGGCG	CTAGTCCATGGTGGTCCTTCTCC
	Internal	TGCCTATCTGTTTAGTGGGTAGGG	GTTTACGAGCCCTTCTCCATTCG

Fc-ephrin-B2 and HyA:ephrin-B2 synthesis

Antibody clustered ephrin-B2 was generated by incubating recombinant mouse ephrin-B2/Fc (R&D Systems) with a goat anti-human IgG Fc antibody (Jackson ImmunoResearch) at a 1:9 ratio (wt/wt) for 90 min at 4°C.

HyA:ephrin-B2 was synthesized as previously described[19,59]. Briefly, the extracellular domain of mouse ephrin-B2 with a C-terminal hexahistidine tag and cysteine (ephrin-B2-cys) was inserted

into the bacterial expression plasmid pBAD (ThermoFisher Scientific). Protein expression was induced with 0.1% (w/v) L-arabinose (Sigma-Aldrich) for 5 h. Ephrin-B2-cys was then purified by immobilized metal affinity chromatography (IMAC) on a BioLogic^{TM} DuoFlow Chromatography System (BioRad) with a Bio-Scale Mini Profinity IMAC Cartridge (BioRad). 800 kDa HyA (LifeCore Biomedical) at 3 mg/mL was activated with 1.2 mg/mL N-ε-maleimidocaproic acid hydrazide (EMCH, ThermoFisher Scientific), 2.8 mg/mL Sulfo-N-hydroxysulfosuccinimide (Sulfo-NHS, ThermoFisher Scientific, and 10 mg/mL 1-ethyl-3-(3-dimethylaminopropyl)carbodiimide hydrochloride (EDC, ThermoFisher Scientific) in 0.1 M 2-(N-morpholino)ethanesulphonic acid (MES) buffer, pH 6.5 (Sigma-Aldrich) at 4°C for 4 h. Activated HyA was then dialyzed into phosphate-buffered saline (PBS), pH 7.0 with 10% glycerol and 2 mM EDTA. Ephrin-B2-cys was reduced with 200-fold molar excess tris(2-carboxyethyl)phosphine hydrochloride (TCEP) (ThermoFisher Scientific) at 4°C for 5 min. Reduced ephrin-B2-cys was then added to activated HyA at a molar ratio of 40:1 and allowed to react at 4°C overnight. HyA:ephrin-B2 was finally dialyzed into PBS, pH 7.0 with 2 mM EDTA. Ephrin-B2-cys and HyA:ephrin-B2 protein concentrations were determined by bicinchoninic acid (BCA) assay (ThermoFisher Scientific).

Differentiation, immunostaining, and microscopy

For the differentiation studies, NSCs (or NSC lines) were seeded in 96-well culture plates at 5×10^3 cells per well in DMEM/F12+N2 supplemented with 0.5 ng/mL FGF-2 and 0.5× P/S. The following day, a half-media change was performed and cells were stimulated with 10 μg/mL (200nM) Fc-ephrin-B2, 200 nM HyA:ephrin-B2, or 1 μM RA (Enzo Life Sciences) and 2% FBS (Life Technologies). Differentiation was carried out for 5 days with two additional half-media changes containing 2× stimulants on days 2 and 4.

For differentiation studies, cell cultures were fixed with 4% paraformaldehyde for 15 min, and then blocked and permeabilized with staining buffer (5% donkey serum (Sigma-Aldrich) with 0.3% Triton X-100 in PBS) for 30 min. Cultures were incubated for 24 - 48 h at 4°C with mouse anti-βIII-tubulin (1:500, T8578, Sigma-Aldrich) and rabbit anti-GFAP (1:500, ab7260, Abcam) in staining buffer; followed by a 2 h incubation with Alexa Fluor 488-labeled donkey anti-mouse IgG (1:1250, 715-545-151, Jackson ImmunoResearch) and Cy3-labeled donkey anti-rabbit IgG (1:1250, 711-165-152, Jackson ImmunoResearch) in staining buffer; and finally a 20 min incubation with 4,6-diamidino-2-phenylindole (DAPI) as a nuclear counterstain (5 μg/mL, Life Technologies).

For EphB4-mCh NSC characterization, cell cultures were similarly immunostained with goat anti-EphB4 (1:20, AF446, R&D Systems), Alexa Fluor 647-labeled donkey anti-goat IgG (1:1250, 705-605-147, Jackson ImmunoResearch), and DAPI.

Immunostained cultures were imaged on an ImageXpress Micro (IXM) high content imager at 20× magnification using DAPI, FITC, Cy3, and Cy5 filter cubes (Molecular Devices). Images were processed and analyzed in ImageJ (National Institutes of Health).

Western blotting

For the signaling studies, NSCs or EphB4-mCh NSCs were seeded in polyornithine/ laminin coated six-well culture plates at 3×10^5 cells per well in standard media conditions. The

following day, cultures were switched to low FGF-2 (0.5 ng/mL) media conditions, and then stimulated for signaling studies 16 h later with 200 nM Fc-ephrin-B2 or HyA:ephrin-B2 for the indicated times.

For Ack1, FAK, Fyn, and Src knockdown NSC line characterization, cells were seeded at 3×10^5 cells per well in six-well culture plates in standard media conditions and lysed the following day.

Cells were lysed in RIPA buffer (50 mM Tris, 150 mM NaCl, 1% NP-40, 0.5% sodium deoxycholate, 0.1% sodium dodecyl sulfate (SDS), pH 8) containing protease and phosphatase inhibitor cocktails (ThermoFisher Scientific). Cell lysates of equal total protein concentrations determined by BCA assay were mixed with 5x Laemmli buffer (final 50 mM Tris, 2% SDS, 0.1% Bromophenol Blue, 10% glycerol), 2-mercaptoethanol was added to 10% v/v, and samples were boiled at 95°C for 5 min. Samples were electrophoretically separated on SDS-PAGE gels of between 8 and 12%T and transferred onto nitrocellulose membranes using standard methods. Blots were blocked for 1 h in tris-buffered saline (TBS) with 0.1% Tween-20 (TBS-T) and 3% bovine serum albumin (BSA) for phoshoprotein antibodies or 5% Blotting Grade Blocker (BioRad) for all other antibodies. Blots were probed overnight at 4°C with primary antibodies in the same blocking buffer: rabbit anti-Ack1 (1:1000, PA5-14765, ThermoFisher Scientific), rabbit anti-phospho-Ack1 (1:500, PA5-37782, ThermoFisher Scientific), rabbit anti-phospho-Akt (1:2000, 4060, Cell Signaling), rabbit anti-β-catenin (1:1000, 9562, Cell Signaling), rabbit anti-non-phospho (Active)-β-catenin (1:1000, 8814, Cell Signaling), goat anti-EphB4 (1:1000, AF446, R&D Systems), rabbit anti-ERK (1:1000, 4695, Cell Signaling), rabbit anti-phospho-ERK (1:2000, 4370, Cell Signaling), rabbit anti-FAK (1:1000, 3285, Cell Signaling), rabbit anti-phospho-FAK (1:1000, ab81298, Abcam), rabbit anti-Fyn (1:1000, ab125016, Abcam), rabbit anti-phospho-Fyn (1:1000, SAB4503872, Sigma-Aldrich), rabbit anti-GAPDH (1:2500, ab9485, Abcam), rabbit anti-phospho-MEK (1:1000, 9154, Cell Signaling), rabbit anti-phosphoserine (1:100, ab9332, Abcam), rabbit anti-phosphothreonine (1:1000, 9381, Cell Signaling), mouse anti-phosphotyrosine (1:1000, 9411, Cell Signaling), rabbit anti-phospho-PI3K (1:1000, 4228, Cell Signaling), mouse anti-Src (1:1000, 05-184, Millipore), rabbit anti-phospho-Src (1:1000, 2101, Cell Signaling); followed by 1 h incubation with appropriate horseradish peroxidase-conjugated secondary antibodies: mouse anti-goat HRP (1:5,000, 31400), goat anti-mouse HRP (1:10,000, 32430), goat anti-rabbit HRP (1:10,000, 32460), all from ThermoFisher Scientific. Protein bands were detected using SuperSignal West Dura Chemiluminescent Substrate (ThermoFisher Scientific), and blots were digitally imaged on a ChemiDoc XRS+ Imaging System. Blots were stripped in a solution of 3% acetic acid, 0.5 M NaCl, pH 2.5, for 10 min, neutralized with 0.5 M NaOH for 1 min, and then reprobed as needed. Blot densitometry analysis was performed in Image Lab software.

Quantitative reverse transcription polymerase chain reaction (qRT-PCR)

NSCs or EphB4-mCh NSCs were seeded in polyornithine/ laminin coated six-well culture plates at 3×10^5 cells per well in standard media conditions. The following day, total RNA was extracted using TRIzol reagent. cDNA transcripts were synthesized from 5 μg RNA using the ThermoScript™ RT-PCR System for First-Strand cDNA Synthesis with Random Hexamer primers (Life Technologies) according to manufacturer's instructions. Gene expression for EphB4 and ribosomal 18S was then quantified with Sybr Green (Life Technologies) detection on an iQ5™ Real-Time PCR Detection System (BioRad) by standard methods. The primer sets

were: EphB4_1: forward, 5'-CATCAAGGTGGACACAGTGG-3'; reverse, 5'-AAAGAGATGCAAGGAGAGCA-3'[60]; EphB4_2: forward, 5'-AAGTTCCCTGGGAGGAAAGA-3'; reverse, 5'-CATTGATCACGTCCTGGTTG-3'; 18S: forward, 5'-GTAACCCGTTGAACCCCATTC-3'; reverse, 5'-CATCCAATCGGTAGTAGCGA-3'[61]. EphB4 gene expression levels were normalized to 18S before assessing cell line variation.

Mass spectrometry sample preparation

EphB4-mCh NSCs or EphB4-FLAG NSCs were seeded in polyornithine/ laminin coated 10 cm culture plates in standard media conditions. 4 × 10cm plates were seeded per experimental condition. Upon reaching 80% confluency, cultures were switched to low FGF-2 (0.5 ng/mL) media conditions, and then stimulated 16 h later with HyA:ephrin-B2 or left untreated. Stimulation times were 30 min for EphB4-FLAG NSCs and 45 min for EphB4-mCh NSCs. Cells were lysed in NP-40 buffer (50 mM Tris, 150 mM NaCl, 1% NP-40, pH 8) containing protease and phosphatase inhibitor cocktails. Cell lysates of equal total protein concentrations determined by BCA assay (4 – 10 mg/sample) were used in IPs and pull-downs described below.

For pTyr IPs, cell lysates were first pre-cleared with 20 µL Protein A/G Agarose (ThermoFisher Scientific) for 30 min rotating at 4°C. Phosphoproteins were then immunoprecipitated by incubating with 15 µL mouse anti-phosphotyrosine antibody overnight rotating at 4°C. Antibody:protein complexes were then captured by incubating with 25 uL Protein A/G agarose for 3 h rotating at 4°C. Finally, proteins were eluted 3× with 50 µL 0.1 M glycine, pH 2.6 buffer for 10 min, followed by 2× 50 µL TBS washes for 5 min, all while shaking at 5000 rpm at 30°C. To neutralize the low pH, 50 uL 2 M Tris, pH 8.5 buffer was added to the elution volume following the final glycine step.

For FLAG pull-downs, cell lysates were first pre-cleared with 20 µL Protein A/G Agarose for 30 min rotating at 4°C. FLAG-tagged proteins were then pulled-down by incubating with 25 uL Anti-FLAG® M2 Affinity Gel (Sigma-Aldrich) for 3 h rotating at 4°C. Finally, proteins were eluted 3× with 150 µL 500 µg/mL 3x FLAG® Peptide (Sigma-Aldrich) for 20 min shaking at 5000 rpm at 30°C.

To prepare eluted samples for mass spectrometry, urea and 1M Tris, pH 8.5 were added to final concentrations of 8 M urea and 100 mM Tris. 100 mM TCEP was then added to a final concentration of 5 mM and incubated for 20 min, followed by 500 mM iodoacetamide (Sigma-Aldrich) to a final concentration of 10 mM and incubated for 15 min protected from light. Samples were then diluted 4× with 100 mM Tris, pH 8.5, and 100 mM $CaCl_2$ was added to a final concentration of 1 mM. Finally, 1 µL 0.5 µg/mL mass spectrometry grade trypsin (Promega) was added and samples were incubated overnight at 37°C. The following day, formic acid was added to 5% and samples were desalted using C18 Spec tips (Agilent). Spec tips were washed with HPLC grade methanol (ThermoFisher Scientific) then 3× with 5% acetonitrile/5% formic acid. Samples were pushed through the Spec tip 2× and then washed 3x with 5% acetonitrile/5% formic acid. Finally, samples were eluted 2× with 80% acetonitrile/5% formic acid and dryed on a vacuum speed concentrator.

Mass spectrometry and analysis

Mass spectrometry was performed by the Vincent J. Coates Proteomics/Mass Spectrometry Laboratory at UC Berkeley. A nano LC column was packed in a 100 μm inner diameter glass capillary with an emitter tip. The column consisted of 10 cm of Polaris c18 5 μm packing material (Varian), followed by 4 cm of Partisphere 5 SCX (Whatman). The column was loaded by use of a pressure bomb and washed extensively with buffer A (see below). The column was then directly coupled to an electrospray ionization source mounted on a Thermo-Fisher LTQ XL linear ion trap mass spectrometer. An Agilent 1200 HPLC equipped with a split line so as to deliver a flow rate of 300 nL/min was used for chromatography. Peptides were eluted using a 8-step MudPIT procedure[62]. Buffer A was 5% acetonitrile/ 0.02% heptaflurobutyric acid (HBFA); buffer B was 80% acetonitrile/ 0.02% HBFA. Buffer C was 250 mM ammonium acetate/ 5% acetonitrile/ 0.02% HBFA; buffer D was same as buffer C, but with 500 mM ammonium acetate.

Protein identification and quantification were done with IntegratedProteomics Pipeline (IP2, Integrated Proteomics Applications) using ProLuCID/Sequest, DTASelect2 and Census[63-66]. Tandem mass spectra were extracted into ms1 and ms2 files from raw files using RawExtract 1.9.9[67] and were searched against *R. rattus* protein database plus sequences of common contaminants, concatenated to a decoy database in which the sequence for each entry in the original database was reversed[68]. The rat database was downloaded from ensembl.org on April 23, 2014; the version date of the database is February 4, 2014. LTQ data was searched with 3000.0 milli-amu precursor tolerance and the fragment ions were restricted to a 600.0 ppm tolerance. All searches were parallelized and searched on the VJC proteomics cluster. Search space included all fully tryptic peptide candidates with no missed cleavage restrictions. Carbamidomethylation (+57.02146) of cysteine was considered a static modification. We required 1 peptide per protein and both tryptic termini for each peptide identification. The ProLuCID search results were assembled and filtered using the DTASelect program (version 2.0)[63] with a peptide false discovery rate (FDR) of 0.001 for single peptides and a peptide FDR of 0.005 for additional peptide s for the same protein. Under such filtering conditions, the estimated false discovery rate was often zero and was never more than 0.67% at the protein level. Ensembl Protein IDs were converted to gene names using BioMart online software (www.biomart.org) and UniProt (www.uniprot.org).

Statistical analysis

Statistical analysis was performed in MATLAB (MathWorks). Statistical significance of the results was determined by analysis of variance (ANOVA) paired with a multiple comparison test (Tukey-Kramer method). All error bars represent ± standard error of the mean.

4.5 Acknowledgements

We acknowledge E. Connelly for experimental assistance with molecular biology, cell culture, immunostaining, and western blots; L. Kohlstaedt at the Vincent J. Coates Proteomics/Mass Spectrometry Laboratory at UC Berkeley for performing mass spectrometry and experimental guidance; M. West at the CIRM/QB3 Shared Stem Cell Facility (SSCF) for assistance with the IXM; H. Nolla at the Cancer Research Laboratory Flow Cytometry Facility at UC Berkeley for performing FACS; and T. Gaj for critical discussion regarding CRISPR/Cas9.

4.6 References

1. Lois, C. & Alvarez-Buylla, A. Long-distance neuronal migration in the adult mammalian brain. *Science* **264,** 1145–1148 (1994).
2. Palmer, T. D., Takahashi, J. & Gage, F. H. The adult rat hippocampus contains primordial neural stem cells. *Mol Cell Neurosci* **8,** 389–404 (1997).
3. Gage, F. H. & Temple, S. Neural stem cells: generating and regenerating the brain. *Neuron* **80,** 588–601 (2013).
4. Murai, K. *et al.* Nuclear receptor TLX stimulates hippocampal neurogenesis and enhances learning and memory in a transgenic mouse model. *Proc Natl Acad Sci USA* **111,** 9115–9120 (2014).
5. Kuhn, H. G., Dickinson-Anson, H. & Gage, F. H. Neurogenesis in the dentate gyrus of the adult rat: age-related decrease of neuronal progenitor proliferation. *J Neurosci* **16,** 2027–2033 (1996).
6. Haughey, N. J. *et al.* Disruption of neurogenesis by amyloid beta-peptide, and perturbed neural progenitor cell homeostasis, in models of Alzheimer's disease. *J Neurochem* **83,** 1509–1524 (2002).
7. Jessberger, S. *et al.* Seizure-associated, aberrant neurogenesis in adult rats characterized with retrovirus-mediated cell labeling. *J Neurosci* **27,** 9400–9407 (2007).
8. Palmer, T. D., Ray, J. & Gage, F. H. FGF-2-responsive neuronal progenitors reside in proliferative and quiescent regions of the adult rodent brain. *Mol Cell Neurosci* **6,** 474–486 (1995).
9. Bracko, O. *et al.* Gene Expression Profiling of Neural Stem Cells and Their Neuronal Progeny Reveals IGF2 as a Regulator of Adult Hippocampal Neurogenesis. *J Neurosci* **32,** 3376–3387 (2012).
10. Lai, K., Kaspar, B. K., Gage, F. H. & Schaffer, D. V. Sonic hedgehog regulates adult neural progenitor proliferation in vitro and in vivo. *Nat Neurosci* **6,** 21–27 (2003).
11. Qu, Q. *et al.* Wnt7a regulates multiple steps of neurogenesis. *Mol Cell Biol* **33,** 2551–2559 (2013).
12. Takahashi, J. & Palmer, T. Retinoic acid and neurotrophins collaborate to regulate neurogenesis in adult-derived neural stem cell cultures. *J Neurobiol* (1999).
13. Battista, D., Ferrari, C. C., Gage, F. H. & Pitossi, F. J. Neurogenic niche modulation by activated microglia: transforming growth factor beta increases neurogenesis in the adult dentate gyrus. *Eur J Neurosci* **23,** 83–93 (2006).
14. Tozuka, Y., Fukuda, S., Namba, T., Seki, T. & Hisatsune, T. GABAergic excitation promotes neuronal differentiation in adult hippocampal progenitor cells. *Neuron* **47,** 803–815 (2005).
15. Song, H., Stevens, C. F. & Gage, F. H. Astroglia induce neurogenesis from adult neural stem cells. *Nature* **417,** 39–44 (2002).
16. Kuwabara, T. *et al.* Wnt-mediated activation of NeuroD1 and retro-elements during adult neurogenesis. *Nat Neurosci* **12,** 1097–1105 (2009).
17. Lie, D.-C. *et al.* Wnt signalling regulates adult hippocampal neurogenesis. *Nature* **437,** 1370–1375 (2005).
18. Ashton, R. S. *et al.* Astrocytes regulate adult hippocampal neurogenesis through ephrin-B signaling. *Nat Neurosci* **15,** 1399–1406 (2012).

19. Conway, A. *et al.* Multivalent ligands control stem cell behaviour in vitro and in vivo. *Nature Nanotech* **8,** 831–838 (2013).
20. Lisabeth, E. M., Falivelli, G. & Pasquale, E. B. Eph receptor signaling and ephrins. *Cold Spring Harb Perspect Biol* **5,** (2013).
21. Suetterlin, P. & Drescher, U. Target-independent ephrina/EphA-mediated axon-axon repulsion as a novel element in retinocollicular mapping. *Neuron* **84,** 740–752 (2014).
22. Clifford, M. A. *et al.* EphA7 signaling guides cortical dendritic development and spine maturation. *Proc Natl Acad Sci USA* **111,** 4994–4999 (2014).
23. Takeuchi, S., Katoh, H. & Negishi, M. Eph/ephrin reverse signalling induces axonal retraction through RhoA/ROCK pathway. *J. Biochem.* mvv042 (2015). doi:10.1093/jb/mvv042
24. Carmona, M. A., Murai, K. K., Wang, L., Roberts, A. J. & Pasquale, E. B. Glial ephrin-A3 regulates hippocampal dendritic spine morphology and glutamate transport. *Proc Natl Acad Sci USA* **106,** 12524–12529 (2009).
25. Chumley, M. J., Catchpole, T., Silvany, R. E., Kernie, S. G. & Henkemeyer, M. EphB receptors regulate stem/progenitor cell proliferation, migration, and polarity during hippocampal neurogenesis. *J Neurosci* **27,** 13481–13490 (2007).
26. Nomura, T., Göritz, C., Catchpole, T., Henkemeyer, M. & Frisén, J. EphB signaling controls lineage plasticity of adult neural stem cell niche cells. *Cell Stem Cell* **7,** 730–743 (2010).
27. Ricard, J., Salinas, J., Garcia, L. & Liebl, D. J. EphrinB3 regulates cell proliferation and survival in adult neurogenesis. *Mol Cell Neurosci* **31,** 713–722 (2006).
28. Barquilla, A. & Pasquale, E. B. Eph receptors and ephrins: therapeutic opportunities. *Annu Rev Pharmacol Toxicol* **55,** 465–487 (2015).
29. Batlle, E. *et al.* Beta-catenin and TCF mediate cell positioning in the intestinal epithelium by controlling the expression of EphB/ephrinB. *Cell* **111,** 251–263 (2002).
30. Stein, E. *et al.* Eph receptors discriminate specific ligand oligomers to determine alternative signaling complexes, attachment, and assembly responses. *Genes Dev* **12,** 667–678 (1998).
31. Peltier, J., O'Neill, A. & Schaffer, D. V. PI3K/Akt and CREB regulate adult neural hippocampal progenitor proliferation and differentiation. *Dev Neurobiol* **67,** 1348–1361 (2007).
32. Steinle, J. J. *et al.* Eph B4 receptor signaling mediates endothelial cell migration and proliferation via the phosphatidylinositol 3-kinase pathway. *J Biol Chem* **277,** 43830–43835 (2002).
33. Xiao, Z. *et al.* EphB4 promotes or suppresses Ras/MEK/ERK pathway in a context-dependent manner: Implications for EphB4 as a cancer target. *Cancer Biol. Ther.* **13,** 630–637 (2012).
34. Choudhary, C. & Mann, M. Decoding signalling networks by mass spectrometry-based proteomics. *Nat Rev Mol Cell Biol* **11,** 427–439 (2010).
35. Azab, F. *et al.* Eph-B2/ephrin-B2 interaction plays a major role in the adhesion and proliferation of Waldenstrom's macroglobulinemia. *Clin. Cancer Res.* **18,** 91–104 (2012).
36. Sharfe, N., Freywald, A., Toro, A. & Roifman, C. M. Ephrin-A1 induces c-Cbl phosphorylation and EphA receptor down-regulation in T cells. *J. Immunol.* **170,** 6024–6032 (2003).

37. Pao-Chun, L., Chan, P. M., Chan, W. & Manser, E. Cytoplasmic ACK1 interaction with multiple receptor tyrosine kinases is mediated by Grb2: an analysis of ACK1 effects on Axl signaling. *J Biol Chem* **284,** 34954–34963 (2009).
38. Sander, J. D. & Joung, J. K. CRISPR-Cas systems for editing, regulating and targeting genomes. *Nat Biotechnol* **32,** 347–355 (2014).
39. Sanjana, N. E., Shalem, O. & Zhang, F. Improved vectors and genome-wide libraries for CRISPR screening. *Nat Methods* **11,** 783–784 (2014).
40. Otto, E. A. *et al.* Mutation analysis in nephronophthisis using a combined approach of homozygosity mapping, CEL I endonuclease cleavage, and direct sequencing. *Hum. Mutat.* **29,** 418–426 (2008).
41. Pitulescu, M. E. & Adams, R. H. Eph/ephrin molecules--a hub for signaling and endocytosis. *Genes Dev* **24,** 2480–2492 (2010).
42. Srivastava, N., Robichaux, M. A., Chenaux, G., Henkemeyer, M. & Cowan, C. W. EphB2 receptor forward signaling controls cortical growth cone collapse via Nck and Pak. *Mol Cell Neurosci* **52,** 106–116 (2013).
43. Platt, M. O., Roman, A. J., Wells, A., Lauffenburger, D. A. & Griffith, L. G. Sustained epidermal growth factor receptor levels and activation by tethered ligand binding enhances osteogenic differentiation of multi-potent marrow stromal cells. *J Cell Physiol* **221,** 306–317 (2009).
44. Deneka, A., Korobeynikov, V. & Golemis, E. A. Embryonal Fyn-associated substrate (EFS) and CASS4: The lesser-known CAS protein family members. *Gene* **570,** 25–35 (2015).
45. Janes, P. W. *et al.* Eph receptor function is modulated by heterooligomerization of A and B type Eph receptors. *J Cell Biol* **195,** 1033–1045 (2011).
46. Kao, T.-J., Palmesino, E. & Kania, A. SRC family kinases are required for limb trajectory selection by spinal motor axons. *J Neurosci* **29,** 5690–5700 (2009).
47. Takasu, M. A., Dalva, M. B., Zigmond, R. E. & Greenberg, M. E. Modulation of NMDA receptor-dependent calcium influx and gene expression through EphB receptors. *Science* **295,** 491–495 (2002).
48. Keung, A. J., de Juan-Pardo, E. M., Schaffer, D. V. & Kumar, S. Rho GTPases Mediate the Mechanosensitive Lineage Commitment of Neural Stem Cells. *STEM CELLS* **29,** 1886–1897 (2011).
49. Samarasinghe, R. A. *et al.* Nongenomic glucocorticoid receptor action regulates gap junction intercellular communication and neural progenitor cell proliferation. *Proc Natl Acad Sci USA* **108,** 16657–16662 (2011).
50. Czopka, T., Holst, von, A., ffrench-Constant, C. & Faissner, A. Regulatory mechanisms that mediate tenascin C-dependent inhibition of oligodendrocyte precursor differentiation. *J Neurosci* **30,** 12310–12322 (2010).
51. Liu, G. *et al.* Netrin requires focal adhesion kinase and Src family kinases for axon outgrowth and attraction. *Nat Neurosci* **7,** 1222–1232 (2004).
52. La Torre, A. *et al.* A role for the tyrosine kinase ACK1 in neurotrophin signaling and neuronal extension and branching. *Cell Death Dis* **4,** e602 (2013).
53. Zhang, J. *et al.* PDGFR-β-activated ACK1-AKT Signaling Promotes Glioma Tumorigenesis. *Int J Cancer* **136,** 1769–1780 (2015).
54. Gage, F. H. *et al.* Survival and differentiation of adult neuronal progenitor cells transplanted to the adult brain. *Proc Natl Acad Sci USA* **92,** 11879–11883 (1995).

55. Yu, J. H. & Schaffer, D. V. Selection of novel vesicular stomatitis virus glycoprotein variants from a peptide insertion library for enhanced purification of retroviral and lentiviral vectors. *J. Virol.* **80,** 3285–3292 (2006).
56. Peltier, J. & Schaffer, D. V. Viral packaging and transduction of adult hippocampal neural progenitors. *Methods Mol Biol* **621,** 103–116 (2010).
57. Shalem, O. *et al.* Genome-scale CRISPR-Cas9 knockout screening in human cells. *Science* **343,** 84–87 (2014).
58. Jang, J.-H. *et al.* An evolved adeno-associated viral variant enhances gene delivery and gene targeting in neural stem cells. *Mol. Ther.* **19,** 667–675 (2011).
59. Conway, A., Spelke, D. P. & Schaffer, D. V. Conjugation of proteins to polymer chains to create multivalent molecules. *Methods Mol Biol* **1202,** 95–102 (2014).
60. Parrinello, S. *et al.* EphB signaling directs peripheral nerve regeneration through Sox2-dependent Schwann cell sorting. *Cell* **143,** 145–155 (2010).
61. Peltier, J., Agrawal, S., Robertson, M. J. & Schaffer, D. V. In vitro culture and analysis of adult hippocampal neural progenitors. *Methods Mol Biol* **621,** 65–87 (2010).
62. Washburn, M. P., Wolters, D. & Yates, J. R. Large-scale analysis of the yeast proteome by multidimensional protein identification technology. *Nat Biotechnol* **19,** 242–247 (2001).
63. Cociorva, D., L Tabb, D. & Yates, J. R. *Validation of Tandem Mass Spectrometry Database Search Results Using DTASelect*. 13.4.1–13.4.14 (John Wiley & Sons, Inc., 2007). doi:10.1002/0471250953.bi1304s16
64. Park, S. K., Venable, J. D., Xu, T. & Yates, J. R. A quantitative analysis software tool for mass spectrometry–based proteomics. *Nat Methods* (2008). doi:10.1038/nmeth.1195
65. Tabb, D. L., McDonald, W. H. & Yates, J. R. DTASelect and Contrast: Tools for Assembling and Comparing Protein Identifications from Shotgun Proteomics. *Journal of proteome research* (2002). doi:10.1021/pr015504q
66. Xu, T., Venable, J. D. & Park, S. K. ProLuCID, a fast and sensitive tandem mass spectra-based protein identification program. *Mol Cell Proteomics* **5,** S174 (2006).
67. McDonald, W. H., Tabb, D. L. & Sadygov, R. G. MS1, MS2, and SQT—three unified, compact, and easily parsed file formats for the storage of shotgun proteomic spectra and identifications - McDonald - 2004 - Rapid Communications in Mass Spectrometry - Wiley Online Library. *Rapid ...* (2004).
68. Peng, J., Elias, J. E., Thoreen, C. C., Licklider, L. J. & Gygi, S. P. Evaluation of Multidimensional Chromatography Coupled with Tandem Mass Spectrometry (LC/LC−MS/MS) for Large-Scale Protein Analysis: The Yeast Proteome. *Journal of proteome research* **2,** 43–50 (2003).

Chapter 5: A Generalized Approach for Optogenetic Clustering of Transmembrane Receptors and Testing with EphB4

This chapter is partly adapted from a manuscript published as

Bugaj, L.J., Spelke, D.P., Mesuda, C.K., Varedi, M., Kane, R.S. & Schaffer, D.V. Regulation of endogenous transmembrane receptors through optogenetic Cry2 clustering. *Nat Comm* **6 SP** (2015).

5.1 Introduction

Cells receive dynamic information via transmembrane receptor signals and integrate these cues to regulate diverse biological processes, including cell proliferation, motility, differentiation and death. Currently utilized approaches to study transmembrane receptor signaling[1,2] often employ overexpression of receptors and receptor fusions, which fundamentally alter how cells respond to extracellular signals and frequently induce hypersensitive or constitutive signal activation[3-5]. Indeed, receptor gene amplification and overexpression is a common driving factor of cancer cell transformation[6,7]. Moreover, current approaches do not provide a high degree of temporal and spatial control that would be desirable to study receptor signaling dynamics and spatially heterogeneous behavior, respectively.

In recent years, the emerging field of optogenetics has offered several methods to optically control and study numerous signaling phenomena with spatiotemporal precision[8-17], although each currently relies on the ectopic expression of the signaling protein of interest. In a recent example, we co-opted the inherent blue light-dependent oligomerization of Arabidopsis Cry2 to regulate clustering and activation of fusion proteins in the cytosol of mammalian cells[9]. To address issues of receptor overexpression, we then demonstrated optogenetic control of endogenous transmembrane receptor activity. Specifically, we re-designed and implemented Cry2 clustering to optically target, cluster and regulate endogenous transmembrane proteins in a modular strategy called Clustering Indirectly using Cryptochrome 2, or CLICR[18].

The CLICR approach makes use of receptor clustering, which is a natural mechanism of activation for many important transmembrane receptors, including receptor tyrosine kinases (for example epidermal growth factor receptor (EGFR), fibroblast growth factor receptor (FGFR), and Eph receptors), immune receptors (for example, T-cell receptor (TCR), B-cell receptor (BCR), and Fc receptor (FcR)), Wnt receptors and integrins[19-27]. Ephs, the largest class of receptor tyrosine kinases, bind to ephrin ligands, GPI-linked A-type or transmembrane B-type, to induce bidirectional signaling in both cells. Eph:ephrin signaling mediates a wide variety of biological processes, from development to cancer[28,29]. Recently, we have demonstrated a novel role for ephrin-B2 in inducing neural stem cell (NSC) neurogenesis in the adult hippocampus, acting through EphB4 receptors[30,31]. Clustering is particularly critical for Eph:ephrin signaling in cell-cell contact-dependent interactions. Upon binding, Eph:ephrin dimers form, then low-affinity circular tetramers, and finally oligomerized clusters[20,29,32]. Furthermore, a number of studies have demonstrated lateral recruitment of un-liganded Ephs into ephrin-nucleated Eph:ephrin signaling clusters[33,34]. Therefore, Ephs are an ideal target for CLICR interrogation.

To enhance the ease of adapting CLICR towards the study of additional signaling systems, in this study we developed a set of generalized CLICR tools. Specifically, we engineered bidirectional CLICR vectors with conveniently located restriction digest sites to allow the expression of any binding domain (BD) – fluorescent protein (FP) – Cry2 fusion. The ability to utilize different FPs enables studies requiring co-expression of CLICR constructs with other fluorescently-tagged proteins, and the ability to "pop-in" different BDs permits targeting of various receptors. We then leveraged these novel tools towards the clustering and activation of EphB4 in NSCs. We successfully designed, expressed, and tested a wide array of CLICR vectors in this system. While none of the constructs examined turned out to be particularly promising for Eph investigation in NSCs, we were able to make a number of useful observations and complete a proof-of-concept study of the application of these generalized CLICR tools.

5.2 Results

Design of generalized CLICR tools

In designing CLICR (Fig. 5.1a), we hypothesized that Cry2 fused to a binding domain (Cry2-BD) possessing limited affinity for a target receptor would remain largely in the cytoplasm in the absence of light. On blue light illumination, clusters of Cry2-BD would assemble and thereby effectively create high local concentrations of the BD that may enable simultaneous binding to multiple receptor endodomains, resulting in receptor clustering and signal activation. We successfully demonstrated the application of CLICR towards a number of commonly studied receptors, including FGFR, platelet-derived growth factor receptor (PDGFR), and integrins[18].

To develop generalized CLICR tools, we designed CLICR constructs with a number of valuable properties (Fig 5.1b). First, to enable application in both easily transfectable cells (e.g. HEK 293Ts) and poorly transfectable cells (e.g. NSCs), we chose the MMLV retroviral vector CLPIT[35] as the backbone for our constructs. CLPIT vectors can be transfected or utilized to produce retroviral particles for infection, so virtually any proliferating mammalian cell type can be studied. Second, as the activity of fusion proteins cannot be predetermined, and often N-terminal and C-terminal fusions exhibit distinctive activity profiles[36], bidirectional CLICR constructs were developed. These constructs result in the expression of Cry2-FP-BD (N-terminal) or BD-FP-Cry2 (C-terminal) fusion proteins. Finally, to optimize customizability, CLICR vectors were designed to contain restriction digest sites enabling the expression of Cry2 fusions with any FP and any BD. Each basal construct contains Cry2 plus a linker: ARDPPVAT (N-terminal fusion) or GGGSGGGS (C-terminal fusion). By simply amplifying a FP of interest with another flexible linker (GGGGSGGGGS) and Mfe1 and Pme1 digest sites, Cry2-linker-FP-linker and linker-FP-linker-Cry2 constructs can be produced. For example, we developed Cry2-mCherry, mCherry-Cry2, Cry2-green fluorescent protein (GFP), and GFP-Cry2 vectors. Then, by amplifying a BD of interest with Mfe1 and Pme1 (N-terminal fusion) or Sfi1 (C-terminal fusion) digest sites, complete Cry2-linker-FP-linker-BD and BD-linker-FP-linker-Cry2 CLICR constructs can be easily developed. Notably, the entire process of designing and producing novel CLCIR vectors with this system takes less than two weeks, and many vectors can be developed simultaneously.

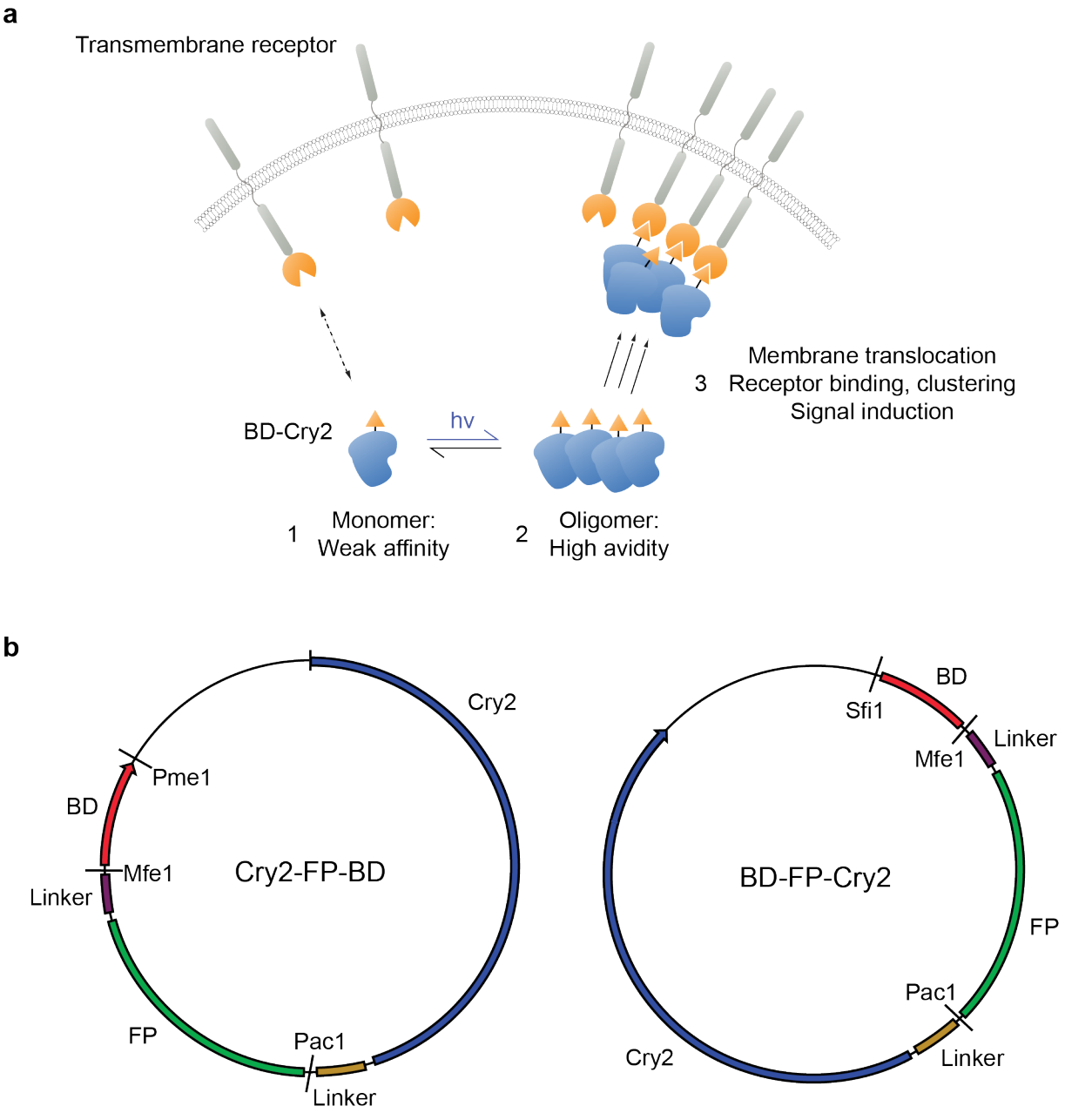

Figure 5.1. Design of generalized CLICR tools. (**a**) The CLICR strategy enables Cry2 activation of transmembrane receptors. CLICR allows modular Cry2 clustering and activation of membrane receptors via noncovalent interactions, avoiding complications associated with overexpression of receptor fusions. With CLICR, Cry2 fused to a receptor-targeting binding domain (BD) is expressed in the cytoplasm. In the dark, unclustered state, BD affinity for the receptor is weak and imparts no or little membrane localization. On light-induced clustering, BD-Cry2 oligomers increase local BD concentration, enabling membrane translocation, binding and nucleation of a receptor cluster. (**b**) Customizable CLICR tools enable the quick design and development of CLICR constructs. Bidirectional vectors allow for the production of both N-terminal and C-terminal fusion proteins. Conveniently located restriction digest sites support the expression of any fluorescent protein (FP) and any BD, enabling readily developed CLICR constructs compatible with other FP-expressing systems and capable of targeting novel receptors.

Design of CLICR constructs to target EphB4

To test our generalized CLICR tools, we developed constructs targeting EphB4, the receptor responsible for transducing ephrin-B2 stimulation in NSC neurogenesis[30,31]. The endodomain of Eph receptors consists of a juxtamembrane region, a kinase domain, a sterile alpha motif (SAM) domain, and a postsynaptic density protein (PSD95), Drosophila disc large tumor suppressor (Dlg1), and zonula occludens-1 protein (zo-1) (PDZ) domain-binding site. Signaling proteins containing specific interaction domains bind to these Eph intracellular regions upon ephrin-induced clustering and trans-phosphorylation. For example, src-homogy 2 (SH2) domain-containing effectors bind to the phosphorylated juxtamembrane region, and PDZ domain-containing proteins associate with the PDZ domain-binding site[28,37]. The SH2 and PDZ domains of Eph-associated signaling targets, therefore, present ideal BDs for utilization in CLICR-mediated Eph investigation.

We chose the BDs from five Eph-associated signaling effectors for our CLICR study: Crk adaptor protein II (CrkII), Dishevelled-2 (Dvl2), the p85 regulatory subunit of phosphoinositide 3-kinase (PI3K) beta (p85), Protein kinase C alpha type (PRKCA)-binding protein 1 (Pick1), and Src proto-oncogene (Src) (Table 5.1). CrkII, p85, and Src contain SH2 domains, while Dvl2 and Pick1 contain PDZ domains. Notably, all five proteins have been demonstrated to interact with EphB receptors[38-42]. The SH2 or PDZ domain from each protein was PCR amplified with the appropriate restriction digest sites and inserted into Cry2-GFP or GFP-Cry2 vectors. As an aside, p85 contains two SH2 domains, so the region spanning both BDs was utilized here. GFP was chosen as the FP to enable co-localization studies with an EphB4-mCherry-expressing NSC line (EphB4-mCh NSCs). Bidirectional vectors encoding N-terminal and C-terminal fusions were developed for each BD, resulting in ten CLICR constructs in total, designated Cry2-GFP-Dvl2, Dvl2-Cry2-GFP, etc.

Table 5.1. Binding domains for CLICR-mediated EphB4 studies. Five Eph-interacting proteins were chosen for investigation of CLICR-induced EphB4 clustering and activation. Each protein contains an interaction domain known to associate with stimulated EphBs. The BD sequence from each protein was amplified and inserted into CLICR constructs.

Protein	Interaction Domain	BD Sequence
CrkII	SH2	WYWGRLSRQEAVALLQGQRHGVFLVRDSSTSPGDYVLSVSENSRVSHYIINS SGPRPPVPPSPAQPPPGVSPSRLRIGDQEFDSLPALLEFYKIHYLDTTTLIE PV
Dvl2	PDZ	TVTLNMEKYNFLGISIVGQSNERGDGGIYIGSIMKGGAVAADGRIEPGDMLL QVNDMNFENMSNDDAVRVLRD
p85	SH2	WYWGDISREEVNERLRDTPDGTFLVRDASSKIQGEYTLTLRKGGNNKLIKVF HRDGHYGFSEPLTFCSVVELISHYRHESLAQYNAKLDTRLLYPVSKYQQDQV VKEDSVEAVGAQLKVYHQQYQDKSREYDQLYEEYTRTSQELQMKRTAIEAFN ETIKIFEEQGQTQEKCSKEYLERFRREGNEKEMQRILLNSERLKSRIAEIHE SRTKLEQDLRAQASDNREIDKRMNSLKPDLMQLRKIRDQYLVWLTQKGARQR KINEWLGIKNETEDQYSLMEDEDALPHHEERTWYVGKINRTQAEEMLSGKRD GTFLIRESSQRGCYACSVVVDGDTKHCVIYRTATGFGFAEPYNLYGSLKELV LHYQHASLVQHNDALTVTLAHPV
Pick1	PDZ	KVTLQKDAQNLIGISIGGGAQYCPCLYIVQVFDNTPAALDGTVAAGDEITGV NGRSIKGKTKVEVAKMIQEVKGEVTIHYNKLQ
Src	SH2	WYFGKITRRESERLLLNAENPRGTFFVRESETTKGAYCLSVSDFDNAKGLNV KHYKIRKLDSGGFYITSRTQFNSLQQLVAYYSKHADGLCHRLTTVCP

Testing of EphB4-targeting CLICR constructs in 293Ts

The EphB4-targting CLICR constructs were first tested in human embryonic kidney (HEK) 293T cells (293Ts). As the expression level of EphB4 in 293Ts was unknown, only the ability of the constructs to cluster in response to blue light was examined. Each CLICR vector was transfected into 293Ts and then analyzed. 488 nm light was pulsed every 10 sec for 200 sec, and was utilized to both excite Cry2 and image GFP. Localization of the fusion proteins was then compared between the dark state and the light-activated state (Fig 5.2). The CLICR constructs displayed a wide variety of expression profiles and light-induced activity. A number of observations are worth noting. First, the expression levels of the fusion proteins were quite varied. For example, Cry2-GFP-CrkII (Fig. 5.2*vi*) was highly expressed, while Pick1-GFP-Cry2 was expressed at a much lower level (Fig. 5.2*iv*). Second, a number of the constructs displayed substantial clustering in the dark state, such as Cry2-GFP-p85 (Fig 5.5*viii*). This clustering could have been due to basal activity levels as a result of overexpression, or BD localization to interacting partners that do not require stimulation for binding. Third, only half of the CLICR constructs tested exhibited visible light-induced clustering (Fig. 5.2*i,v,vi,vii,x*), demonstrating the unpredictability of the system. Finally, the architecture or "directionality" of the construct

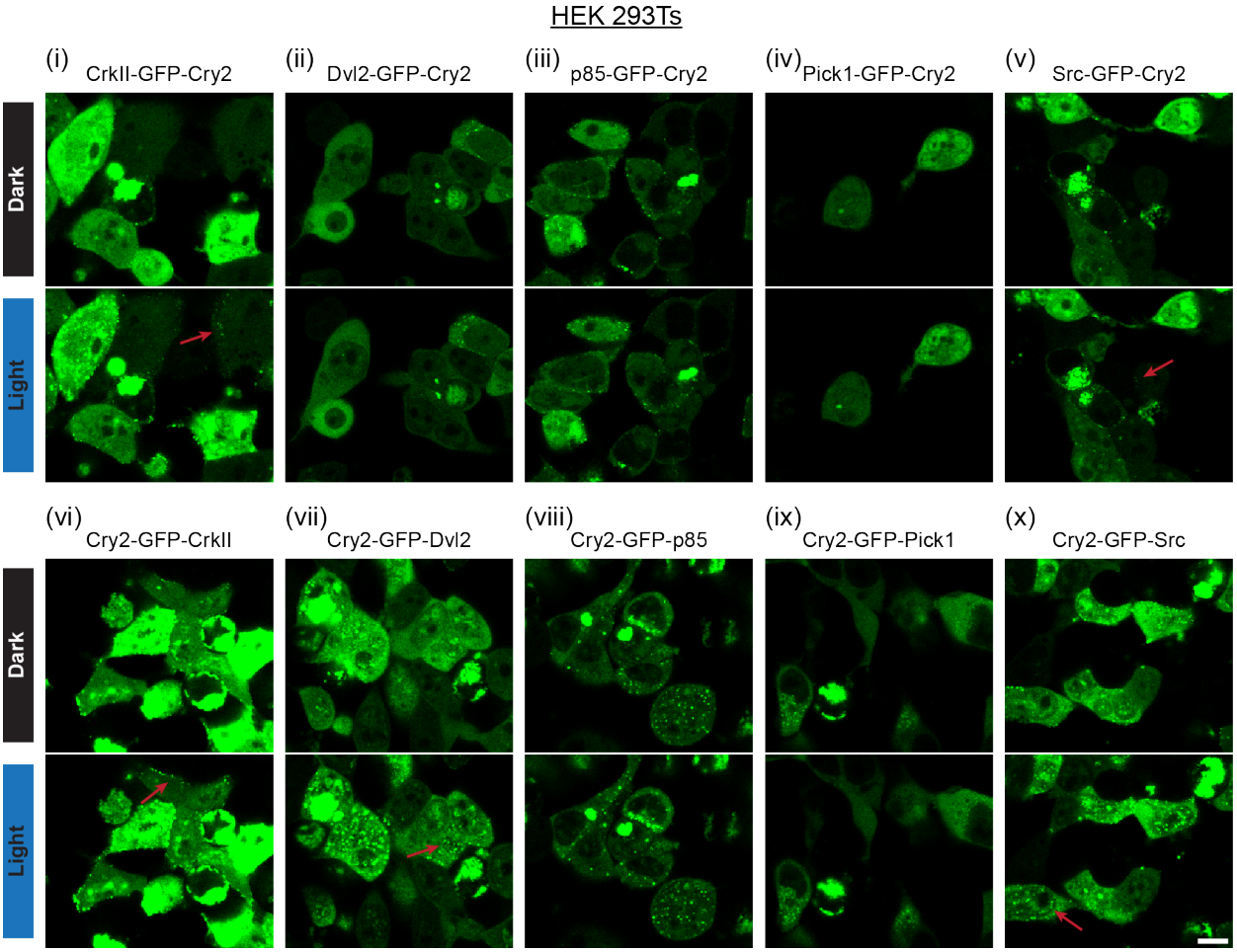

Figure 5.2. Testing of CLICR constructs in 293Ts. CLICR vectors expressing Eph-targeting BDs were transfected into 293Ts. Both C-terminal (*i-v*) and N-terminal (*vi-x*) fusions were investigated. 293Ts were pulsed with blue light to both activate Cry2 and image GFP, and the activity of constructs was examined. Red arrows denote light-induced clustering. Scale bar, 10 μm.

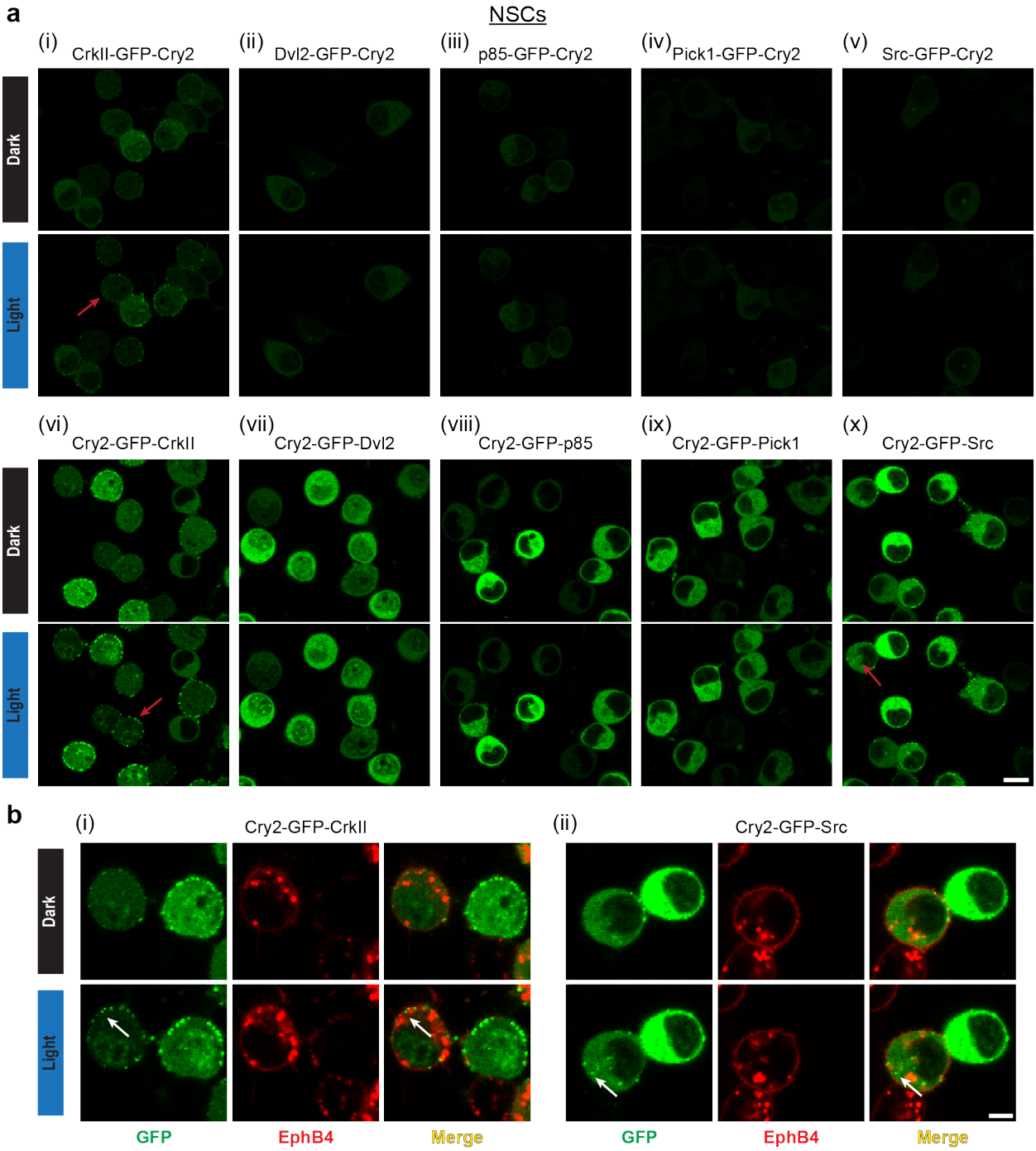

Figure 5.3. Testing of CLICR constructs in NSCs. (**a**) CLICR retroviruses were produced and EphB4-mCh NSCs were infected. Both C-terminal (*i-v*) and N-terminal (*vi-x*) fusions were investigated. EphB4-mCh NSCs were pulsed with blue light and the clustering activity of constructs was examined. Red arrows denote light-induced clustering. Scale bar, 10 µm. (**b**) Zoomed-in images of selected cells from (**a**) show localization of Cry-GFP-BD fusions and EphB4-mCh. White arrows denote light-induced clustering of GFP fusions. Scale bar, 5 µm.

determined activity for some BD fusions. For example, while N- and C-terminal fusions of CrkII displayed light-induced clustering (Fig. 5.2*i,vi*), only the N-terminal fusion of Dvl2 was light-responsive (Fig. 5.2*ii,vii*). Overall, testing of the EphB4-targeting constructs in 293Ts

demonstrated the variability of CLICR, and confirmed the need to systematically test novel vectors for activity.

Testing of EphB4-targeting CLICR constructs in NSCs

We then tested our ten CLICR constructs in NSCs. To enable the examination of co-localization of Cry2-GFP fusion proteins with EphB4, EphB4-mCh NSCs were used in these studies. Because NSCs do not transfect well, CLICR retroviruses were produced, and EphB4-mCh NSCs were infected and then analyzed. As in the 293T experiments, 488 nm light was pulsed to both excite Cry2 and image GFP. Additionally, 561 nm light pulses were used to image EphB4-mCh. Localization was then compared between the dark and light-activated states (Fig 5.3). Examining only the Cry2 fusions (Fig 5.3a), observations similar to those in 293Ts can be made. Again, expression levels were highly variable. EphB4-mCh NSCs required transduction at a multiplicity of infection (MOI) of 3 to permit visualization, and even so, all of the C-terminal fusions expressed quite poorly (Fig. 5.3a*i-v*). Some basal clustering in the dark state was also apparent, particularly with the CrkII constructs (Fig. 5.3.a*i,vi*). Finally, only three of the CLICR vectors tested exhibited visible light-induced clustering: CrkII-GFP-Cry2, Cry2-GFP-CrkII, and Cry2-GFP-Src (Fig 5.3.a*i,vi,x*). Notably, all of these vectors were also active in the 293Ts. Overall, these results in NSCs were a further demonstration of CLICR variability.

For CLICR to successfully be utilized as a tool for interrogating EphB4 signaling, upon blue light stimulation, Cry2 fusion proteins should cluster, localize to the membrane, and induce EphB4 clustering. To assess this activity, we examined the co-localization of fusion proteins and EphB4 in two of the CLICR constructs that demonstrated light-induced clustering: Cry2-GFP-CrkII and Cry2-GFP-Src (Fig. 5.3b). While GFP puncta clearly formed in response to blue-light, EphB4 did not appear to co-localize with these Cry2 clusters. Therefore, none of the ten CLICR constructs tested demonstrated light-induced EphB4 clustering.

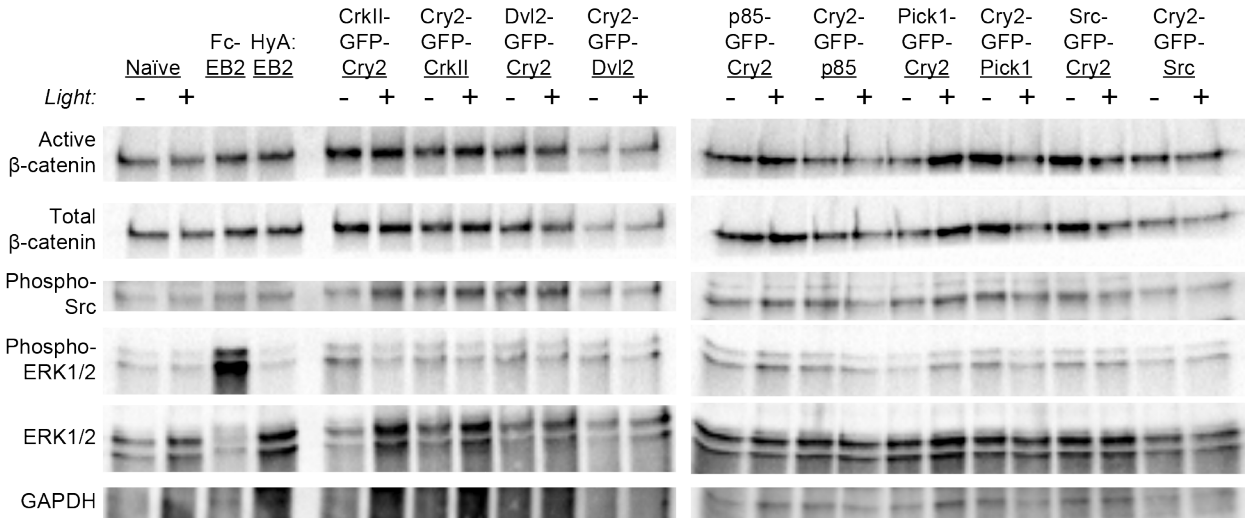

Figure 5.4. CLICR constructs in NSCs do not promote light-induced stimulation of downstream signaling. Western blots for EphB4 signaling targets. EphB4-mCh NSCs harboring CLICR constructs were kept in the dark or stimulated for 1 h with pulsed blue light. As negative controls, naïve EphB4-mCh NSCs were kept in the dark or exposed to pulsed light for 1 h. As positive controls, EphB4-mCh NSCs were stimulated for 1 h with Fc-ephrin-B2 or HyA:ephrin-B2.

As a final test of the CLICR constructs in EphB4-mCh NSCs, light-induced stimulation of downstream signaling was investigated. While EphB4 clustering was not apparent in the previous studies, we hypothesized that nanoscale clustering may have occurred, which could potentially induce EphB4-mediated signaling. Utilizing a home-built device capable of whole-plate illumination, cells were pulsed with blue light every 5 sec for 1 h, or kept in the dark. To control for any affects solely due to blue light exposure, naïve EphB4-mCh NSCs were also pulsed. Additionally, as positive controls, naïve EphB4-mCh NSCs were stimulated with antibody-clustered Fc-fused ephrin-B2 molecules (Fc-ephrin-B2)[30] or multivalent ephrin-B2 created by conjugating ephrin-B2 to a linear hyaluronic acid (HyA) polymer at high valency (HyA:ephrin-B2)[31] for 1 h. All of these samples were then probed by western blot for activation of signaling proteins known to be downstream of ephrin-B2:EphB4, including β-catenin, extracellular regulated MAP kinase (ERK), and Src proto-oncogene (Src)[30,40,43] (Fig 5.4). Blue light alone had no effect on signaling, and the Fc-ephrin-B2 and HyA:ephrin-B2 stimulated EphB4-mCh NSCs demonstrated the usual signal activation (*Chapter 4*), so the cells responded as expected. Unfortunately, none of the CLICR vectors induced EphB4 downstream signaling upon blue light stimulation. Therefore, while some of the CLICR constructs did exhibit light-induced clustering, none of them were capable of clustering and activating EphB4.

5.3 Discussion

Spatially defined and rapidly time-varying signals are the key regulatory factors in diverse biological processes including cell migration[44], asymmetric cell division[45], differentiation[5] and apoptosis[46]. The difficulties of perturbing biological systems with such spatiotemporal precision, however, often preclude our understanding of how dynamic signals regulate cellular function. Optogenetic tools address this need. Although methods for optical protein homodimerization[17,47], heterodimerization[12-14,16] and homo-oligomerization[9] of ectopically expressed proteins have been developed, ectopic expression of many signaling proteins—particularly transmembrane receptors—can fundamentally alter how the system of study behaves, potentially confounding conclusions reached with even the most sophisticated perturbative techniques. We devised the CLICR method[18] to address this dilemma.

In this study, we created generalized CLICR tools to enable the rapid design and development of CLICR constructs targeting novel signaling proteins and receptors. These vectors are bidirectional and contain convenient restriction digest sites permitting the utilization of any FP and any BD, allowing for the rapid application of the CLICR method in any system of interest. We then utilized these CLICR tools to target the neurogenic receptor EphB4. We chose the SH2 or PDZ BDs from five EphB signaling effectors, developed bidirectional CLICR fusion proteins with GFP, and then tested the constructs in 293Ts and EphB4-mCh NSCs. Overall, testing revealed a high degree of variability, both in the basal expression levels of fusion proteins and the clustering activity in response to blue light stimulation. Additionally, none of the ten constructs examined demonstrated co-localization with EphB4 clusters or activation of EphB4 downstream signaling in response to light stimulation. Therefore, while we successfully developed and tested a number of constructs, we were unsuccessful in applying CLICR towards EphB4 interrogation.

Our failed attempt at leveraging CLICR to stimulate EphB4 may have been due to a couple of factors, and points towards additional aspects of the system that could be optimized in future work. One hypothesis to explain our findings is that, because the signaling effectors chosen do not specifically interact with EphB4, the fusion proteins associated with other cellular proteins upon light activation and clustering. EphB4 is present at very low levels in NSCs (*Chapter 4*), so while the EphB4-mCh NSCs do express more EphB4, widely distributed receptors, such as FGFR and PDGFR (as studied in our previous work[18]), may have been preferentially targeted with our CLICR constructs. Alternatively, the signaling effectors may not naturally associate with EphB4 in NSCs, since they were selected based solely on the criterion of a published interaction with an EphB in some cell type. Eph:ephrin signaling is complex and downstream signal activation can be cell type-dependent[29,37], so the BDs tested may not have been functional in our system. These hypotheses point two directions for future work in both targeting EphB4 with CLICR, as well as in advancing CLICR technology. First, the use of BDs from experimentally validated signaling effectors of target receptors may increase the success of CLICR applications. For example, we have recently demonstrated a role for activated Cdc42 kinase 1 (Ack1) and Fyn proto-oncogene (Fyn) in ephrin-B2-mediated EphB4 signaling in NSCs (*Chapter 4*), so the BDs of Ack1 and Fyn would be ideal candidates for future attempts at CLICR-induced EphB4 activation. Additionally, development of alternative, 'orthogonal' binding domains, for example an intracellular antibody domain specifically evolved to target a receptor endodomain[48], may in the future offer additional versatility, specificity and reduction of basal signal perturbation. Overall, CLICR is a versatile tool for interrogating endogenous receptors, and this study, along with future work, may contribute to the further development of this powerful technology.

5.4 Materials and Methods

Cell culture

Neural stem cells (NSCs) were isolated from the hippocampi of adult female Fisher 344 rats[49] and cultured on tissue culture-treated polystyrene plates coated with 10 μg/mL polyornithine (Sigma-Aldrich) and 5 μg/mL laminin (Life Technologies). NSCs were cultured in 1:1 Dulbecco's Modified Eagle Medium: Nutrient Mixture F-12 (DMEM:F12, Life Technologies) supplemented with N-2 (Life Technologies) and 20 ng/mL recombinant human FGF-2 (PeproTech), and were subcultured at 80% confluency using Accutase (Life Technologies) for cell detachment. The EphB4-mCh NSC line was created through stable retroviral infection as previously described (*Chapter 4*).

HEK 293Ts (293Ts) were cultured in DMEM (Corning) with 10% fetal bovine serum (FBS) (Life Technologies) and 1% penicillin/streptomycin (P/S) (Life Technologies). 293Ts were cultured on tissue culture-treated polystyrene plates and subcultured at 90% confluency using Trypsin - Ethylenediaminetetraacetic acid (EDTA) 1× (Corning).

CLICR construct development

All vectors were assembled through standard restriction digest cloning techniques. Cry2 was PCR amplified from CLPIT SH2 (PLCγ)-mCherry-Cry2PHR[18]. GFP was amplified from FUGW[50]. SH2 and PDZ BDs were amplified from cDNAs encoding CrkII (Plasmid #50730), Dvl2 (Plasmid #38876), p85 (Plasmid #1406), Pick1 (Plasmid #38803), and Src (Plasmid

#42202) (all from Addgene). All constructs were produced in the MMLV retroviral vector CLPIT[35]. Retroviruses were packaged, purified, and titered on NSCs as previously described[51].

Confocal Microscopy

For CLICR testing in 293Ts, 293Ts were seeded in 35 mm glass bottom dishes (Mattek) at 2 × 10^5 cells per dish in standard media conditions. The following day, cultures were transfected with 2 μg CLICR vector using polyethylenimine (Polysciences). Three days later, cultures were imaged.

For CLICR testing in NSCs, EphB4-mCh NSCs were seeded in polyornithine/ laminin coated 35 mm glass bottom dishes at 1.5 × 10^5 cells per dish in standard media conditions. 4 h later, EphB4-mCh NSCs were infected with CLICR retroviruses at MOI = 3 for 2 h, followed by a media change. Three days later, cultures were imaged.

Time-lapse microscopy of activated Cry2 fusions was performed at the Molecular Imaging Center at UC Berkeley on a Zeiss LSM 710 AxioObserver confocal microscope in conjunction with the Zeiss ZEN software. Cry2 translocation experiments were carried out at 25°C. Whole-field Cry2 activation was achieved using 488 nm illumination. GFP and mCherry were visualized with 488 and 561 nm laser excitation, respectively, through a 63× oil immersion objective (the same 488 nm pulses were used to both excite Cry2 and image GFP). Laser light was set at 5–50% power depending on expression levels. Cells were excited every 10 sec for 200 sec total. Images were processed and analyzed in ImageJ (National Institutes of Health).

Western blotting

EphB4-mCh NSCs were seeded in polyornithine/ laminin coated 12-well culture plates at 1.5 × 10^5 cells per well in standard media conditions. 4 h later, EphB4-mCh NSCs were infected with CLICR retroviruses at MOI = 3 for 2 h, followed by a media change. Three days later, cultures were switched to low FGF-2 (0.5 ng/mL) media conditions, and then stimulated for signaling studies 16 h later. For positive controls, naïve EphB4-mCh NSCs were stimulated with 200 nM Fc-ephrin-B2 or HyA:ephrin-B2 for 1 h. Fc-ephrin-B2 and HyA:ephrin-B2 were synthesized as previously described (*Chapter 4*). For light-induction, cultures were stimulated with 500 ms blue light pulses every 5 sec for 1 h using a home built device capable of whole-plate illumination in standard cell culture incubating conditions.

Cells were lysed in RIPA buffer (50 mM Tris, 150 mM NaCl, 1% NP-40, 0.5% sodium deoxycholate, 0.1% sodium dodecyl sulfate (SDS), pH 8) containing protease and phosphatase inhibitor cocktails (ThermoFisher Scientific). Cell lysates were mixed with 5x Laemmli buffer (final 50 mM Tris, 2% SDS, 0.1% Bromophenol Blue, 10% glycerol), 2-mercaptoethanol was added to 10% v/v, and samples were boiled at 95°C for 5 min. Samples were electrophoretically separated on 10%T SDS-PAGE gels and transferred onto nitrocellulose membranes using standard methods. Blots were blocked for 1 h in tris-buffered saline (TBS) with 0.1% Tween-20 (TBS-T) and 3% bovine serum albumin (BSA) for phoshoprotein antibodies or 5% Blotting Grade Blocker (BioRad) for all other antibodies. Blots were probed overnight at 4°C with primary antibodies in the same blocking buffer: rabbit anti-β-catenin (1:1000, 9562, Cell Signaling), rabbit anti-non-phospho (Active)-β-catenin (1:1000, 8814, Cell Signaling), rabbit anti-ERK (1:1000, 4695, Cell Signaling), rabbit anti-phospho-ERK (1:2000, 4370, Cell

Signaling), rabbit anti-GAPDH (1:2500, ab9485, Abcam), rabbit anti-phospho-Src (1:1000, 2101, Cell Signaling); followed by 1 h incubation with goat anti-rabbit horseradish peroxidase (HRP) (1:10,000, 32460, ThermoFisher Scientific). Protein bands were detected using SuperSignal West Dura Chemiluminescent Substrate (ThermoFisher Scientific), and blots were digitally imaged on a ChemiDoc XRS+ Imaging System (BioRad). Blots were stripped in a solution of 3% acetic acid, 0.5 M NaCl, pH 2.5, for 10 min, neutralized with 0.5 M NaOH for 1 min, and then reprobed as needed.

5.5 Acknowledgements

We acknowledge D. Blondel for aiding in project inception and CLICR construct design; C. Fuentes for experimental assistance; E. Connelly for experimental assistance; N. Repina for design and development of the whole-plate illumination device; and L. Bugaj for critical discussion regarding CLICR technology.

5.6 References

1. Coward, P. *et al.* Controlling signaling with a specifically designed Gi-coupled receptor. *Proc Natl Acad Sci USA* **95,** 352–357 (1998).
2. Spencer, D. M., Wandless, T. J., Schreiber, S. L. & Crabtree, G. R. Controlling signal transduction with synthetic ligands. *Science* **262,** 1019–1024 (1993).
3. Dikic, I., Schlessinger, J. & Lax, I. PC12 cells overexpressing the insulin receptor undergo insulin-dependent neuronal differentiation. *Curr Biol* **4,** 702–708 (1994).
4. Jiang, Y., Woronicz, J. D., Liu, W. & Goeddel, D. V. Prevention of constitutive TNF receptor 1 signaling by silencer of death domains. *Science* **283,** 543–546 (1999).
5. Traverse, S. *et al.* EGF triggers neuronal differentiation of PC12 cells that overexpress the EGF receptor. *Curr Biol* **4,** 694–701 (1994).
6. Prelich, G. Gene overexpression: uses, mechanisms, and interpretation. *Genetics* **190,** 841–854 (2012).
7. Snuderl, M. *et al.* Mosaic amplification of multiple receptor tyrosine kinase genes in glioblastoma. *Cancer Cell* **20,** 810–817 (2011).
8. Airan, R. D., Thompson, K. R., Fenno, L. E., Bernstein, H. & Deisseroth, K. Temporally precise in vivo control of intracellular signalling. *Nature* **458,** 1025–1029 (2009).
9. Bugaj, L. J., Choksi, A. T., Mesuda, C. K., Kane, R. S. & Schaffer, D. V. Optogenetic protein clustering and signaling activation in mammalian cells. *Nat Methods* **10,** 249–252 (2013).
10. Cao, J. *et al.* Light-inducible activation of target mRNA translation in mammalian cells. *Chem. Commun. (Camb.)* **49,** 8338–8340 (2013).
11. Fenno, L., Yizhar, O. & Deisseroth, K. The development and application of optogenetics. *Annu Rev Neurosci* **34,** 389–412 (2011).
12. Kennedy, M. J. *et al.* Rapid blue-light-mediated induction of protein interactions in living cells. *Nat Methods* **7,** 973–975 (2010).
13. Levskaya, A., Weiner, O. D., Lim, W. A. & Voigt, C. A. Spatiotemporal control of cell signalling using a light-switchable protein interaction. *Nature* **461,** 997–1001 (2009).
14. Strickland, D. *et al.* TULIPs: tunable, light-controlled interacting protein tags for cell biology. *Nat Methods* **9,** 379–384 (2012).

15. Wu, Y. I. *et al.* A genetically encoded photoactivatable Rac controls the motility of living cells. *Nature* **461,** 104–108 (2009).
16. Yazawa, M., Sadaghiani, A. M., Hsueh, B. & Dolmetsch, R. E. Induction of protein-protein interactions in live cells using light. *Nat Biotechnol* **27,** 941–945 (2009).
17. Zhou, X. X., Chung, H. K., Lam, A. J. & Lin, M. Z. Optical control of protein activity by fluorescent protein domains. *Science* **338,** 810–814 (2012).
18. Bugaj, L. J. *et al.* Regulation of endogenous transmembrane receptors through optogenetic Cry2 clustering. *Nat Commun* **6 SP ,**
19. Cong, F., Schweizer, L. & Varmus, H. Wnt signals across the plasma membrane to activate the beta-catenin pathway by forming oligomers containing its receptors, Frizzled and LRP. *Development* **131,** 5103–5115 (2004).
20. Davis, S. *et al.* Ligands for EPH-related receptor tyrosine kinases that require membrane attachment or clustering for activity. *Science* **266,** 816–819 (1994).
21. Duchemin, A. M., Ernst, L. K. & Anderson, C. L. Clustering of the high affinity Fc receptor for immunoglobulin G (Fc gamma RI) results in phosphorylation of its associated gamma-chain. *J Biol Chem* **269,** 12111–12117 (1994).
22. Heldin, C. H. Dimerization of cell surface receptors in signal transduction. *Cell* **80,** 213–223 (1995).
23. Letourneur, F. & Klausner, R. D. T-cell and basophil activation through the cytoplasmic tail of T-cell-receptor zeta family proteins. *Proc Natl Acad Sci USA* **88,** 8905–8909 (1991).
24. Margadant, C., Monsuur, H. N., Norman, J. C. & Sonnenberg, A. Mechanisms of integrin activation and trafficking. *Curr Opin Cell Biol* **23,** 607–614 (2011).
25. Romeo, C. & Seed, B. Cellular immunity to HIV activated by CD4 fused to T cell or Fc receptor polypeptides. *Cell* **64,** 1037–1046 (1991).
26. Schlessinger, J. Cell signaling by receptor tyrosine kinases. *Cell* **103,** 211–225 (2000).
27. Zhao, Y., Tong, C. & Jiang, J. Hedgehog regulates smoothened activity by inducing a conformational switch. *Nature* **450,** 252–258 (2007).
28. Barquilla, A. & Pasquale, E. B. Eph receptors and ephrins: therapeutic opportunities. *Annu Rev Pharmacol Toxicol* **55,** 465–487 (2015).
29. Himanen, J.-P., Saha, N. & Nikolov, D. B. Cell-cell signaling via Eph receptors and ephrins. *Curr Opin Cell Biol* **19,** 534–542 (2007).
30. Ashton, R. S. *et al.* Astrocytes regulate adult hippocampal neurogenesis through ephrin-B signaling. *Nat Neurosci* **15,** 1399–1406 (2012).
31. Conway, A. *et al.* Multivalent ligands control stem cell behaviour in vitro and in vivo. *Nature Nanotech* **8,** 831–838 (2013).
32. Nikolov, D. B., Xu, K. & Himanen, J. P. Eph/ephrin recognition and the role of Eph/ephrin clusters in signaling initiation. *Biochim Biophys Acta* **1834,** 2160–2165 (2013).
33. Seiradake, E., Harlos, K., Sutton, G., Aricescu, A. R. & Jones, E. Y. An extracellular steric seeding mechanism for Eph-ephrin signaling platform assembly. *Nat. Struct. Mol. Biol.* **17,** 398–402 (2010).
34. Wimmer-Kleikamp, S. H., Janes, P. W., Squire, A., Bastiaens, P. I. H. & Lackmann, M. Recruitment of Eph receptors into signaling clusters does not require ephrin contact. *J Cell Biol* **164,** 661–666 (2004).
35. Yu, J. H. & Schaffer, D. V. Selection of novel vesicular stomatitis virus glycoprotein variants from a peptide insertion library for enhanced purification of retroviral and lentiviral vectors. *J. Virol.* **80,** 3285–3292 (2006).

36. Snapp, E. Design and use of fluorescent fusion proteins in cell biology. *Curr Protoc Cell Biol* **Chapter 21,** Unit 21.4 (2005).
37. Pasquale, E. Eph receptors and ephrins in cancer: bidirectional signaling and beyond. *Nat Rev Cancer* (2010).
38. Noren, N. K., Foos, G., Hauser, C. A. & Pasquale, E. B. The EphB4 receptor suppresses breast cancer cell tumorigenicity through an Abl-Crk pathway. *Nat Cell Biol* **8,** 815–825 (2006).
39. Pandey, A., Lazar, D. F., Saltiel, A. R. & Dixit, V. M. Activation of the Eck receptor protein tyrosine kinase stimulates phosphatidylinositol 3-kinase activity. *J Biol Chem* **269,** 30154–30157 (1994).
40. Steinle, J. J. *et al.* Eph B4 receptor signaling mediates endothelial cell migration and proliferation via the phosphatidylinositol 3-kinase pathway. *J Biol Chem* **277,** 43830–43835 (2002).
41. Tanaka, M., Kamo, T., Ota, S. & Sugimura, H. Association of Dishevelled with Eph tyrosine kinase receptor and ephrin mediates cell repulsion. *EMBO J* **22,** 847–858 (2003).
42. Torres, R. *et al.* PDZ proteins bind, cluster, and synaptically colocalize with Eph receptors and their ephrin ligands. *Neuron* **21,** 1453–1463 (1998).
43. Xiao, Z. *et al.* EphB4 promotes or suppresses Ras/MEK/ERK pathway in a context-dependent manner: Implications for EphB4 as a cancer target. *Cancer Biol. Ther.* **13,** 630–637 (2012).
44. Kraynov, V. S. *et al.* Localized Rac activation dynamics visualized in living cells. *Science* **290,** 333–337 (2000).
45. Habib, S. J. *et al.* A localized Wnt signal orients asymmetric stem cell division in vitro. *Science* **339,** 1445–1448 (2013).
46. Purvis, J. E. *et al.* p53 dynamics control cell fate. *Science* **336,** 1440–1444 (2012).
47. Wang, X., Chen, X. & Yang, Y. Spatiotemporal control of gene expression by a light-switchable transgene system. *Nat Methods* **9,** 266–269 (2012).
48. Hyland, S., Beerli, R. R., Barbas, C. F., Hynes, N. E. & Wels, W. Generation and functional characterization of intracellular antibodies interacting with the kinase domain of human EGF receptor. *Oncogene* **22,** 1557–1567 (2003).
49. Gage, F. H. *et al.* Survival and differentiation of adult neuronal progenitor cells transplanted to the adult brain. *Proc Natl Acad Sci USA* **92,** 11879–11883 (1995).
50. Lois, C., Hong, E. J., Pease, S., Brown, E. J. & Baltimore, D. Germline transmission and tissue-specific expression of transgenes delivered by lentiviral vectors. *Science* **295,** 868–872 (2002).
51. Peltier, J. & Schaffer, D. V. Viral packaging and transduction of adult hippocampal neural progenitors. *Methods Mol Biol* **621,** 103–116 (2010).

Appendix A: Supplementary Material for Chapter 2

This appendix contains material adapted from a manuscript published as

Hughes, A.J.*, Spelke, D.P.*, Xu, Z., Kang, C., Schaffer, D.V. & Herr, A.E. Single-cell western blotting. *Nat Methods* **11,** 749-755 (2014).

**Authorship equally shared*

A.1 Supplementary Figures and Tables

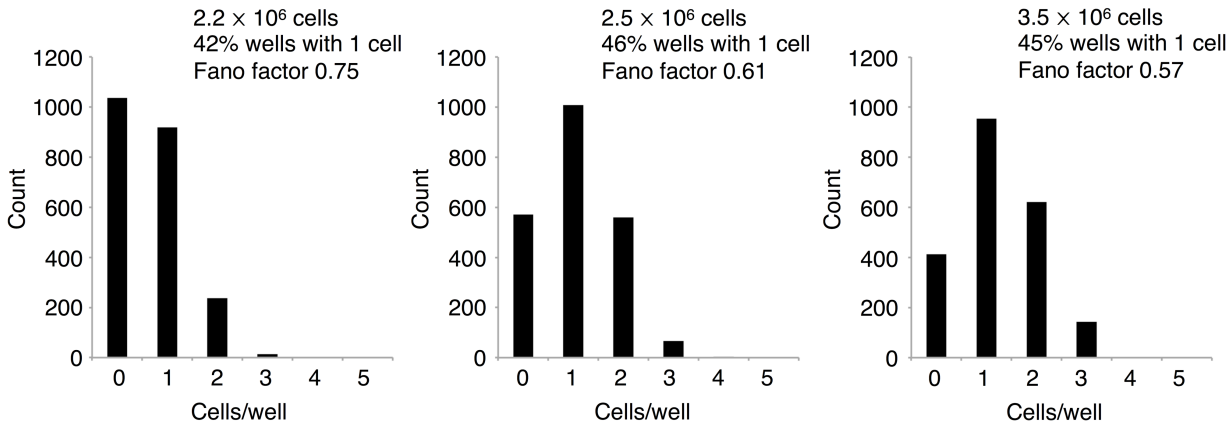

Figure A.1. Cell-per-microwell counts for neural stem cells (NSCs). NSCs were settled into 2,240 scWestern microwells of nominal dimensions 20 μm in diameter and 30 μm in depth for 5 min and counted by hand from brightfield micrographs for 3 cell densities in the original suspension. Single cell-per-microwell occupancies are in the 40–50% range, with Fano factors (σ^2/μ) of between 0.55 and 0.75, indicating departure from a Poissonian seeding distribution, likely due to restricted seeding of >4 cells per microwell (Note A.4).

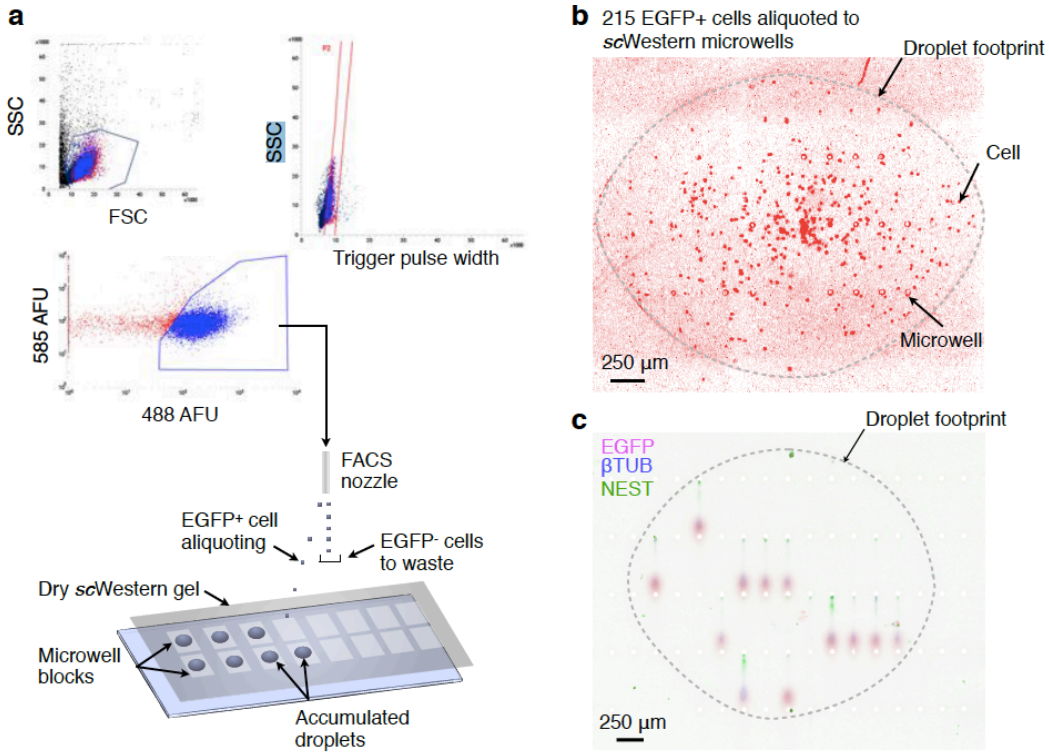

Figure A.2. Integration of scWestern blotting and fluorescence-activated cell sorting (FACS) for analysis of sparing, gated cell populations. (**a**) Gating of single EGFP+ NSCs and spatial sorting to a dry scWestern slide (SSC, side scatter; FSC, forward scatter)[1]. (**b**) Inverted fluorescence micrograph at 4x magnification of 215 propidium iodide-stained cells aliquoted to a block of scWestern microwells from the FACS nozzle and dried. Note the initial droplet footprint is visible. (**c**) 3-color scWestern analysis for EGFP, β-tubulin (βTUB), and nestin (NEST) targets after settling cells from FACS droplet, slide rehydration, and scWestern analysis. Note all cells analyzed are EGFP+, as prescribed by FACS gating.

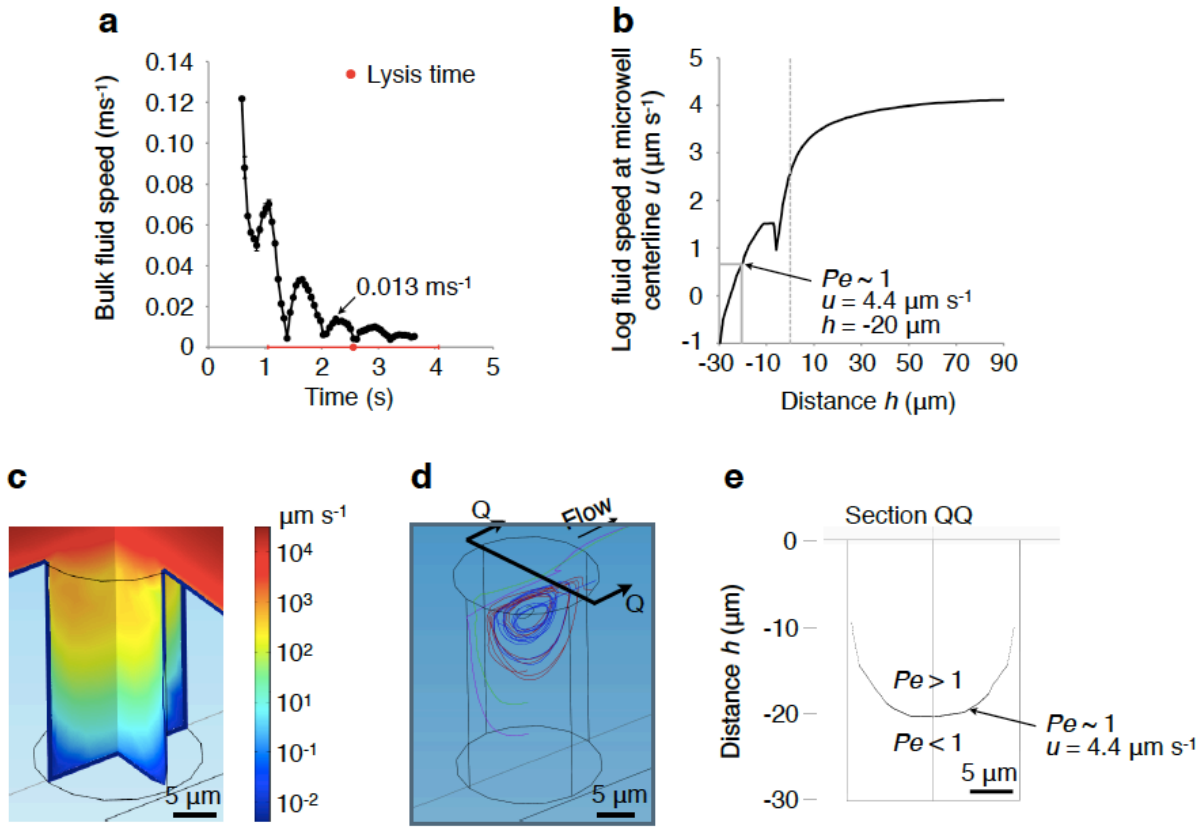

Figure A.3. COMSOL model of microwell fluid velocity during cell lysis. (**a**) Measured bulk buffer speed during pouring into the scWestern electrophoresis chamber by particle image velocimetry. Lysis time is also shown for context (± S.D., n = 6 cells). The maximum bulk velocity in the vicinity of the mean lysis time is 0.013 ms^{-1}, and was used for fluid flow simulations in (**b**)–(**e**). (**b**)–(**d**) A COMSOL model of unidirectional, steady-state laminar flow during pouring of water over a 20 µm diameter microwell in a 30 µm-thick scWestern gel film with a bulk fluid velocity of 0.013 ms^{-1}. Note the presence of a vortex in the microwell parallel to the bulk flow direction that is traced by streamlines representing the movement of massless, non-buoyant particles from starting locations at 5, 10, 15, 20, and 25 µm into the microwell. Flow boundary conditions on the microwell surfaces were "no slip". (**e**) A centerline slice transverse to the flow direction for the model velocity distribution; the u = 4.4 µm s^{-1} isotach demarcates regions of the microwell in which mass transport is diffusively (Pe < 1) or advectively (Pe > 1) dominated during cell lysis.

a

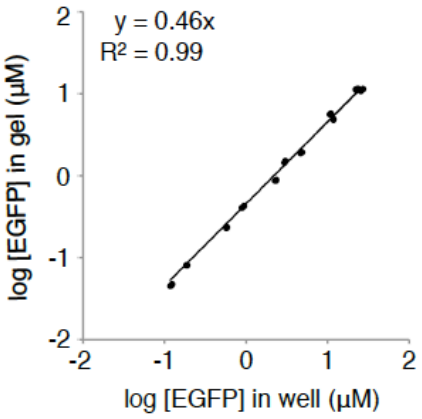

b

Species	Molecular weight (kDa)	*K* (± SD, *n* = 32)
EGFP	27	0.44 ± 0.05
GAPDH	36	0.42 ± 0.02
βTUB	50	0.51 ± 0.04
ERK	70	0.28 ± 0.04
MEK	72	0.25 ± 0.03
IgG	150	0.17 ± 0.01

c Purified dronpa

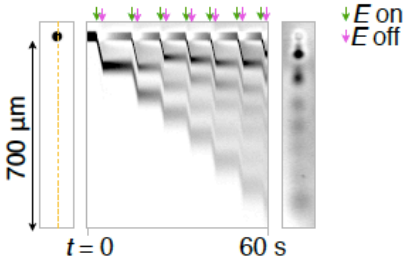

Figure A.4. Partitioning of proteins into scWestern microwells. (**a**) Partitioning curve for EGFP determined for microwell blocks in an 8%T gel sheet incubated with a dilution series of EGFP in denaturing RIPA buffer via $K = ([EGFP]_{gel} - [EGFP]_{gel,bg})/([EGFP]_{microwell} - [EGFP]_{microwell,bg})$, where $[EGFP]_{gel}$ and $[EGFP]_{microwell}$ are in-gel and in-microwell concentrations of EGFP at equilibrium determined by fluorescence calibration in a separate microchannel of 30 µm depth. $[EGFP]_{gel,bg}$ and $[EGFP]_{microwell,bg}$ correct for the background fluorescence of the scWestern slide prior to incubation with the EGFP solutions. (**b**) Partition coefficients for several Alexa Fluor 568-labeled proteins determined as in (**a**), except "IgG", which is for Alexa Fluor 647-labeled donkey anti-rabbit IgG; n is for separate microwells in single experiments for each target. (**c**) Repeated injections of the fluorescent protein Dronpa from a coverglass-enclosed, 50 µm diameter microwell in an 8%T scWestern gel sheet incubated with 1 µM Dronpa in denaturing RIPA buffer for 30 min. Partitioning of Dronpa into the microwell allows repeated injections against a background gel concentration of Dronpa.

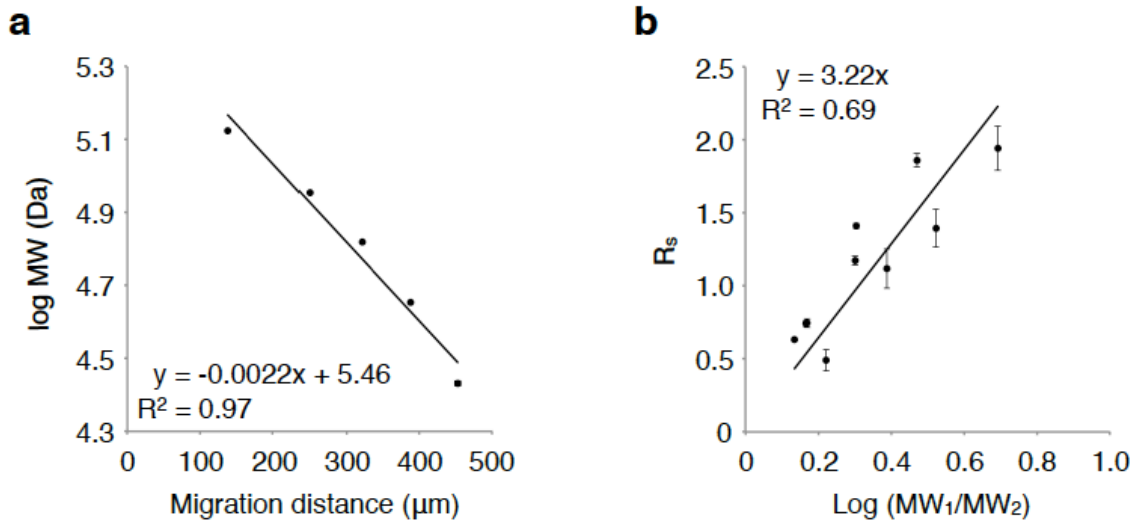

Figure A.5. Separation properties of fluorescently-labeled proteins in scWestern gel sheets. (**a**) Log-linear plot of species molecular weight against migration distance in an 8%T scWestern gel forthe fluorescently labeled species in Fig. 2.1d (x-axis error bars within point size (± s.d., n = 3 separations); Dronpa, 27 kDa; OVA, 45 kDa; BSA, 66 kDa; OVA', 90 kDa; BSA', 132 kDa). (**b**) Assuming consistent protein band widths (s.d. σ_i), plots of separation resolution $R_s = |x1 - x2|/(2\sigma_1 + 2\sigma_2)$, where x_i are migration distances, between band pairs are expected to be linear in the log ratio of their molecular weights[2]. A linear fit of these data is shown, yielding a resolvable molecular weight difference of 51 ± 1.6% (± s.d., n = 3 separations) for purified proteins separated from scWestern microwells upon substitution of $R_s = 1$.

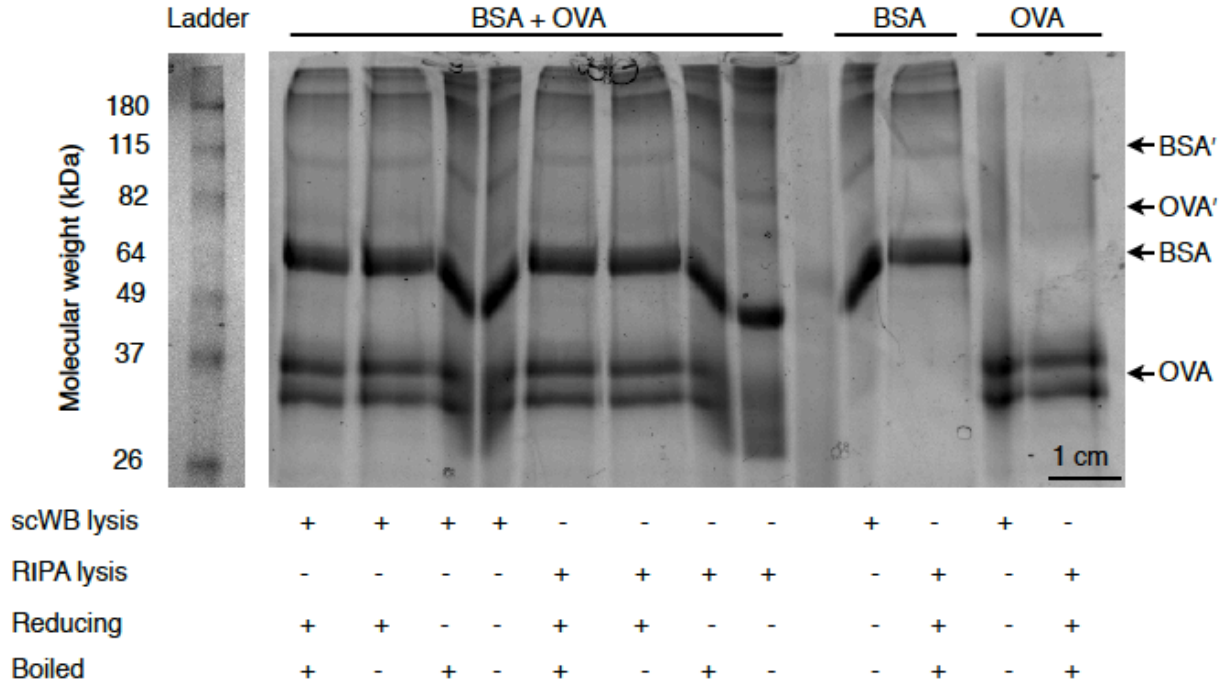

Figure A.6. Identification of covalent dimers in purified Alexa Fluor 488-labeled OVA and BSA samples by conventional SDS-PAGE. Intrinsic fluorescence distributions are similar to scWestern distributions (Figs. 2.1d and A.7) under a range of sample treatments from denaturing to denaturing and reducing, both with and without sample boiling. Note the presence of covalent dimers of OVA and BSA (OVA' and BSA', respectively).

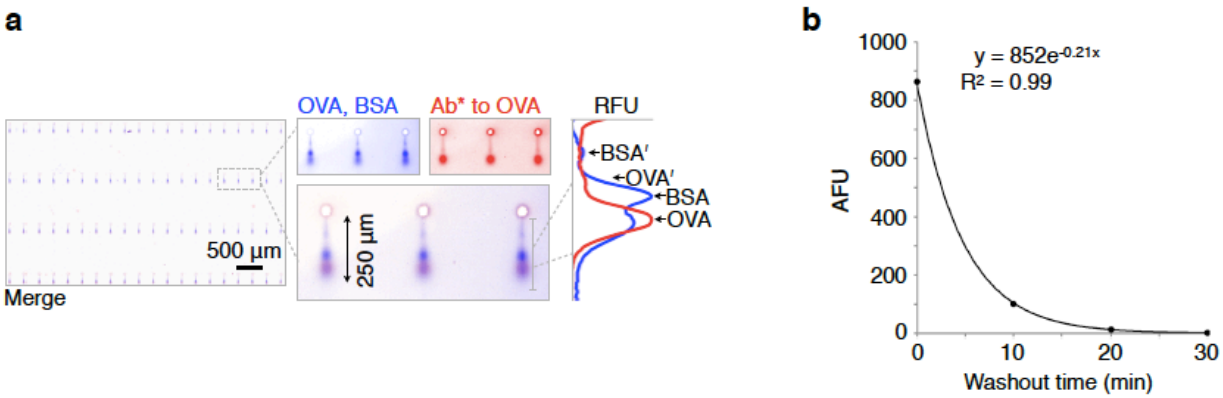

Figure A.7. In-gel probing of gel-captured purified protein separations. (**a**) A mixture of Alexa Fluor 488 labeled OVA and BSA was separated and captured in the sandwich slide configuration over separation distances consistent across the slide (distance of probed OVA band from microwell lip within block: 167 ± 6.5 µm, ± s.d., n = 6 separations; between blocks: 164 ± 3.8 µm, ± s.d., n = 3 blocks). OVA species were probed using a specific primary antibody and an Alexa Fluor 568-labeled goat anti-rabbit IgG secondary antibody, utilizing a separate spectral channel from the Alexa Fluor 488 dye used to label the captured analytes. RFU: relative fluorescence units. (**b**) Residual slide fluorescence determined by fluorescence microscopy for TBST washing of an 80 µm-thick gel layer after incubation with 100 nM Alexa Fluor 568-labeled anti-ovalbumin in free solution for 30 min. The time constant τ = 4.8 min for antibody equilibration with the scWestern gel layer is the inverse of the exponent of the fit.

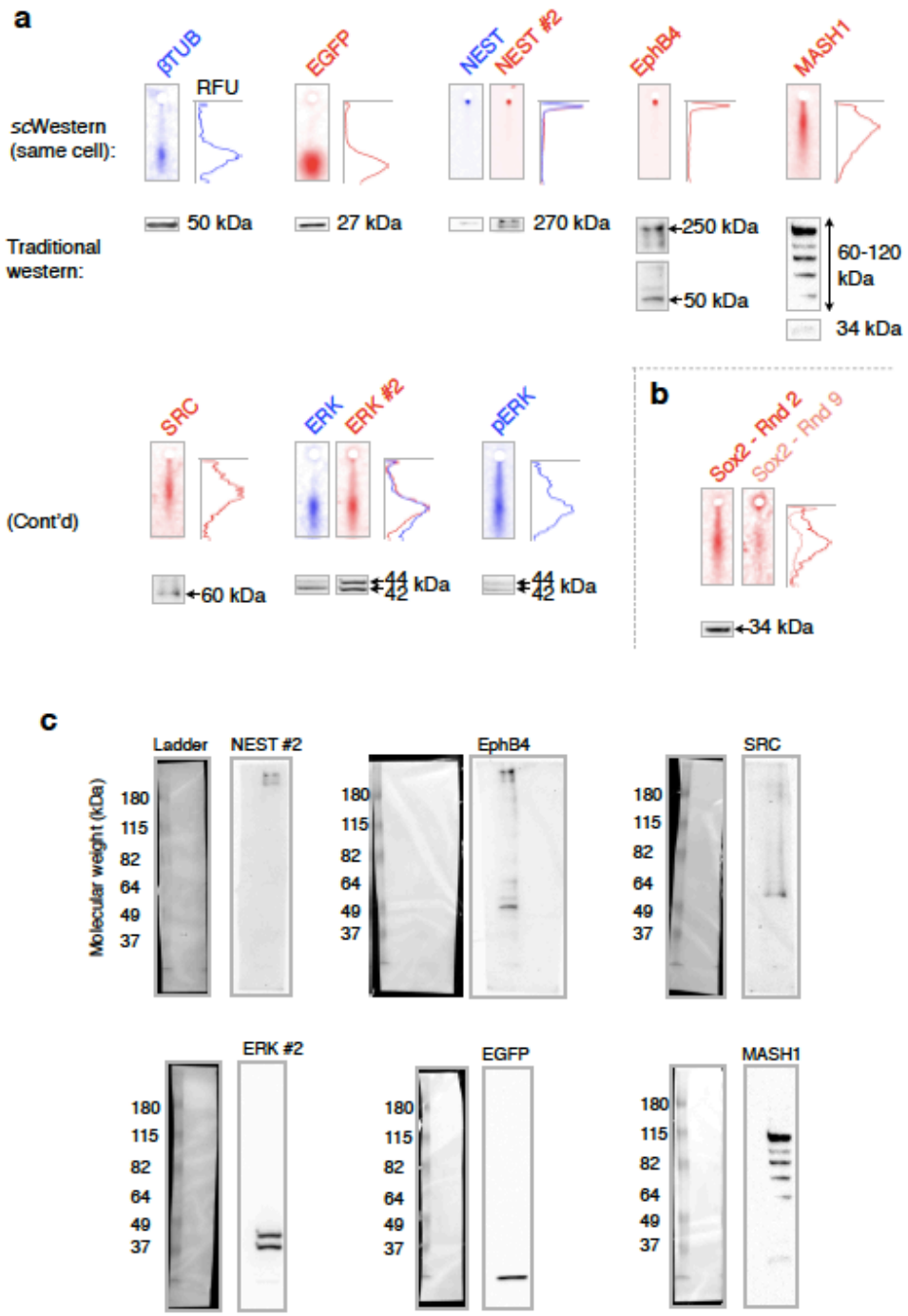

Figure A.8. 11-plex scWestern assay by stripping and reprobing. (**a**) Representative scWestern blots for 9 unique protein targets assayed in the same NSC in 9 stripping and reprobing rounds using 11 antibody probe sets. NEST and ERK targets were each probed with two different probe sets. (**b**) Sox2 was probed with the same probe set in rounds 2 and 9, showing 50% relative signal recovery by comparing area under fluorescence curves. (**c**) Full conventional western blots.

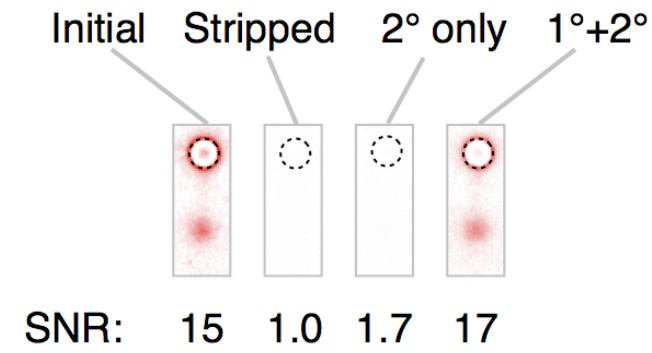

Figure A.9. Stripping and reprobing of scWestern slides. The "direct" EGFP calibration slide from Fig. 2.2d was imaged, stripped and reprobed with either an Alexa Fluor 555-labeled secondary (2°) antibody only (negative control), or with a primary (1°) and Alexa Fluor 555-labeled secondary antibody to EGFP. The signal-to-noise ratio (SNR) of the example reprobed separation approximately matches that of the original probing, while the example negative control separation shows negligible specific signal.

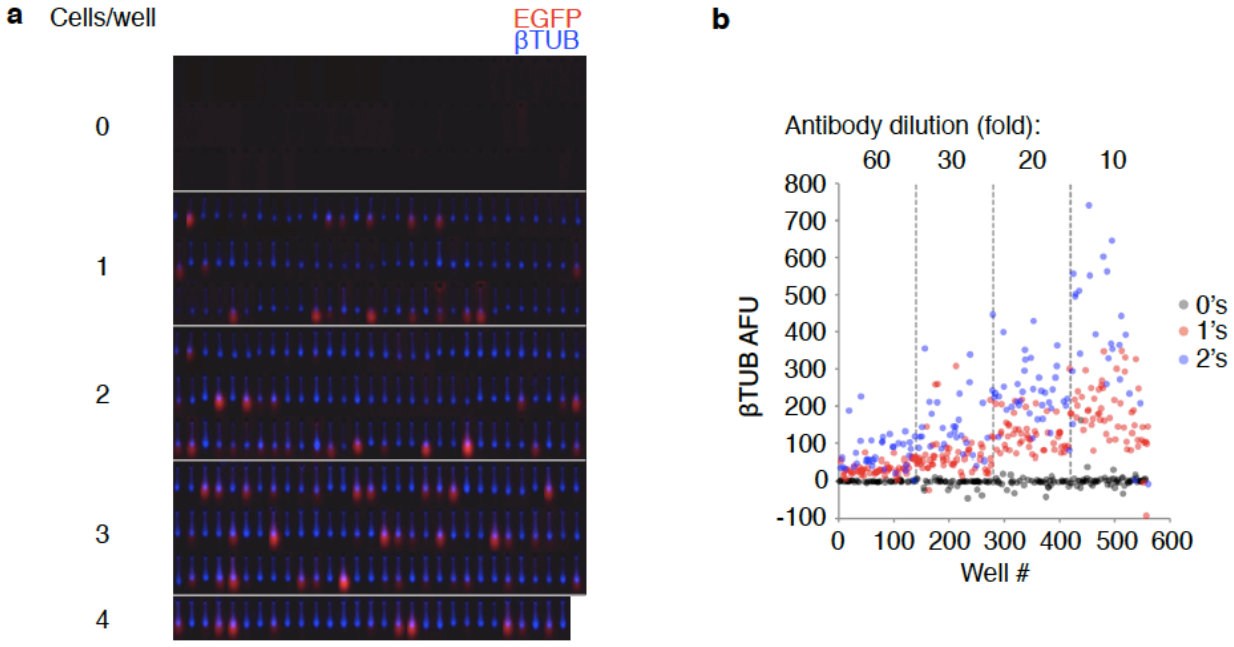

Figure A.10. Cell number and antibody dilution dependence of scWestern readouts. (**a**) A random sample of separations presented in Fig. 2.2 ranked by cells/microwell. All separations passed semi-automated screening for dust and other fluorescence artifacts. **(b)** In a separate experiment, scWesterns were performed on undifferentiated NSCs at anti-β-tubulin primary and Alexa Fluor 555-labeled secondary antibody dilutions of between 60× and 10×. Gains in absolute fluorescence signal above zero cell/microwell controls are observed for one and two cell/microwell separations across the dilution range. AFU: arbitrary fluorescence units.

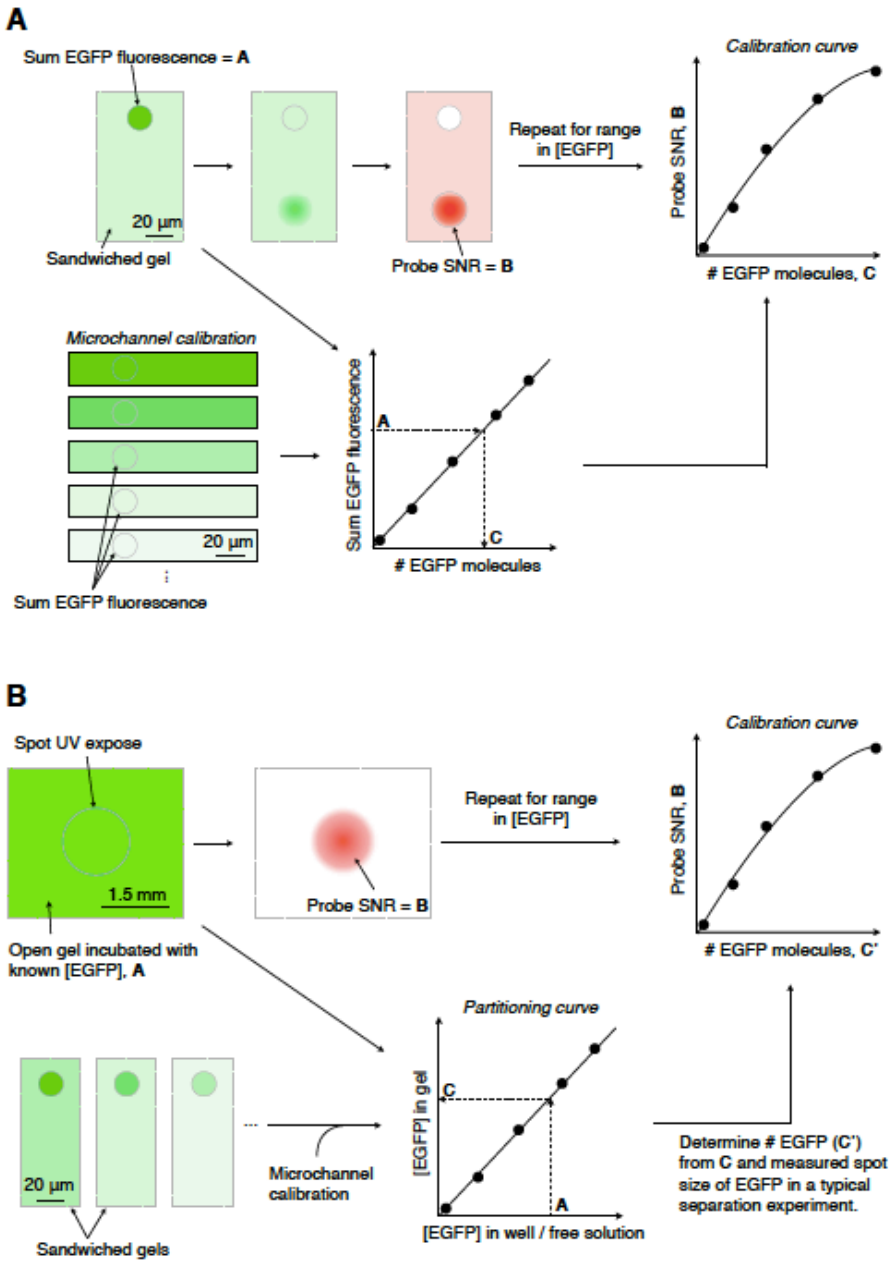

Figure A.11. Direct and indirect calibration procedures for the example of purified EGFP. A sketch of two calibration methods used to determine dynamic range and limit of detection in the scWestern assay (Note A.6). (**a**) Direct calibration by counting EGFP molecules in microwells prior to separation and capture. (**b**) Indirect calibration by inferring number of EGFP molecules from a partitioning curve (Fig. A.4) constructed in a separate experiment in which the microwell and gel EGFP concentrations are inferred from fluorescence values taken at equilibrium.

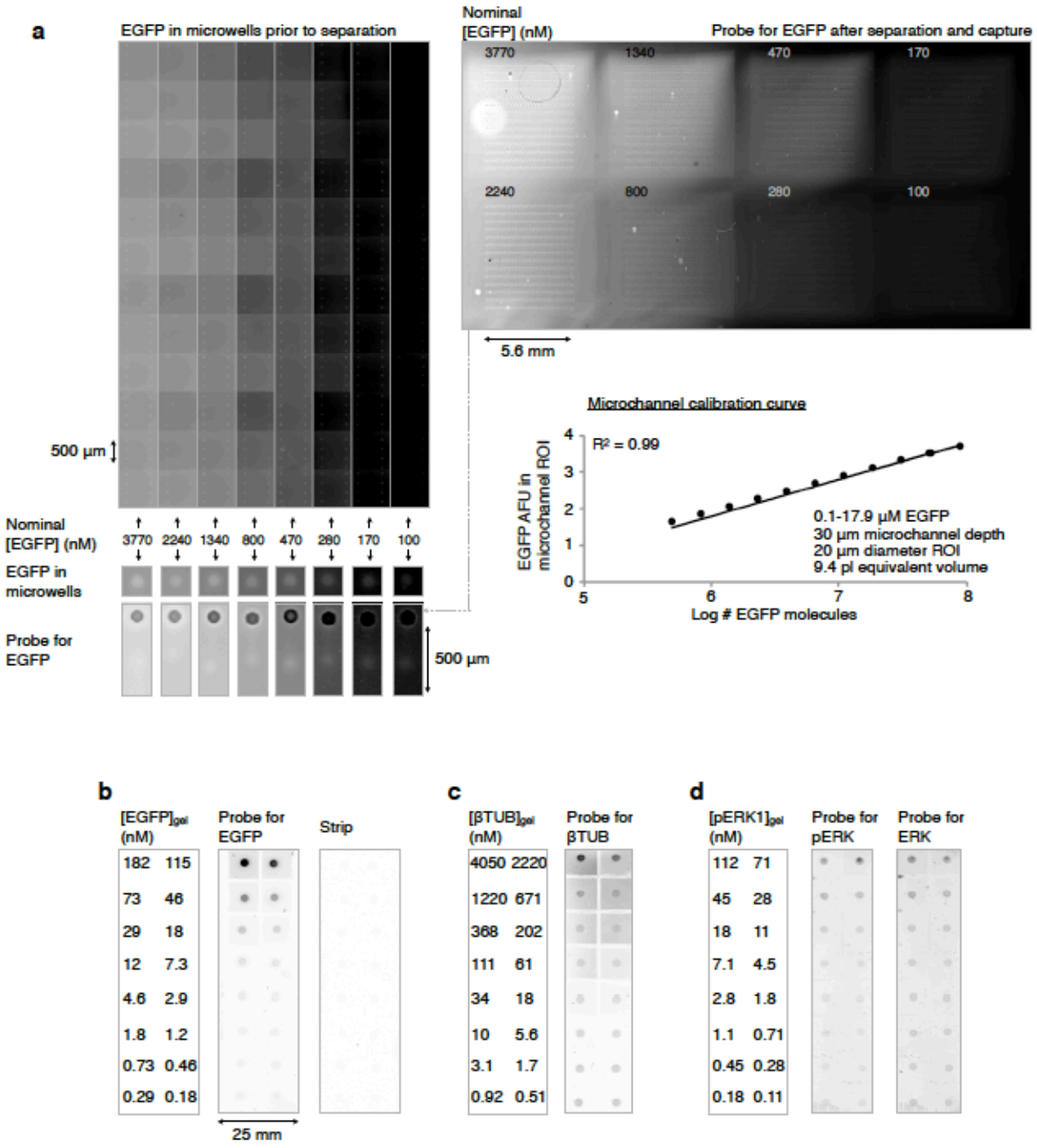

Figure A.12. Direct and indirect calibration slides used for calibration curves in Fig. 2.2d. (**a**) Top-left: Log transformed montage of a subset of microwells from blocks incubated with a range in purified EGFP concentrations, enclosed with a cover glass, and imaged for intrinsic EGFP fluorescence using widefield fluorescence microscopy. Top-right: Log-transformed probe fluorescence after separation, capture, and probing the same slide for EGFP (Alexa Fluor 555-labeled secondary antibody). Bottom-right: Calibration curve for EGFP in a separate microfluidic channel used to determine molecule numbers of EGFP in microwells (AFU: arbitrary fluorescence units; ROI: region of interest). Bottom left, example microwells and probed separations over the EGFP concentration range. (**b**) scWestern slide incubated with purified EGFP concentrations achieving the indicated in-gel concentrations after adjustment for partitioning (Fig. A.4b), spot exposure to UV, and probing for EGFP (Alexa Fluor 555-labeled secondary antibody). Slide was subsequently stripped and re-imaged under identical scanner settings. (**c,d**) Similar indirect calibration slides for purified β-tubulin (Alexa Fluor 647-labeled secondary antibody) and ERK1/pERK1 (both Alexa Fluor 555-labeled secondary antibody; slide stripped between pERK and ERK probing).

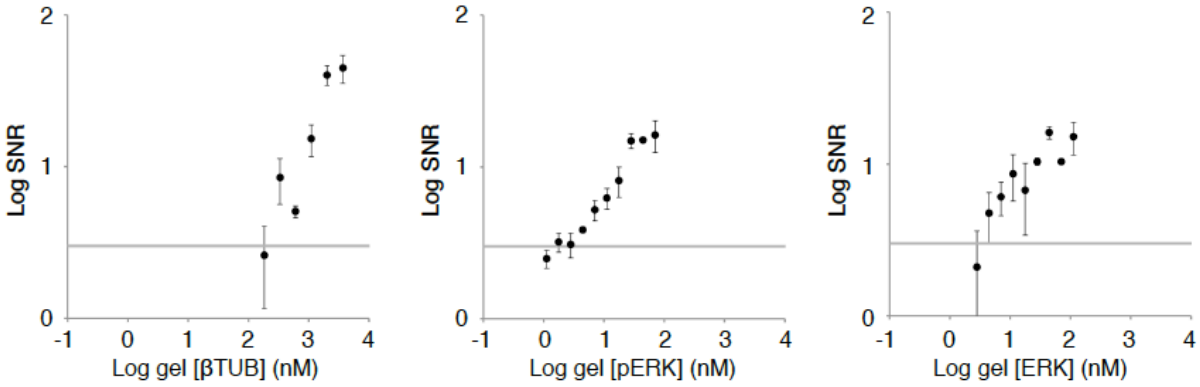

Figure A.13. Plots of SNR for indirect calibration curves in Fig. 2.2d. Signal-to-noise ratios (SNRs) for indirect calibration curves in Fig. 2.2d set concentration limits of detection for each purified target at SNR = 3.

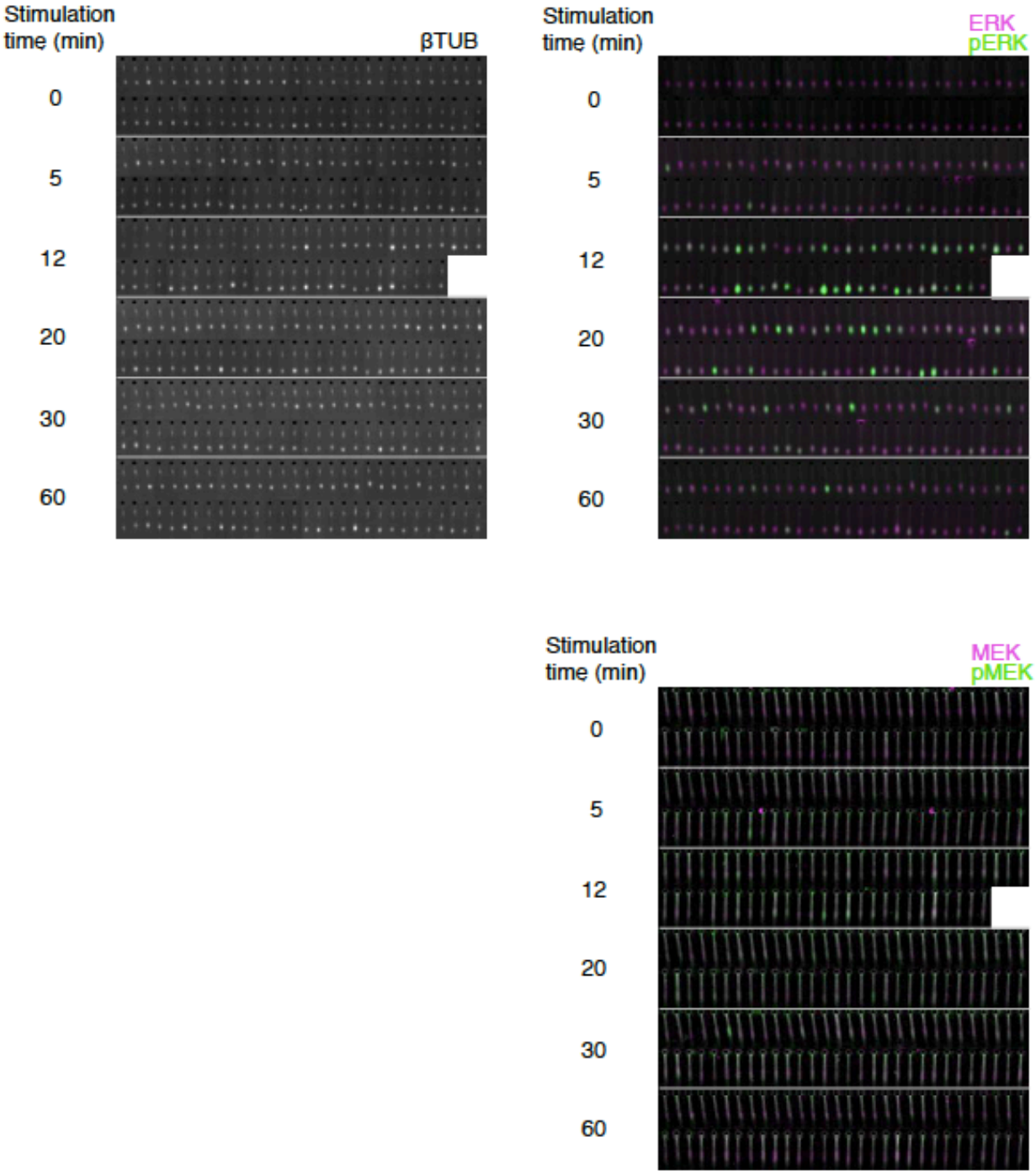

Figure A.14. A random sample of separations for data presented in Fig. 2.3d. All micrographs are for the same set of separations. All separations are for single cell-per-microwell devices, and passed semi-automated screening for dust and other fluorescence artifacts, as well as for spectral bleedthrough from EGFP co-probing with ERK. We observed distinct bands at inferred molecular masses of 38.8 ± 1.0 kDa (pERK), 39.1 ± 0.6 kDa (ERK), 47.4 ± 1.1 kDa (pMEK), and 48.1 ± 1.8 kDa (MEK; ± S.D., n = 3 separations); nominal masses are pERK-ERK: 43 kDa, pMEKMEK: 46 kDa.

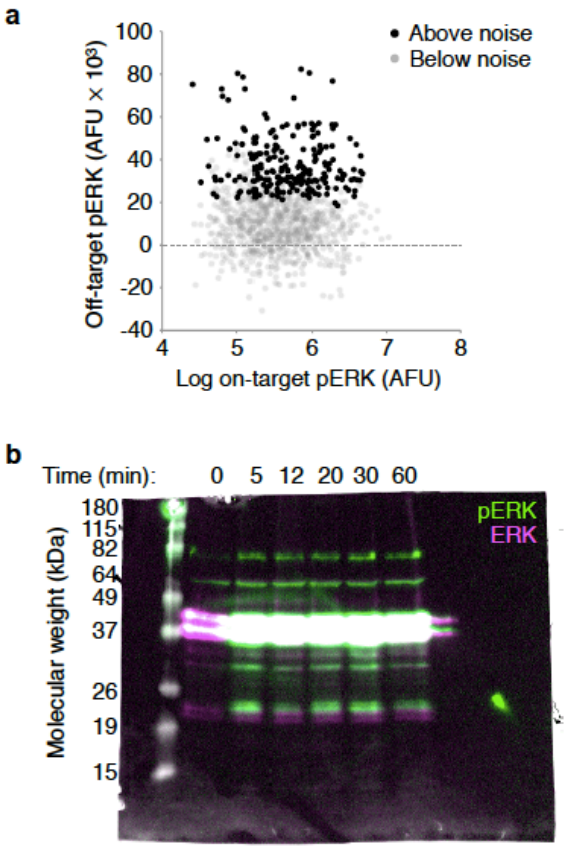

Figure A.15. Off-target signal in scWestern and conventional western blotting for pERK. (**a**) Plot of total scWestern fluorescence of the putative off-target pERK band at 103 kDa against the specific fluorescence at the 39 kDa pERK band across all time points of the FGF stimulation experiment in Fig. 2.3. AFU: arbitrary fluorescence units. (**b**) Over-exposed conventional western blots of pERK and ERK showing putative non-specific pERK bands at ~65 and 80 kDa.

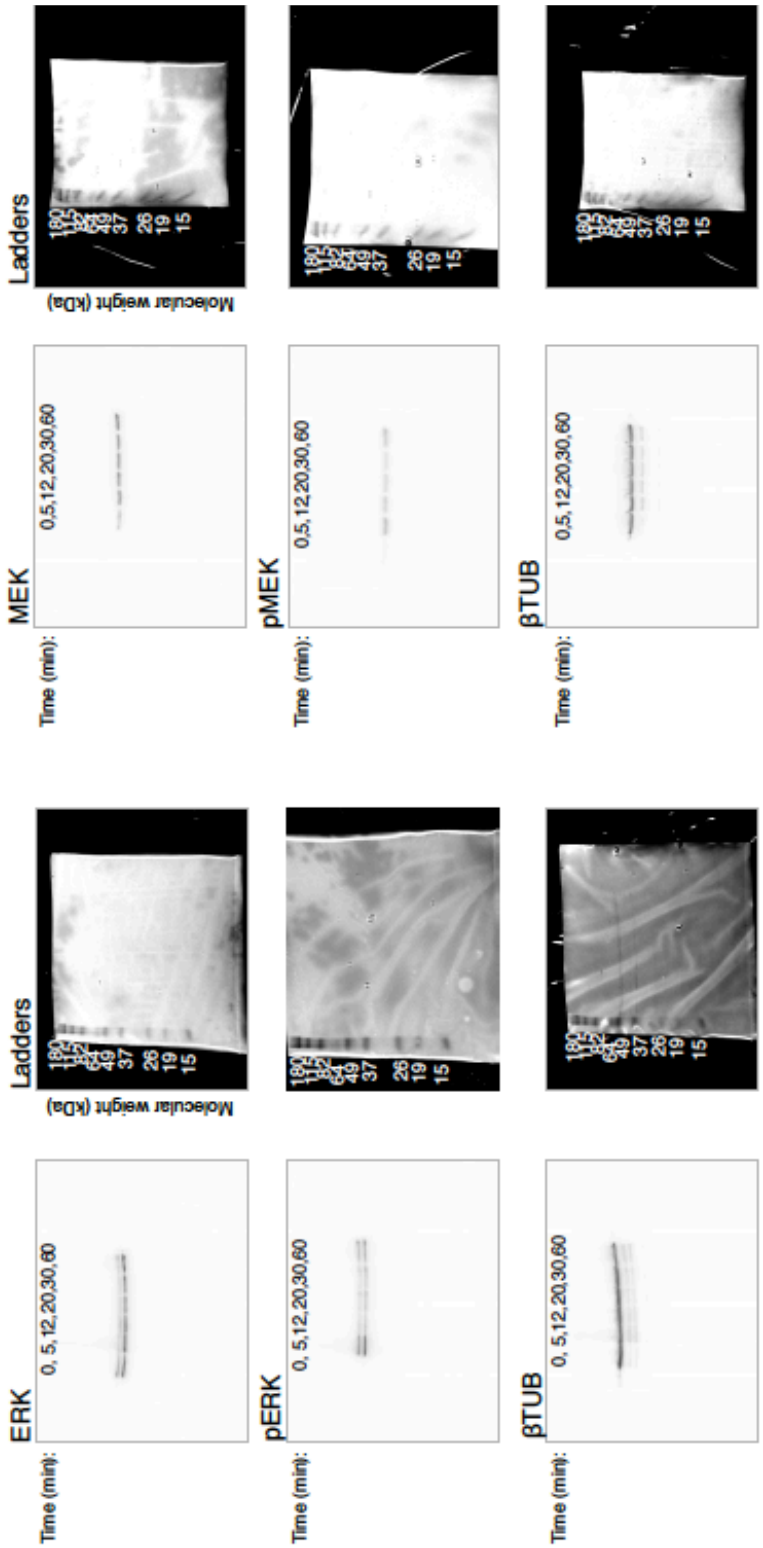

Figure A.16. Full conventional western blots for the stimulation experiment in Fig. 2.3c.

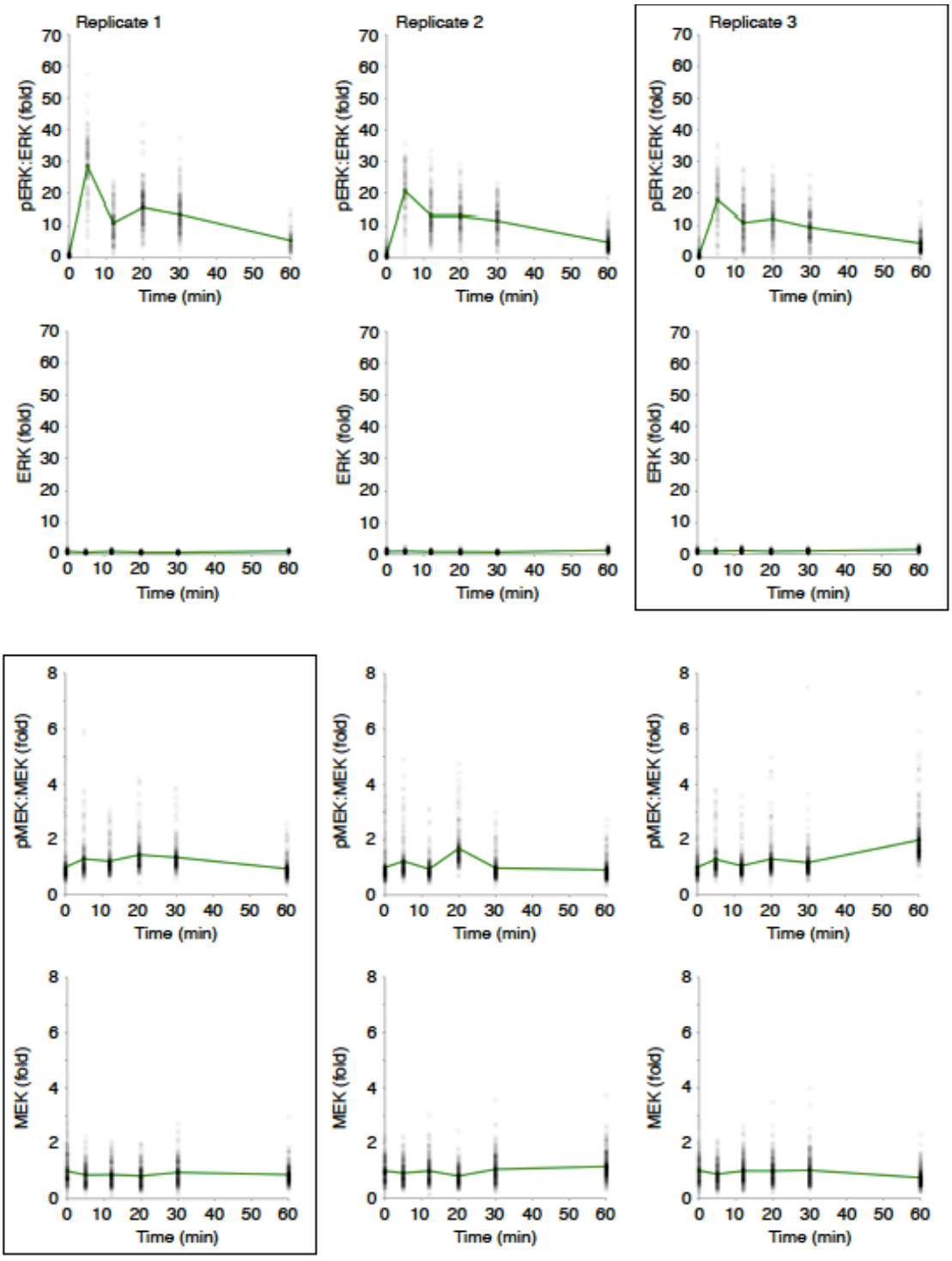

Figure A.17. Full data for the ICC study complementing scWestern data for FGF stimulation of NSCs in culture plates in Fig. 2.3f. Cells were co-probed for pERK/ERK and pMEK/MEK pairs, phosphorylated targets were probed using an Alexa Fluor 555-labeled secondary antibody, and total targets with Alexa Fluor 647-. Data for pMEK/MEK probed separately are presented in Fig. A.18. Specific replicates presented in Fig. 2.3f are shown in boxes. Mean pMEK:MEK ratio does not exceed 2 across the 3 replicates; mean ERK and MEK values show little variation over the stimulation time course.

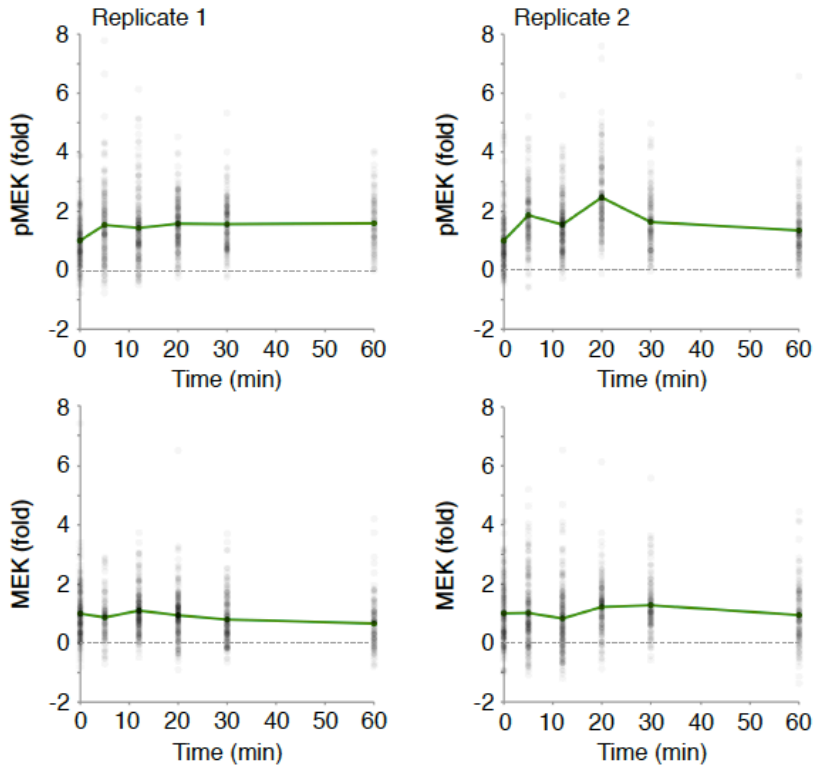

Figure A.18. Single-probe pMEK/MEK distributions for the ICC study in Fig. 2.3f. pMEK and MEK targets were probed in separate cells to examine the possibility of epitope competition between antibodies in the co-probing experiment (Cy3-labeled secondary antibody). No evidence of competition is observed, since mean pMEK fold-change values are in a similar range as mean pMEK:MEK values in Fig. A.17.

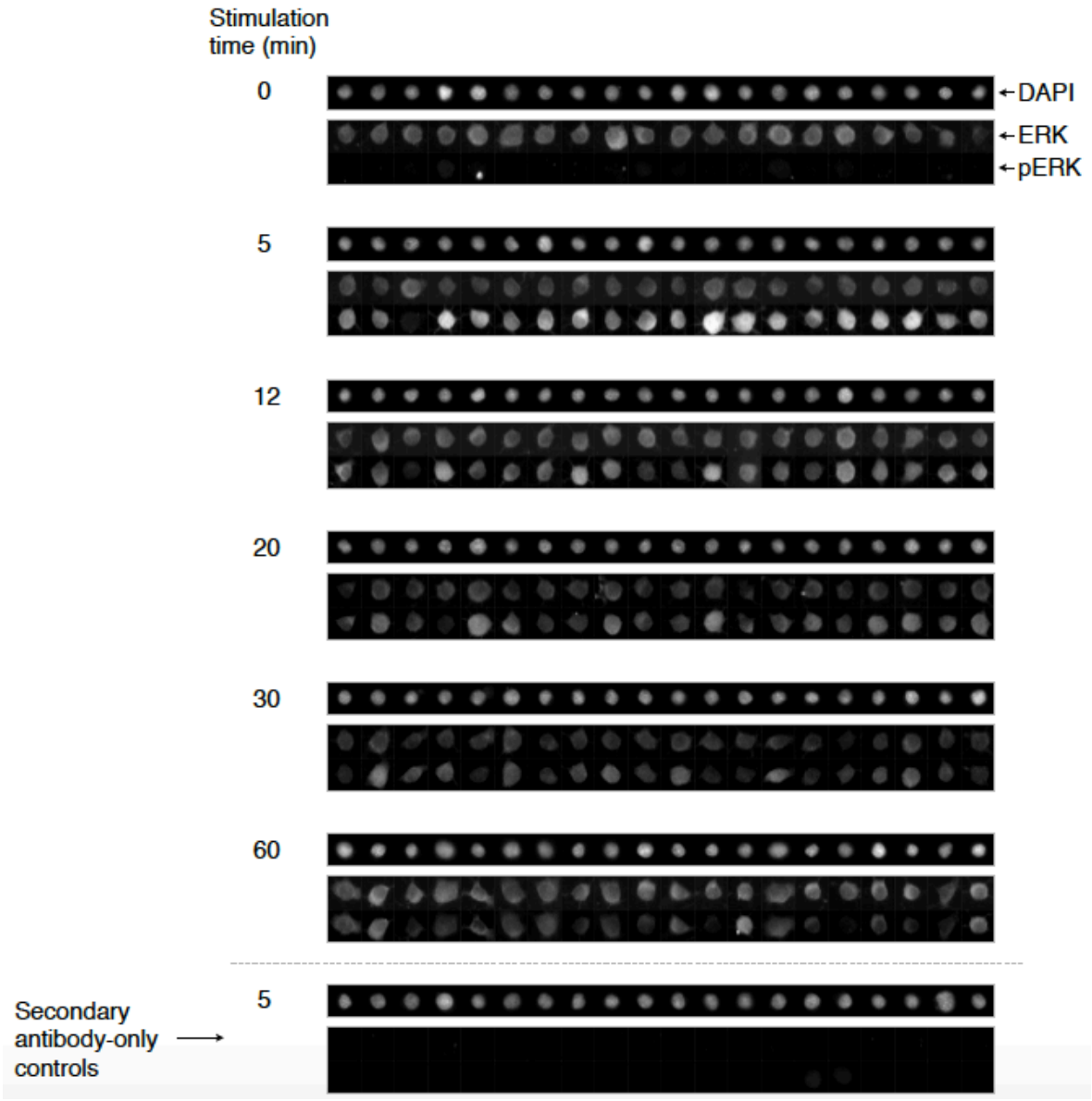

Figure A.19. Example single-cell ROIs chosen at random, as determined by automated analysis of culture plate ICC fluorescence micrographs of pERK and ERK targets for the FGF stimulation experiment in Fig. 2.3f. See Fig A.17 for experimental details.

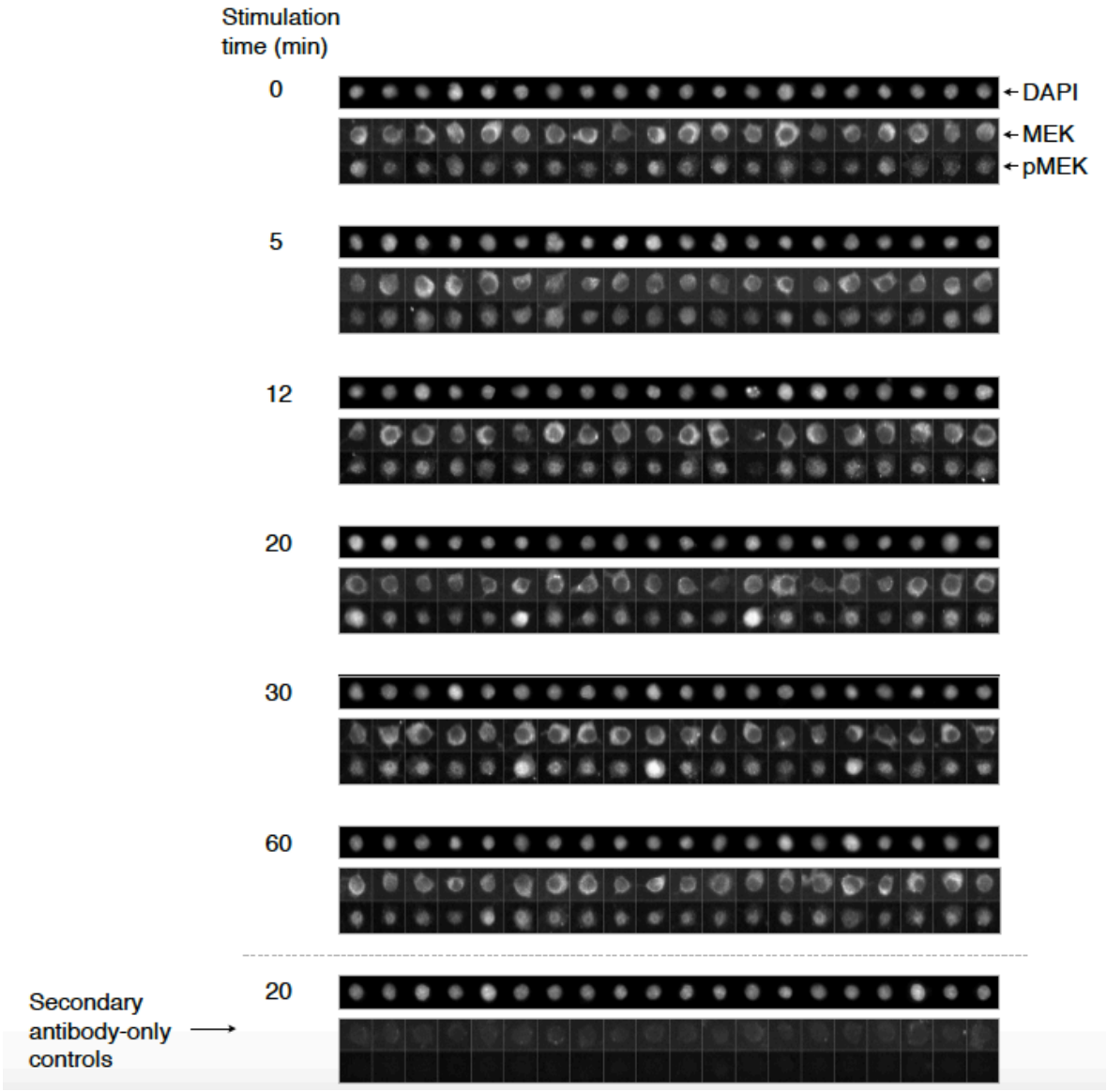

Figure A.20. Example single-cell ROIs chosen at random, as determined by automated analysis of culture plate ICC fluorescence micrographs of pMEK and MEK targets for the FGF stimulation experiment in Fig. 2.3f. See Fig. A.17 for experimental details. Note improper nuclear localization of the primary antibody to pMEK; secondary antibody controls do not account for this apparent localization.

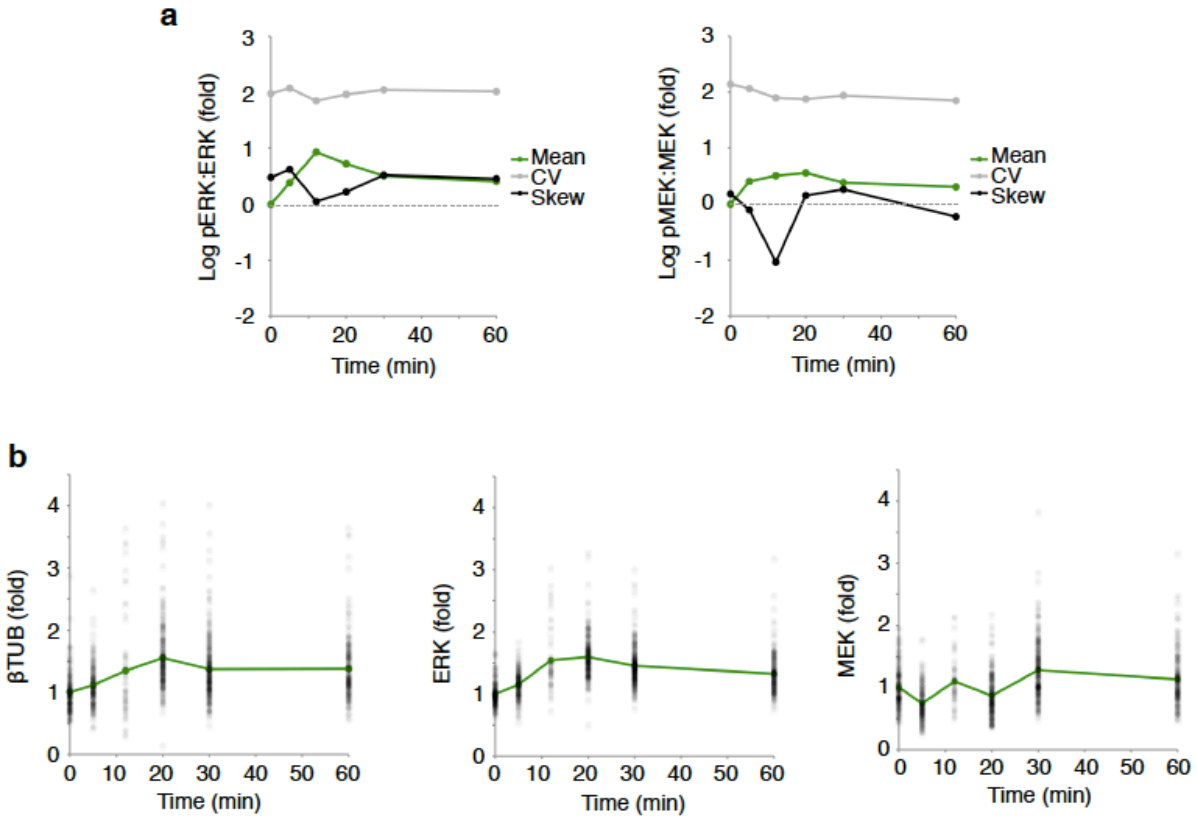

Figure A.21. Distribution statistics for pERK:ERK and pMEK:MEK, and fold-change dot plots for β-tubulin, ERK, and MEK over the FGF stimulation time course for scWestern data in Fig. 2.3d. (**a**) Relationship between skewness and mean for pERK:ERK and pMEK:MEK distributions over the stimulation time course. Note CV and skewness are in percentage and dimensionless units, respectively, plotted on the same scale as fold fluorescence ratio data for convenience. (**b**) Fold-change in arbitrary fluorescence for β -tubulin, ERK, and MEK show little variation across the cell populations at each stimulation time.

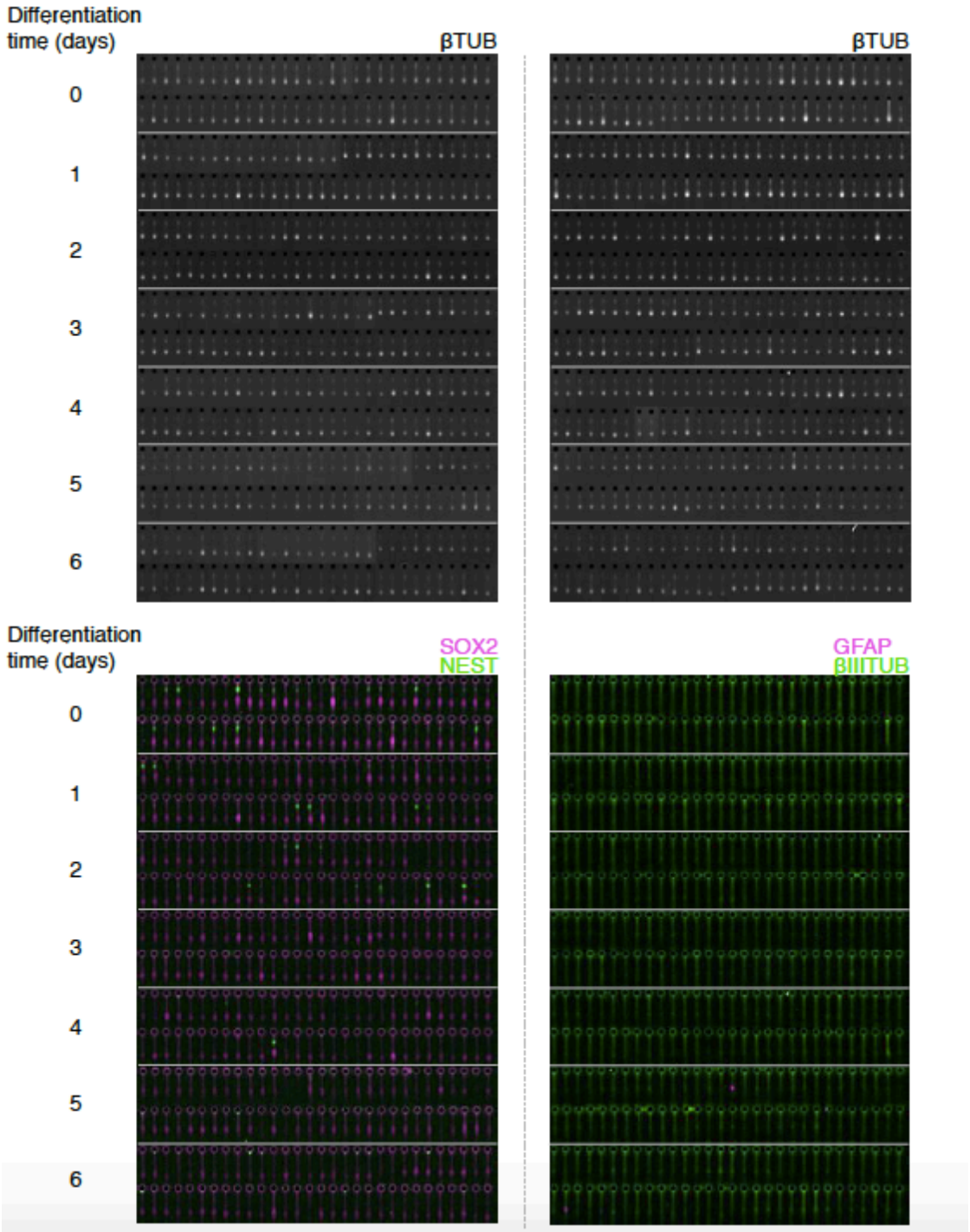

Figure A.22. A random sample of scWestern separations for data presented in Fig. 2.4f. β-tubulin (βTUB) micrographs match separations for two-color micrographs within columns. All blots are for single cell-per-microwell devices, passed semi-automated screening for dust and other fluorescence artifacts, and screening for spectral bleedthrough from EGFP co-probing with β-tubulin.

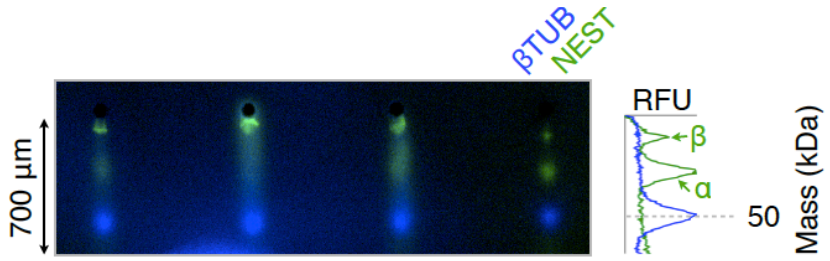

Figure A.23. An example fluorescence micrograph of scWestern separations of single undifferentiated NSCs produced similarly to Fig. 2.4d by probing for NEST and βTUB targets, except using a longer overall separation distance. At right, a NEST fluorescence profile beginning at the microwell edge shows that the NEST$^{\beta}$ isoform fully penetrates the scWestern gel.

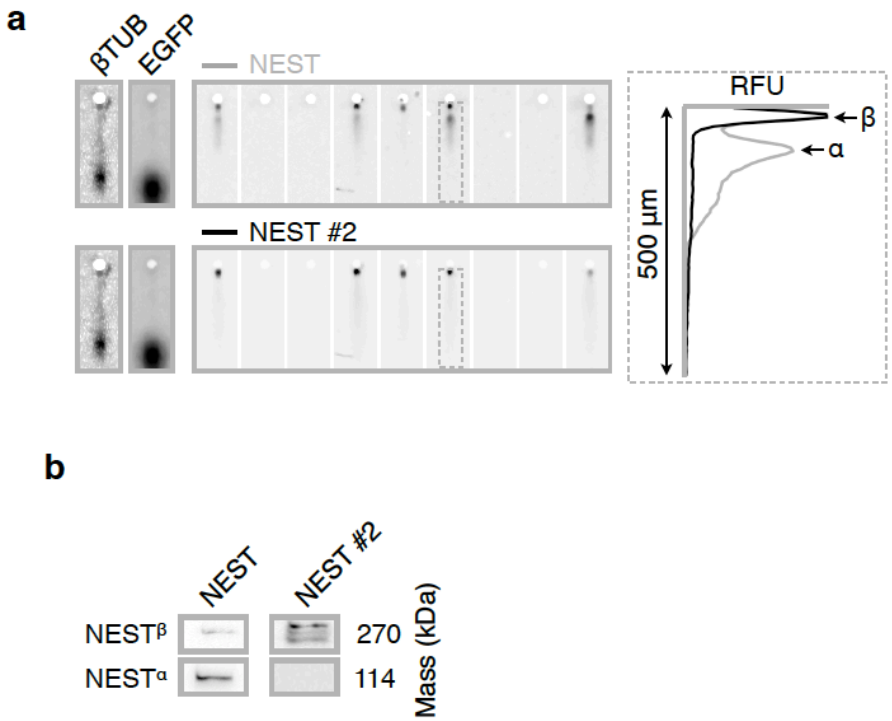

Figure A.24. Differential NEST isoform detection using alternative probe sets. (**a**) Inverted fluorescence micrographs of example scWestern blots probed with two probe sets for NEST in separate stripping and reprobing rounds. Note a lack of detection of the NEST$^{\alpha}$ isoform via the NEST #2 (rat-401) antibody. (**b**) Conventional western blots corroborating isoform specificity of the two NEST probe sets (see Figs. A.8 and A.25 for full conventional blots).

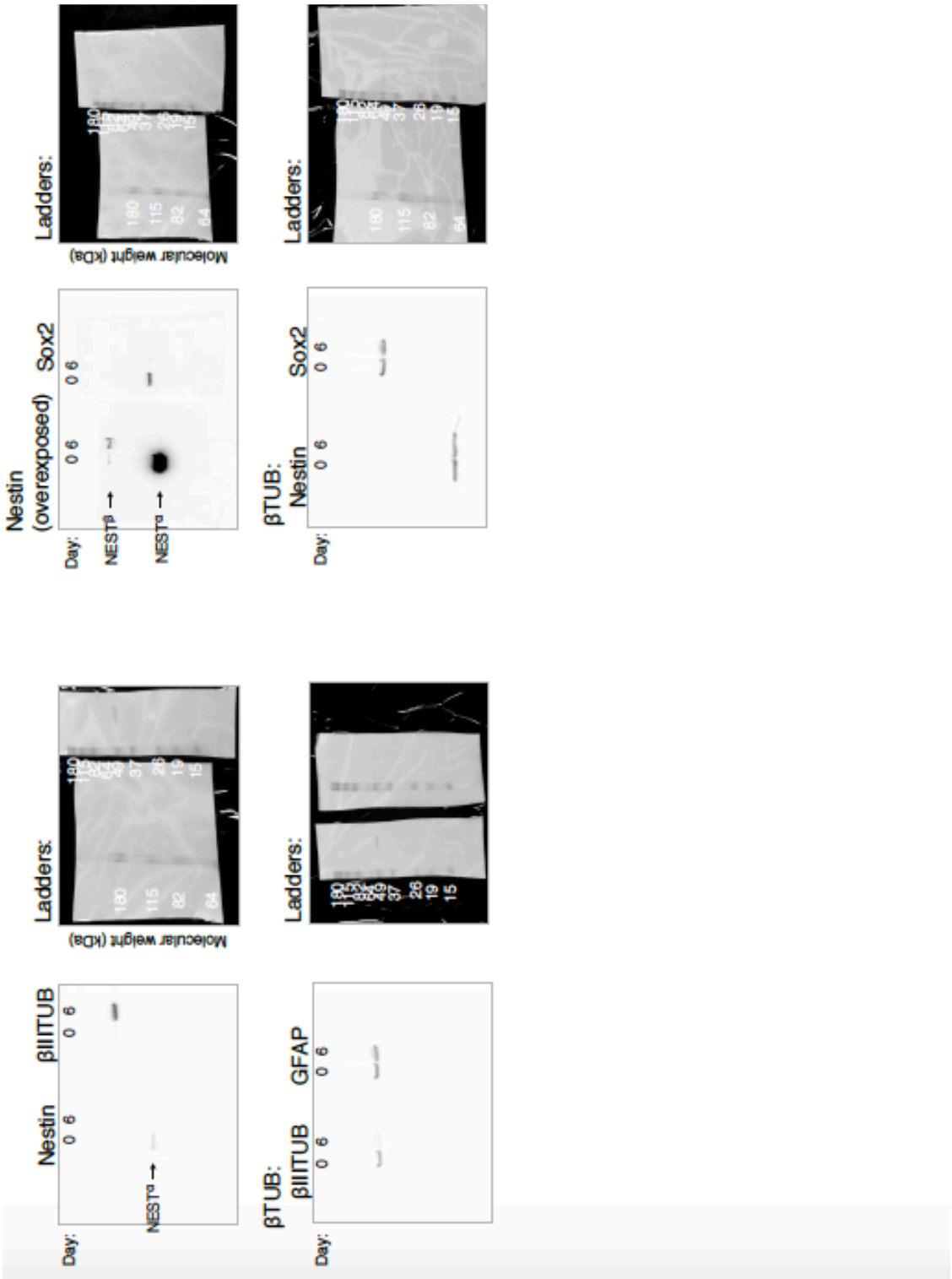

Figure A.25. Full conventional western blots for the differentiation experiment in Fig. 2.4e.

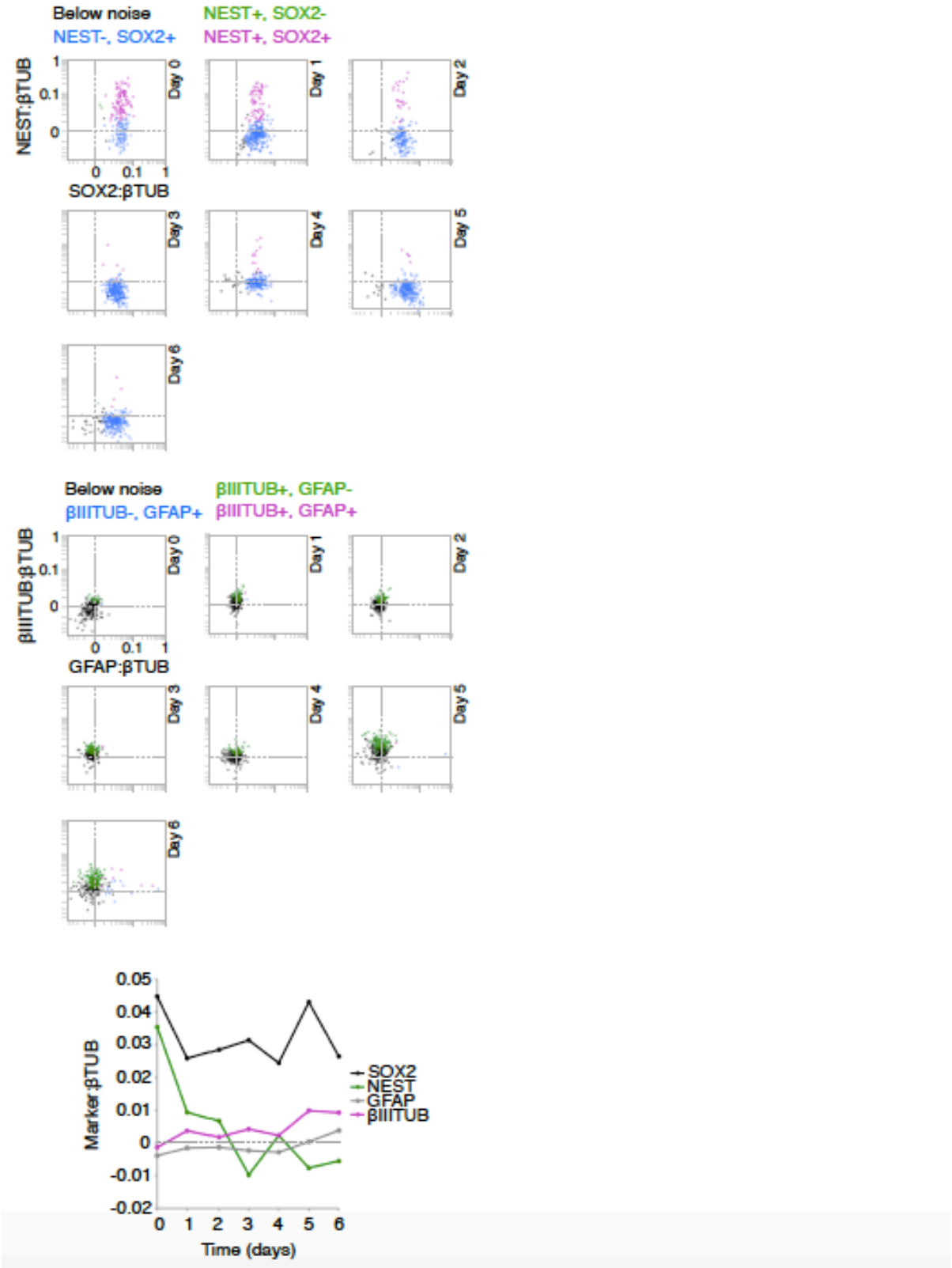

Figure A.26. Full stem cell and differentiation marker expression data for Fig. 2.4f.

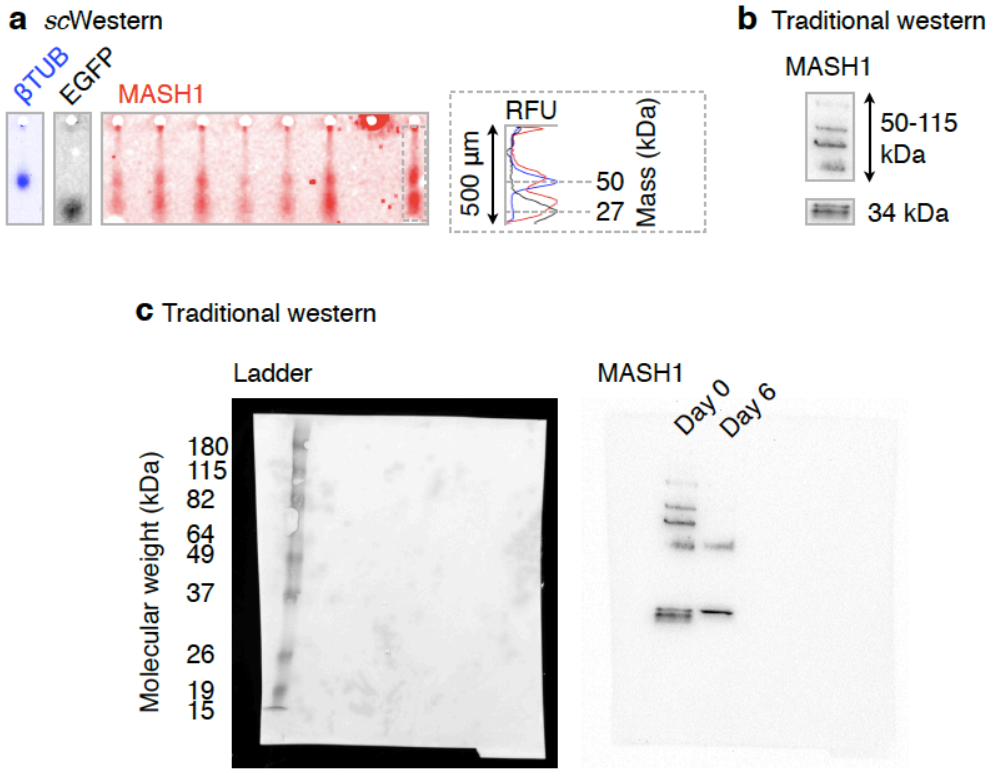

Figure A.27. Detection of the 34 kDa transcription factor MASH1 against strong off-target antibody specificity by scWestern blotting. (**a**) Example inverted fluorescence scWestern blots of late-passage (passage 39) undifferentiated (day 0) NSCs assayed for MASH1, βTUB, and EGFP. Note separation of the specific 34 kDa peak from a nonspecific peak in the 50–100 kDa range. Specific fluorescence signal (area under curve) is 49% of total signal for the example separation shown. (**b,c**) corresponding conventional western blots for MASH1 confirming a distribution of specific and off-target bands.

Table A.1. **Percentage of cells scoring as marker positive by culture plate and in-microwell ICC (± s.d., n = 3 technical replicates, >100 cells scored per replicate), and by thresholds set at technical noise levels in single-cell scWestern fluorescence data from Fig. 2.4f at differentiation days 0 and 6**. Of particular interest are endpoint counts for neurons (βIIITUB+) and astrocytes (GFAP+), in bold. N.B. both ICC and scWestern assays do not reflect the precipitous drop in SOX2 expression observed by conventional western blotting between days 0 and 6 (Fig. 2.4e), perhaps indicating off-target antibody readouts in each, further evidenced by the relatively high error in the molecular mass of SOX2 predicted by scWestern analysis (Note A.8).

	Culture plate ICC		In-microwell ICC		*sc*Western	
	Day 0	Day 6	Day 0	Day 6	Day 0	Day 6
SOX2+	98.8 ± 2.1	99.3 ± 0.7	93.3 ± 7.1	73.4 ± 4.6	97.9	89.1
NEST+	93.6 ± 4.1	46.1 ± 9.4	87.3 ± 10.0	40.3 ± 2.1	52.6	1.8
βIIITUB+	2.8 ± 1.4	**51.8 ± 3.0**	1.9 ± 1.5	**61.9 ± 2.1**	12.3	**52.7**
GFAP+	0.0 ± 0.0	**8.0 ± 2.7**	0.6 ± 0.2	**11.9 ± 2.7**	0.6	**7.1**

A.2 Supplementary Notes

Note A.1. Mass transport regimes during in-microwell lysis.
Overall, fluid dynamics simulations suggest a recirculating flow in the first ~20 μm of microwell depth with a nearly stagnant flow occupying the bottom 10 μm of the microwells (Péclet number $Pe < 1$). As cells settled in the stagnant zone at the base of microwells are largely shielded from advective transport, we hypothesize that diffusion is largely responsible for protein loss from the microwells.

Specifically, COMSOL modeling showed a monotonic decrease in local fluid velocity as a function of vertical distance into the microwell beneath the gel surface, except in the vicinity of a recirculating eddy near the top of the microwell. Beneath this, a critical local fluid speed of 4.4 μm s^{-1} giving a Peclet number of 1 was determined via $Pe = Lu/D$, where the characteristic length L is the microwell diameter (20 μm), and u is the local fluid velocity. $D = k_B T/6\pi\mu r_H = 8.8 \times 10^{-11}$ m^2 s^{-1} is the free-solution diffusivity of EGFP as a low molecular weight model analyte, with the Boltzmann constant $k_B = 1.38 \times 10^{-23}$ m^2 kg s^{-2} K^{-1}, temperature $T = 293.15$ K, dynamic viscosity of water $\mu = 0.001$ kg m^{-1} s^{-1}, hydrodynamic radius $r_H = 0.595(M_w)^{0.427} = 2.43$ nm (Mw = 27 kDa, the molecular weight of EGFP)[3].

The isotach at this critical speed of 4.4 μm s^{-1} approximately demarcates regions of diffusively and advectively-dominated mass transport regimes during lysis buffer pouring for microwell coordinates below ($Pe < 1$) and above ($Pe > 1$) it in the z direction, respectively (Fig. A.3).

Note A.2. Partitioning of proteins between free solution and polyacrylamide gels.
Particles including proteins are expected to partition between dense hydrogel networks and free solution according to a partition coefficient, K, a ratio of c_l and c_b, the local gel and bulk free solution protein concentrations[4]:

$$K = \frac{c_\ell}{c_b} = e^{-\phi\left(1+\frac{a}{a_f}\right)^2} \quad (1)$$

Where ϕ is the volume fraction of the polymer network, a is the Stokes-Einstein radius of the protein and a_f is the polymer fiber radius. A demonstration of equilibrium partitioning and repeated injections of the fluorescent protein Dronpa from scWestern microwells is reported in Fig. A.4, along with measured partition coefficients for a range of proteins targets.

Given the anticipated partitioning effect, which is expected to be exacerbated by the large (~150 kDa) size of probe antibodies, we determined the equilibration time of probe antibodies in an 80 μm-thick scWestern gel layer (Fig. A.7). After incubating a fluorescently labeled primary antibody in the free solution above a gel-coated slide for more than 30 min, the slide was washed in TBST and imaged periodically. As antibody left the slide by diffusion, an exponential decay in the slide fluorescence was observed with a time constant τ of roughly 5 min, and the time for complete washout of $\sim 4\tau = 20$ min compares well with an estimated diffusion time $t \sim x^2/2D =$ 12 min where $D \sim 4.3 \times 10^{-12}$ m^2 s^{-1} for diffusion of a 150 kDa antibody in an 8%T PA gel[3]. In practice, the gel layers are typically 30 μm thick to limit the incidence of vertical stacking of multiple cells within the microwells by more closely matching the dimension of a cell. Here, we would expect antibody diffusion times of less than 5 min.

This experiment indicates that rapid equilibration of probe antibodies with the scWestern gel can be achieved during probing and washing, given its microscale thickness, although the solution concentration of probe must be increased to compensate for the effect of partitioning in reducing the gel concentration of the probe by a measured partition coefficient of 0.17 with respect to its bulk solution concentration (Fig. A.4). Specifically, we chose antibody dilution factors of 1:20 to provide an acceptable balance between scWestern fluorescence signal and reagent consumption for EGFP and β-tubulin (Fig. A.10). Under these probing conditions, we estimate consumption of 2 μg of each antibody per gasket well comprised of 420 scWestern separations or 4.8 ng per separation (comparable to ~0.5–10 μg of each primary antibody per lane of a conventional slab-gel western blot or 1–5 μg per well in a 6-well ICC plate).

Note A.3. Effect of lysis buffer composition on separation performance in scWestern blotting.
We have observed that scWestern separations performed under denaturing conditions alone are comparable to conventional western blot separations performed under denaturing and reducing conditions for both purified proteins (Figs. 2.1c and A.6) and cellular proteins (Figs. 2.3a,c; 2.4d,e; and A.8). Also, scWestern separations follow a log-linear relationship between protein molecular weight and migration distance that is characteristic of denaturing, reducing conditions[5,6] (Fig. A.5). We hypothesize that reductants in the scWestern separation buffer system are redundant for many protein targets since, firstly, the vast majority of cellular proteins do not contain disulfide bonds under the reducing conditions of the cell; notable exceptions being those targeted for extracellular secretion or to the plasma membrane via the endoplasmic reticulum[7,8] (members of the latter membrane protein class cannot be reliably sized by conventional SDS-PAGE in any case, even when quantitatively reduced[9]). Secondly, unlike in conventional western blotting, disulfide bonds would not form appreciably during the 10 s lysis time prior to electrophoresis in scWestern blotting, since the characteristic time for disulfide bond formation under non-reducing conditions at a pH similar to that in the assay can be estimated as being in the range of 5–30 min[10]. However, current and future technology development will allow enclosed buffer conditions during cell lysis prior to scWestern blot, enabling exposure of single-cell lysates to sample buffers (including reductants, if desired) over longer timescales.

Note A.4. Cell settling statistics and effect on β-tubulin fluorescence distributions.
The Fano factor describing cell-per-microwell settling distributions deviated from a Poissonian distribution ($F = \sigma^2/\mu = 1$ for Poissonian distributions; $F \sim 0.55$–0.75 for cell-per-microwell distributions; Fig. A.1). We hypothesize that the curtailed cell-per-microwell distributions reflect size bias imposed by microwell seeding, which would reduce the per-cell contribution of β-tubulin along the cell-per-microwell axis. On average, each additional cell above 1 cell/microwell added 79% and 42% of the β-tubulin contribution of the original cell for 2 and 3 cell/microwell separations respectively; with standard deviations of 105% and 36% relative to the expected standard deviations based on simple addition of identical 1 cell/microwell β-tubulin distributions (i.e. $\mu_{f,2} = \mu_{f,1} + 0.79\mu_{f,1}$, $\mu_{f,3} = \mu_{f,2} + 0.42\mu_{f,1}$; $\text{s.d.}_{f,2} = \text{s.d.}_{f,1} + 1.05(\sqrt{2}\text{-}1)\text{s.d.}_{f,1}$, $\text{s.d.}_{f,3} = \text{s.d.}_{f,2} + 0.36(\sqrt{2}\text{-}1)\text{s.d.}_{f,1}$; where $\mu_{f,i}$ and $\text{s.d.}_{f,i}$ are the means and standard deviations in β-tubulin fluorescence signal for i cell/microwell separations, respectively).

Note A.5. Analytical performance of the scWestern assay.
scWestern dynamic range was estimated from the technical noise limit and the maximal cell fluorescence intensity. We determined scWestern technical noise by assessing signal from separations with two characteristics: (i) the microwell contained no cells and (ii) the microwell was distant from microwells that did contain cells. We chose these criteria since scWestern signals from zero cell-per-well separations that are proximal to finite-cell-per-microwell assays were ~10-fold higher than scWestern signals from spatially isolated zero cell-per-microwell separations (from a pixel number-normalized threshold of $\mu_{zeros}+3\sigma_{zeros}$ = 2.5 × 10^4 to 2.4 × 10^5 molecules of EGFP). Consequently, in cell populations with high dynamic range targets, a design tradeoff exists between array density and the fidelity of low copy number limit measurements. After determining technical noise limits, we found ideal dynamic ranges to be comparable for scWestern and conventional flow cytometry assays at 2.9 and 2.6 orders of magnitude, respectively.

Comparing scWestern assays with the recently published microwestern array (MWA) technology[11], increases in sensitivity offered by the scWestern assay architecture that enable single-cell analysis follow primarily from three key engineering developments: (i) a 20-fold reduction in the initial sample dispersion caused by use of in-situ microwell lysis in scWesterns rather than robotic lysate spotting in MWAs, (ii) direct injection of cell contents into the scWestern gel, rather than delivery of lysate proteins by diffusion into the MWA gel, which incurs sample losses due to partitioning and introduces "injection bias" due to variation in partitioning between protein species, and (iii) a 6-fold reduction in sample dispersion during electrophoresis in scWestern assays due to an 18-fold reduction in separation length and 36-fold reduction in separation time in comparison to MWAs, without sacrificing separation resolution.

Specifically, consider Gaussian-distributed bands of EGFP undergoing separations in scWestern assay (scWB) and MWA formats in which the mass of EGFP analyte k is assumed to be a constant for the duration of each separation and diffusion the dominant dispersion mechanism. The analytical limit of detection (LOD) in these assays is inversely proportional to peak height $A = k/(\sigma\sqrt{(2\pi)})$ as a first-order approximation (rather than peak area) where $\sigma = \sqrt{(\sigma_0^2 + 2Dt)}$ is the standard deviation of the peak, here with the term σ_0 taking into account the initial peak width following sample aliquoting and immediately before electrophoretic separation, and a diffusion term $2Dt$ accounting for dispersion of the peak during separation over time t with diffusion coefficient $D \approx 1.35 \times 10^{-11}$ m^2 s^{-1} for EGFP in an 8%T polyacrylamide gel[2,3]. The ratio of detection limits is thus estimated via:

$$\frac{\mathrm{LOD_{scWB}}}{\mathrm{LOD_{MWA}}} \approx \frac{\mathrm{A_{MWA}}}{\mathrm{A_{scWB}}} \approx \frac{\frac{k}{\sigma_{\mathrm{MWA}}\sqrt{2\pi}}}{\frac{k}{\sigma_{\mathrm{scWB}}\sqrt{2\pi}}} \approx \frac{\sqrt{\sigma_{0,\mathrm{scWB}}^2 + 2Dt_{\mathrm{scWB}}}}{\sqrt{\sigma_{0,\mathrm{MWA}}^2 + 2Dt_{\mathrm{MWA}}}} \quad (2)$$

A rough estimate of relative LODs of the two methods can thus be obtained by substituting estimates for:

$\sigma_{0,scWB} \approx 35 \times 10^{-6}$ m
$t_{scWB} = 20$ s
$\sigma_{0,MWA} \approx 750 \times 10^{-6}$ m
$t_{MWA} = 720$ s

Substituting into (2) yields:

$$\frac{\mathrm{LOD_{scWB}}}{\mathrm{LOD_{MWA}}} = 0.0550\ldots$$

Additionally, we correct for partitioning losses in MWAs by accounting for a partition coefficient[4] of ~0.3 depending on the protein species of interest (see Note A.2) and diffusional protein losses of 40% in scWesterns, i.e. the scWestern assay for EGFP is expected to be at least $(1 \times 0.6)/(0.0550 \times 0.3) \approx 36$-fold more sensitive than a comparable MWA considering the effect of differences in aliquoting and separation length/time alone, which is within 20% of the 45-fold improvement from empirical comparison of the estimated limits of detection of scWesterns and MWAs (see "*Quantitative performance and calibration of scWesterns*" in Chapter 2).

Note A.6. Calibration of scWesterns using purified proteins.
In order to determine the linear dynamic range and limit of detection of the scWestern assay, we devised two methods to calibrate it using purified proteins (Figs. 2.2d and A.11,12). The first ("direct") method relies on direct measurement of EGFP concentrations in microwells immediately before separation, capture and probing, for microwells incubated with a range in nominal concentrations of EGFP. The endpoint probe fluorescence is plotted on a curve against the number of EGFP molecules originally present in the corresponding microwell, inferred by calibrating the EGFP fluorescence measurements against those made in microchannels of the same depth as the thickness of the scWestern gel sheet (30 μm). The second ("indirect") method does not require direct measurement of the protein molecules present within the microwells, and instead uses large spot exposures to capture purified proteins from free solution, where their gel concentrations are inferred from partition coefficient measurements (Fig. A.4). The end result is a calibration curve of the fluorescent probe readout for a given protein against the number of protein molecules present within a spot roughly the size of that expected if the captured protein had originated from a single cell in an scWestern experiment. Thus, lower concentrations of proteins than can be directly observed can be used in the indirect calibration curve, since the gel concentration of a given protein is known from the nominal solution concentration and the partition coefficient.

The efficacy of antibody stripping was verified for the indirect EGFP calibration slide, showing residual signal at the detection threshold (SNR = 3) for the majority of the calibration range (from ~10^4–10^6 molecules), and fold-reductions in SNR of >10 above this range (Figs. 2.2d and A.12).

Note A.7. Statistical analysis of scWestern and ICC data in FGF stimulation experiments (Fig. 2.3d-f).
Fold-change ratios at 12 and 20 min maxima in the single-cell pERK:ERK and pMEK:MEK scWestern data, respectively, differed significantly from corresponding time zero ratios (pERK:ERK: Mann-Whitney $U = 537$, $n_{0\ \mathrm{min}} = 186$, $n_{12\ \mathrm{min}} = 57$, $P < 0.001$; pMEK:MEK: Mann Whitney $U = 6{,}884$, $n_{0\ \mathrm{min}} = 186$, $n_{20\ \mathrm{min}} = 236$, $P < 0.001$). For context, average fold-changes for β-tubulin, ERK, and MEK by scWestern analysis were <1.6 across cell populations at each stimulation time (Fig. A.21). Similarly, fold-change ratios at 5 and 20 min maxima for pERK:ERK and pMEK:MEK ICC data (Fig. A.17) differed significantly from corresponding

time zero ratios (pERK:ERK: Mann-Whitney U = 123, $n_{0\ min}$ = 160, $n_{5\ min}$ = 115, $P < 0.001$; pMEK:MEK: Mann-Whitney U = 6,653, $n_{0\ min}$ = 184, $n_{20\ min}$ = 223, $P < 0.001$). For context, average fold-changes for ERK and MEK by ICC were <1.5 across cell populations at each stimulation time (Fig. A.17).

Note A.8. Molecular mass analysis of SOX2.
For the differentiation experiment (Fig. 2.4d), each target protein was within 20% of its expected mass as determined by conventional western blotting, except for SOX2. SOX2 differed by 28% from its nominal mass of 34 kDa. Differences in the observed SOX2 mass may have arisen from one of three sources: (i) the high p*I* of SOX2 (p*I* = 9.7) and the denaturing, but non-reducing PAGE conditions used in the scWestern, (ii) the limited lysis time and differential impact on extraction of SOX2 from the nucleus as compared to the other protein targets, which are all cytosolic, or (iii) off-target probing.

A.3 References

1. Alberti, S., Stovel, R. & Herzenberg, L. A. Preservation of cells sorted individually onto microscope slides with a fluorescence-activated cell sorter. *Cytometry* **5,** 644–647 (1984).
2. Giddings, J. C. *Unified separation science*. (1991).
3. Hughes, A. J., Lin, R. K. C., Peehl, D. M. & Herr, A. E. Microfluidic integration for automated targeted proteomic assays. *Proc Natl Acad Sci USA* **109,** 5972–5977 (2012).
4. Tong, J. & Anderson, J. L. Partitioning and diffusion of proteins and linear polymers in polyacrylamide gels. *Biophys J* **70,** 1505–1513 (1996).
5. Hughes, A. J. & Herr, A. E. Microfluidic Western blotting. *Proc Natl Acad Sci USA* **109,** 21450–21455 (2012).
6. Shapiro, A. L., Viñuela, E. & Maizel, J. V. Molecular weight estimation of polypeptide chains by electrophoresis in SDS-polyacrylamide gels. *Biochem Biophys Res Commun* **28,** 815–820 (1967).
7. Cumming, R. C. *et al.* Protein disulfide bond formation in the cytoplasm during oxidative stress. *J Biol Chem* **279,** 21749–21758 (2004).
8. Go, Y.-M. & Jones, D. P. Redox compartmentalization in eukaryotic cells. *Biochimica et Biophysica Acta (BBA) - General Subjects* **1780,** 1273–1290 (2008).
9. Rath, A., Glibowicka, M., Nadeau, V. G., Chen, G. & Deber, C. M. Detergent binding explains anomalous SDS-PAGE migration of membrane proteins. *Proc Natl Acad Sci USA* **106,** 1760–1765 (2009).
10. Creighton, T. E. Disulfide bond formation in proteins. *Meth. Enzymol.* **107,** 305–329 (1984).
11. Ciaccio, M. F., Wagner, J. P., Chuu, C.-P., Lauffenburger, D. A. & Jones, R. B. Systems analysis of EGF receptor signaling dynamics with microwestern arrays. *Nat Methods* **7,** 148–155 (2010).

Appendix B: Supplementary Material for Chapter 3

This appendix is the product of a collaboration with Meimei Dong, PhD in the laboratory of Jay Groves, Ph.D

B.1 Supplementary Figures

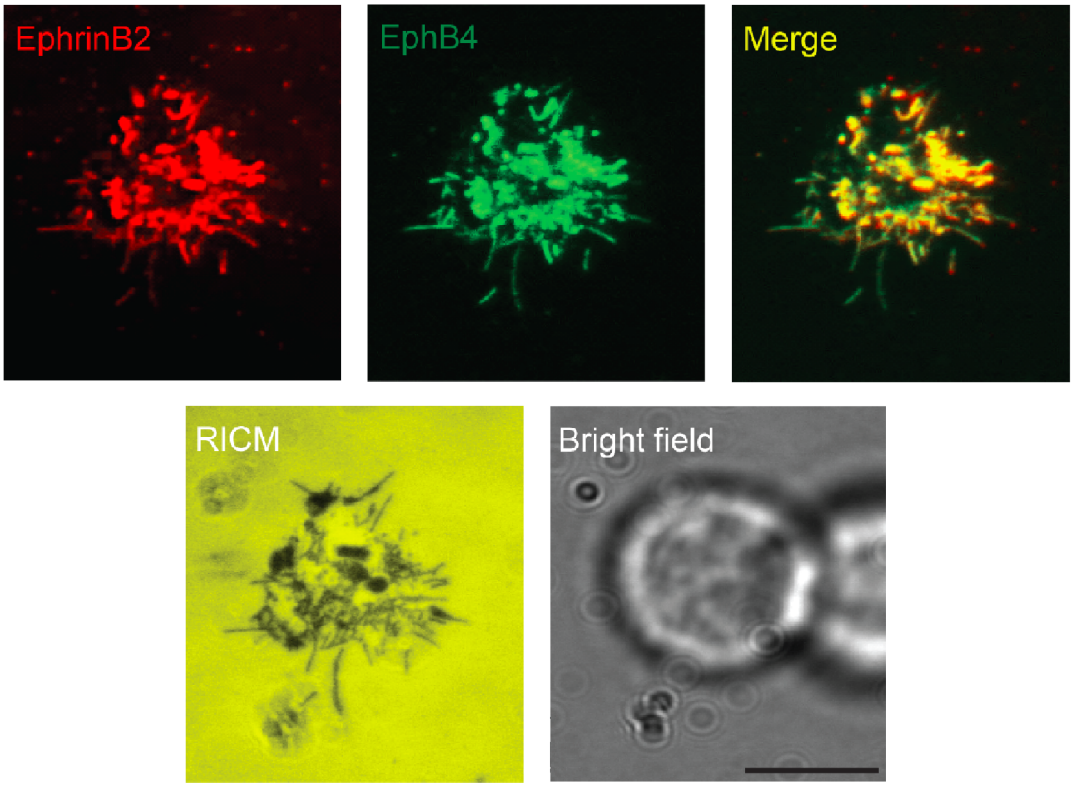

Figure B.1. TIRFM images of EphB4-mCherry expressing NSCs on an ephrin-B2 SLB. TIRF microscopy images were taken 45 min after seeding. Top left: ephrin-B2 on SLB (red); Top middle: EphB4 on NSC (green); Top right: merge of ephrin-B2 and EphB4 images (yellow); Bottom left: cell adhesion imaged by RICM; Bottom right: Brightfield image of adhered NSC. Scale bar, 10 μm

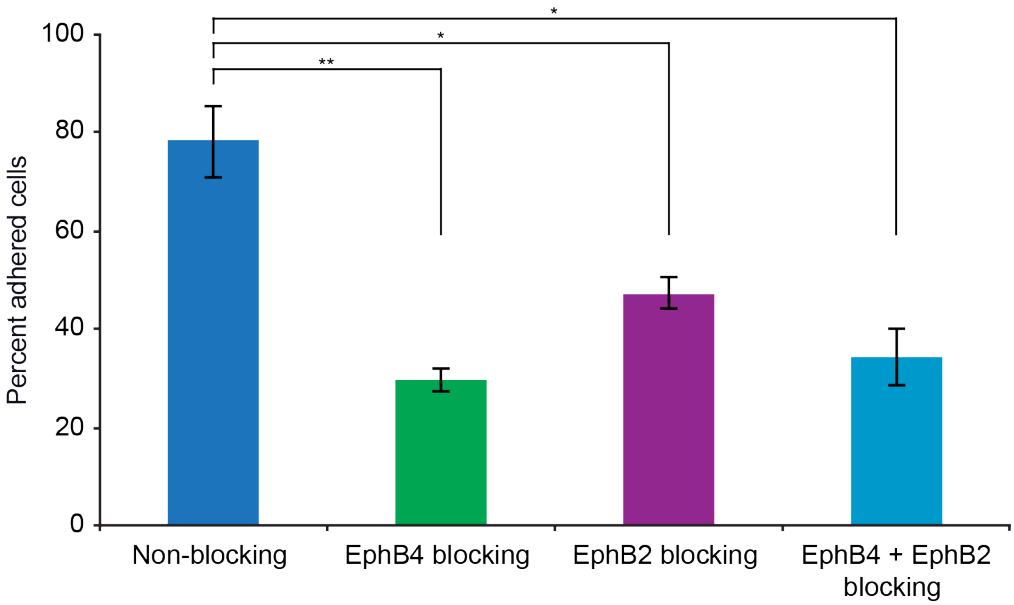

Figure B.2. NSC adhesion after Eph blocking. NSCs were pre-blocked with EphB4, EphB2, or EphB4 + EphB2 for 1 h then allowed to adhere to the SLB for 30 min. Percent adhered cells was calculated as cells detected by RICM/ total cells visible by bright field microscopy. *P < 0.05, **P < 0.01, ANOVA with Tukey-Kramer multiple comparison, n = 2 experimental replicates.

Appendix C: Supplementary Material for Chapter 4

C.1 Supplementary Tables

Table C.1. **Upregulated proteins in phosphotyrosine immunoprecipitation as analyzed by mass spectrometry in response to ephrin-B2 stimulation.** EphB4-mCh NSCs were stimulated for 45 m with HyA:ephrin-B2 or left untreated. Lysates were then immunoprecipitated with a phosphotyrosine antibody, trypsin digested, and sent for proteomic analysis by mass spectrometry. Spectral counts of proteins were compared between naïve and HyA:ephrin-B2-stimulated samples over three rounds of mass spectrometry. Proteins with increased spectral counts in HyA:ephrin-B2 treated samples in at least two data sets were determined to be upregulated. Bolded proteins indicate those chosen for further analysis.

Gene Name	Protein Name
AABR07065886.2	uncharacterized protein
Actb	actin, beta
Actc1	actin, alpha, cardiac muscle 1
Actg1	actin, gamma 1
Actn4	actinin alpha 4
Aip	aryl-hydrocarbon receptor-interacting protein
Alb	albumin
Atp5b	ATP synthase, H+ transporting, mitochondrial F1 complex, beta polypeptide
Bcar1	breast cancer anti-estrogen resistance 1
Cct3	chaperonin containing Tcp1, subunit 3 (gamma)
Cct8	chaperonin containing Tcp1, subunit 8 (theta)
Ckb	creatine kinase, brain
Cltc	clathrin, heavy chain (Hc)
Cnp	2',3'-cyclic nucleotide 3' phosphodiesterase
Coro1c	coronin, actin binding protein 1C
Cse1l	CSE1 chromosome segregation 1-like (yeast)
Ddx17	DEAD (Asp-Glu-Ala-Asp) box helicase 17
Ddx5	DEAD (Asp-Glu-Ala-Asp) box helicase 5
Dpysl2	dihydropyrimidinase-like 2
Eef1a1	eukaryotic translation elongation factor 1 alpha 1
Eef2	eukaryotic translation elongation factor 2
Efs	embryonal Fyn-associated substrate
Eif4a1	eukaryotic translation initiation factor 4A1
Ephb4	EPH receptor B4
Eprs	glutamyl-prolyl-tRNA synthetase
Erh	enhancer of rudimentary homolog (Drosophila)
Ezr	ezrin
Fyn	**FYN proto-oncogene, Src family tyrosine kinase**
Gapdh	glyceraldehyde-3-phosphate dehydrogenase
Git2	G protein-coupled receptor kinase interacting ArfGAP 2
Grn	granulin
Gstp1	glutathione S-transferase pi 1
Hist1h1b	histone cluster 1, H1b
Hist1h1d	histone cluster 1, H1d
Hist1h2ak	histone H2A
Hnrnpa2b1	heterogeneous nuclear ribonucleoprotein A2/B1
Hnrnpa3	heterogeneous nuclear ribonucleoprotein A3
Hpx	hemopexin

Hsp90aa1	heat shock protein 90, alpha (cytosolic), class A member 1
Hsp90ab1	heat shock protein 90 alpha (cytosolic), class B member 1
Hspa1l	heat shock protein 1-like
Hspa2	heat shock protein 2
Hspa5	heat shock protein 5
Hspa8	heat shock 70kDa protein 8
Hspa9	heat shock protein 9
Ighm	immunoglobulin heavy constant mu
Insr	insulin receptor
Khsrp	KH-type splicing regulatory protein
Krt1	keratin 1
Krt10	keratin 10
Krt15	keratin 15
Krt19	keratin 19
Krt4	keratin 4
Krt5	keratin 5
Krt7	keratin 7
Krt72	keratin 72
Krt73	keratin 73
Krt77	keratin 77
Krt8	keratin 8
Krt84	keratin 84
Ldha	lactate dehydrogenase A
LOC100360117	ribosomal protein L8-like
LOC100360413	eukaryotic translation elongation factor 1 alpha 1-like
LOC100360679	ribosomal protein S18-like
LOC100362298	ribosomal protein S18-like
LOC100362987	ribosomal protein S27-like
LOC100363469	ribosomal protein S24-like
LOC100910370	60S ribosomal protein L8-like
LOC100910474	myosin light polypeptide 6-like
LOC100912024	uncharacterized LOC100912024
LOC306079	similar to RIKEN cDNA 3100001N19
LOC684828	similar to Histone H1.2 (H1 VAR.1) (H1c)
LOC689899	similar to 60S ribosomal protein L23a
Ncl	nucleolin
Npm1	nucleophosmin
Pabpc1	poly(A) binding protein, cytoplasmic 1
Pabpc6	poly(A) binding protein, cytoplasmic 6
Pcbp2	poly(rC) binding protein 2
Pdgfra	platelet derived growth factor receptor, alpha polypeptide
Pfn2	profilin 2
Phgdh	phosphoglycerate dehydrogenase
Plekhg1	pleckstrin homology domain containing, family G (with RhoGef domain) member 1
Prss1	protease, serine, 1 (trypsin 1
Ptk2 (FAK)	**protein tyrosine kinase 2 (Focal adhesion kinase)**
Pxn	paxillin
RGD1561333	similar to 60S ribosomal protein L8
RGD1563145	similar to 60S ribosomal protein L13
RGD1566344	similar to eukaryotic translation elongation factor 1 alpha 1
Rpl14	ribosomal protein L14

Rpl17	ribosomal protein L17
Rpl23	ribosomal protein L23
Rpl24	ribosomal protein L24
Rpl4	ribosomal protein L4
Rpl7	ribosomal protein L7
Rpl8	ribosomal protein L8
Rplp0	ribosomal protein, large, P0
Rps14	ribosomal protein S14
Rps16	ribosomal protein S16
Rps18	ribosomal protein S18
Rps23	ribosomal protein S23
Rps27	ribosomal protein S27
Rps27a	ribosomal protein S27a
Rps27l	ribosomal protein S27-like
Rps27l2	ribosomal protein S27-like 2
Rps3	ribosomal protein S3
Rps8	ribosomal protein S8
Rpsa	ribosomal protein SA
Snx18	sorting nexin 18
Src	**SRC proto-oncogene, non-receptor tyrosine kinase**
Tmpo	thymopoietin
Tnk2 (Ack1)	**tyrosine kinase, non-receptor, 2 (Activated CDC42 kinase 1)**
Tpm1	tropomyosin 1
Tuba1a	tubulin, alpha 1A
Tubb2b	tubulin, beta 2B class IIb
Tubb4a	tubulin, beta 4A class IVa
Tubb4b	tubulin, beta 4B class IVb
Tubb5	tubulin, beta 5 class I
Tubb6	tubulin, beta 6 class V
Ubc	ubiquitin C
Uqcrc2	ubiquinol cytochrome c reductase core protein 2
Vcp	valosin-containing protein
Vim	vimentin
Ybx1	Y box binding protein 1

Table C.2. **Downregulated proteins in phosphotyrosine immunoprecipitation as analyzed by mass spectrometry in response to ephrin-B2 stimulation.** EphB4-mCh NSCs were stimulated for 45 m with HyA:ephrin-B2 or left untreated. Lysates were then immunoprecipitated with a phosphotyrosine antibody, trypsin digested, and sent for proteomic analysis by mass spectrometry. Spectral counts of proteins were compared between naïve and HyA:ephrin-B2-stimulated samples over three rounds of mass spectrometry. Proteins with decreased spectral counts in HyA:ephrin-B2 treated samples in at least two data sets were determined to be downregulated.

Gene Name	**Protein Name**
Actbl2	actin, beta-like 2
Atp5a1	ATP synthase, H+ transporting, mitochondrial F1 complex, alpha subunit 1, cardiac muscle
Hnrnpf	heterogeneous nuclear ribonucleoprotein F
Hnrnph1	heterogeneous nuclear ribonucleoprotein H1
Jup	junction plakoglobin
RGD1562055	similar to ribosomal protein L31
RGD1564839	similar to ribosomal protein L31

Tf	transferrin
Tuba4a	tubulin, alpha 4A
Tubb3	tubulin, beta 3 class III
Txn1	thioredoxin 1

Table C.3. **Upregulated proteins in EphB4-FLAG pull-down as analyzed by mass spectrometry in response to ephrin-B2 stimulation.** EphB4-mCh NSCs were stimulated for 30 m with HyA:ephrin-B2 or left untreated. Lysates were then pulled-down using FLAG agarose, trypsin digested, and sent for proteomic analysis by mass spectrometry. Spectral counts of proteins were compared between naïve and HyA:ephrin-B2-stimulated samples over three rounds of mass spectrometry. Proteins with increased spectral counts in HyA:ephrin-B2 treated samples in at least two data sets were determined to be upregulated.

Gene Name	**Protein Name**
AABR07008379.1	protein LOC100909878
AABR07011951.1	protein LOC102549957
AABR07027458.1	uncharacterized protein
AABR07042903.1	uncharacterized protein
AABR07043748.1	Eukaryotic translation initiation factor 5B
AABR07061003.1	uncharacterized protein
AABR07061057.1	uncharacterized protein
AABR07061078.1	uncharacterized protein
AC136661.1	uncharacterized protein
Actb	actin, beta
Actg1	actin, gamma 1
Actr2	ARP2 actin-related protein 2 homolog (yeast)
Atp5a1	ATP synthase, H+ transporting, mitochondrial F1 complex, alpha subunit 1, cardiac muscle
Atp5b	ATP synthase, H+ transporting, mitochondrial F1 complex, beta polypeptide
Cct8	chaperonin containing Tcp1, subunit 8 (theta)
Cdc37	cell division cycle 37
Ckb	creatine kinase, brain
Clasp2	cytoplasmic linker associated protein 2
Clns1a	chloride channel, nucleotide-sensitive, 1A
Ddx17	DEAD (Asp-Glu-Ala-Asp) box helicase 17
Ddx5	DEAD (Asp-Glu-Ala-Asp) box helicase 5
Eif2ak3	eukaryotic translation initiation factor 2 alpha kinase 3
Eif5b	eukaryotic translation initiation factor 5B
Ephb4	EPH receptor B4
Gapdh	glyceraldehyde-3-phosphate dehydrogenase
Hist1h1b	histone H1.5
Hist1h1d	histone cluster 1, H1d
Hist2h2aa2	histone cluster 2, H2aa2
Hist2h2ac	histone cluster 2, H2ac
Hnrnph1	heterogeneous nuclear ribonucleoprotein H1

Hspa8	heat shock 70kDa protein 8
Ighg	Immunoglobulin heavy chain (gamma polypeptide)
Ighm	immunoglobulin heavy constant mu
Krt1	keratin 1, type II
Krt5	keratin 5, type II
LOC100359616	60S ribosomal protein L36
LOC100359960	ribosomal protein S2-like
LOC100360150	eukaryotic translation elongation factor 1 alpha 2
LOC100360491	60S ribosomal protein L13
LOC100361060	ribosomal protein L36-like
LOC100364191	hCG1994130-like
LOC100911453	methylosome protein 50-like
LOC100911515	triosephosphate isomerase-like
LOC102555453	60S ribosomal protein L12-like
LOC680121	similar to heat shock protein 8
LOC680161	similar to 60S ribosomal protein L7a
LOC684828	similar to Histone H1.2 (H1 VAR.1) (H1c)
LOC686074	similar to 60S ribosomal protein L35
LOC689899	similar to 60S ribosomal protein L23a
Map2	microtubule-associated protein 2
Mdh2	malate dehydrogenase 2, NAD (mitochondrial)
Myh10	myosin, heavy chain 10, non-muscle
Myl6	myosin light polypeptide 6
Myl6l	Protein LOC100910474
Myo1c	myosin IC
Pfkm	ATP-dependent 6-phosphofructokinase, muscle type
Ppm1b	protein phosphatase, Mg2+/Mn2+ dependent, 1B
Rbbp4	retinoblastoma binding protein 4
Rbbp7	retinoblastoma binding protein 7
RGD1560789	similar to ribosomal protein S2
RGD1561333	similar to 60S ribosomal protein L8
RGD1563620	similar to retinoblastoma binding protein 4
RGD1563705	similar to ribosomal protein S23
RGD1565117	similar to 40S ribosomal protein S26
Rlf	rearranged L-myc fusion
Rpl11	ribosomal protein L11
Rpl12	ribosomal protein L12
Rpl12-ps1	60S ribosomal protein L10
Rpl26-ps2	ribosomal protein L26, pseudogene 2
Rpl30	ribosomal protein L30
Rpl36	ribosomal protein L36

Rps15a	ribosomal protein S15a
Rps15al2	ribosomal protein S15A-like 2
Rps2-ps6	ribosomal protein S2, pseudogene 6
Rps23	ribosomal protein S23
Rpsa	ribosomal protein SA
Shmt2	serine hydroxymethyltransferase 2 (mitochondrial)
Slc25a3	solute carrier family 25 (mitochondrial carrier, phosphate carrier), member 3
Sptbn1	spectrin, beta, non-erythrocytic 1
Tpi1	triosephosphate isomerase 1
Uba52	ubiquitin A-52 residue ribosomal protein fusion product 1
Ubc	polyubiquitin-C
Vcp	valosin-containing protein
Wdr77	WD repeat domain 77

Table C.4. **Downregulated proteins in EphB4-FLAG pull-down as analyzed by mass spectrometry in response to ephrin-B2 stimulation.** EphB4-mCh NSCs were stimulated for 30 m with HyA:ephrin-B2 or left untreated. Lysates were then pulled-down using FLAG agarose, trypsin digested, and sent for proteomic analysis by mass spectrometry. Spectral counts of proteins were compared between naïve and HyA:ephrin-B2-stimulated samples over three rounds of mass spectrometry. Proteins with decreased spectral counts in HyA:ephrin-B2 treated samples in at least two data sets were determined to be downregulated.

Gene Name	**Protein Name**
AABR07027451.1	uncharacterized protein
AABR07051726.1	uncharacterized protein
AABR07061044.1	uncharacterized protein
AABR07061048.1	uncharacterized protein
AABR07065438.1	60S ribosomal protein L6
Actc1	actin, alpha, cardiac muscle 1
Alb	albumin
Cnp	2',3'-cyclic nucleotide 3' phosphodiesterase
Col11a1	collagen alpha-1(XI) chain
Coprs	coordinator of PRMT5, differentiation stimulator
Eef1a1	eukaryotic translation elongation factor 1 alpha 1
Eif4b	eukaryotic translation initiation factor 4B
Epha2	Eph receptor A2
Epha4	Eph receptor A4
Epha5	EPH receptor A5
Epha7	Eph receptor A7
Epha8	Eph receptor A8
Ephb1	Eph receptor B1
Ephb3	Eph receptor B3
Flii	flightless I homolog (Drosophila)
Flna	filamin alpha

Gsn	gelsolin
Hdac6	histone deacetylase 6
Hectd4	HECT domain containing E3 ubiquitin protein ligase 4
Hnrnpu	heterogeneous nuclear ribonucleoprotein U
Hsp90aa1	heat shock protein 90, alpha (cytosolic), class A member 1
Hsp90ab1	heat shock protein 90 alpha (cytosolic), class B member 1
Hspa5	heat shock protein 5
Kctd17	potassium channel tetramerization domain containing 17
Krt42	keratin 42
Krt73	keratin 73, type II
LOC100360117	ribosomal protein L8-like
LOC100360604	ribosomal protein L21-like
LOC100361103	ribosomal protein L21-like
LOC100361811	ribosomal protein L21-like
LOC100361854	ribosomal protein S26-like
LOC100362366	40S ribosomal protein S17-like
LOC100910370	60S ribosomal protein L8-like
LOC100911372	40S ribosomal protein S6-like
LOC100911597	myosin-9-like
LOC100912267	40S ribosomal protein S24-like
LOC683961	similar to ribosomal protein S13
LOC684988	similar to ribosomal protein S13
LOC690096	similar to ribosomal protein L28
LOC691195	similar to ribosomal protein L21
Lrrfip1	leucine rich repeat (in FLII) interacting protein 1
Lrrfip2	leucine rich repeat (in FLII) interacting protein 2
Map1b	microtubule-associated protein 1B
Mybbp1a	MYB binding protein (P160) 1a
Myef2	myelin expression factor 2
Myh9	myosin, heavy chain 9, non-muscle
Myl12a	myosin, light chain 12A, regulatory, non-sarcomeric
Myl6b	myosin, light chain 6B, alkali, smooth muscle and non-muscle
Myo18a	myosin XVIIIa
Ncl	nucleolin
Npm1	nucleophosmin (nucleolar phosphoprotein B23, numatrin)
P4hb	prolyl 4-hydroxylase, beta polypeptide
Pabpc1	poly(A) binding protein, cytoplasmic 1
Ppia	peptidyl-prolyl cis-trans isomerase A
Prkra	protein kinase, interferon inducible double stranded RNA dependent activator
Prmt5	protein arginine methyltransferase 5
Prpf31	PRP31 pre-mRNA processing factor 31 homolog (Yeast) (Predicted)

Prss1	protease, serine, 1 (trypsin 1)
Psmd4	proteasome (prosome, macropain) 26S subunit, non-ATPase, 4
RGD1562469	similar to ribosomal protein L21
RGD1565183	similar to ribosomal protein L28
Rpl10	60S ribosomal protein L10
Rpl10a	ribosomal protein L10A
Rpl13	ribosomal protein L13
Rpl13a	ribosomal protein L13A
Rpl23	ribosomal protein L23
Rpl24	ribosomal protein L24
Rpl26	ribosomal protein L26
Rpl28	ribosomal protein L28
Rpl3	ribosomal protein L3
Rpl4	ribosomal protein L4
Rpl6	ribosomal protein L6
Rpl7	ribosomal protein L7
Rpl7a	ribosomal protein L7a
Rpl8	ribosomal protein L8
Rps13	40S ribosomal protein S13
Rps2	ribosomal protein S2
Rps26	40S ribosomal protein S26
Rps27a	ribosomal protein S27a
Rps27a-ps1	ribosomal protein S27a, pseudogene 1
Rps3	ribosomal protein S3
Rps3a	ribosomal protein S3a
Rps8	40S ribosomal protein S8
Rrbp1	ribosome binding protein 1
Scyl2	SCY1-like 2 (S. cerevisiae)
Setx	senataxin
Sptan1	spectrin, alpha, non-erythrocytic 1
Tmod3	tropomodulin 3
Tuba1a	tubulin alpha-1A chain
Tuba1c	tubulin, alpha 1C
Tubb2b	tubulin, beta 2B class IIb
Tubb4b	tubulin, beta 4B class IVb
Tubb5	tubulin beta-5 chain
Ybx1	Y box binding protein 1